The Dissertation Committee for Alexander John Heltzel certifies that this is the approved version of the following dissertation:

Laser/Microstructure Interaction and Ultrafast Heat Transfer

Committee:

John R. Howell, Supervisor

Shaochen Chen

John H. Davis

Ofodike Ezekoye

Li Shi

Laser/Microstructure Interaction and Ultrafast Heat Transfer

by

Alexander John Heltzel, B.S.; M.S.M.E.

Dissertation

Presented to the Faculty of the Graduate School of
The University of Texas at Austin
in Partial Fulfillment
of the Requirements
for the Degree of

Doctor of Philosophy

The University of Texas at Austin
August, 2006

Dedication

To my wife and my parents

Acknowledgements

I am sincerely grateful for the instruction provided by my advisor, Professor John R. Howell. His patient and astute guidance has made my time at the University of Texas a success. I am a wiser person and better engineer due to my experience with Dr. Howell.

I also deeply appreciate the help and advice from my other committee members, Dr. Shaochen Chen, Dr. John Davis, Dr. Ofodike Ezekoye, and Dr. Li Shi. From each, I have received unique and helpful instruction as well as exemplars for my new profession.

My parents loved me and taught me how to survive and now be a parent myself. For some reason, my wonderful wife now gives me the same unconditional love and support. This work would never have been written without my parents and my wife, therefore it is dedicated to them.

Laser/Microstructure Interaction and Ultrafast Heat Transfer

Publication No._____________

Alexander John Heltzel, Ph.D.
The University of Texas at Austin, 2006

Supervisor: John R. Howell

The industrial demand for smaller structures required for the manufacture of quantum devices, high-density recording media, etc., have resulted in the need for fabrication technology at the nanometer scale. However, most lithography and milling techniques are limited either by their inability for large-area fabrication or by the diffraction limit and in most cases the high manufacturing costs. To overcome the diffraction limit and to spatially-control matter on a nanometer scale, near-field optics techniques have been employed. It has been shown that laser/microstructure interaction can create surface modifications below the diffraction limit in both localized and parallel fashions.

This dissertation investigates laser/microstructure interaction using both numerical and analytical tools for computation. Two fundamental problems required for predictive optical nanolithography are addressed: the electrodynamic response of the laser energy in the vicinity of micro/nanostructures, and the resulting energy transport through the target material. The dissertation first concentrates on the interaction between lasers and dielectric microspheres. Analytical solutions provided by near-field Mie theory and numerical solutions to Maxwell's equations are obtained. Three-dimensional electromagnetic fields are resolved in the near-field of these spheres and functional dependencies on several experimental parameters are uncovered.

Energy transport through the substrate is modeled numerically in both two and three dimensions using conventional conduction formulae and ultrafast electron density evolution for the case of femtosecond pulse irradiation. The combined electrodynamic/heat transfer solutions generate final lithographic predictions which are compared to experimental characterizations.

The final segment of this dissertation investigates the interaction between lasers and gold, silver, and carbon nanotube structures for the purposes of optical lithography and photonic signal propagation. Fundamentals of surface plasmons, coupled electron/photon waves at conductor/dielectric interfaces, are explored computationally. Practical lithographic and photonic applications are optimized theoretically in an effort to advance knowledge in this area.

Table of Contents

List of Tables

List of Figures

Chapter 1:
Introduction

1.1 Motivation

Optical machining with lasers has been an important material processing tool since their invention in 1958. The confined property of laser radiation has made it valuable for applications ranging from cutting, drilling, welding, and marking, to micro-machining, ultrafast machining, surface activation, and ablation. Consequently, a fundamental understanding of laser-material interaction is needed to provide for descriptive and predictive design capabilities.

At a macroscopic level, the heat transfer and phase change resulting from continuous and long pulse (duration > 10^{-12} s) lasers is well understood and modeled successfully using Fourier's heat flux approximation. The combination of Fourier's law, which assumes an infinite speed of energy transport, and the principle of energy conservation have long since allowed investigators to determine the transient response of materials to an incident laser pulse.

The spatial and temporal limitations of these models have not been restrictive until recently. Due to clean features and small heat affected zone, ultrafast (sub-picosecond) lasers have become popular machining tools. Rapid development of femtosecond lasers in recent years has opened a further range of applications such as high-speed data transfer, quantum-bit fabrication, and waveguiding. The introduction of exciting new technologies coincides with the departure from standard theoretical modeling tools. The conventional representation of radiant energy input simply as an exponential decay from the surface is no longer accurate. In its place, three major processes are said to drive energy transport: excitation of conduction band electrons by impact and multi-photon ionization (MPI), excitation of conduction band electrons by radiation, and excitation of the lattice system by electrons and plasma. These complex, non-thermal processes are highly dynamic and require a deep understanding of the physics involved to obtain predictive modeling capability. The non-equilibrium situation between the electron and lattice systems of the material has made ultrafast laser/material interaction a challenging research topic. In this work, a physical model is utilized which describes the reaction of wide bandgap materials to ultrashort laser pulses. Quantitative predictions including threshold fluence, ablation depth, crater shape, and optical response of select materials to a range of femtosecond pulse inputs can be compared to experimental characterizations.

Only in the previous decade has laser/material interaction at the microscale become an investigative concern. Laser material processing in the nanometer range is very difficult or impossible using conventional optics due to the diffraction limit of the beam wavelength (on the order of hundreds of nanometers). Because the microprocessor and data storage industries have driven lithography technology to the nanometer scale, more expensive, non-diffraction limited methods of material removal such as electron-beam and ion-beam lithography are often used.

The recent discovery of optical near-field effects has resulted in a breakthrough that overcomes the diffraction limit and pushes the resolution down to tens of nanometers for optical imaging and measurement. Emerging applications, such as Near-field Scanning Optical Microscopy (NSOM) and Surface-enhanced Raman Spectroscopy (SERS) have proven the value of optical near-field effects and provoked much research into near-field laser material interaction. The physical mechanisms behind near-field optical phenomena are not entirely understood, though a number of analytical and numerical techniques can accurately describe the evanescent electromagnetic fields. This work presents an investigation into the dynamics of near-field enhancement and design parameters that optimize the phenomenon for useful applications. Analytical (Mie) theory is used for scattering of light from microspheres, and extended numerically to reveal the effect of complex geometries. The scattered and localized energy profiles are in turn coupled with both conventional and ultrafast heat transfer analysis to predict optical lithography results.

The localization and guiding of electromagnetic energy below the diffraction limit has generated enough interest to merit its own field of study: plasmonics. A surface plasmon polariton (SPP) is defined as a coherent electron oscillation confined to a metal/dielectric interface. An SPP generated by a coupling of incident light to an interface can propagate a distance of up to tens of micrometers, be processed as a logical signal, and convert back into light. This conception of a photonic circuit has sustained wide scientific research at a time when the heat generation of densely packed electronic circuits has become one of the largest barriers to increased miniaturization. Other uses of plasmon sub-wavelength optics include the generation of light through organic light-emitting diodes, enhanced solar cell absorption, and superlens capability.

Controlling subwavelength light remains a complicated design and fabrication problem. Generation of the plasmon requires bridging a momentum gap between the incident photons and the free electrons in the metal, usually accomplished by scattering from small topological defects which locally enhance the field. The energy is transferred to the surface electrons, which coherently oscillate at the interface. The plasmon can propagate in the interface plane, giving potential for signal transfer, but decays evanescently into the dielectric and metal. Choice of material, geometry, and surface texture allows tailoring of plasmon propagation distance, modes of oscillation, and even the existence of a full photonic bandgap, though the methodology is still uncertain. Thin metallic films have the ability to propagate plasmons up to distances of a centimeter, but lack mode confinement. Nanowires can confine subwavelength modes both longitudinally and laterally, but have shorter propagation lengths before radiant decay. Linear arrays of nanoparticles can theoretically confine modes and offer substantial propagation distances, with recent experimental confirmation.

An investigation into the metal-dielectric structures that support SPP's is an accessible extension of the aforementioned near-field enhancement study. This work presents theoretical calculations of the interaction between lasers and plasmonic nanostructures in an attempt to elucidate SPP behavior and introduce avenues of design. Maxwell's equations are discretized and calculations of the internal and external near-fields are given for a variety of potential photonic devices. A significant understanding of electromagnetic interaction at the microscale is achieved and presented.

1.2 Literature Review

A comprehensive picture of the current state of research is necessary to identify and understand meaningful progress. Though relatively young, the areas of ultrafast heat transfer/ablation, near-field electromagnetics, and plasmonics have substantial documented progress due to their exciting potential.

1.2.1 Ultrafast laser/material interaction

Laser heating of matter progresses through three general stages: radiation energy deposition on the electrons, exchange of energy between the electron and lattice systems, and the transport of energy through the lattice system. Several theoretical models have been presented to describe material transformation due to laser irradiation. Thermal studies by Olstad and Olander (1975a, 1975b), Chan and Mazumder (1987), and Ho et al. (1995) represent a progressive understanding of Fourier-based laser/material interaction. Maurer (1969) derived a hyperbolic heat conduction model for metals, which accounts for the finite speed of energy propagation, but neglected electron/lattice interaction. In a non-equilibrium state, the conventional idea of temperature must be expanded to address at least those two dynamic systems. Kaganov et al. (1957) first presented a theoretical analysis of electron and lattice system energy exchange. Anisimov et al. (1974) proposed a two-temperature (electron and lattice) model for short pulse laser heating of metals, but predicts an infinite speed of energy transport. Qiu and Tien (1993) attempted to resolve the inconsistencies and derived a two-temperature, finite-speed model from the Boltzmann transport equation. This hyperbolic two-step model given in Eq. (1.1) is popularly used today, but is limited to metals, i.e. electronic systems with populated conduction bands.

$$C_e(T_e)\frac{\partial T_e}{\partial t} = -\frac{\partial Q}{\partial x} - \frac{\partial Q}{\partial z} - G(T_e - T_l) + S \qquad (1.1a)$$

$$C_l(T_l)\frac{\partial T_l}{\partial t} = G(T_e - T_l) \qquad (1.1b)$$

$$\tau_F \frac{\partial Q}{\partial t} + \kappa\frac{\partial T_e}{\partial x} + \kappa\frac{\partial T_e}{\partial z} + Q = 0 \qquad (1.1c)$$

C_e and C_l are the electron and phonon specific heats, T_e and T_l are the electron and lattice (or phonon) temperatures, Q is the heat flux, S is the source term due to the volumetric laser absorption, G is the electron-phonon coupling factor, κ is the effective thermal conductivity, and τ_F is the thermal relaxation time. Note the hyperbolic form of the heat flux Eq. (1.1c) which accounts for finite speed of energy transport.

Phase change has been addressed through approximation within the two-temperature framework by Pronko et al. (1996), Anisimov and Rethfeld (1997), and Ye and Grigoropoulos (2001). The two-temperature model is limited, however, in its ability to accurately describe the plasma dynamics important to the ablation process. A key assumption used to derive Eqs. (1.1) from the Boltzmann transport equation is the domination of electron scattering by the phonons. Competing ionization mechanisms are neglected in favor of a continuum approach to increasing electron energy.

In wide bandgap materials like dielectrics, the majority of electrons are tightly bound to the ions. Electrical breakdown of glass by lightning was first investigated by Van Marum (1799). Electron breakdown due to laser irradiation of insulators was first modeled using the Fokker-Planck equation by Holway and Fradin (1974), and compared to experimental data by Sparks et al. (1981), Stuart et al. (1995), and Town et al. (1995), who performed experimental and theoretical analyses of ultrafast breakdown in dielectrics. The excitation and collisional (avalanche) ionization of the conduction electrons was modeled using the Fokker-Planck equation as a function of electron distribution, N(ε,t).

$$\frac{\partial N(\varepsilon,t)}{\partial t}+\frac{\partial}{\partial \varepsilon}\left[R_j(\varepsilon,t)N(\varepsilon,t)-\gamma(\varepsilon)E_p N(\varepsilon,t)-D(\varepsilon,t)\frac{\partial N(\varepsilon,t)}{\partial \varepsilon}\right]=S(\varepsilon,t) \quad (1.2)$$

where ε is the electron kinetic energy, R_j is the heating rate of the electrons, $E_p*\gamma*N$ is the rate of energy transfer from the electrons to the lattice, and $D*\partial N/\partial\varepsilon$ is the electron energy diffusion. S(ε,t) represents sources and sinks of electrons, including multiphoton ionization (MPI) and impact ionizations.

The Fokker-Planck evolution of free electron density is naturally material dependent. For femtosecond pulse durations, coefficients have been experimentally determined for fused silica (FS) and barium-aluminum borosilicate glass (BBS or Pyrex) in detailed studies by Lenzner et al. (1998). Several quantitative studies have described the femtosecond machining process. Optical breakdown thresholds of FS and BBS were determined by Perry et al. (1999) and Kautek et al. (1996), respectively. Comparisons between ultrafast and long pulse reactions have been presented by Zhao et al. (2001) and Stuart et al. (1996). Surface morphology of femtosecond laser ablated BBS has been discussed by Ben-Yakar et al. (2003). Both single-pulse and multi-pulse characterizations have been presented for glass by Campbell et al. (2005) and Ben-Yakar and Byer (2004).

The wealth of information gained from these experimental studies has been utilized in successive theoretical models. Ki and Mazumder (2005) put forth a combined finite-difference time-domain/two-temperature model for silicon describing femtosecond laser interaction with silicon. Jiang and Tsai (2005) and Heltzel et al. (2006) have employed the empirical constants determined by Stuart et al. (1995) in Fokker-Planck-based ablation models of BBS, where electron energies are treated quantum mechanically. Near-field enhanced femtosecond ablation of metals has been presented by Chimmalgi et al. (2005), and of glass by Zhou et al. (2006) and Heltzel et al. (2006).

1.2.2 Near-field electromagnetics

Near-field optics is a field of study dealing with evanescent, or vanishing, electromagnetic waves around mesoscopic objects. Mesoscopic refers to sizes on the order of incident wavelength, λ, therefore the evanescent waves corresponding to optical light are confined to regions in the range of 100 nanometers to about 1 micrometer. Theoretical understanding of these regions, which satisfy Maxwell's equations as do macro- and microscopic fields, is limited.

The existence of evanescent electromagnetic waves was first acknowledged in an analysis of the skin depth effect in metallic surfaces by Zenneck (1907) and Sommerfeld (1909). The following decades showed little interest or progress until the problem of light diffraction by subwavelength apertures was studied. The non-trivial form of the free space Green dyadic was established by Levine and Schwinger (1950), allowing resolution of the distorted electromagnetic field, although the near-field of the apertures was not investigated. Henry and Hopfield (1965) presented the concept of polaritons, or polarization waves in matter excited by incident light, and observed their dispersion relations using Raman spectroscopy. Their work elucidated the conditions under which evanescent waves existed at surfaces and interfaces. Attention was returned to the solution of light scattering by mesoscopic spheres by Mie (1908) and van de Hulst (1957). It was realized that observed coupling of small particles to planar surfaces was highly dependent on separation distance, corresponding to an exponential attenuation of the near-field of the particle. As stated in Bohren and Huffman (1983), it has long been recognized that the scattering of light from small particles differs from the scattering of the same bulk materials. Surface and geometrical effects become dominant at the mesoscale, responsible for both the evanescent fields of interest as well as analytical complexity that make their investigation a challenge.

There are currently several methods for quantitatively investigating near-field optics. A review of the coupled dipole approximation (CDA) technique is presented by Draine and Flatau (1994). Originally introduced in astrophysics to study optical properties of interstellar dust, CDA obtains the complete electric field around nanosystems from the internal field distribution, in turn calculated from individual dipole moments within the discretized volume. The direct space integral equation method (DSIEM) is described by Girard (2005) and Martin and Paulus (2002) as a volumetric integration technique which can successfully calculate the near-field of non-resonant dielectric nanostructures by using Green dyadic tensors to solve the integral form of Maxwell's equations. The method of perturbative diffraction theory makes the assumption that the fluctuation amplitude of a surface undergoing arbitrary excitation is negligible compared to the incident wavelength. Girard and Dereux (1996) indicate that the assumption limits a perturbative diffraction analysis to relatively smooth surfaces. Finally, the finite difference time domain scheme (FDTD) directly solves the time-dependent Maxwell's equations in differential form using an explicit "leap-frogging" technique. The FDTD method has achieved popularity due to its success over a wide range of length and frequency scales including versatility with dispersive materials (metals), as documented by Taflove and Hagness (2005). A thorough discussion of these methods and their origins can be found in reviews by Girard and Dereux (1996) and Girard (2005).

The initial interest in near-field optics stemmed from microscopy applications, but has expanded considerably in recent years. Near-field scanning optical microscopy was first developed by several independent groups in the 1980's (Betzig et al., 1986, Fischer et al., 1988, Reddick et al., 1989). Advancement in resolution has progressed steadily. Subwavelength spatial resolution was recently combined with nano-electron volt energy resolution by Guest et al. (2001) for coherent spectroscopy and microscopy of a quantum dot system. Milster (2001) presented a design for near-field optical data storage. Near-field optical thermometry techniques have been proposed by Goodson and Asheghi (1997) which theorized high potential sensitivity in the infrared range. Optical addressing of single nano-structures has been demonstrated by Maier et al. (2003a) and Chevalier et al. (2005). Microscale optical lithography using near-field enhancement has become attractive due to relatively low-cost ability to perform sub-diffraction limit machining. Lithographic studies have been presented by Kik et al. (2002), Lu and Chen (2003), and Zhou et al. (2006). Optical near-field applications involving surface plasmonics is reviewed in the proceeding section.

Radiative heat transfer due to evanescent electromagnetic waves has been discussed by Volokitin and Persson (2001), Pendry (1999), Carminati and Greffet (1999), and Loomis and Maris (1994). The added understanding they have provided is becoming increasingly important with the prevalence of nanofabrication, where optical fields are often the lithographic instrument. Micro- and nano-electromechanical systems must be designed with potential near-field enhancements in mind, and optical characterizations provided by Mullin et al. (2000), Balistreri et al. (2001), Krenn et al. (2002) and others contribute to this understanding.

1.2.3 Plasmonics

The field of plasmonics can derive its existence from the same works of Mie (1908), Sommerfeld (1909) and others who initiated the investigations into evanescent waves mentioned above. The specific physical distinction is that the evanescent field of a plasmon is the result of a coupled radiation/electron wave at the surface of a conductor. These oscillations, also referred to as surface plasmon polaritons (SPP's) were first analyzed by Ritchie (1957) during an analysis of energy loss by electrons in thin films. Their basic description as trapped light waves has initiated a flood of research focusing on, but not limited to, photonic circuit applications, sensing, and fabrication. Thorough reviews have been published recently by Homola et al. (1999), Kneipp et al. (2002), Barnes et al. (2003), and Maier and Atwater (2005a), and Ozbay (2006) just to keep pace with the explosive progress.

Single molecule direct detection first became possible when spectroscopic signals were noticed to exhibit strong enhancement when molecules were attached to gold or silver nanoparticles. This effect, noted by Fleischman et al. (1974) and confirmed by Jeanmaire and Duyne (1977) and Albrecht and Creighton (1977) became the principle of surface enhanced Raman spectroscopy (SERS). SERS-based plasmonics applications have proven exciting. Safanov et al. (1998) and Kneipp et al. (2002) have shown spatial resolution of smaller than 10 nm, even less than the NSOM systems noted above. Kneipp et al. (1998) have applied SERS to detecting individual bases in specific DNA fragments. Molecular sensitivity has opened the door to many biophysical SERS applications, noted in reviews by Cotton et al. (1991), Sokolov et al. (1993), and Kneipp et al. (2000). Work presented here is geared more toward optical circuit design and lithography, therefore the focus of current understanding will be on these technology niches.

Sambles et al. (1991) presented the condition requiring satisfaction in order for incident light to be coupled with surface charges of a noble metal. Equation 1.3 is the surface plasmon dispersion relation, which indicates the momentum of a surface plasmon mode, $\hbar k_{sp}$, is about 3% greater than the momentum of a free-space photon of the same frequency, $\hbar k_0$. ε_m and ε_d are the frequency dependent permittivities of the metal and dielectric.

$$k_{SP} = k_0 \sqrt{\frac{\varepsilon_d \varepsilon_m}{\varepsilon_d + \varepsilon_m}} \tag{1.3}$$

Momentum can be provided to the incident photons through prism coupling as shown by Otto (1968), scattering from a surface defect (Ditlbacher, 2002), or periodic corrugation of the metallic surface (Ritchie et al. 1968). All three techniques give rise to propagation of the combined radiation/electron wave parallel to the metal/dielectric interface, and exponential decay perpendicular to the interface. Worthing and Barnes (2001), showed how the coupling can be reversed, allowing the possibility of development of surface plasmon based photonic circuits, i.e. ones based on a logic signal carried by photons rather than an electric current. Along these lines, Teperik et al. (2004) theoretically analyzed the radiative decay of plasmons back into uncoupled light.

Modern experimental investigations of light interaction with metallic nanostructures are made possible through top-down fabrication technologies such as electron-beam and ion-beam lithography, colloidal synthesis, and other sophisticated techniques. Kuwata et al. (2003) was able to examine the scattering spectra of gold nanoparticles using dark field microscopy, which compared favorably to analytical Mie theory. Wurtz et al. (2003) characterized the optical scattering of individual silver and gold nanoparticles as well as linear arrays, noting intense peak intensity enhancements. Krenn et al. (1999) and Maier et al. (2002) observed collective excitations of surface plasmons on chains of gold nanoparticles. Plasmon propagation in solid nanowires was observed by Dickson and Lyon (2000), but it wasn't until Maier et al. (2003b) placed fluorescent detection particles between gold nanospheres in a chain, that local detection of electromagnetic energy transport along a plasmon waveguide was achieved. This was conclusive experimental evidence that a sub-diffraction limit photonic circuit is achievable. Later, Maier et al. (2005b) experimentally demonstrated an energy coupling of a nanoparticle plasmon waveguide with an optical fiber, which could potentially route the energy elsewhere for signaling or sensing.

Periodic arrays of nanoparticles and nanoholes can also exhibit useful plasmonic behavior. Kitson et al. (1996) and Barnes et al. (1997) showed that if a surface has periodicity of nanostructures, plasmonic modes can be prevented from propagating in any in-plane direction, creating a full photonic bandgap. More characterization of modulated surfaces was performed by Murray et al. (2004) who determined the dispersion of plasmon modes associated with periodic silver nanostructures.

A great deal can be learned about plasmonic behavior from advanced modeling techniques, and is a focus of this work. Yang et al. (1995) used a discrete-dipole approximation method to investigate energy enhancement due to nanostructures of arbitrary shape, primarily for Raman sensing applications. Sweatlock et al. (2005) used 3-D finite element integration techniques to solve Maxwell's equations in the vicinity of extremely small (~10 nm) irradiated silver particles, which predicted enormous 5000-fold increase in energy intensity with a particle spacing of 1 nm. Gray and Kupka (2003) presented a dispersive model incorporated in the FDTD architecture to model silver nanowires, obtaining accurate cross-sectional data. Oubre and Norlander (2004) used the FDTD method to calculate optical properties of metal-coated dielectric nanospheres, both smooth-surfaced and with realistic defects. Krug et al. (2002) resolved the electromagnetic field around conical gold nanotips using FDTD for optimizing design of near-field optical probes. Another FDTD analysis by Sun and Kim (2004) predicted the ability of plasmon-based metallic lenses, first proposed as a "superlens" by Pendry (2000). Recently Fang et al. (2005) experimentally confirmed sub-diffraction limit optical imaging with a silver superlens.

1.3 Dissertation outline

This work is presented in four sections. Sections two through four are segmented by investigations into microscale laser/material interaction, resulting heat transfer through adjacent materials due to the laser/material interaction, and an investigation into specific plasmonic behavior due to microscale laser/metal interaction.

Section two begins the analysis of laser/material interaction at the microscale by the calculation of analytical Mie theory of scattering for spheres. These calculations disregard any far-field and material approximations in favor of the more rigorous exact terms which can then provide for near-field solutions. A parametric study of the solutions is presented along with discussion of applications and limitations of the near-field. A numerical study based on the finite difference time domain (FDTD) method is then presented and compared to the analytical results. The numerical model is validated against analytical solutions for radiating dipoles and current sources. The FDTD study then extends to investigations which have no closed analytical form, including variations on microscale geometries and boundaries. A wide parametric study will show the effect on near-field energy distributions with variations of geometry, materials, separation distances, incident radiation angles, radiation frequencies, and solo particle vs. array effects.

Section three of this work presents the results of heat transfer analysis of surrounding substrates/materials due to both the incident and near-field energy distributions. Fundamental laser/material interaction is discussed, including conventional heat transfer due to incident radiation, phase change associated with the energy transport, and situations when conventional, or Fourier, heat transfer analysis is inadequate. Ultrafast analysis is then presented, along with a discussion of energy transport mechanisms at short time and length scales. Theoretical results for both conventional and ultrafast analyses are compared to experimental results.

The fourth and final section of this work presents a numerical investigation of laser/metal interaction at the nanoscale. The computations presented will elucidate the behavior and characteristics of surface plasmons generated at the boundaries of noble metals and air. A parametric study will show the variation in plasmon behavior with different materials, geometries, and laser sources. The use of plasmons for nanolithography applications is investigated using gold nanospheres on substrates. AFM/STM tip interaction with lasers for nanolithography is theoretically optimized through a series of simulations that uncover strong dependencies on experimental geometries and laser wavelengths. Novel modeling of carbon nanotube-based plasmonic waveguides is conducted, including the use of dielectric micro-amplifiers to provide signal propagation distances great enough for use in photonic circuit applications. A discussion of plasmonic behavior and applications is presented in an attempt to advance the knowledge of this field.

Appendices provide information on how an interested researcher can reproduce and extend the computational results presented here. A user's guide for the three-dimensional finite-difference time-domain code built for this dissertation is supplied as Appendix A. The computational techniques outlined in Chapter 2 can be used to predict intrinsic reflection and transmission properties for use in thermal radiation analyses. A demonstration of this is supplied in Appendix B.

Chapter 2:
Near-field Laser Enhancement around Microstructures

2.1 Experimental Setup

The focus of this work is analytical and computational study of laser/material interaction, which is necessarily compared to experimental data for validation and empirical purposes. Experiments have been performed at the University of Texas at Austin in a collaborative effort to advance fundamental knowledge and develop novel lithography tools. The general details of these experiments are briefly described to elucidate the means of correlation presented later.

The industrial demand for smaller structures required for the manufacture of quantum devices, high-density recording media, etc., have resulted in the need for fabrication technology at the nanometer scale. To overcome the diffraction limit and to spatially-control matter on a nanometer scale, several fabrication techniques based on near-field optics have been employed. One such technique creates structuring using the near-field created around a nanosphere by laser radiation. Experiments performed by Theppakuttai (2006) and Battula et al., (2006) are described here.

Silica microspheres of diameter on the order of laser wavelength are deposited on silicon substrate and irradiated with a pulsed Nd: YAG laser. As a result, nanofeatures are created on the surface by the melting and resolidification of silicon. The experiment is repeated for different laser wavelengths (532 nm, and 355 nm), sphere diameters (640 nm, and 1.76 µm) and laser energies, and the effect of each of these parameters on the features created have been studied.

The schematic of the experimental setup is shown in Figure 2.1a. The output from a pulsed Nd:YAG laser passes through a beam splitter, which splits the incident laser beam into two - one part for patterning and the other for measuring the laser energy. The sample is mounted on a 3-D stage and the laser beam is focused onto the sample by using a plano-convex lens. A single pulse from the laser is incident on the spheres as shown in Figure 2.1b. Since the sphere is resting on the substrate, the incident laser beam induces a near-field around the sphere which irradiates the silicon. This enhanced field is responsible for the formation of nanofeatures.

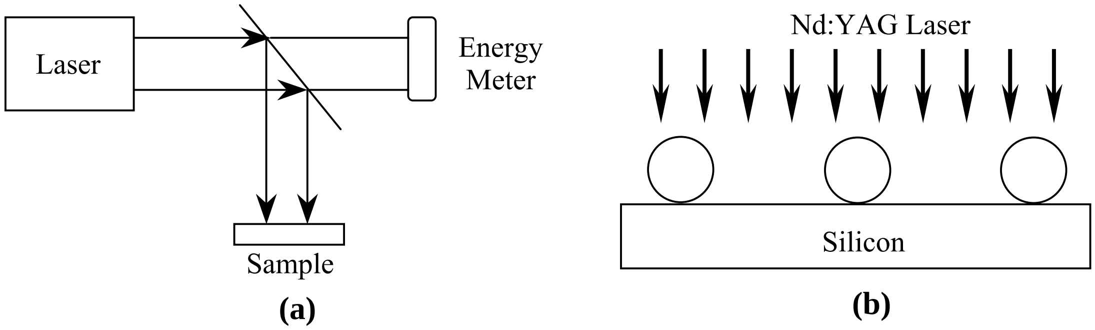

Figure 2.1: Laser irradiation of disperse silica spheres on silicon substrate: a) Schematic of the experimental setup, b) Schematic of silica microspheres on silicon

Such experiments can be performed with disperse concentrations of microspheres on the substrate surface or with close-packed arrays formed by self assembly due to surface forces. An SEM micrograph of a typical experiment and resulting damage to the substrate is shown in Figure 2.2, provided by Theppakuttai (2006).

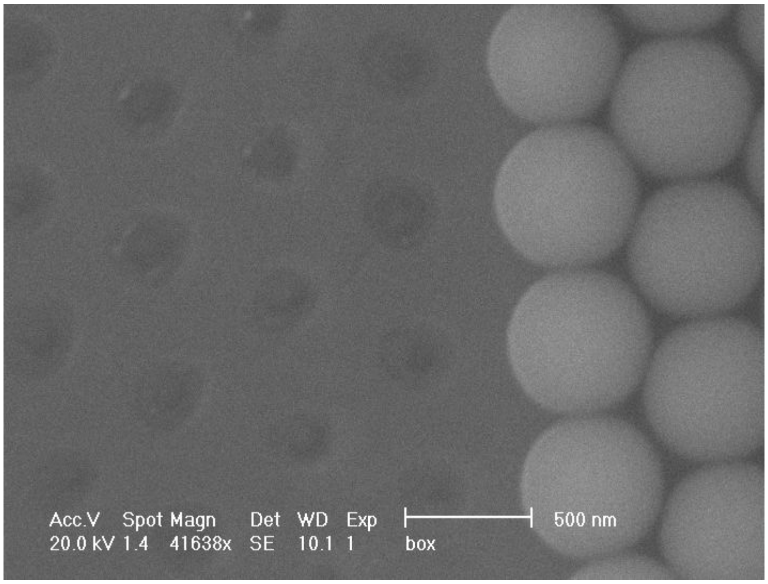

Figure 2.2: Scanning electron microscope image of self-assembled microspheres and near-field damage to substrate

2.2 Mie Scattering Analysis

The problem of resolving the effect of laser/microsphere interaction can be approached both analytically and numerically. There are inherent limitations and advantages of each method. An analytical solution should provide an unconditionally exact distribution of energy surrounding the sphere constrained only by approximations made during the solution procedure. No instability or numerical error will exist in the resulting electromagnetic field distribution. On the other hand, analytical solutions are only possible for very specific geometries and/or environments, which may or may not describe a realistic experiment. While limited in accuracy by inherent numerical considerations, a computational approach will provide far greater flexibility in simulation environment and material structure. The experiments described above are uniquely suited to both analytical and numerical study.

2.2.1 Analytical Mie Theory

The solution of plane monochromatic light scattering from a perfect sphere has been available since the work of Mie (1908) and is derived in detail by Born and Wolf (1999). This work provides a starting point for theoretical analysis of the laser/microsphere interaction described in section 2.1. The electric field components satisfying Maxwell's equations are given by

$$
\begin{aligned}
E_r^{(s)} &= \frac{1}{k^2}\frac{\cos\phi}{r^2}\sum_{l=1}^{\infty} l(l+1) eB_l \zeta_l^{(1)}(kr) P_l^{(1)}(\cos\theta), \\
E_\theta^{(s)} &= -\frac{1}{k}\frac{\cos\phi}{r}\sum_{l=1}^{\infty}[eB_l \zeta_l^{(1)}{}'(kr) P_l^{(1)}{}'(\cos\theta)\sin\theta - i\cdot mB_l \zeta_l^{(1)}(kr)\frac{P_l^{(1)}(\cos\theta)}{\sin\theta}] \qquad (2.1) \\
E_\phi^{(s)} &= -\frac{1}{k}\frac{\sin\phi}{r}\sum_{l=1}^{\infty}[eB_l \zeta_l^{(1)}{}'(kr)\frac{P_l^{(1)}(\cos\theta)}{\sin\theta} - i\cdot mB_l \zeta_l^{(1)}(kr) P_l^{(1)}{}'(\cos\theta)\sin\theta]
\end{aligned}
$$

The magnetic field components are given by

$$
\begin{aligned}
H_r^{(s)} &= \frac{1}{k^2}\frac{\sin\phi}{r^2}\sum_{l=1}^{\infty} l(l+1) mB_l \zeta_l^{(1)}(kr) P_l^{(1)}(\cos\theta), \\
H_\theta^{(s)} &= \frac{i}{k}\frac{\sin\phi}{r}\sum_{l=1}^{\infty}[eB_l \zeta_l^{(1)}{}'(kr) P_l^{(1)}{}'(\cos\theta)\sin\theta - i\cdot mB_l \zeta_l^{(1)}(kr)\frac{P_l^{(1)}(\cos\theta)}{\sin\theta}] \qquad (2.2) \\
H_\phi^{(s)} &= -\frac{i}{k}\frac{\cos\phi}{r}\sum_{l=1}^{\infty}[eB_l \zeta_l^{(1)}{}'(kr) P_l^{(1)}{}'(\cos\theta)\sin\theta - i\cdot mB_l \zeta_l^{(1)}(kr)\frac{P_l^{(1)}(\cos\theta)}{\sin\theta}]
\end{aligned}
$$

The coefficients eB_l and mB_l characterize the wave scattered by the sphere and are given by

$$eB_l = i^{l+1}\frac{2l+1}{l(l+1)}\frac{n\psi_l{}'(q)\psi_l(nq) - \psi_l(q)\psi_l{}'(nq)}{n\zeta_l^{(1)}{}'(q)\psi_l(nq) - \zeta_l^{(1)}(q)\psi_l{}'(nq)} \qquad (2.3)$$

$$mB_l = i^{l+1}\frac{2l+1}{l(l+1)}\frac{n\psi_l(q)\psi_l{}'(nq) - \psi_l{}'(q)\psi_l(nq)}{n\zeta_l^{(1)}(q)\psi_l{}'(nq) - \zeta_l^{(1)}{}'(q)\psi_l(nq)} \qquad (2.4)$$

The terms containing $P_l^{(1)}(\cos\theta)$ and its derivatives are forms of the associated Legendre functions (Abramowitz, 1965), (Lowan et al., 1945) defined as

$$P_l^{(m)}(\cos\theta) = (\sin\theta)^m \frac{d^m P_l(\cos\theta)}{d(\cos\theta)^m} \tag{2.5}$$

with the (non-associated) Legendre polynomial given by

$$P_l(\cos\theta) = \sum_{m=0}^{l/2} (-1)^m \frac{(2l-2m)!}{2^l\, m!(l-m)!(l-2m)!} (\cos\theta)^{l-2m} \tag{2.6}$$

$\zeta_l^{(1)}$ is proportional to the spherical Hankel function, which is a complex combination of first and second-order Bessel functions.

$$\zeta_l^{(1)}(\rho) = \psi_l(\rho) - i \cdot \chi(\rho) = \sqrt{\frac{\pi\rho}{2}} \cdot H_{l+\frac{1}{2}}^{(1)}(\rho) \tag{2.7}$$

The parameter, n, is the complex refractive index of the sphere. The parameter, k, in Eqs. (2.1) and (2.2) is equal to 2π divided by the wavelength of the incident laser. The parameter, q, is equal to k times the radius of the sphere. The final solution to Maxwell's equations both inside and outside the sphere is obtained by adding the scattered electromagnetic field components to the incident field components (plane wave of the laser) given by Eqs. (2.8) and (2.9), which have been reduced to the case of a sphere in a vacuum environment.

$$\begin{aligned} E_r^{(i)} &= e^{ikr\cos\theta}\sin\theta\cos\phi \\ E_\theta^{(i)} &= e^{ikr\cos\theta}\cos\theta\cos\phi \\ E_\phi^{(i)} &= -e^{ikr\cos\theta}\sin\phi \end{aligned} \tag{2.8}$$

$$\begin{aligned} H_r^{(i)} &= e^{ikr\cos\theta}\sin\theta\sin\phi \\ H_\theta^{(i)} &= e^{ikr\cos\theta}\cos\theta\sin\phi \\ H_\phi^{(i)} &= e^{ikr\cos\theta}\cos\phi \end{aligned} \tag{2.9}$$

There is some difficulty associated with the exact calculation of the field components, specifically the Bessel functions, Legendre functions, and their derivatives. Much of this difficulty can be circumvented by substituting asymptotic approximations for these terms that acceptably describe the field at a large distance from the particle. The critical coefficients eB_l and mB_l can be approximated for relatively large or highly conductive particles. In addition to individual term approximations, the overall intensity of the field is often approximated by squaring the amplitude of the electric vector. Under the conditions of the experiments presented, none of these simplifications can be acceptably included. Most importantly, the far field approximation cannot be utilized, as it is specifically the near field enhancement that is assumed responsible for the substrate damage.

Because of the limitations, all terms in Mie's theory, Eqs. (2.1) and (2.2), were calculated exactly up to the critical value of $l_{cut\text{-}off}$, after which the terms in the infinite sum were equal to zero. This was done through the use of recurrence relations for the Bessel functions and Legendre functions provided by Abramowitz and Stegun, (1965), and Lowan et al., (1945). General formulae for the Legendre relations are

$$P_1(\cos\theta) = \cos\theta$$

$$P_2(\cos\theta) = \frac{1}{2}\left(3(\cos\theta)^2 - 1\right) \tag{2.10b}$$

$$P_n(\cos\theta) = (2n-1)\cos\theta \cdot P_{n-1}(\cos\theta) - \frac{n-1}{n}P_{n-2}(\cos\theta) \tag{2.10c}$$

The derivatives of these functions were determined numerically, with 45,000 values calculated in the range of θ = 0 to 45°, with the origin taken at the center of the sphere. The summation cut-off value of *l*, was chosen to be

$$l_{cut-off} = \frac{2\pi \cdot a \cdot n}{\lambda} + 4 \tag{2.11}$$

where a is the sphere radius, n is the real refractive index of the sphere, and λ is the incident wavelength of the laser. An investigation was carried out to determine the effectiveness of the $l_{cut\text{-}off}$ value. The magnitude of the real and imaginary coefficients, eB_l and mB_l fell to zero through four decimal places by the final term included in the summation for all theoretical cases. Therefore $l_{cut\text{-}off}$ was chosen large enough to contain every term of value in the infinite series.

The intensity of the radiation incident on the plane of the substrate is quantified using the Poynting vector of the EM field. The spherical components of the time-averaged Poynting vector are

$$\begin{aligned} S_r &= I_0 \cdot \mathrm{Re}\left[E_\theta H_\phi^* - E_\phi H_\theta^*\right] \\ S_\theta &= I_0 \cdot \mathrm{Re}\left[E_\phi H_r^* - E_r H_\phi^*\right] \\ S_\phi &= I_0 \cdot \mathrm{Re}[E_r H_\theta^* - E_\theta H_r^*] \end{aligned} \tag{2.12}$$

I_0 is the intensity of the incident laser, and the asterisk superscript indicates the complex conjugate of the magnetic field components. The z-direction is taken longitudinal to the incident laser and normal to the substrate lying beneath the particle. The z-component of the Poynting vector is therefore a description of the energy incident upon the substrate surface due to the laser and the presence of the nanosphere. The coordinate convention used dictates the z-component equal to

$$S_z = \cos\theta \cdot S_r - \sin\theta \cdot S_\theta \tag{2.13}$$

Calculations have been performed for a range of sphere sizes, sphere materials, and incident wavelengths. Figure 2.3 indicates the two-dimensional plane of observation on which S_z is calculated. The plane corresponds to the location of the substrate on which the spheres lie.

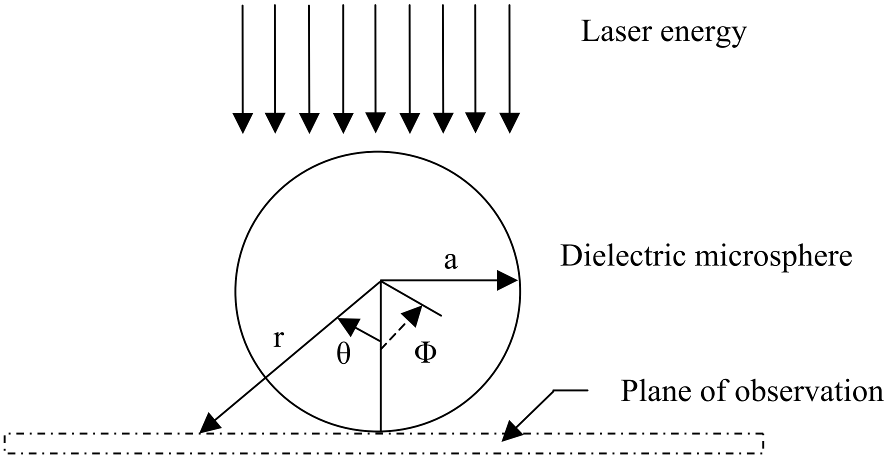

Figure 2.3: Coordinate system and Mie theory calculation domain

2.2.2 Wavelength Dependence

Figures 2.4a and 2.4b show the result of an intensity distribution calculation corresponding to experimental parameters: radius=0.88 μm, λ=532 nm, and n=1.37, the refractive index of silica. The resulting peak intensity predicted is approximately 15 times the incident intensity, and exists directly "underneath" the sphere. At this wavelength, the fluence required to damage the substrate is in the range of 400-450 mJ/cm^2. Theoretically, the enhancement predicted by the model would lower the input energy threshold to a value of roughly 25 mJ/cm^2.

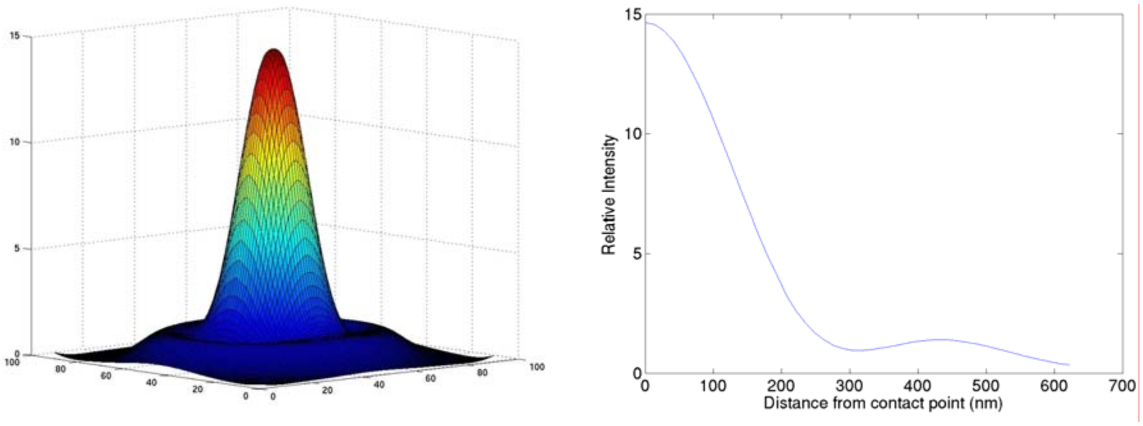

(a) (b)

Figure 2.4: Intensity enhancement on silicon surface due to laser/nanosphere interaction

Figure 2.4b indicates a confinement of the enhanced energy to a radius of about 300 nm, giving a near-field spot size of less than 600 nm, well under the peak diffraction limit resolution. The enhanced electromagnetic field is extremely dependent on the size of the microsphere as well as the sphere material and wavelength of incident light. Figure 2.5 shows the calculated intensity distributions surrounding a 1.76 µm silica sphere (refractive index, n=1.37) that would result from the four laser wavelengths available at UT-Austin’s Nano-Optical Bio-Engineering Laboratory (NOBEL).

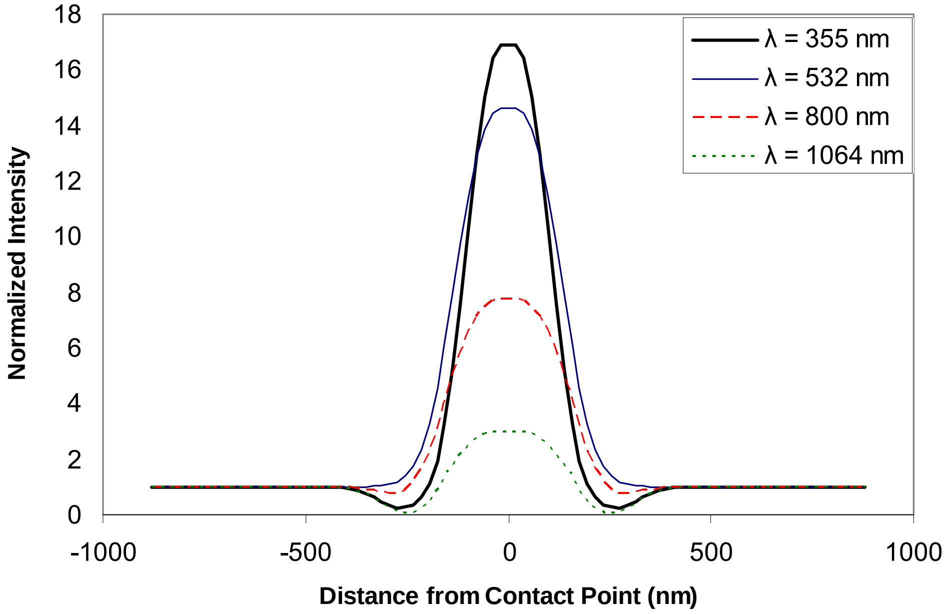

Figure 2.5: Laser intensity enhancement due to presence of 1.76 μm silica sphere

It is important to note that despite the implied two-dimensionality of incident energy, i.e. a revolution of Figure 2.4 about distance=0 would describe the energy surface, this is untrue. There is generally a weak dependence on the spherical angle, Φ, unnoticeable in Figure 2.4a, and negligible for the four cases presented in Figure 2.5. When the variation of enhancement with Φ is significant, it is assumed a result of polarization of the incident light.

Figure 2.5 exhibits the strong dependence on the near-field enhancement effect to the incident wavelength. An investigation was performed to determine the specific dependence on wavelength for the case of a 1.76 μm silica sphere. Results of these calculations are shown in Figures 2.6.

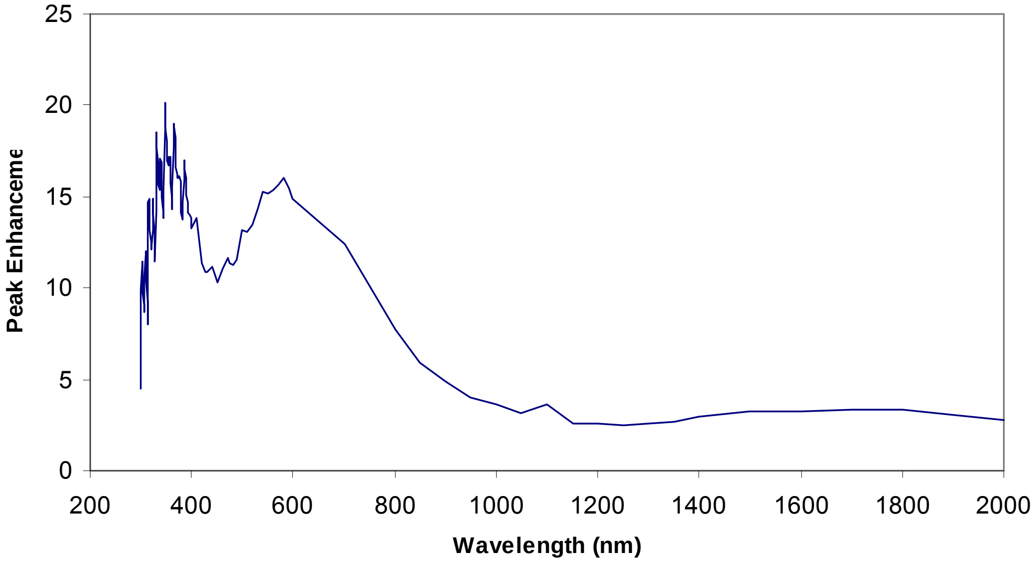

(a)

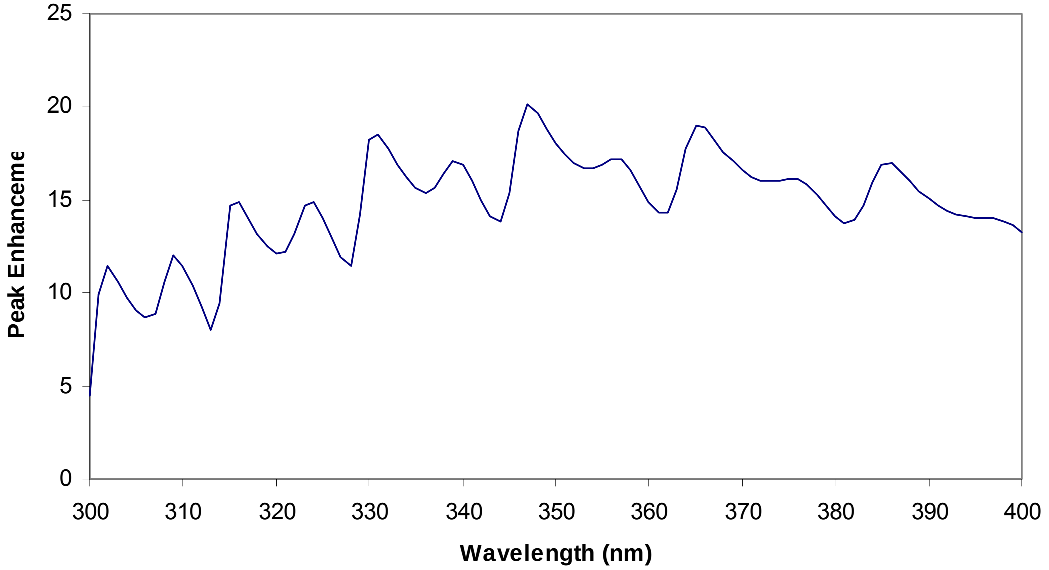

(b)

Figure 2.6: Wavelength dependence of near-field enhancement around a 1.76 μm silica sphere for (a) near-ultraviolet to near-infrared range and (b) expanded view of near-ultraviolet range.

Figure 2.6(a) gives the enhancement under the contact point of the sphere and plane of observation. What initially seems to be random fluctuation in the near-ultraviolet wavelength region, is shown to be regular local minima and maxima, seen in Figure 2.6b. These curves are superpositions of the harmonic resonances of the sphere and incident wave. It is clear that as the wavelength increases through the visible range, the period of these resonances increase and the magnitude decreases. Eventually, Mie theory, which describes interaction of wavelengths and spheres on the same order of size, could be replaced by the less rigorous Rayleigh scattering or geometric optics solutions.

Experiments have been performed in the NOBEL lab with silica spheres of diameter 640 nm in order to demonstrate confinement of light even further beyond the diffraction limit. Figure 2.7 predicts the near-field enhancement due to the lasers available and the smaller spheres.

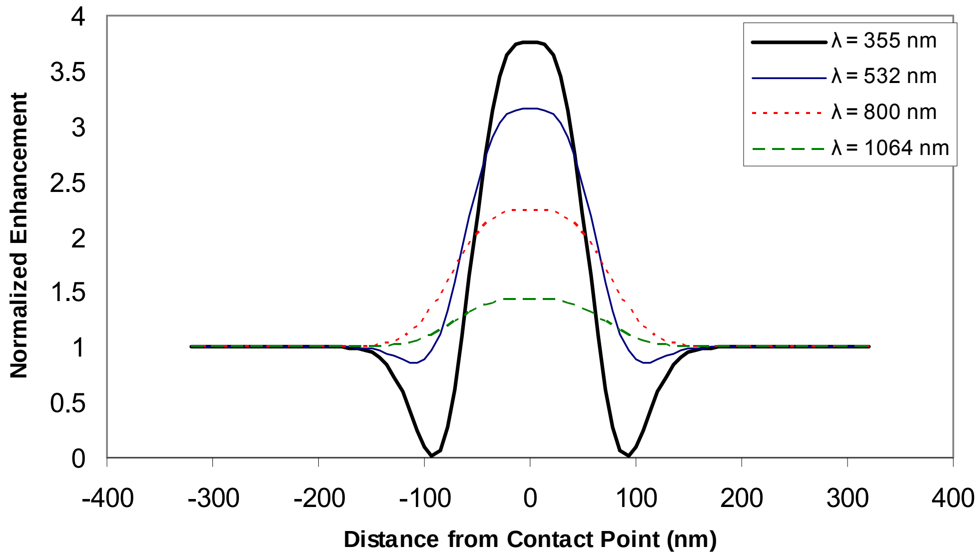

Figure 2.7: Laser intensity enhancement due to presence of 640 nm silica sphere

Comparing Figures 2.7 and 2.5, Mie theory predicts a much greater enhancement in the vicinity of the 1.76 μm sphere than the 640 nm diameter sphere. The energy is confined, however, to a roughly 200 nm spot size, a factor of three smaller than beneath a

1.76 μm sphere and approaching the lithographic resolution of much more expensive techniques such as e-beam and ion-beam lithography. Unlike the previous case, the near-field enhancement around the 640 nm sphere is very minimal when illuminated with infrared light. An investigation into the wavelength dependence surrounding the smaller sphere elucidates the dependence of the near-field enhancement on the size of the sphere.

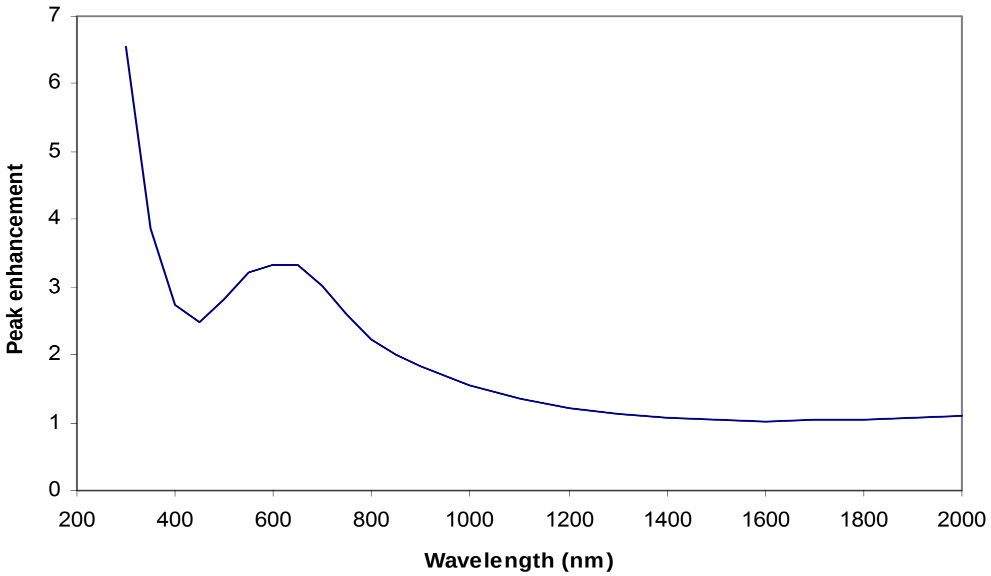

Figure 2.8: Wavelength dependence of near-field enhancement around a 640 nm silica sphere for near-ultraviolet to near-infrared range

2.2.3 Size factor dependence

Figure 2.8 predicts a local enhancement maximum of ~3.5*I_0, similar to Figure 2.6a, but at a much smaller wavelength. Upon examining the derivation of Mie's solution, it is recognized that the dependent variable of the Bessel functions was changed to be proportional to the ratio of sphere radius and wavelength. The curves in Figures 2.8 and Figure 2.6(a) are therefore mathematically similar, and can be reduced to a function of the new single variable, size factor $q=2*\pi*a/\lambda$. Figure 2.9 then presents the general dependence of near-field enhancement on the size factor, q, for a silica microsphere.

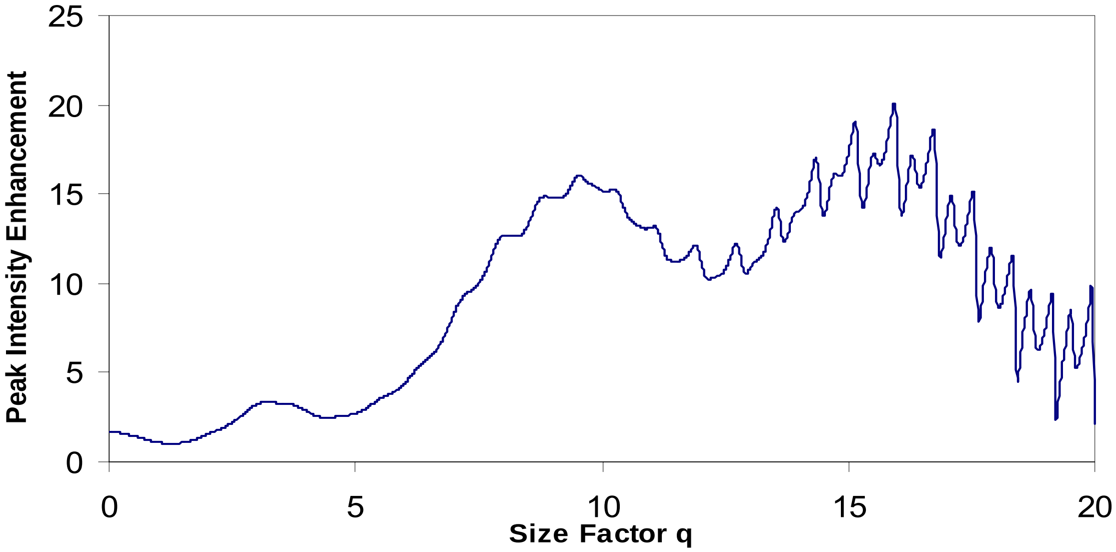

Figure 2.9: Size factor dependence of near-field enhancement for a silica sphere (n=1.37)

The enhancement effect demonstrates local maxima imposed on more global fluctuations, a consequence of the spherical harmonic functions that satisfy Maxwell's equations. Figure 2.9 provides the information needed to tailor the near-field effect to a specific application based on the amount of enhancement required.

2.2.4 Material dependence

Another useful investigation determines the dependence of the near-field effect on the sphere material. Polystyrene microspheres with a refractive index of n=1.589 have been used in near-field lithographic experiments in the NOBEL lab. Figure 2.10 shows the calculated enhancement profiles for the experimental cases of λ=355 nm and λ=532 nm with spheres of radius=0.88 μm for the different materials.

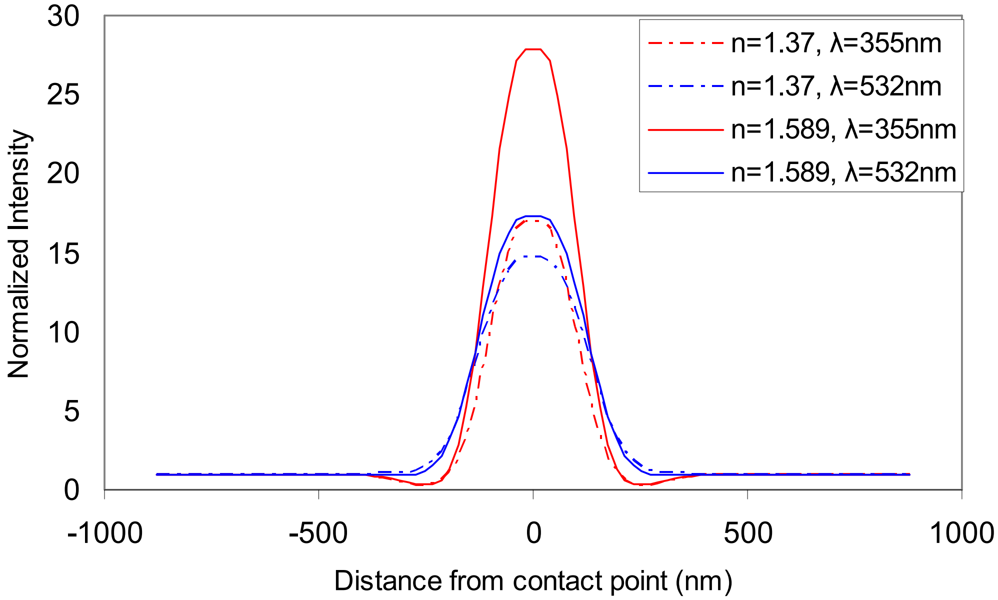

Figure 2.10: Intensity profiles around silica (n=1.37) and polystyrene (n=1.589) spheres

The higher refractive index of the polystyrene serves to increase the peak laser energy enhancement and slightly narrow the enhanced profile. This is a potentially useful effect if low-power optical lithography with the smallest possible spatial resolution is the goal. The peak enhancement as a function of the refractive index can be studied at discrete wavelengths. Referring to Figure 2.9, size factors of ~9 and ~16 are chosen to conduct the material dependence investigation because of the global maxima of enhancement at those points. Figure 2.11 predicts the near-field effect at these size factors throughout the logical range of refractive indices for dielectric materials.

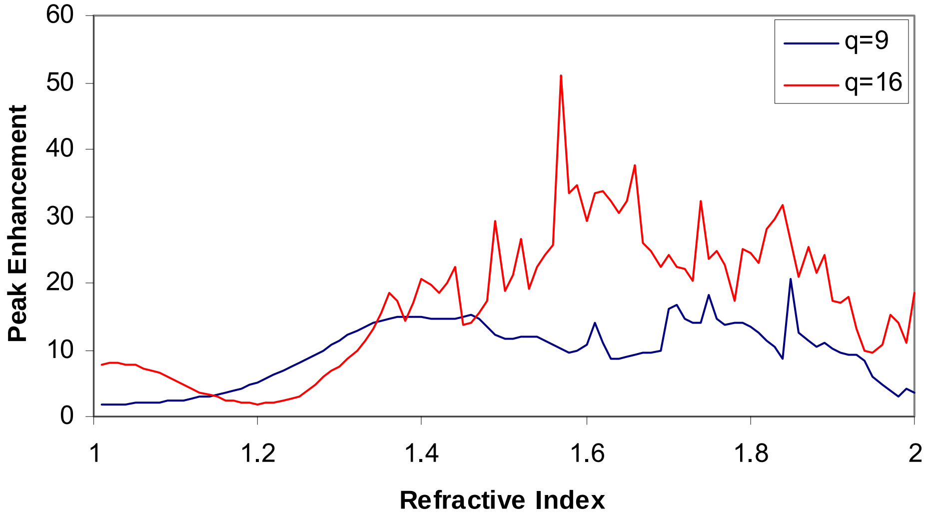

Figure 2.11: Material dependence of near-field Enhancement

In general, a higher refractive index is more likely to exhibit a stronger peak intensity enhancement, however there is much fluctuation in the distribution. One property common to both size factors is the smoothness of the curve as the index approaches one. Very specific combinations of sphere size, wavelength and material can produce intensity enhancements up to a factor of 50 or more. An application involving fusing or ignition initiated by the near-field energy may use design parameters obtained from a study of this type.

2.2.5 Evanescent decay

One last theoretical investigation of potential value is the decay of the near-field with distance from the sphere. Lithographically, this would apply to cases in which the laser is incident from an angle relative to the substrate, creating space between the “far side” of the sphere and substrate to be patterned. If a transparent film is coating the substrate, a user-defined separation could be created even with normal laser incidence. At a fundamental level, it is important to understand the evanescent behavior of electromagnetic energy surrounding a microscale object. Figure 2.12 presents intensity surface distributions on a plane of observation 250 nm (a) and 1μm (b) below a 1.76 μm silica sphere irradiated with a λ=532 nm wave. Figure 2.13 plots the normalized intensity at the would-be contact point beneath the sphere against sphere distance from the plane of observation.

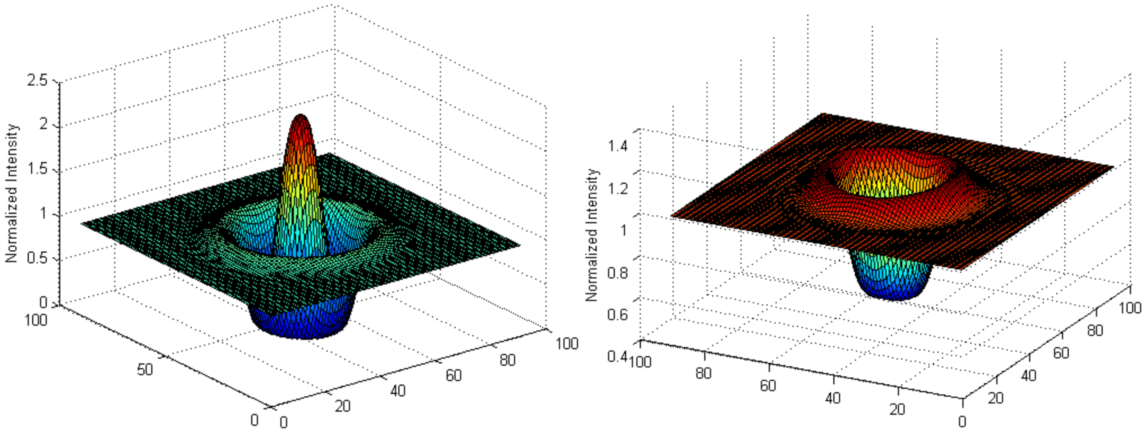

(a) (b)

Figure 2.12: Intensity profiles at plane of observation as 1.76 μm silica sphere is moved (a) 250 nm and (b) 1μm from plane.

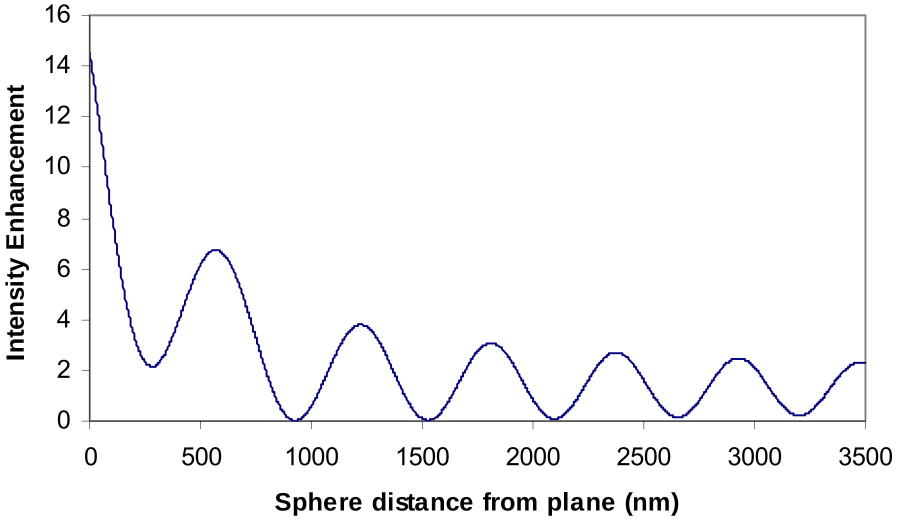

Figure 2.13: Near-field decay of energy with distance from microsphere surface

Comparing Figures 2.12(a) and 2.12(b) to Figure 2.4, it is evident that the peak energy enhancement rapidly diminishes with distance from the sphere boundary. Energy is distributed in complicated secondary and tertiary peaks under the sphere. Referring to Figure 2.13, the near-field quickly decays, though not quite in the smooth exponential manner assumed by many researchers. At two full diameters distance from the plane of observation (3520 nm), the spatially averaged intensity is slightly above unity, and the near-field can be considered decayed. From a mathematical standpoint, the oscillations are a result of the Bessel functions in Eqs. (2.1) and (2.2). These terms are normally approximated in the far field by exponentials, but are calculated exactly in this study.

A final Mie theory calculation, pictured in Figure 2.14 gives decay plots for several size factors. Because distance from the observing plane is specified along the x-axis, it is necessary to define a datum for sphere size. In this case, the microsphere diameter was held constant at 1.0 μm, while q was varied by changing the incident wavelength. Therefore, the plot extends to two diameters separation distance in all cases.

Oscillatory decay is predicted for all cases. It is interesting to note that only one of the cases (q=9) exhibits the most intense enhancement with the sphere resting on the surface. The three other calculations show moderate to mild increase with initial separation, following a more general decay that could be fit to an exponential if spatially averaged. This effect, if a reality and not a mathematical artifact, could have potential applications involving sub-surface modification where an interior zone of a low-loss dielectric is affected more intensely by laser radiation than the surface.

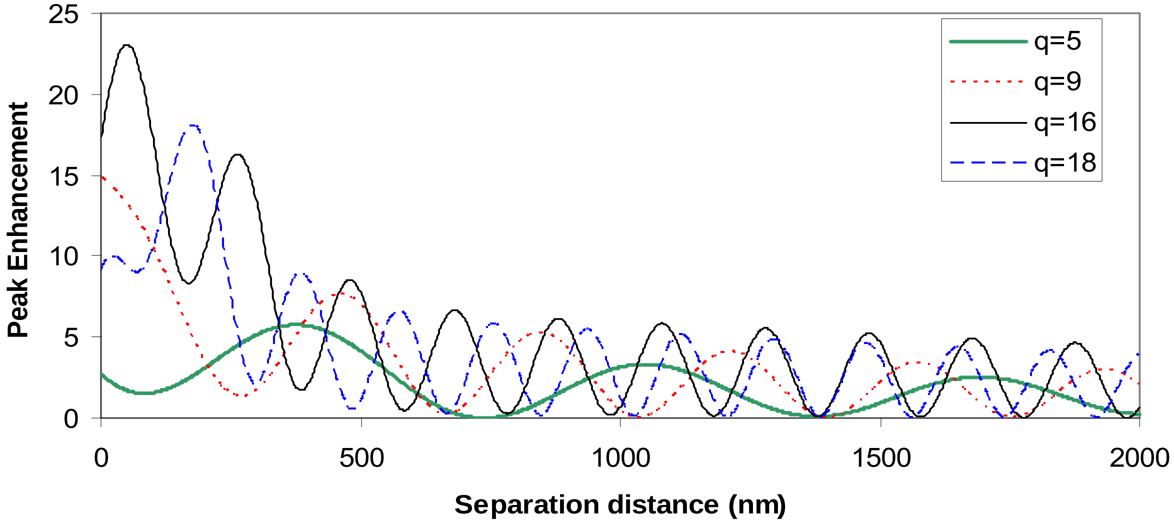

Figure 2.14: Near-field decay of energy with distance from microsphere surface, various size factors

2.2.6 Limitations of Mie analysis

At this point, it is useful to discuss the limitations of the calculations presented. While the analytical form is extremely useful for conducting the variable dependence investigations given above, there are mitigating factors that compromise their correlative value. To begin, Mie theory is often used as a validation tool by which to compare numerical light scattering codes in the far-field. At large distances from the sphere, this is an accurate and valuable tool because the approximations used in the solution only negligibly affect the resulting spectrum. However, despite the fact that the calculations presented here do not rely on the exponential or perfectly-conducting approximations, the derivation of Mie's original solution contains a similar far-field approximation when obtaining the Debye potentials for satisfaction of the boundary conditions of the problem (Born and Wolf, pp. 760-783). This approximation is based on the fact that at large distances from the sphere, the scattered wave is geometrically spherical. It is unclear whether this holds in the near-field and is a potential source of error. This topic will be revisited later in this chapter.

A more experimental consideration has to do with the effect of the substrate itself on the distribution of energy it "sees". Reflection between the flat and spherical geometries will occur and have been assumed responsible for modification of the near-field intensity (Huang et al., 2002). The material of the substrate itself would undoubtedly weight the geometric reflection based upon its own dielectric function. Mie theory is unable to account for this reflection. Others have presented solutions for the cases of spheres on mirror-like surfaces (Nahm and Wolfe, 1987, Bobbert and Vlieger, 1986), but the solutions are constricted to special cases, and do not account for any potential effect of nearby spheres such as those shown in Figure 2.2. Mie theory also does not account for any array effect, and must be considered limited by these arguments.

2.3 The Finite-Difference Time-Domain (FDTD) Method

Numerically solving Maxwell's equations eliminates the constraints of Mie theory described above. In their stead, other considerations arise including numerical inaccuracy, computational expense, and stability which will all be discussed. The finite-difference time-domain (FDTD) method was chosen as the investigative technique because it has the ability to incorporate arbitrary geometries as well as both dielectric and metallic materials used in NOBEL lab experiments.

2.3.1 Numerical development

The FDTD method explicitly marches through time by solving Maxwell's curl equations at the nodes of a discretized spatial grid. The relations are given by Eqs. (2.14) for a linear, isotropic material.

$$\nabla \mathrm{x} \mathrm{E} = -\mu \frac{\partial \mathrm{H}}{\partial t} \tag{2.14a}$$

$$\nabla \mathrm{x} \mathrm{H} = \sigma \mathrm{E} + \varepsilon \frac{\partial \mathrm{E}}{\partial t} \tag{2.14b}$$

The vectors E and H are the electric and magnetic field components, respectively, while ε is the electrical permittivity, σ is the electric conductivity, and μ is the magnetic permeability.

Kane Yee (1966) developed the algorithm to solve for both electric and magnetic field components in time and space. Solution of all field components allows treatment of both electric and magnetic materials, an advantage over previous methods of solving either the electric or the magnetic fields with a wave equation. The Yee algorithm is based upon the staggered lattice he introduced called the Yee cell, shown in Figure 2.15.

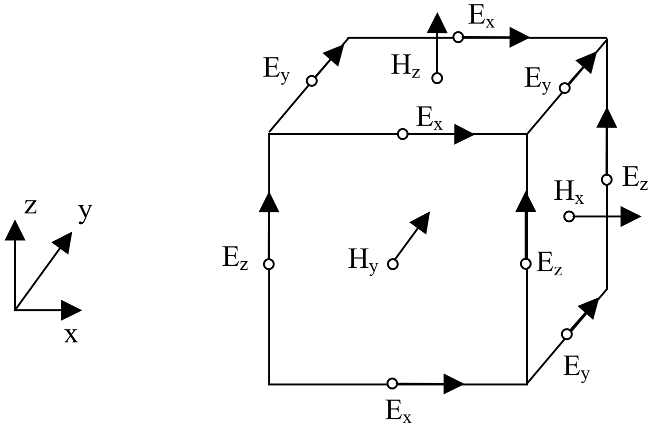

Figure 2.15: Electric and magnetic field components in a unit Yee cell

The solution method involves a leapfrog procedure in which the electric fields are solved using finite-differences at integer time-steps, while the magnetic components then access the electric vectors at integer-plus-1/2 time steps. This procedure as well as many advanced techniques are detailed in Taflove and Hagness (2005).

In anticipation of simulating metallic materials in the plasmonics investigation of Chapter 4, the current density form of Maxwell's equations are used, which can treat negative real parts of the dielectric function defining reflection from metals as well as positive values defining dielectrics.

$$\frac{\partial \mathrm{E}}{\partial t} = \frac{1}{\varepsilon}\left[\nabla \mathrm{x}\mathrm{H} - \mathrm{J}\right] \tag{2.15a}$$

$$\frac{\partial \mathrm{H}}{\partial t} = -\frac{1}{\mu}\left[\nabla \mathrm{x}\mathrm{E}\right] \tag{2.15b}$$

$$\frac{\partial \mathrm{J}}{\partial t} = k_d \mathrm{J} + \beta \mathrm{E} \tag{2.15c}$$

where J is the electric current density vector, and k_d and β are material-based coefficients to be defined in Chapter 4.

Nano-optical simulations that realistically describe NOBEL lab experiments require additional FDTD implementations to the basic algorithm. One of the most important aspects of any FDTD environment is the boundary condition. In order to prevent spurious reflection of electromagnetic waves at the grid edges, an absorbing boundary condition (ABC) is needed. Mur (1981) and Liao et al. (1984) presented ABC's based on gradients in time and space. Though successful, both methods become unstable at many thousands of time steps and lose accuracy based on the incident angle of the wave at the boundary. Berenger (1994) introduced the perfectly-matched layer (PML) which eliminated angle dependence, increased absorption levels by two orders of magnitude and remained stable at the cost of splitting the field components and a difficult implementation. Gedney (1996) then presented the anisotropic PML or uniaxial PML (UPML) which retained the un-split field components and was proven mathematically identical to Berenger's PML. Currently the UPML is used by many high-end commercial and research codes with success. Roden and Gedney (2000) further increased the absorption precision and computational efficiency by an order of magnitude with their convolution PML (CPML). Gedney et al. (2001) have characterized the relative error due to the reflected wave that re-enters the FDTD environment with a ten cell CPML at $\sim 10^{-5}$ to 10^{-6}. The CPML is the most advanced and flexible ABC available, and is implemented in this work due to its accuracy and abilities to absorb evanescent waves and treat dispersive materials such as the noble metals in the plasmonic investigation of Chapter 4.

The discretized versions of field components E_x, J_x, and H_x *with CPML incorporation* used for the explicit updates are given by

$$
\begin{aligned}
E_x\big|^{n+1/2}_{i+1/2,j,k} &= C_a\big|_{i+1/2,j,k}\, E_x\big|^{n-1/2}_{i+1/2,j,k} \\
&+ C_b\big|_{i+1/2,j,k}\left(\begin{array}{c}
\dfrac{H_z\big|^{n}_{i+1/2,j+1/2,k} - H_z\big|^{n}_{i+1/2,j-1/2,k}}{\kappa_{y_j}\Delta y} - \dfrac{H_y\big|^{n}_{i+1/2,j,k+1/2} - H_y\big|^{n}_{i+1/2,j,k-1/2}}{\kappa_{z_k}\Delta z} \\
+\psi_{E_{x,y}}\big|^{n}_{i+1/2,j,k} - \psi_{E_{x,z}}\big|^{n}_{i+1/2,j,k} - \dfrac{1}{2}\left(1+k_d\right)J_x\big|^{n-1/2}_{i+1/2,j,k}
\end{array}\right)
\end{aligned}
\tag{2.16}
$$

$$
J_x\big|^{n+1/2}_{i+1/2,j,k} = k_d J_x\big|^{n-1/2}_{i+1/2,j,k} + \beta\left(\frac{E_x\big|^{n+1/2}_{i+1/2,j,k} - E_x\big|^{n-1/2}_{i+1/2,j,k}}{\Delta t}\right)
\tag{2.17}
$$

$$
\begin{aligned}
H_x\big|^{n+1}_{i,j+1/2,k+1/2} &= D_a\big|_{i,j+1/2,k+1/2}\, H_x\big|^{n}_{i,j+1/2,k+1/2} \\
&- D_b\big|_{i,j+1/2,k+1/2}\left(\begin{array}{c}
\dfrac{E_z\big|^{n+1/2}_{i,j+1,k+1/2} - E_z\big|^{n+1/2}_{i,j,k+1/2}}{\kappa_{y_{j+1/2}}\Delta y} - \dfrac{E_y\big|^{n+1/2}_{i,j+1/2,k+1} - E_y\big|^{n+1/2}_{i,j+1/2,k}}{\kappa_{z_{k+1/2}}\Delta z} \\
+\psi_{H_{x,y}}\big|^{n+1/2}_{i,j+1/2,k+1/2} - \psi_{H_{x,z}}\big|^{n+1/2}_{i,j+1/2,k+1/2}
\end{array}\right)
\end{aligned}
\tag{2.18}
$$

where i, j, and k are the Cartesian indices. The terms $\psi_{E_{i,j}}$ and $\psi_{H_{i,j}}$ are stored only in the CPML regions with i-normal and j-normal interface boundaries and act as radiation sources to destructively interfere with the waves hitting the boundary. The CPML regions are ten-cell thick slabs on each of the six faces of the Cartesian FDTD environment. The CPML terms are defined by

$$
\psi_{E_{x,y}}\big|^{n}_{i+1/2,j,k} = b_y\psi_{E_{x,y}}\big|^{n-1}_{i+1/2,j,k} + c_y\left(\frac{H_z\big|^{n}_{i+1/2,j+1/2,k} - H_z\big|^{n}_{i+1/2,j-1/2,k}}{\Delta y}\right)
\tag{2.19a}
$$

$$
\psi_{E_{x,z}}\big|^{n}_{i+1/2,j,k} = b_z\psi_{E_{x,z}}\big|^{n-1}_{i+1/2,j,k} + c_z\left(\frac{H_y\big|^{n}_{i+1/2,j,k+1/2} - H_y\big|^{n}_{i+1/2,j,k-1/2}}{\Delta z}\right)
\tag{2.19a}
$$

$$\psi_{H_{x,y}}\Big|^{n+1/2}_{i,j+1/2,k+1/2} = b_y \psi_{H_{x,y}}\Big|^{n-1/2}_{i,j+1/2,k+1/2} + c_y\left(\frac{E_z\big|^{n+1/2}_{i,j+1,k+1/2} - E_z\big|^{n+1/2}_{i,j,k+1/2}}{\Delta y}\right) \tag{2.19a}$$

$$\psi_{H_{x,z}}\Big|^{n+1/2}_{i,j+1/2,k+1/2} = b_z \psi_{H_{x,z}}\Big|^{n-1/2}_{i,j+1/2,k+1/2} + c_z\left(\frac{E_y\big|^{n+1/2}_{i,j+1/2,k+1} - E_y\big|^{n+1/2}_{i,j+1/2,k}}{\Delta z}\right) \tag{2.19a}$$

with coefficients b_w and c_w given by

$$b_w = e^{-\left(\frac{\sigma_w}{\varepsilon_0 \kappa_w} + \frac{a_w}{\varepsilon_0}\right)\Delta t} \tag{2.20}$$

$$c_w = \frac{\sigma_w}{\sigma_w \kappa_w + \kappa_w^2 a_w}\left[e^{-\left(\frac{\sigma_w}{\varepsilon_0 \kappa_w} + \frac{a_w}{\varepsilon_0}\right)\Delta t} - 1\right] \tag{2.21}$$

The scaled tensors κ_w, σ_w, and a_w are important parameters that act within the CPML terms to damp the electromagnetic waves as they travel through the ten-cell region, reflect off the perfect-electric conductor final outer boundary, and travel back through the CPML region a second time. The exact scaling of these parameters is simulation-specific. For the results presented in this work, the parameters are defined by the polynomial grading:

$$\sigma_x(x) = \sigma_{x,\max}\left(\frac{x}{d}\right)^m \tag{2.21}$$

$$\kappa_x(x) = 1 + \left(\kappa_{x,\max} - 1\right)\left(\frac{x}{d}\right)^m \tag{2.22}$$

$$a_x(x) = a_{x,\max}\left(\frac{d-x}{d}\right) \tag{2.23}$$

using $a_{x,\max}$=0.2, $\kappa_{x,\max}$=1 (vacuum boundary), and

$$\sigma_{x,\max} = \frac{0.8(m+1)}{\eta_0 \Delta \sqrt{\varepsilon_0 \mu_0}} \tag{2.24}$$

where η_0 is the free-space wave impedance, Δ is the cubic lattice cell dimension, ε_0 and μ_0 are the permittivity and permeability of free space, and m is the polynomial grade=3. The constant d defines the thickness of the CPML in cells (here d=10).

Returning to Eqs. (2.16-2.18), the material coefficients C_a, C_b, D_a, D_b, k_d, and β are defined at individual node calculations, and characterize the mesh with a physical nanostructure or free space. For non-dispersive materials, such as the dielectric simulations to be presented, the coefficients take the form

$$C_a = \left(1 - \frac{\sigma \Delta t}{2\varepsilon}\right) \Big/ \left(1 + \frac{\sigma \Delta t}{2\varepsilon}\right) \tag{2.25}$$

$$C_b = \left(\frac{\Delta t}{\varepsilon}\right) \Big/ \left(1 + \frac{\sigma \Delta t}{2\varepsilon}\right) \tag{2.26}$$

$$D_a = \left(1 - \frac{\sigma^* \Delta t}{2\mu}\right) \Big/ \left(1 + \frac{\sigma^* \Delta t}{2\mu}\right) \tag{2.25}$$

$$D_b = \left(\frac{\Delta t}{\mu}\right) \Big/ \left(1 + \frac{\sigma^* \Delta t}{2\mu}\right) \tag{2.26}$$

where Δt is the timestep, and σ^* is the magnetic loss (generally=0 ohms/m), while k_d=1 and β=0. Material parameters for dispersive materials such as gold and silver are more complicated and will be covered in Chapter 4 of this work. Field components E_y, J_y, H_y, and E_z, J_z, H_z can be determined analogously by permuting the i, j, and k indices appropriately.

With the FDTD interior, boundary, and material definition procedures in place, the excitation field is required for a transient scattering analysis. The experimental condition of a monochromatic plane wave has been implemented in FDTD using the total field/scattered field (TFSF) formulation with matched dispersion compensation. The assumption of no spatial variation of intensity (pre-interaction) is made, reasonable because the Gaussian profile of the beams used are resolved on the order of millimeters, compared to the micrometer simulation environment.

The TFSF construct (Yee, 1966) takes advantage of the linearity of Maxwell's equation, meaning the total electric (and likewise magnetic) field is equal to the sum of the incident and scattered electric fields. The incident field is arbitrary and user-defined. The procedure involves choosing a total field zone that contains the object of interest (microsphere and substrate) and designating six planar faces that mark the boundary of this cube-within-a-cube. Straddling the boundary will be electric and magnetic field pairs whose connection would intersect perpendicularly with the TFSF plane. At every node on these planes, the incident field is either added or subtracted, depending on the component, directly resulting in the generation of the plane wave within the TFSF zone. Because only the incident field is subtracted, the TFSF boundaries are transparent to scattered radiation. E_x and H_x field components straddling the y-minimum TFSF plane would be modified as follows.

$$E_x \big|_{i,j0,k}^{n+1} = \left\{ E_x \big|_{i,j0,k}^{n+1} \right\}_{2.16} - \frac{\Delta t}{\varepsilon_0 \Delta} H_{z,inc} \big|_{i,j-1/2,k}^{n+1/2} \tag{2.27}$$

$$H_x \big|_{i,j0-1/2,k}^{n+1/2} = \left\{ H_x \big|_{i,j0-1/2,k}^{n+1/2} \right\}_{2.18} + \frac{\Delta t}{\mu_0 \Delta} E_{z,inc} \big|_{i,j0,k}^{n} \tag{2.28}$$

The bracketed terms in Eqs. (2.27) and (2.28) indicate the original update values performed using Eqs. (2.16) and (2.18). The incident field components are obtained through a number of steps. First, a one-dimensional auxiliary FDTD grid is used as a lookup table. The sinusoidal waveform in this grid would continuously propagate defined by the excitation

$$E_{inc,0} = I_0 \sin(\omega \cdot t \cdot \Delta t) \tag{2.29}$$

where ω is the desired laser frequency. Then, a user-specified orientation is accessed. The plane wave can propagate through the Cartesian space at any incident angle θ and Φ. These values define the origin corner of the TFSF zone. A linear distance from this origin to each node is calculated, giving a correlation between a point on the TFSF planes and the 1-D auxiliary grid. Next, the Yee algorithm is modified for auxiliary grid calculation to account for numerical dispersion. In any discretized grid, a numerical phase-velocity anisotropy will occur that will lead to field leakage from the TFSF zone if unaddressed. Taflove and Hagness (2005) detail the dispersion compensation techniques needed for inclusion in the 1-D FDTD algorithm. Finally, an appropriate trigonometric function based on the propagation angles is applied to each field component to obtain the Cartesian vector magnitudes.

In order to maintain numerical stability, the Courant condition must be satisfied regarding the time step employed:

$$\Delta t < \frac{1}{c\sqrt{\frac{1}{(\Delta x)^2} + \frac{1}{(\Delta y)^2} + \frac{1}{(\Delta z)^2}}} \tag{2.29}$$

An additional requirement to yield accurate results is keeping the largest grid spacing, Δx, Δy, or Δz much less than the smallest wavelength (< λ/10) that will be propagating through the system. In order to resolve structures at the nanoscale with clarity, this requirement generally takes care of itself. Grid spacing used in this work maintained λ/25 to λ/1000 fidelity. The FDTD modeling environment and numerical algorithm for the developed code (MaxTex) are given in Figures 2.16 and 2.17. Other than the laser/microsphere and plasmonic simulations discussed in Chapters 2-4 of this work, the FDTD method has been employed to solve novel problems involving thermal radiation property prediction given in Appendix B. A user's guide for the MaxTex code is supplied in Appendix A.

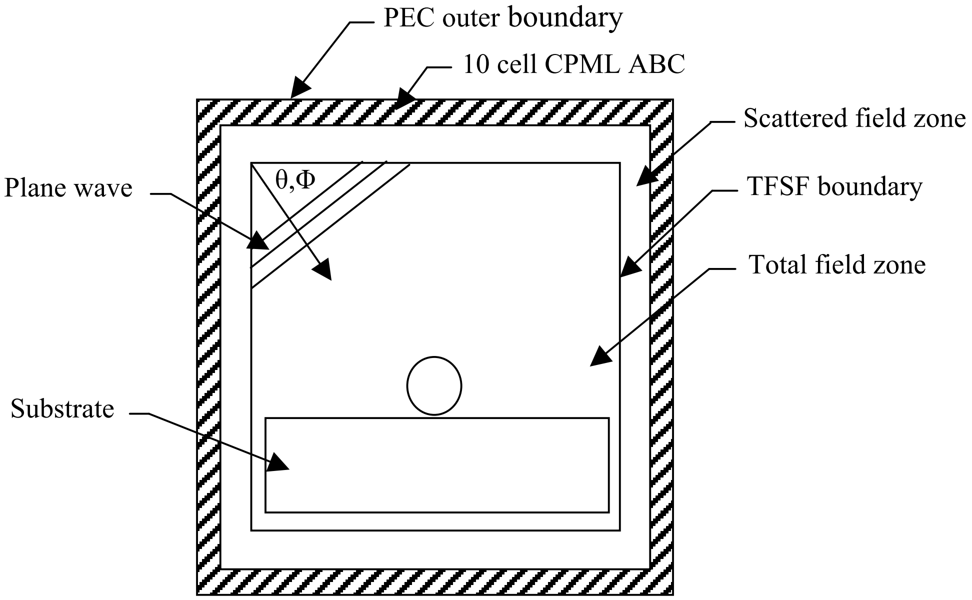

Figure 2.16: 2-D cross-section of 3-D FDTD modeling environment

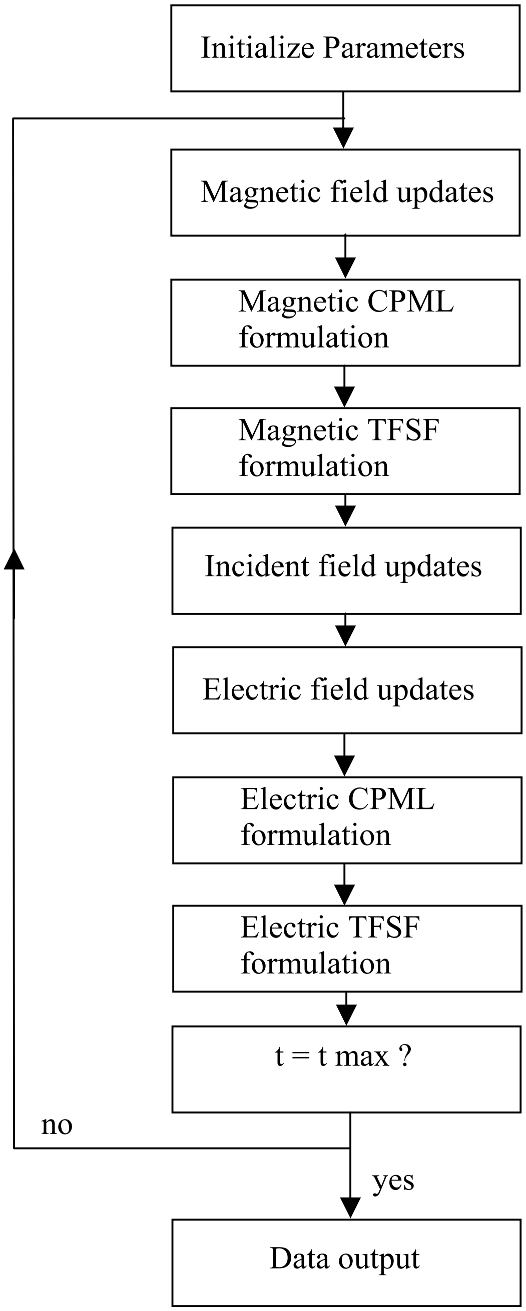

Figure 2.17: FDTD algorithm employed in MaxTex code

2.3.2 FDTD Validation

The stability and accuracy of the Yee algorithm as well as the ability of the absorbing boundary condition to prevent extraneous error-causing reflection must first be evaluated. First, a radiating electric dipole, P_e, was placed at the center of the computational domain consisting of 44 x 44 x 44 cubic cells. Implementation was carried out by defining the field component

$$E_{z,center}^{n+1} = E_{z,center}^{n} + \frac{\Delta t}{\varepsilon_0} \nabla \mathrm{x} \mathrm{H}^{\mathrm{n+1/2}} - \frac{\Delta t}{\varepsilon_0 \Delta x^3} \frac{dP_e\left(t_{n+1/2}\right)}{dt} \tag{2.30}$$

where a Gaussian pulse was used of the form

$$P_e(t) = 10^{-10} \exp\left(-\left(\frac{t-3T}{T} \right)^2 \right) \tag{2.31}$$

with T=2 ns.

The field component E_z was recorded in time at a node ten cells removed from the center in the y-direction. With a ten-cell CPML, the recording node was therefore two cells from the boundary. The cells were 5 cm x 5 cm x 5 cm, and a time step of 83.333 ps was used. The analytical solution for the transient response of the field at that point is compared in Figure 2.18 to the FDTD simulation records for the case of an active CPML as well as CPML turned off. The comparison shows that this implementation of the Yee algorithm correctly describes the propagation of the field through space. The effect of reflected wave from the outer boundary is evident without the CPML. Any scattered field solution obtained without proper absorption would undoubtedly be erroneous. The existence of the active CPML absorbs the dipole radiation so as to provide a solution indistinguishable from the analytical form.

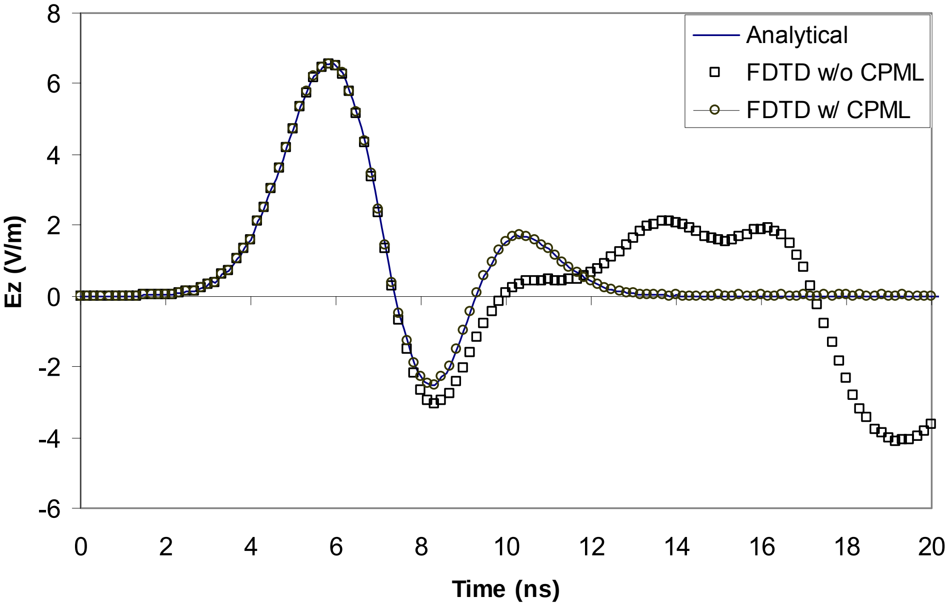

Figure 2.18: Electric field component two cells from boundary of computational domain

The precise characterization of the CPML's absorption capability can also be determined with another test specifying a current source within the domain, as described in Taflove and Hagness (2005). A y-directed electric current source is inserted with a time variation of a differentiated Gaussian pulse.

$$J_{y,center}(t) = -2\left[(t-t_0)/t_w\right]\exp\left\{-\left[(t-t_0)/t_w\right]^2\right\} \tag{2.32}$$

where t_w=26.53 ps and t_0=4t_w. In this simulation, the FDTD grid has cells of length 1 mm, and 1000 time-steps are performed. A 10 cell CPML is used. Points were recorded at the edge-center of the domain (Point A) and the edge-corner of the domain (Point B), which would expect to exhibit the largest numerical error. The quantity plotted in Figure 2.19, relative error, is defined as

$$\text{Rel.error} = \left| E\,\big|_{i,j}^{n} - E_{ref}\,\big|_{i,j}^{n} \right| / \left| E_{ref,\max}\,\big|_{i,j} \right| \tag{2.33}$$

where $E_{ref,max}|_{i,j}$ is the maximum amplitude of the reference field (analytical solution) at (i,j) observed during the simulation.

Figure 2.19 indicates a peak relative error of approximately 10^{-4} for both Point A and Point B. In general, the error is significantly lower, in the range of 10^{-5} to 10^{-6}. This extremely high level of absorption represents the peak current achievability for FDTD and provides for accurate solutions within the computational domain.

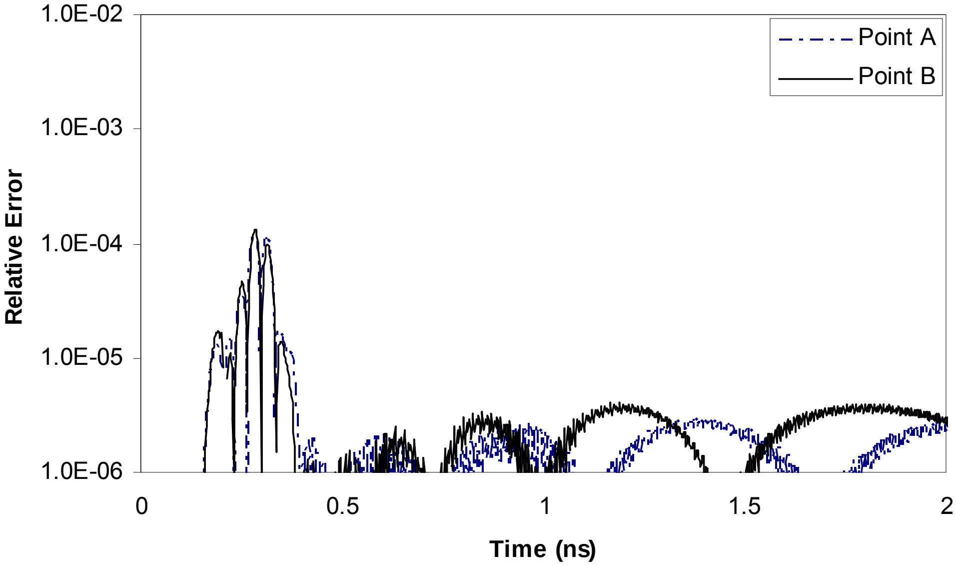

Figure 2.19: Relative FDTD error with employment of CPML ABC.

2.3.3 FDTD Simulations and Results

An initial FDTD simulation modeled the interaction between a laser of wavelength λ=532 nm and a suspended silica sphere of diameter 1.76 μm, i.e., the experimental case shown in Figure 2.2 and analyzed in section 2.2.2. A cubic Yee cell of 8 nm per side was used, corresponding to $\lambda/67$, well within the spatial convergence criteria. A time step of .01334 fs was employed, satisfying the Courant condition. A relative permittivity value of $\varepsilon_r=3.7$ was used for calculation of the electric field nodes within the spherical volume of fused silica. The sphere was suspended in a vacuum surrounding, and convergence was achieved after approximately 300 fs. The time-averaged (after convergence) electromagnetic field intensity is given in Figure 2.20 for a cross-sectional slice midway through the simulation volume.

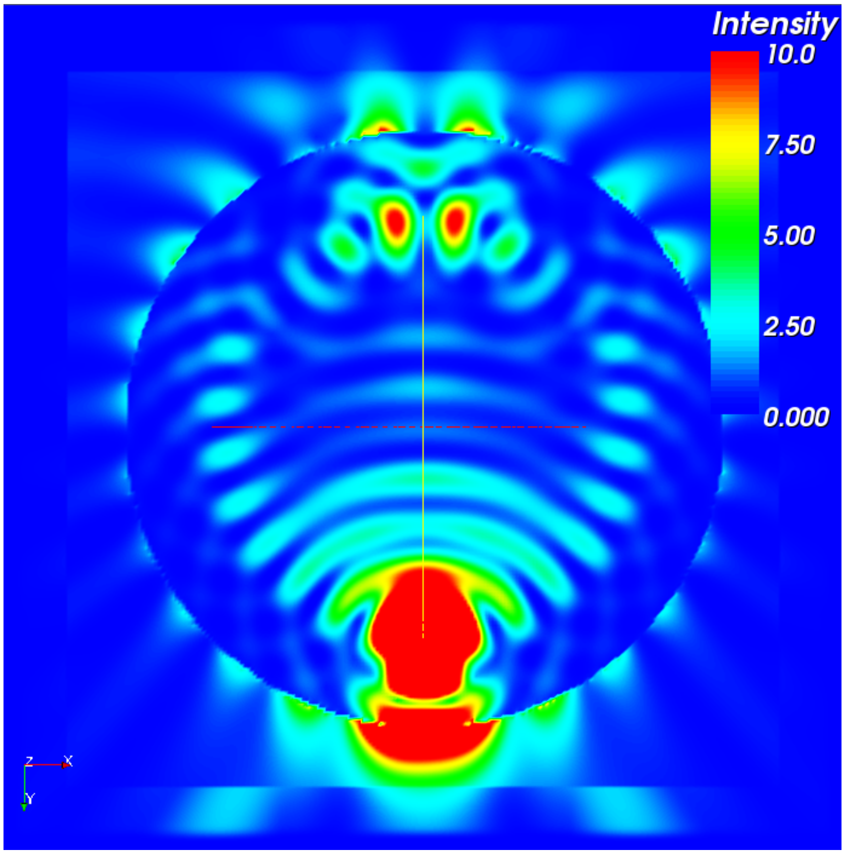

Figure 2.20: FDTD-predicted intensity cross-section due to scattering of λ=532 nm light by 1.76 μm silica sphere suspended in vacuum.

Unlike the Mie scattering analysis, a full visualization of the field is possible without multiple runs. The complex scattering pattern in Figure 2.20 clearly shows a localized zone of substantial enhancement both within the interior of the "bottom" of the sphere and outside the silica. Smaller lobes of backscattered enhancement are visible toward the “top” of the sphere interior, and seem to be part of a periodic constructive interference pattern.

Another subtle point of note is the slightly visible staircasing unavoidable when describing a spherical geometry using Cartesian cells. A spherical coordinate system would alleviate this concern, however the linear plane wave would then contain the same numerical issue, and in anticipation of a flat substrate beneath the sphere, a Cartesian coordinate system was deemed no less numerically inaccurate. Advanced hybrid finite-element/FDTD techniques have been developed that can reduce the numerical inaccuracy caused by a curved surface at the cost of complexity and computational expense (Cohen and Monk, 1998), (Rylander and Bondeson, 2000).

Figure 2.21 presents the intensity surface at the plane of observation defined in Figure 2.3 generated from the FDTD calculation. The single “hump” of enhancement is very similar to the Mie calculation presented in Figure 2.4a. The slight radial asymmetry of the secondary rings of enhancement is due to the polarization of the incident wave. This effect is also contained within the near-field Mie results, though the two-dimensional curve comparisons naturally neglect that. It will be shown that the polarization of incident light strongly affects the intensity distributions with the inclusion of the substrate geometry.

A comparison can be made between the results of near-field Mie theory in the previous section with the corresponding field at the plane of observation adjacent to the sphere modeled using FDTD. Figure 2.22 plots the 1-D intensity profiles directly below the sphere predicted from both methods. The discrepancy between the curves can be attributed to both the numerical/geometrical concerns discussed above as well as the uncharacterizable inaccuracy of the near-field Mie approximations discussed at the end of section 2.2.6. However the qualitative and quantitative agreement is fair, and the two physical effects that lead to lithographic capabilities are contained: order of magnitude enhancement of laser fluence, and localization of such enhancement to sub-diffraction limit space.

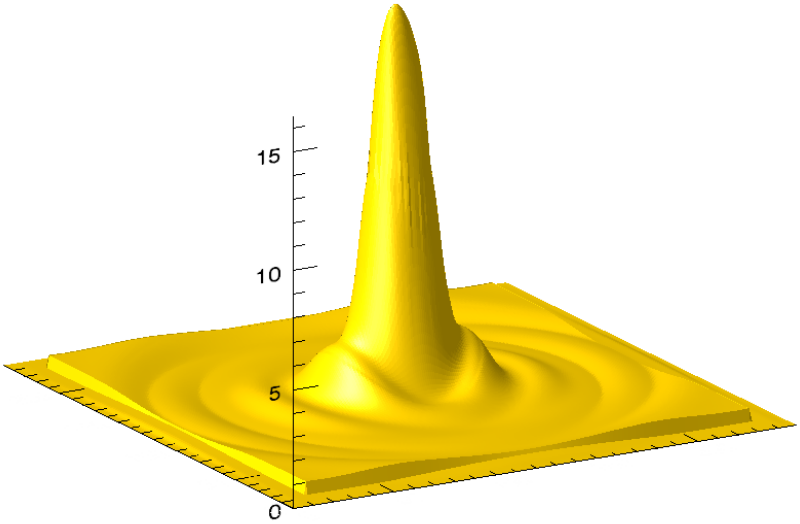

Figure 2.21: Surface intensity distribution predicted by FDTD in the plane of observation for a 1.76 μm suspended SiO_2 sphere, λ=532 nm pulse.

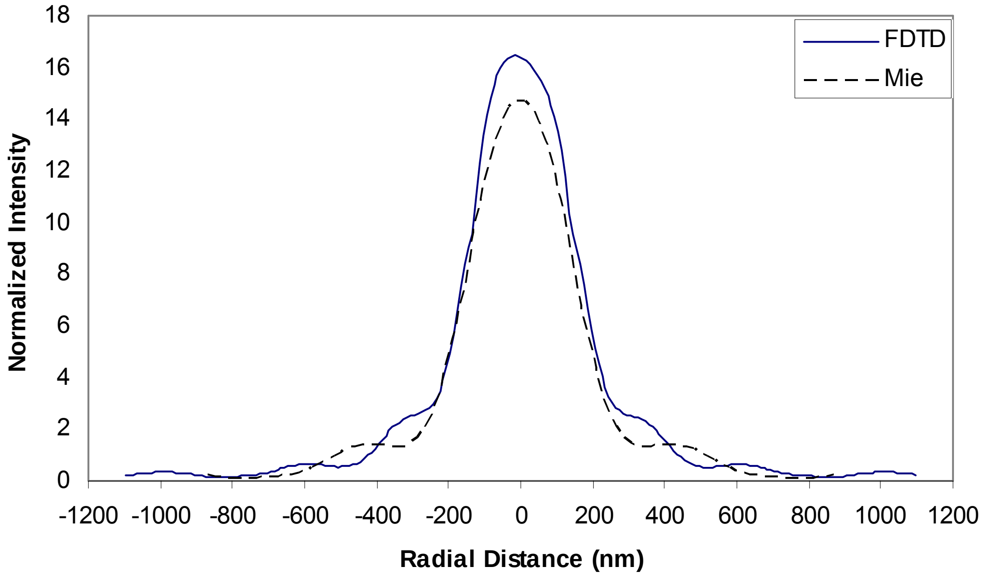

Figure 2.22: Comparison of near-field Mie and FDTD calculations in the plane of observation for a 1.76 μm suspended SiO_2 sphere, λ=532 nm pulse.

A physical understanding of the scattering mechanism which leads to the intense concentration of light can be gained from a series of time-elapsed electric field components. Figure 2.23(a-f) allows the user to visualize the effect of a spherical refractive interface. The incident plane wave is bent into a spherical shape in the interior of the sphere, with a larger radius, however, than the sphere itself. The convex wave collapses, concentrating the light in a very small area within the interior of the sphere but close to the "bottom" surface. The wave then expands spherically, eventually to the far-field pattern dictated by Mie theory.

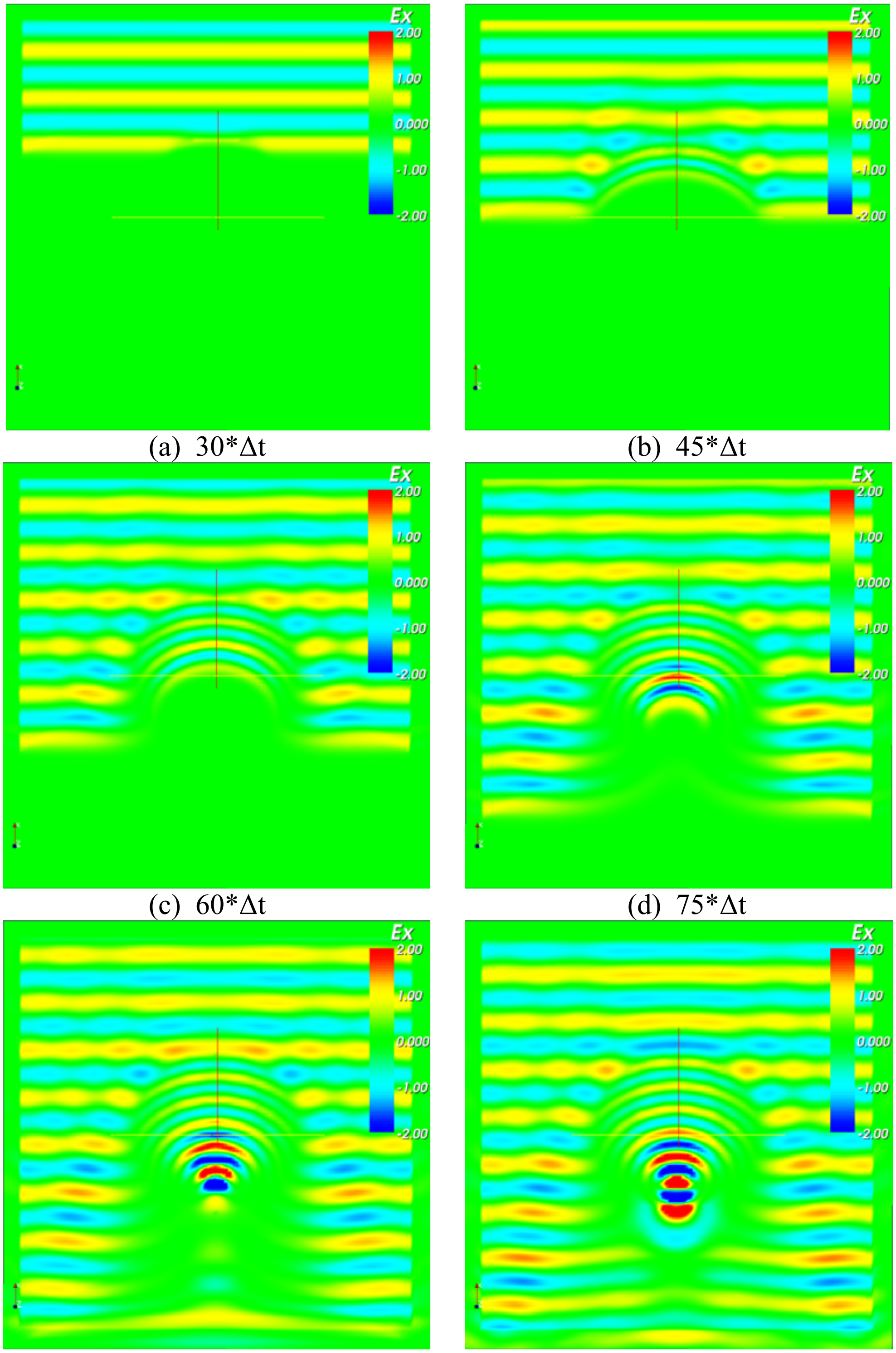

(a) 30*Δt

(b) 45*Δt

(c) 60*Δt

(d) 75*Δt

(e) 90*Δt

(f) 105*Δt

Figure 2.23: Transient analysis of laser/ dielectric microsphere interaction

A close examination of this event can reveal the limitation of Mie theory in the near-field. Mie's solution accurately describes the spherical wave front at great distances from the sphere, and is derived in spherical coordinates with the origin at the center of the sphere. As shown in Figure 2.23(a-f), the origin of the spherical expansion is not actually at the center of the sphere's interior, but closer to the far side from which the wave is incident. In the far-field, this difference is certainly negligible, however for the purposes of quantifying the energy in the immediate vicinity of the microsphere, the conclusion is made here that Mie theory is a useful predictive tool, but cannot be exact in the near-field.

2.3.4 Grid-independence investigation

An analysis of numerical mesh size dependence on the solution is an important consideration before conducting simulations with added geometrical complexities. Because the primary drawback of the finite-difference time-domain method is memory storage and computational expense, a compromise of precision and wall-clock hours must be made if large numbers of simulations contributing to parametric studies are needed. Figure 2.24 presents near-field scattering patterns for identical physical parameters using several different mesh sizes. All runs simulated a 1.0 μm silica sphere irradiated at a wavelength of 500 nm. The parameter 'dd' refers to the cell side length. The value plotted in Figure 2.24 is the intensity along a vertical line directly through the sphere's axis, parallel to the incident laser. The high intensity values toward the right side of the plot represent the enhanced area toward the bottom of the sphere seen in Figure 2.20.

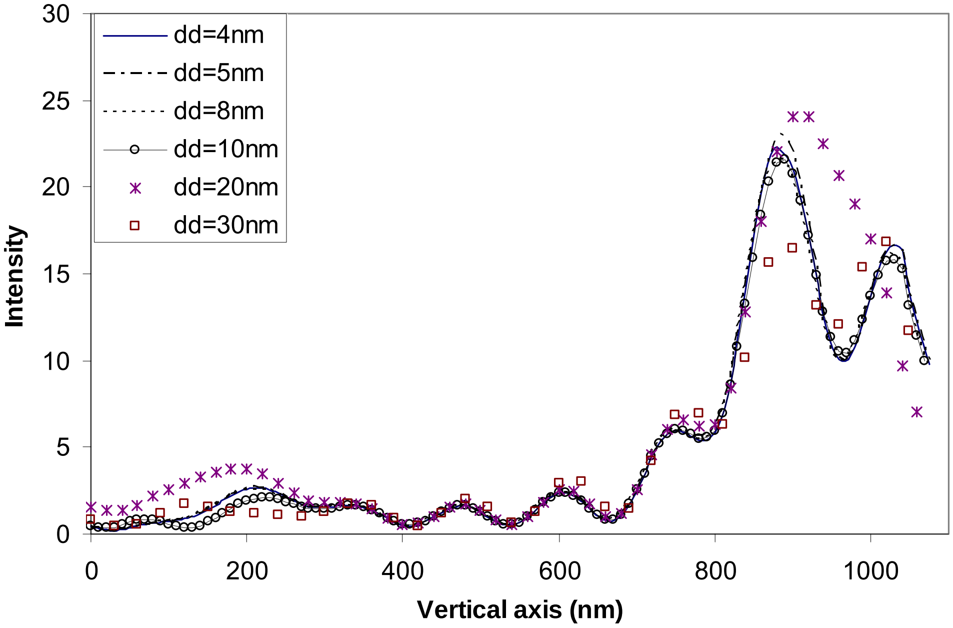

Figure 2.24: Grid-independence investigation for spherical object modeling using the FDTD method

The modeling of a spherical scattering object using Cartesian cells is essentially the best test of grid-independence. Figure 2.24 indicates a strong dependence on mesh size if the cubic cells exceed 10nm, or diameter/100. At the FDTD stability criterion of dd< λ/15 or ~ 30nm, the sphere is clearly not resolved geometrically to give an accurate solution, so further refinement is necessary. All results presented in this work have minimum refinement of dd=diameter/100, but usually dd~diameter/200 to ensure precision.

2.3.5 Substrate effect

The case of a solitary sphere resting on a flat substrate of varying material was simulated. The only geometric approximation needed was a simulated substrate volume far smaller than the plates used experimentally. As long as the lateral distance was greater than the sphere diameter, the substrate edge diffraction effects did not creep into the enhancement profile directly beneath the sphere. The thickness of the modeled substrate could potentially affect the solution due to reflection of transmitted energy from the far surface back in the direction of the sphere. Increasing the thickness of the modeled substrate greater than a few hundred nanometers did not seem to affect the solution, but greatly increased computational expense. Figure 2.25 shows the cross-sectional intensity distribution midway through the simulation volume for the identical case given in Figure 2.20, but with the presence of a silicon substrate. Figure 2.26 gives the surface intensity "seen" by the silicon due to the short-pulse and presence of the silica sphere.

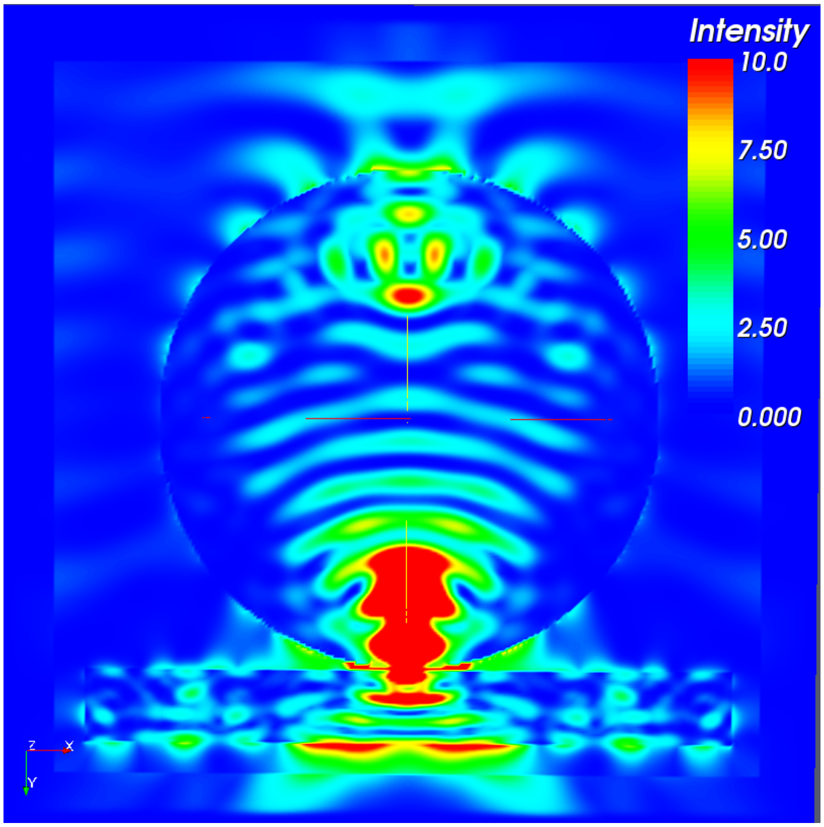

Figure 2.25: FDTD-predicted intensity cross-section due to scattering of λ=532 nm light by 1.76 μm silica sphere resting on a silicon substrate.

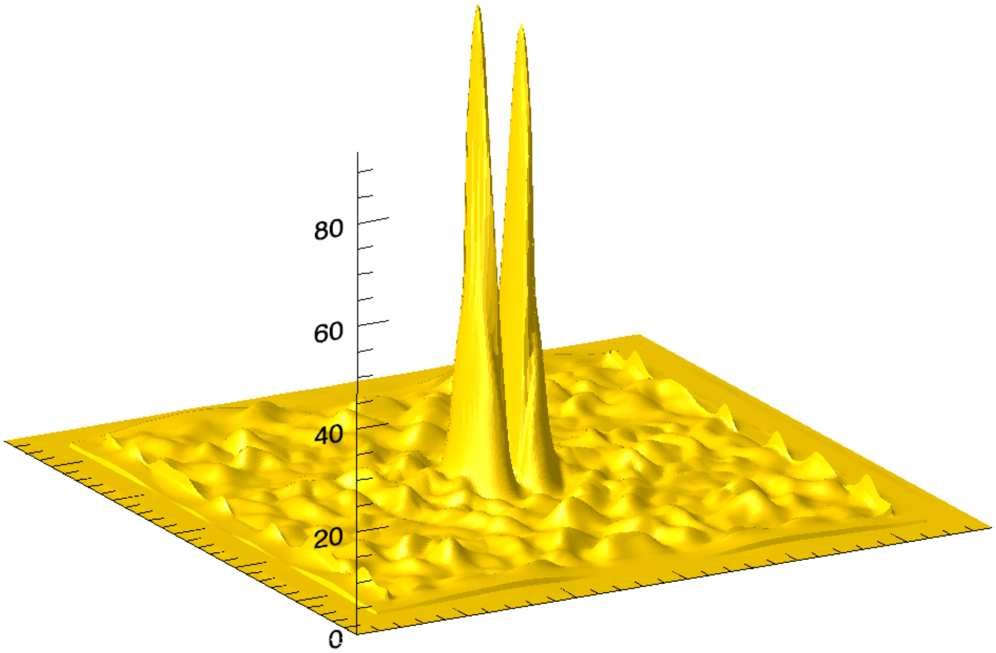

Figure 2.26: Surface intensity distribution predicted by FDTD on the surface of a silicon subtrate beneath a 1.76 µm SiO_2 sphere, λ=532 nm pulse.

It is clear that the presence of the substrate drastically changes the energy profile directed to the surface, an effect unable to be predicted using Mie theory alone. The most obvious difference between Figure 2.26 and Figure 2.21 is the dual enhancement peaks due to reflection and interference of the waves from the silicon surface. In addition, the dual peaks exhibit a higher relative level of enhancement, and are slightly more localized than the corresponding single peak in Figure 2.22.

The effect of substrate opacity on the surface profile is investigated. At a laser wavelength of 532 nm, silicon is opaque. A transparent substrate, Pyrex (barium aluminum borosilicate glass), is modeled by changing the electrical permittivity appropriately. A value of relative permittivity for Pyrex of ε_r=5.1 is used for Pyrex.

Figures 2.27 and 2.28 give the updated cross-sectional and surface intensities for the case of transparent substrate.

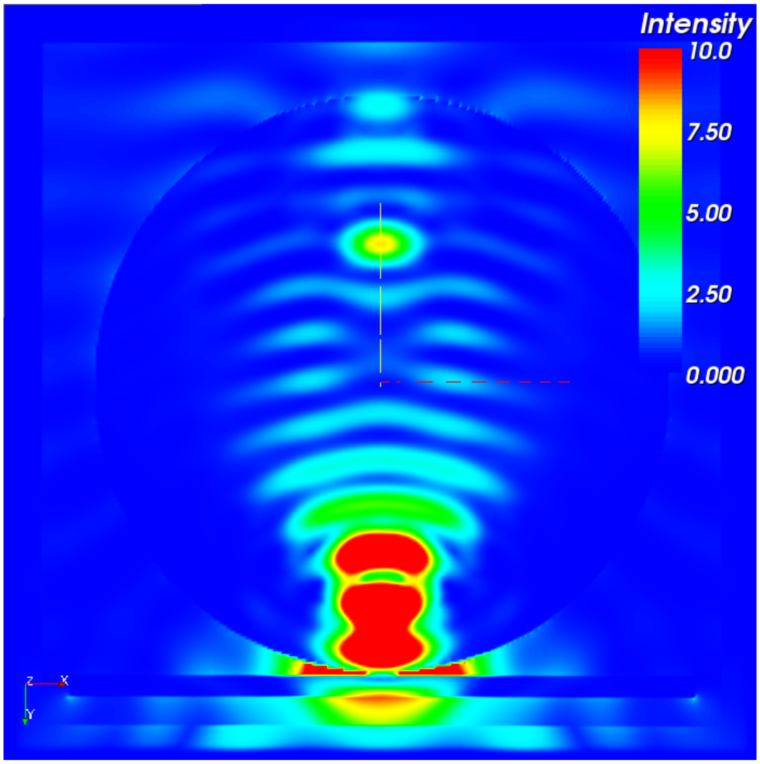

Figure 2.27: FDTD-predicted intensity cross-section due to scattering of λ=532 nm light by 1.76 μm silica sphere resting on a Pyrex substrate.

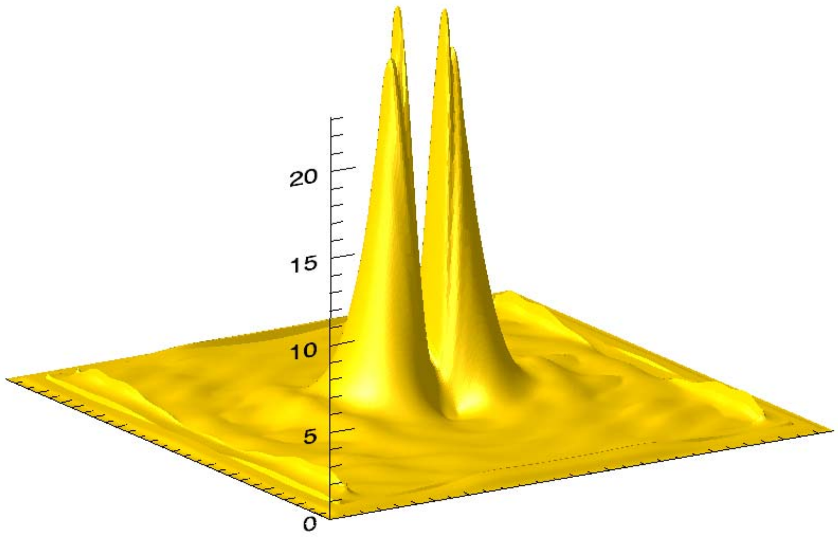

Figure 2.28: Surface intensity distribution predicted by FDTD on the surface of a Pyrex subtrate beneath a 1.76 µm SiO_2 sphere, λ=532 nm pulse.

Comparing Figures 2.26 and 2.28, the effect of the optical property of the substrate is large. For the transparent Pyrex, the dual peak enhancements are much lower than for highly reflecting silicon. The difference in reflection can be visualized by comparing Figures 2.25 and 2.27, which show stronger energy patterns inside the sphere resting on silicon. The enhancement is slightly more confined over the silicon as well, with “sharper” peaks, which could lead to more localized lithographic effects. Consistency exists between the cases also, with the presence of either substrate deforming the solo peak enhancement into two peaks of even higher intensity. The general effect of the near-field enhancement of laser energy surrounding a microsphere is therefore highly dependent on both surrounding geometries and their optical properties.

Pyrex is chosen for micromachining due to its structural properties suitable for micro-electromechanical systems (MEMS) applications. The utility of a nearly totally transmitting wavelength/substrate combination for optical lithography purposes is dubious, unless the conventional energy transport mechanisms are replaced with ones that can initiate absorption in the borosilicate glass. This is the case with femtosecond laser pulse irradiation, where material removal is accomplished via ablation due to non-equilibrium electron and lattice situations. Energy transport under these conditions will be discussed in depth in Chapter 3 of this work, however the electrodynamic problem remains the same. The femtosecond laser used in the NOBEL lab has a wavelength of 800 nm. The FDTD results corresponding to the conditions of a femtosecond laser pulse irradiating a silica sphere on a Pyrex substrate are given in Figures 2.29 and 2.30, and without the Pyrex in Figure 2.31.

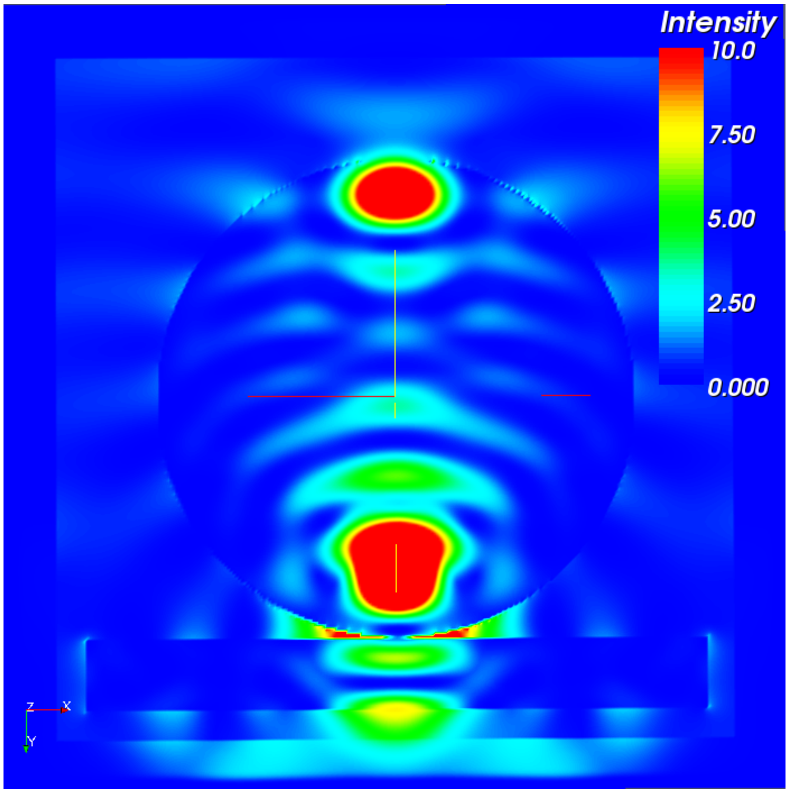

Figure 2.29: FDTD-predicted intensity cross-section due to scattering of λ=800 nm light by 1.76 μm silica sphere resting on a Pyrex substrate.

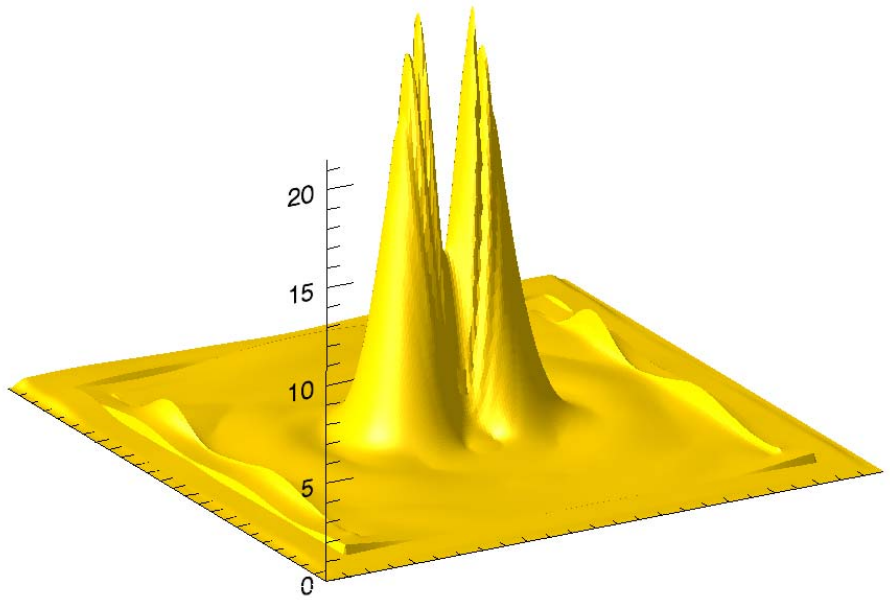

Figure 2.30: Surface intensity distribution predicted by FDTD on the surface of a Pyrex subtrate beneath a 1.76 µm SiO_2 sphere, λ=800 nm pulse.

The presence of the substrate is clear with comparison to Figure 2.31, which plots the same value of surface intensity distribution in the plane of observation where the Pyrex substrate was removed. Again, similar to the results of Mie theory, a single enhancement peak is generated, however in this case the presence of the substrate does not lead to more energetic peak enhancements. The primary physical difference between cases is the transparent property of the substrate. This provides further evidence that the subsequent reflection of light between silicon and sphere is what creates the disparity in enhancements between Figures 2.21 and 2.26, rather than a purely geometric effect. The other essential point is the asymmetry lost between profiles with the addition of the substrate. This directly affects the lithographic result as well as adding a dimension to any theoretical energy transport model in the substrate, discussed in Chapter 3.

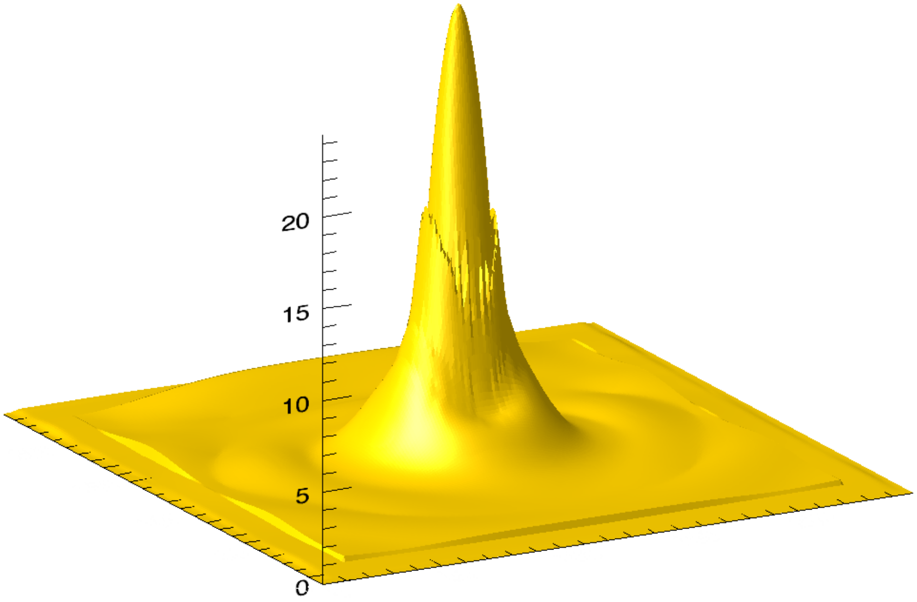

Figure 2.31: Surface intensity distribution predicted by FDTD at the plane of observation beneath a *suspended* 1.76 µm SiO_2 sphere, λ=800 nm pulse.

2.3.6 Size factor dependence

The previous figures lead into the more comprehensive size factor study, similar to the one conducted using Mie theory in section 2.2.3, but with the additional substrate complexity. The reduction of variables from two (wavelength and sphere size) to one (size factor q=2*pi*radius/wavelength) allows a single set of simulations to determine the enhancement characteristics for a given sphere and substrate material combination. An experimenter/lithographer desiring a specific localization and intensity can then use an existing laser resource and procure microspheres based upon the following data. Figure 2.31 (a-f) presents intensity cross-sections obtained for six size factors. The values of q= 5, 9, 12, 16, 18, and 20 were chosen from the results of the Mie analysis in Figure 2.9 to represent local minima or maxima in the overall size factor resonances. All simulations were conducted using silicon substrates and SiO_2 spheres. Figure 2.32 (a-f) presents the surface intensity distributions for each simulation. Note the small change in plot ranges between simulations.

Progressing through Figure 2.32 (a-f), the relative sizes of the microsphere and the electromagnetic wave becomes an obvious consideration. With a size factor of five, only a couple periods of the incident wave can actually “fit” within the sphere, providing limited opportunity for constructive (and destructive) interference. With a high size factor of 16, 18, or 20, there are complex interference patterns and competing resonances that contribute to the intensity at a given spot.

Despite fluctuating behavior, in general a higher peak enhancement is exhibited in the vicinity of a *suspended* sphere in a higher size factor situation, as shown in Figure 2.9. Interestingly, the presence of the substrate somewhat reverses this effect when the enhanced wave is deformed through reflection. The dual peaks are all more intense than their solo counterparts (no substrate present), however they are more intense in general at the low size factor situations shown in Figure 2.33 (a-f) than the higher size factor situations. The disparity is small with peak enhancements all in the range of 20-35 times the incident, partially mitigating the more drastic disparity in peak enhancement as a function of size factor given in Figure 2.9.

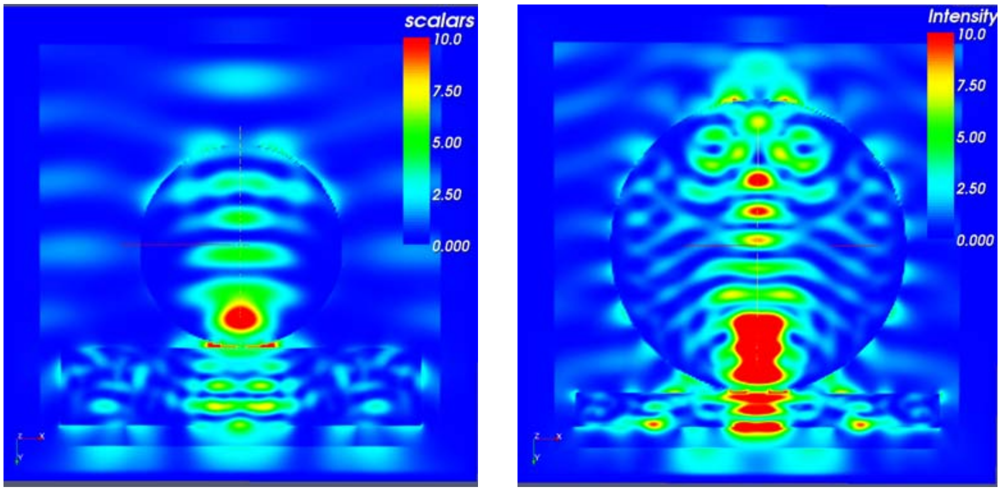

(a) q=5 (b) q=9

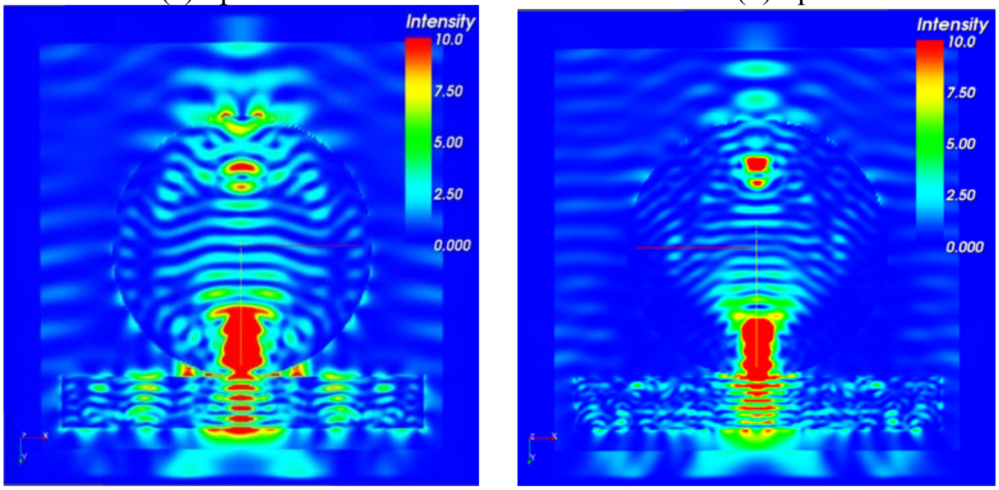

(c) q=12 (d) q=16

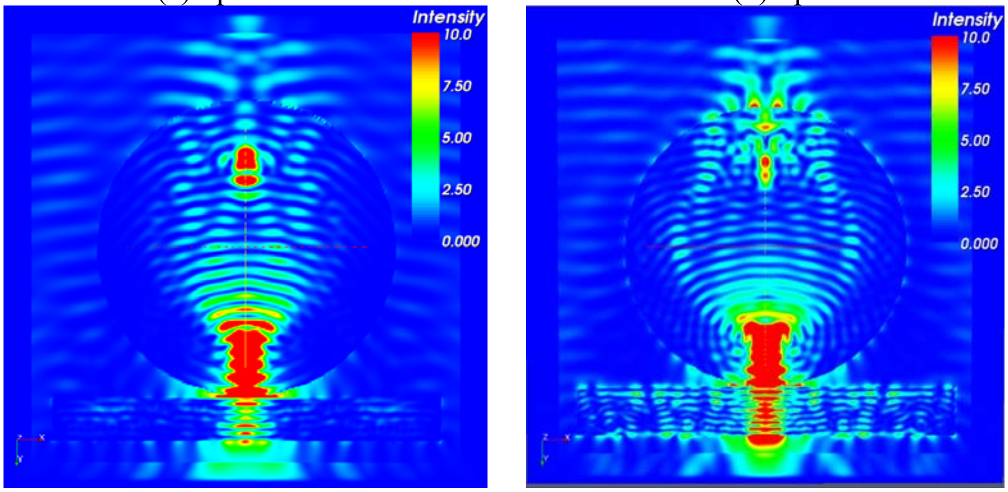

(e) q=18 (f) q=20

Figure 2.32: FDTD-predicted intensity cross-sections for several size factors, $q=2\pi r/\lambda$

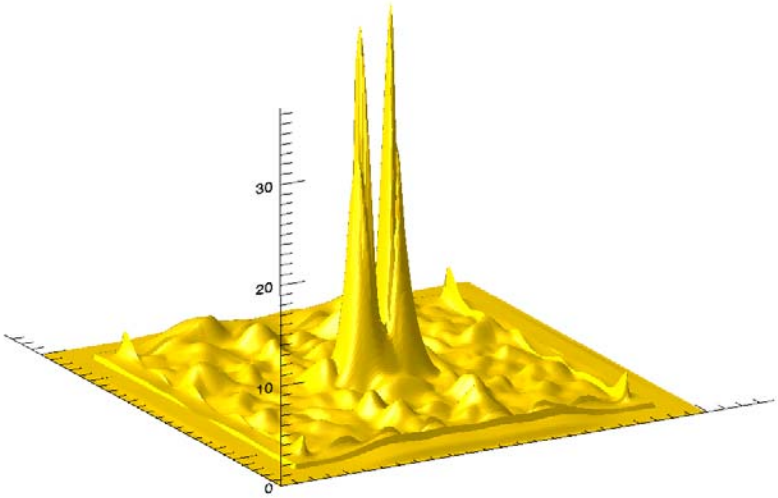

(a) q=5 (2000nm x 2000nm)

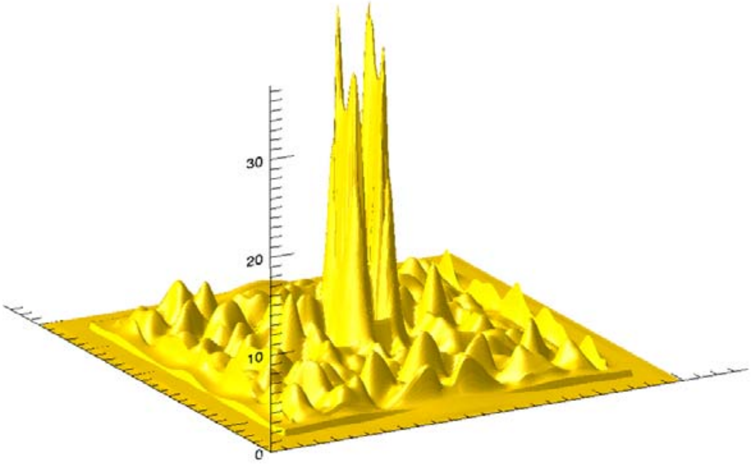

(b) q=9 (2500nm x 2500nm)

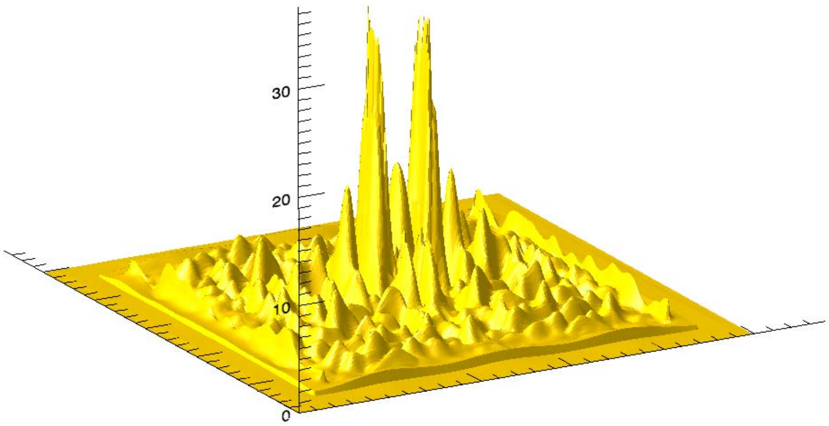

(c) q=12 (3750nm x 3750nm)

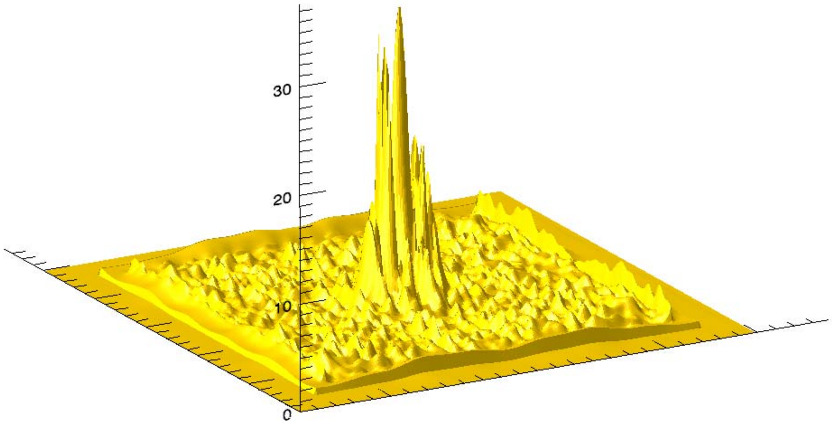

(d) q=16 (5800nm x 5800nm)

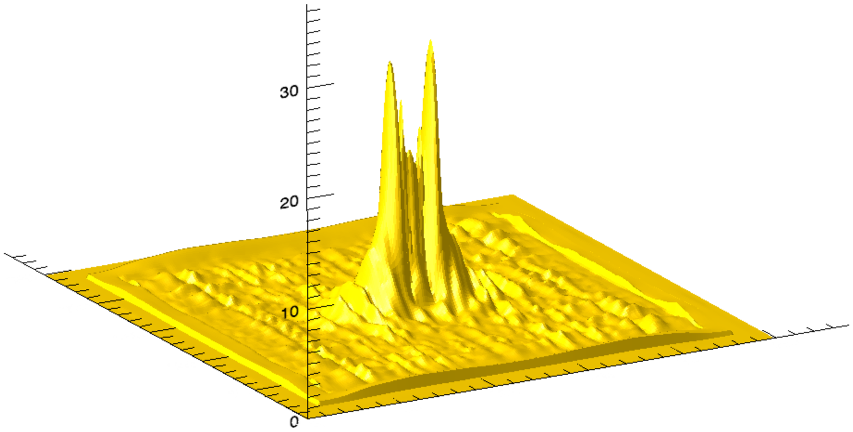

(e) q=18 (3900nm x 3900nm)

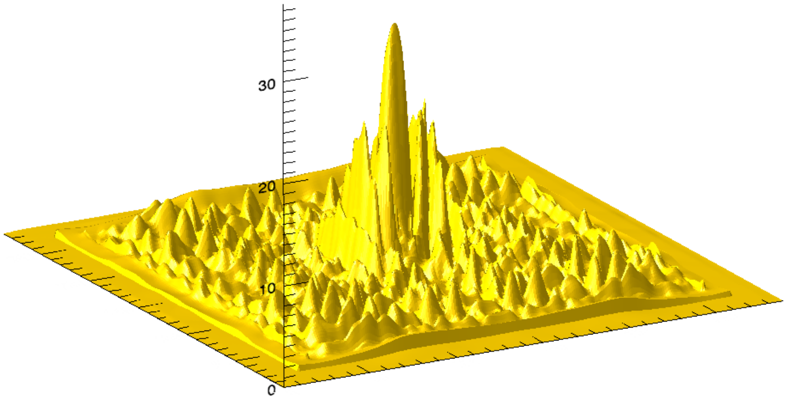

(f) q=20 (5800nm x 5800nm)

Figure 2.33: FDTD-predicted silicon substrate surface intensities for several size factors.

Section 2.3.7 Angle Effect

The effect of incident laser angle upon the near-field enhancement surrounding the sphere and subjected to the substrate is investigated in this section. Adjusting this parameter is relatively easy in an experimental setting, so any dynamic change in potential lithographic effects should be investigated as potentially valuable. Again, the correlative experimental case of a 1.76 μm diameter silica sphere on a silicon substrate was simulated, using a 532 nm wavelength laser pulse. The total field/scattered field FDTD formulation described in section 2.3.2 has the flexibility of an arbitrary plane wave angle, allowing a constant property grid defining the sphere and substrate. The cross-sectional intensities averaged using six incident angles of 90^o (normal), 75^o, 60^o, 45^o, 30^o, and 15^o are presented in Figure 2.34 (a-f). The corresponding surface intensities on the silicon beneath the sphere are shown in Figure 2.35 (a-f).

From Mie theory, strong forward scattering is expected. With varying incident angle, this effectively creates a distance between the far side of the sphere and the silicon. Decay of the evanescent field with distance is presumed exponential from Mie theory, however any coupling effect between the sphere and substrate at the contact point, as well as glancing reflection from the substrate cannot be addressed from analytical theory. Further, the limitations of near-field Mie theory have already been discussed, so the actual decay of the field in the vicinity of the sphere is an interesting topic worthy of separate investigation.

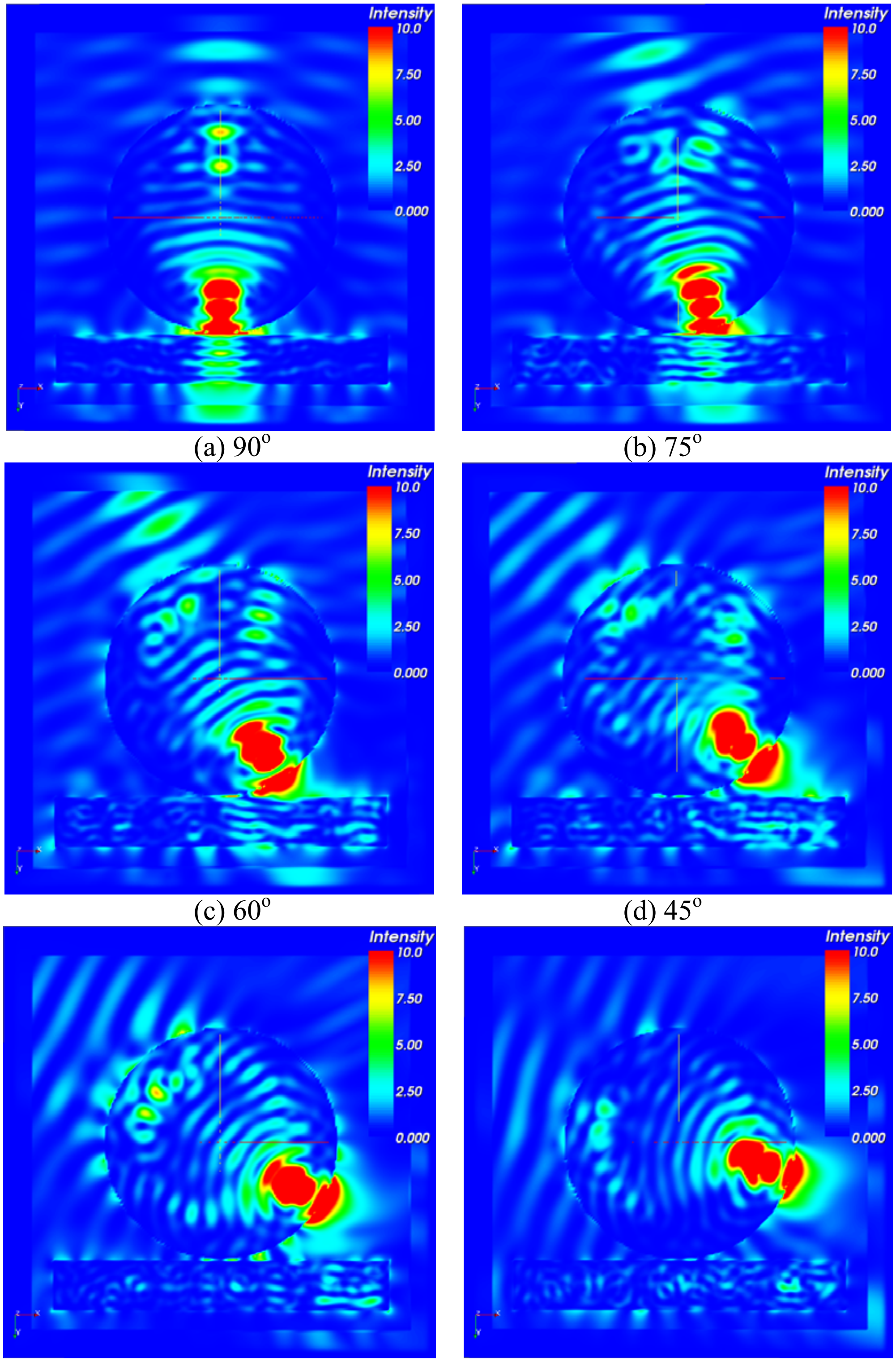

(a) 90°
(b) 75°
(c) 60°
(d) 45°
(e) 30°
(f) 15°

Figure 2.34: Cross-sectional intensities, angle effect investigation

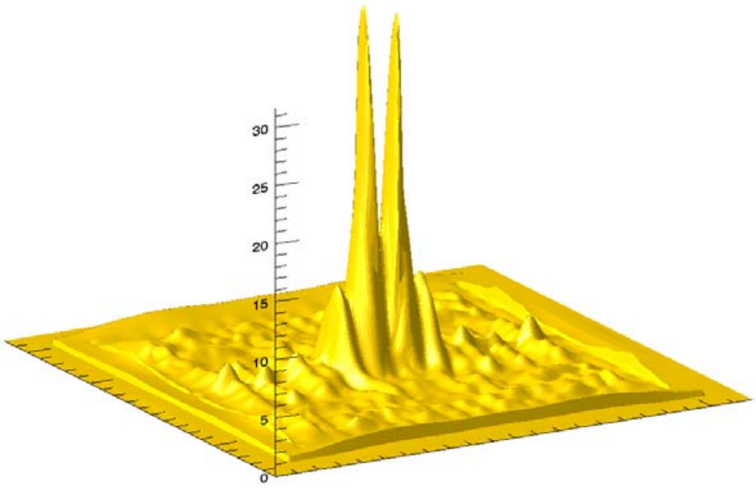

(a) 90°

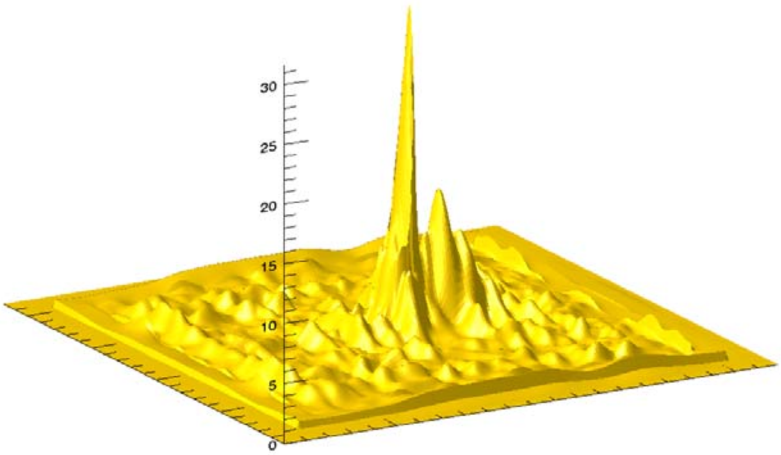

(b) 75°

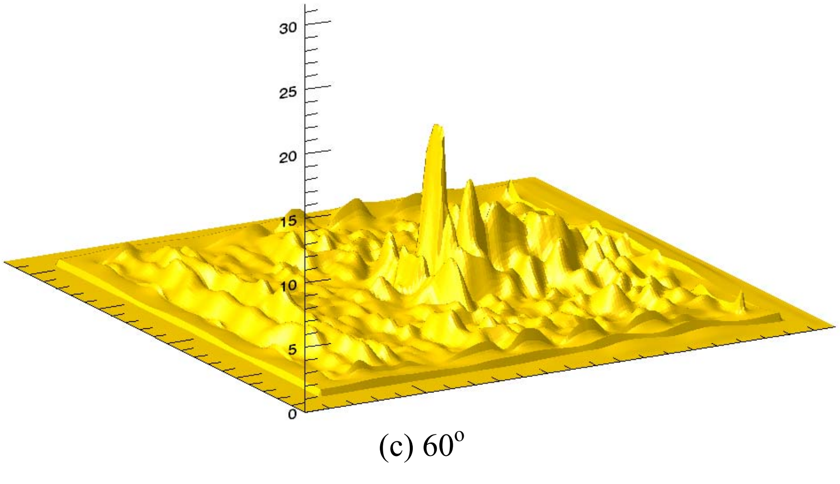

(c) 60°

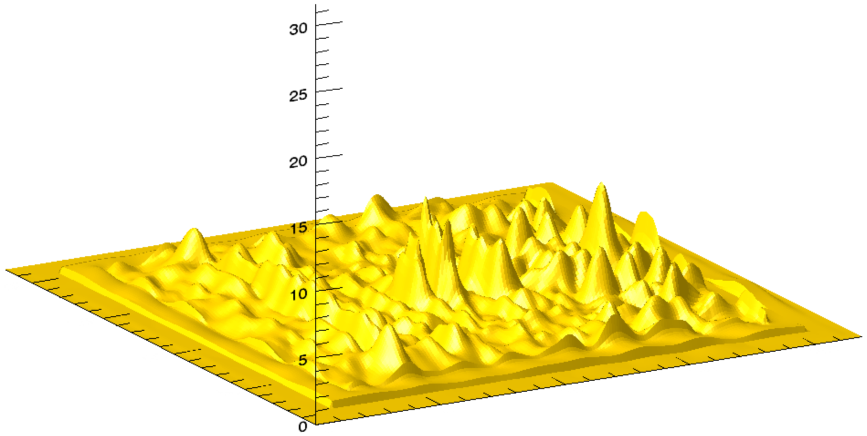

(d) 45^o

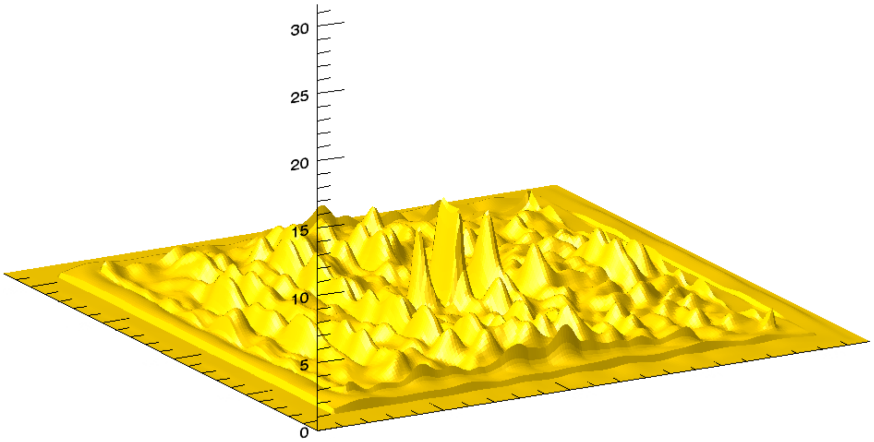

(e) 30^o

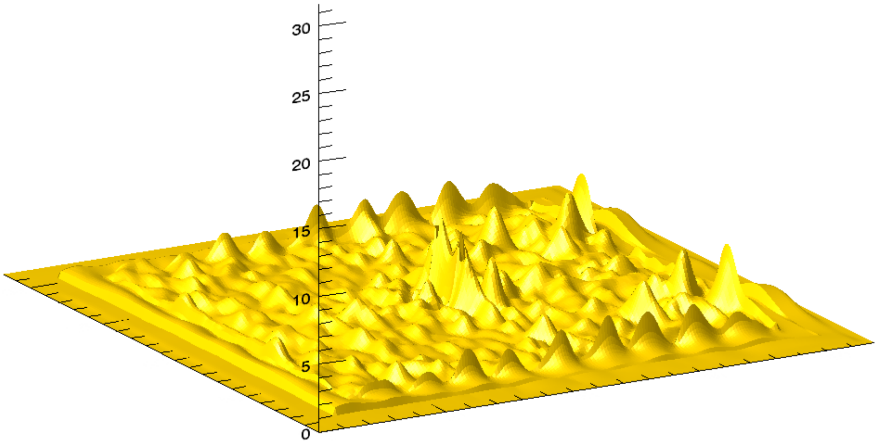

(f) 15^o

Figure 2.35: FDTD-predicted silicon surface intensities for several incident angles.

Figures 2.34 and 2.35 indicate a large dependence for potential lithographic effect on the angle of the incident laser beam. Adjusting thirty degrees from normal causes a substantial decrease in the energy actually felt by the silicon. At even lower glancing angle, all localization of enhancement is lost. Studying Figures 2.34 (a-f), there does not appear to be a coupling effect between the substrate and sphere near the contact point, so the scattering spectra most likely retains the general shape predicted from Mie theory. It will be shown in Chapter 4 that this lack of coupling is not universal, but in fact highly dependent on the sphere material. In the case of dielectric spheres, however, changing the incident angle serves mainly to increase distance between the intense point of enhancement and the substrate. Quantifying this separation effect on the evanescent field is the topic of the following section.

Section 2.3.8 Decay of evanescent field

Revisiting Mie's solution in Equations (2.1) and (2.2), one can see explicit dependence on the radial distance from the origin in the denominator of the field components as well as dependence on r within the Bessel functions. Because these functions are usually approximated by a form proportional to 1/r, a decay of $1/r^3$ of the evanescent field is often assumed in the literature. However, the functions are actually oscillatory, giving rise to the type of fluctuating decay predicted in Figures 2.13 and 2.14 by the near-field Mie analysis. Once more, due to the inherent and geometric shortcomings of the Mie analysis, an investigation is conducted on the near field decay that includes the more realistic surface reflections and origin of spherical expansion.

Before including the substrate effects, a series of simulations was conducted for two sizes of silica microspheres available for experimental use: 640 nm and 1.76 μm diameter irradiated with a 355 nm laser pulse (Nd:YAG). Figure 2.36 presents the intensity profiles as a function of sphere distance (1.76 μm) from the plane of observation. Figure 2.37 plots the decay curve of peak enhancement generated from the FDTD simulations and the $1/r^3$ approximation.

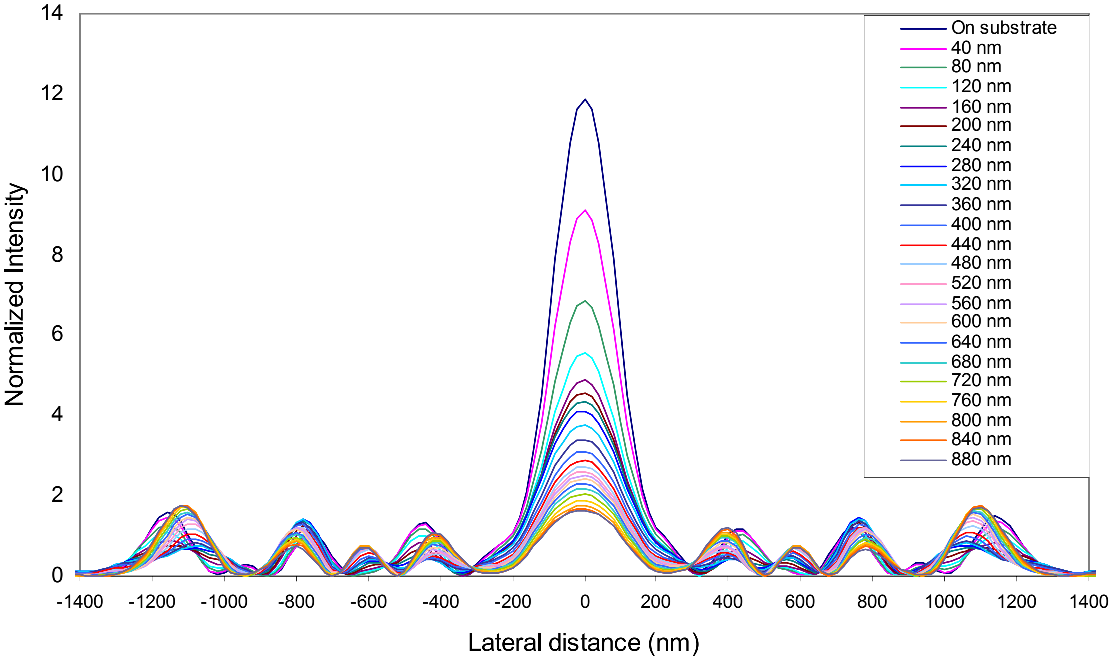

Figure 2.36: Decay of near-field intensity in the plane of observation beneath a 1.76 μm silica sphere with λ=355 nm irradiation

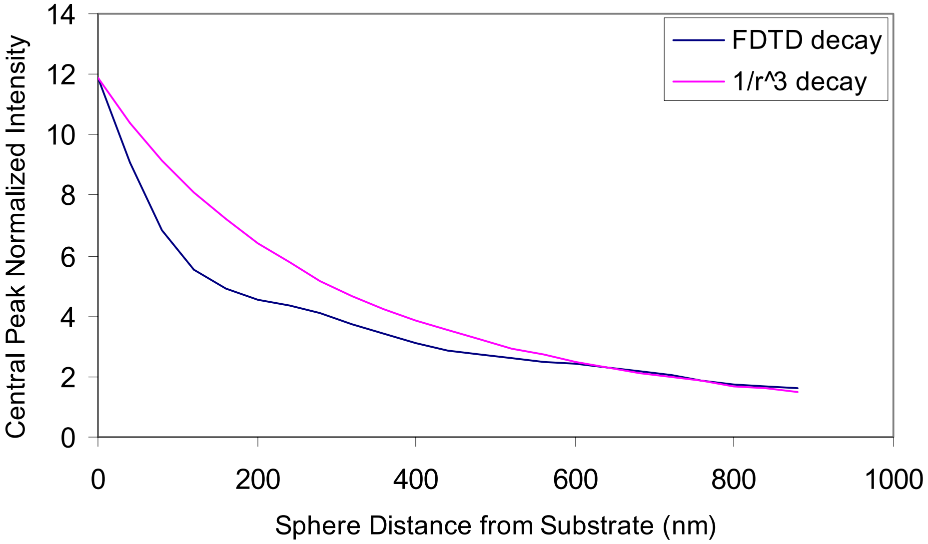

Figure 2.37: Decay of near-field intensity in the point of observation beneath a 1.76 μm silica sphere with λ=355 nm irradiation

Both Figures 2.36 and 2.37 indicate a rapid decay of intensity beyond the surface of the sphere, however Figure 2.37 sheds some light on the accuracy of the $1/r^3$ approximation. After just a short distance (less than a radius) from the sphere, the decay indeed conforms well with the polynomial value. This is as expected because the replacement of the Bessel function is for far-field quantification. Prior to 600 nm distance, a slight oscillation is detectable, though the derivative of the curve does not actually reach zero or change sign at any point. This general behavior is consistent qualitatively with the near-field Mie analysis in section 2.2.5 and is not acknowledged in the literature to the author's knowledge. Figures 2.38 and 2.39 plot identical variables for the corresponding case of the 640 nm diameter silica sphere.

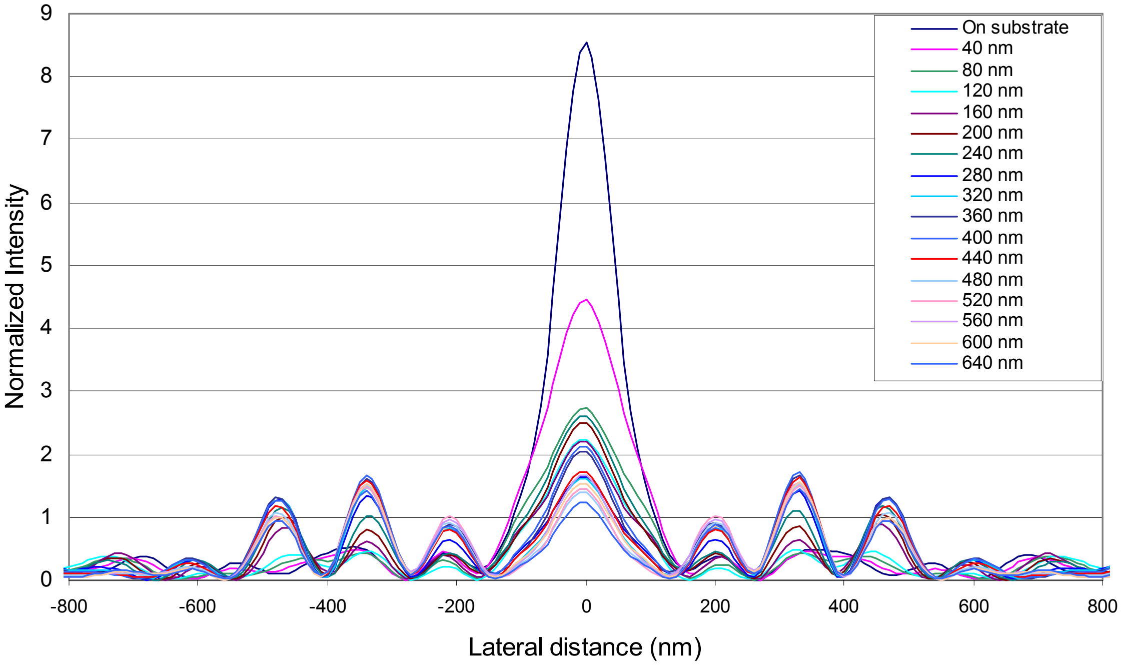

Figure 2.38: Decay of near-field intensity in the plane of observation beneath a 640 nm silica sphere with λ=355 nm irradiation

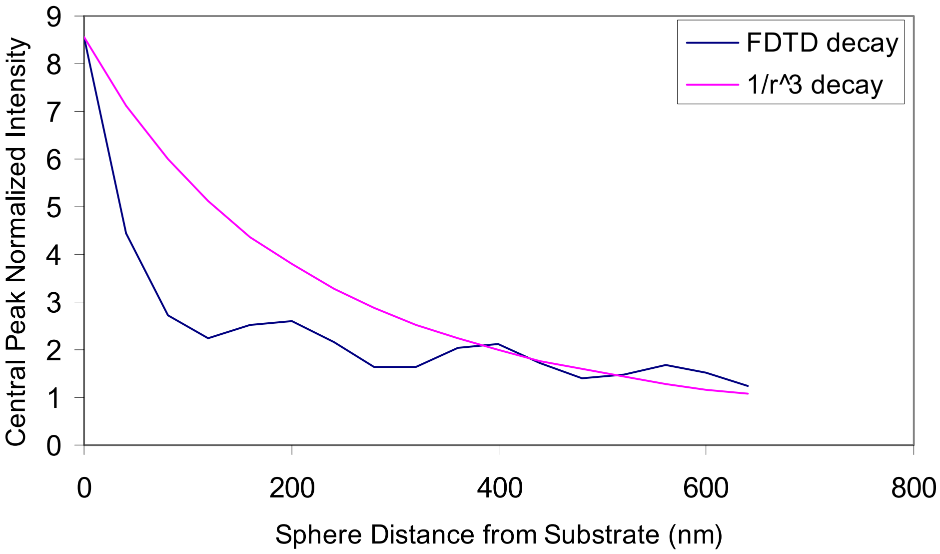

Figure 2.39: Decay of near-field intensity in the point of observation beneath a 640 nm silica sphere with λ=355 nm irradiation

The energy profiles beneath a 640 nm sphere exhibit similar behavior, decaying rapidly to far-field values. The decay of the central enhancement peak in both Figures

2.36 and 2.38 coincides with increases in the several other less intense waves of energy, to the satisfaction of energy conservation. The oscillatory decay exhibited in Figure 2.39 is more pronounced than underneath the 1.76 μm sphere. In this case, the derivative of the curve does reach zero and the intensity can in fact increase with distance from the sphere before converging to the $1/r^3$ far-field approximation.

The effect of the substrate is now introduced into the investigation of near-field decay. Because most experiments performed in UT's NOBEL lab have used silicon, this is the substrate material simulated. From the data presented above, the range of distance between sphere and substrate is limited to one sphere diameter. Figure 2.40 (a-d) shows the variation in cross-sectional intensity for a third case as a 1.0 μm sphere is moved from the surface, this time with λ=500 nm irradiation. Figure 2.41 (a-d) gives the substrate surface intensities for the same cases. The presumed roughness of the substrate surface at about 2 nm is neglected here, with the assumption that the corresponding effect is negligible.

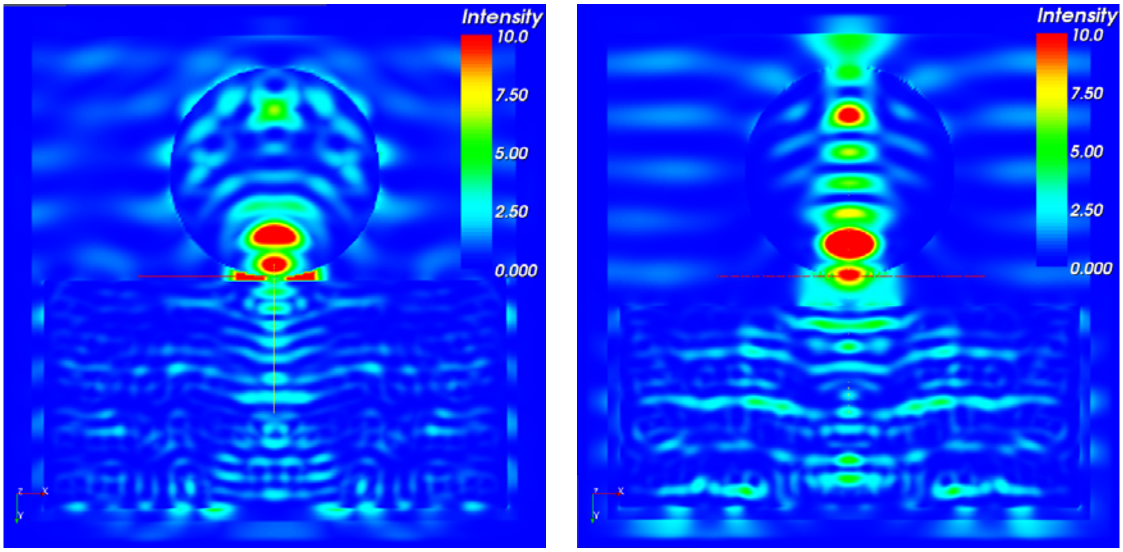

(a) Δ=10 nm

(b) Δ=125 nm

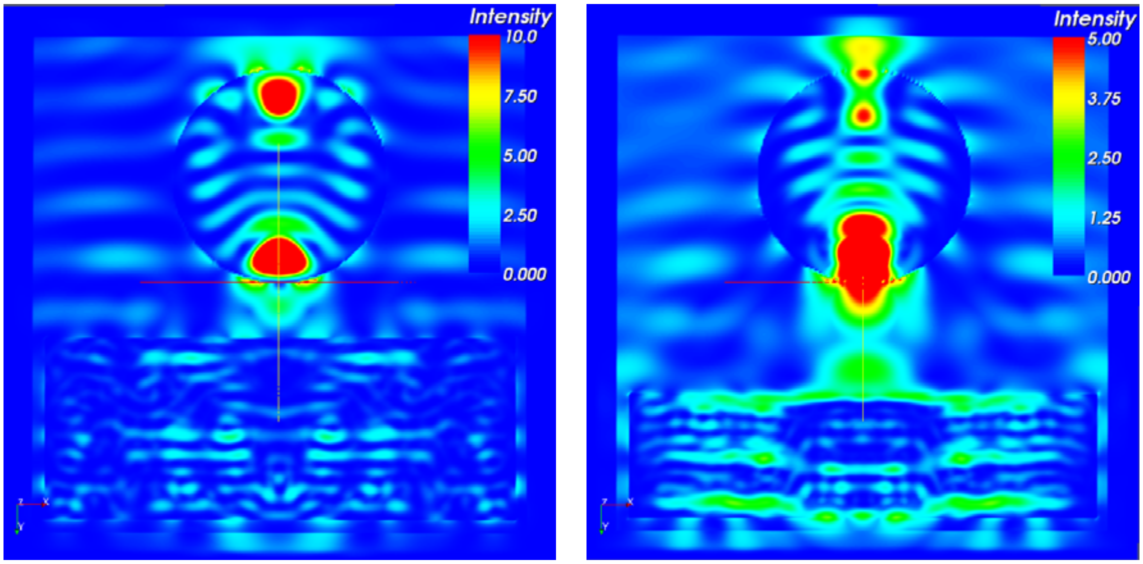

(c) Δ=250 nm (c) Δ=500 nm

Figure 2.40: Decay of near-field intensity on substrate beneath a 1.76 μm silica sphere with λ=532 nm irradiation

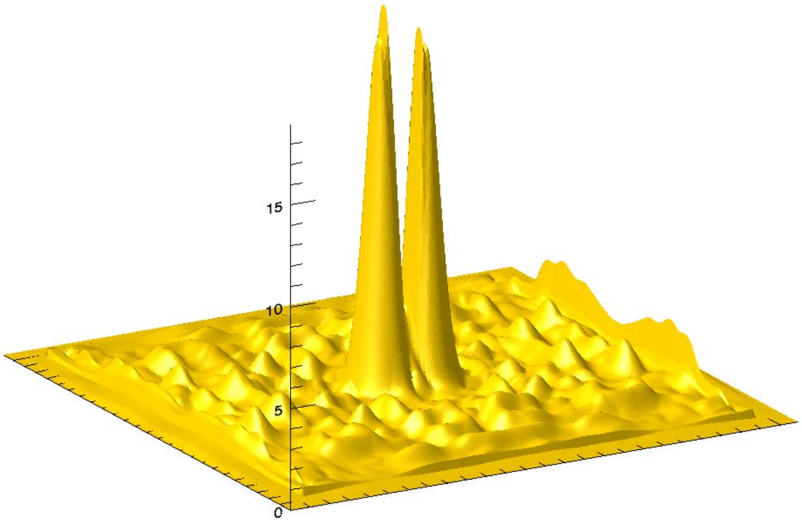

(a) Δ=10 nm

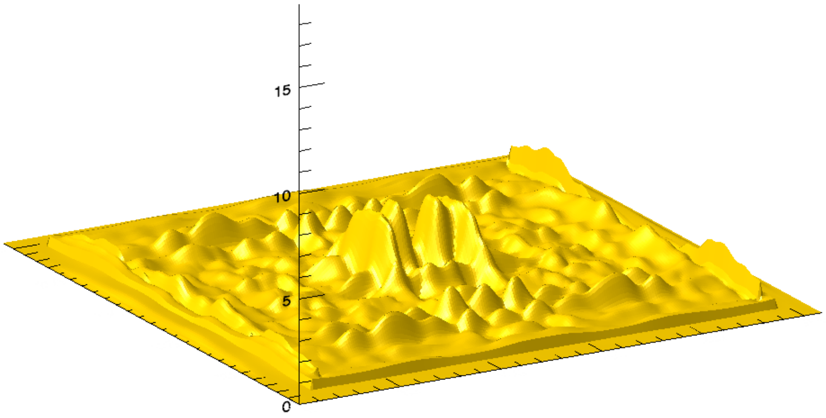

(a) Δ=125 nm

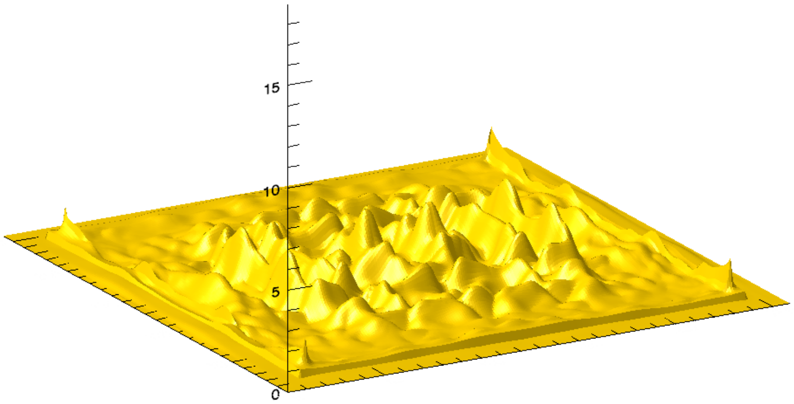

(a) Δ=250 nm

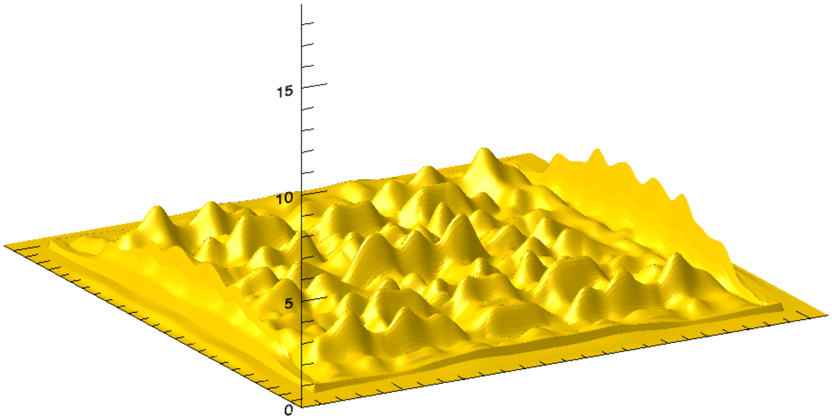

(a) Δ=500 nm

Figure 2.41: Surface intensity distributions on substrate beneath a 1.76 μm silica sphere with λ=532 nm irradiation at several separation distances

It is evident mainly from Figures 2.41 (a-d) how quickly the surface intensity decays. After merely a radius separation distance from the silicon, the enhancement has essentially vanished into a conglomeration of interference effects that homogenize laterally along the surface. Another subtle effect faintly distinguishable from Figures 2.40 (a-d) is the reduction of the dual enhancement peaks back into a more singular localization of energy on the substrate before the near-field decays altogether.

Section 2.3.9 Array effect

The experimental procedure outlined in Section 2.1 often employ a self-assembly technique taking advantage of surface forces to generate a hexagonally close-packed monolayer of spheres, visible in Figure 2.2. In this situation, the effect of neighboring spheres on the evanescent field is uncertain. Mie theory is unable to resolve this question, however an FDTD analysis can provide insight.

Two simulations were performed to identify any array effect for dielectric spheres. A property grid was defined placing six spheres in appropriate positions around a central sphere on the silicon substrate. The spheres were “touching”, within the limits of mesh discretization. Field calculations were performed until convergence, generating intensity distributions beneath the spheres. For the second simulation, the six neighboring spheres were removed with all other parameters remaining the same. Figure 2.42 gives the surface intensity profile for the array setup as well as a comparison between simulations. The values plotted lay along the line demarcated in Figure 2.42 (a).

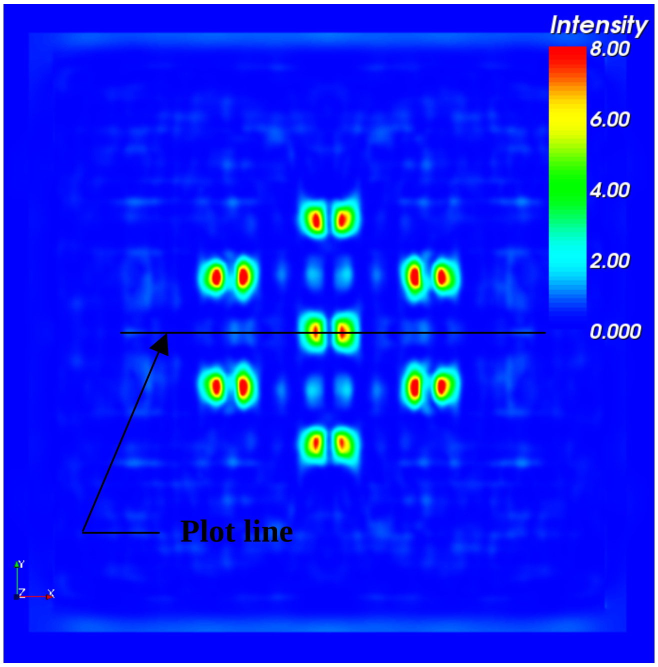

(a)

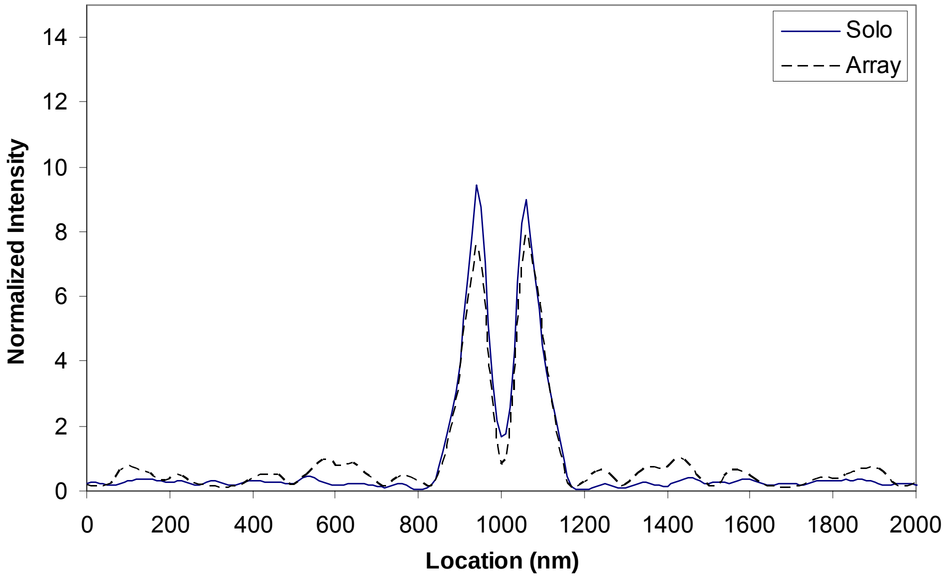

(b)

Figure 2.42: Comparison of intensities beneath solo SiO_2 sphere and HCP-array of SiO_2 microspheres

From the results presented in Figure 2.42, there seems to be a detectable but minimal effect on the substantially enhanced field beneath the central sphere due to the presence of adjacent spheres. This result is consistent with the findings of the angle effect investigation, which did not find a coupling effect between dielectric spheres and substrate. It can be concluded that the results of the preceding investigations of solo sphere enhancement can be applied to both sparsely scattered experiments as well as massively parallel patterning efforts using the HCP self-assembled formations with a reasonable expectation of accuracy when laser incidence is near normal. Small incident laser angles have not been simulated with HCP formations. Judging from the intensity distributions predicted from the angle investigation with solo spheres, this solo/array independence would not apply when the localized enhancement was directed at a neighboring sphere rather than the substrate, i.e. glancing angles.

As with the lack of coupling seen in the angular investigation, this result will be shown to be highly material specific. In Chapter 4, the solo vs. array effect will be revisited simulating interaction between laser light and noble metals.

2.4 Summary

Experiments have been conducted which take advantage of the near-field electromagnetic enhancement phenomena surrounding microstructures irradiated at wavelengths ranging from near-ultraviolet to near-infrared. These experiments have shown the possibility of using laser/microsphere interaction as a sub-wavelength optical lithography tool. In this chapter, an investigation of light scattering in the near-field of dielectric spheres using

Mie theory was presented in an attempt to describe the physical process and develop design criteria for the method.

The near-field Mie analysis obtained curves describing the enhancement dependence on the size of the sphere, wavelength of irradiation, and the ratio of the two values in a collapsed similarity variable. The decay of the near-field perpendicular to the microstructure boundary was investigated analytically. While the field components decay quickly as the observation point moves from the sphere, a fluctuating behavior is uncovered that is lost when using exponential functions in place of the Bessel functions in the less rigorous far-field application of Mie theory. Limitations of a near-field Mie analysis are then discussed, which include the inability to treat surrounding geometries as well as inherent far-field assumptions when deriving the Debye potentials used in the Mie solution. For these reasons, near-field Mie theory is concluded to be a qualitatively useful tool, but a numerical investigation that can alleviate the limitations is desirable.

A three dimensional finite-difference time-domain (FDTD) code is therefore built to expand the investigation of the evanescent field with application to nanolithography. The program employs the convolutional perfectly matched layer (CPML) absorbing boundary condition, and generates the laser waveform using the total-field/scattered field (TFSF) technique. The code is verified by comparison to the analytical solution for a radiating dipole, and a grid independence investigation determines the appropriate numerical constraints. FDTD simulations are then conducted of suspended dielectric spheres and compared to near-field Mie analysis, giving good enhancement and localization agreement.

A transient analysis is conducted, uncovering a potential physical root to discrepancies between FDTD and near-field Mie results. Whereas Mie theory assumes an origin of spherical expansion at the center of the sphere, FDTD analysis shows that the origin is slightly offset from center toward the opposite side from the incident wave. In the far-field the effect of this is negligible, however in the near field, the absolute level of enhancement predicted between analyses could be affected.

FDTD simulations are conducted including the substrate to account for geometric and reflection effects. It is shown that the profile of enhancement "seen" by the substrate is deformed due to its presence. Further material investigation shows that this level of deformation is highly dependent on the optical properties of the substrate. A more highly reflecting material (at optical wavelengths) such as silicon will generate higher levels of more localized enhancement than an optically transparent substrate such as Pyrex. Simulations were conducted using several size factors (~radius/wavelength) providing a quantitative data set for a solo silica sphere on a silicon substrate irradiated by a 532nm laser.

Simulations were then performed to investigate the angular and distance dependencies on the enhanced intensities directed to a substrate. Based on the angle effect simulations, it was concluded that adjusting the angle of laser incidence serves mainly to design a separation distance between the area of greatest enhancement and the substrate. No coupling due contact between sphere and substrate was observed. Simulations predicting the effect of separation distance with the inclusion of substrate effects found an oscillatory behavior predicted by the near-field Mie analysis. It is shown that the effect is contained within a diameter's separation distance, after which the solution converges to the far-field approximation.

Lastly, an investigation into any possible effect of neighboring spheres on the enhanced field under a *dielectric* sphere was conducted. It was found that with normal laser incidence, the surrounding spheres can be neglected from an electrodynamic standpoint. Heat transfer analysis due to the electrodynamic solutions presented here are given in Chapter 3 of this work.

Chapter 3:
Energy Transport

3.1 Conventional Microscale Heat Transfer

The preceding chapter addressed the mechanism by which sub-wavelength optical lithography is made possible. The resolved electromagnetic fields clearly indicate a subwavelength focusing of energy to be used for substrate surface modification. The challenge remains to develop a design tool that predicts the final lithographic capabilities of the novel method. This requires addressing energy and mass transfer through the affected material by a number of transport mechanisms, which depend on the characteristic time, scale and material structure. Surface modification using a nanosecond pulsed laser is investigated initially, followed by an analysis of energy transport due to femtosecond (or ultrafast) lasing.

3.1.1 Model development

Calculation of the laser intensity enhancement from Chapter 2 provides a source condition to employ in a model of the heat transfer within the substrate. The goal of the simulation is to obtain a maximum temperature distribution in the silicon, which indicates the size and shape of the melt zone. This data is then compared with experimental observations characterized using an SEM.

A pulsed Nd:YAG laser is used for the initial experiments. The ~ 12 nanosecond duration of the laser pulse allows the use of Fourier conduction within the substrate, which is modeled as a semi-infinite slab. The enthalpy method was used explicitly to account for the moving phase boundary within the material. This is referred to as the Stefan problem and has been accurately modeled using this method in the past

(Shamsundar and Sparrow, 1975, Minkowycz and Sparrow, 1996). The heat equation as a function of the enthalpy in the solid silicon is

$$\rho \frac{\partial h}{\partial t} = \frac{\partial}{\partial x}\left(k \frac{\partial T}{\partial x} \right) + \frac{\partial}{\partial y}\left(k \frac{\partial T}{\partial y} \right) + \dot{q} \tag{3.1}$$

with the generation term $\dot{q}$ (W/m^3) equal to

$$\dot{q} = (1 - R) \cdot q_{inc}(x_{\text{int}}, t) \cdot \gamma \cdot e^{(-\gamma \cdot z)} \tag{3.2}$$

where R is the reflectivity of silicon dependent on the wavelength of the incident light and phase of the silicon, and γ is the absorption coefficient, given by:

$$R = \frac{(n-1)^2 + k_x^2}{(n+1)^2 + k_x^2} \tag{3.3}$$

$$\gamma = \frac{4 \cdot \pi \cdot k_x}{\lambda} \tag{3.4}$$

q_{inc} is the enhanced value of laser energy taken at x_{int}, the surface intercept node between the node in the solid and the center of the sphere. It follows a Gaussian shape through time given by

$$q_{inc}(x_{\text{int}}, t) = A \cdot \exp\left[-(B - t)^2 / C \right] \cdot I(x_{\text{int}}) \tag{3.5}$$

The constants B and C are fit to the laser waveform, while A ensures the total energy incident corresponds to the proper fluence, and $I(x_{\text{int}})$ refers to the intensity distribution developed from the near-field Mie analyses and finite-difference time-domain results presented in Chapter 2.

New values of h are calculated explicitly at every time step, relying only on the surrounding temperatures from the previous iteration. This precludes the need to invert matrices or employ other convergence algorithms, but requires the following expression be obeyed to prevent divergence of the solution.

$$\frac{\Delta t}{\Delta x^2} \le \frac{\rho \cdot c}{4 \cdot k} \tag{3.6}$$

This expression limits the numerical time and space steps in terms of the specific heat, density, and thermal conductivity of the material. Using the extreme values of all three variables in the anticipated temperature range, the left-hand side of Eqn. (3.6) must be less than approximately 6000 s/m^2. Time steps of 75 fs and space steps of 19.5 nm were used to obtain the following results, and were proven adequate by grid-independence investigations.

At the surface of the substrate in the presence of opaque liquid silicon, an energy conserving boundary condition is used to account for energy loss due to radiation, which was found to be significant.

$$\left(1 - R\right) \cdot q_{inc} - \varepsilon \cdot \sigma \cdot T^4 = k \frac{\Delta t}{\Delta y} + \rho \cdot c \cdot \Delta y \frac{\Delta T}{\Delta t} \tag{3.7}$$

The emissivity, ε, of the liquid silicon is determined from the following relation:

$$\varepsilon(\lambda, T) = \frac{4n}{n^2 + k_x^2 + 2n + 1} \tag{3.8}$$

where the refractive indices n and k_x are obtained from Jellison (1987) and Hull (1999).

The new value of enthalpy calculated determines the temperature at the node based on the following relations:

$$T_{x,y}^{t+1} = h_{x,y}^{t+1} / c_l \qquad h^{t+1} < (c \cdot T_m) \tag{3.9a}$$

$$T_{x,y}^{t+1} = T_m \qquad (c \cdot T_m) < h^{t+1} < (c \cdot T_m + L) \tag{3.9b}$$

$$T_{x,y}^{t+1} = \left(h_{x,y}^{t+1} - (c - c_l) \cdot T_m - L_m\right) / c_l \qquad h^{t+1} \geq (c \cdot T_m + L) \tag{3.9c}$$

The silicon is therefore separated into three regimes: solid, liquid, and a transition or mushy zone in which the silicon is at the melting temperature, yet has not overcome the latent heat of fusion. The boundaries of these regions are tracked through time using the preceding method.

Material property dependencies are given as follows (Hull, 1999), (Theppakuttai et al., 2004):

Specific heat: $c = 1000 * \left(.71239 + \left(1.9612e - 4\right) * T(x,y,t)\right)$ [J/kg-K] T≤ Tm (3.10a)

$c = 1032$ [J/kg*K] T>Tm (3.10b)

Thermal conductivity: $k = \dfrac{29900}{T(x,y,t) - 99}$ [W/m-K] T≤ Tm (3.11a)

$k = 70$ [W/m-K] T>Tm (3.11b)

Density: $\rho = 2329$ [kg/m^3] T≤ Tm (3.12a)

$\rho = 2560$ [kg/m^3] T>Tm (3.12b)

3.1.1 Near-field Mie/conventional heat transfer results

A suitable starting point for the heat transfer analysis due to the enhanced energy is the application of near-field Mie theory to the model outlined above. In addition to providing a comparison with lithographic results predicted by the FDTD profiles, which would then determine the necessity of the far more computationally expensive finite-difference simulations, analysis using Mie theory is facilitated by the symmetric enhancement profiles. A two-dimensional heat transfer analysis is possible in this case, implied by the coordinate system in Eq. (3.1). Due to the dual enhancement peaks and polarization effects predicted by FDTD simulations, three-dimensional analysis is performed and presented in the following section. Mie theory's inability to treat neighboring geometries should be kept in mind, however the use of such profiles in a heat transfer effort is considered a valuable first-order design prediction.

The heat transfer simulations were conducted using 1.76 μm SiO_2 spheres irradiated by a single 532 nm laser pulse at four fluences: 50, 100, 200, and 300 mJ/cm^2. The input condition of Figure 2.4(a) employed in Eq. (3.1) was used in all cases. Figure 3.1 (a-d) gives the numerical results predicting the width and depth of the melt and mushy zones in the silicon for the four laser energies.

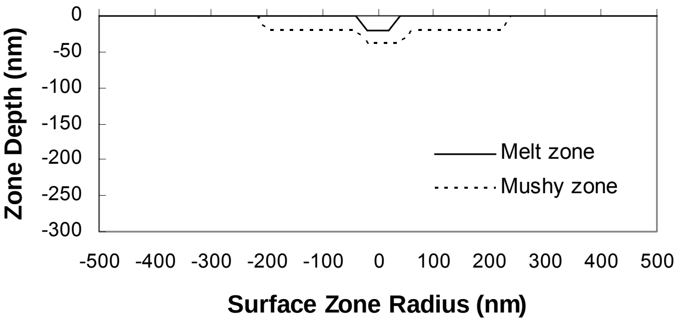

(a) 50 mJ/cm2

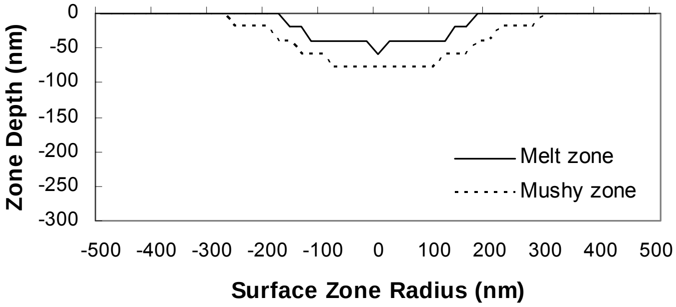

(b) 100 mJ/cm2

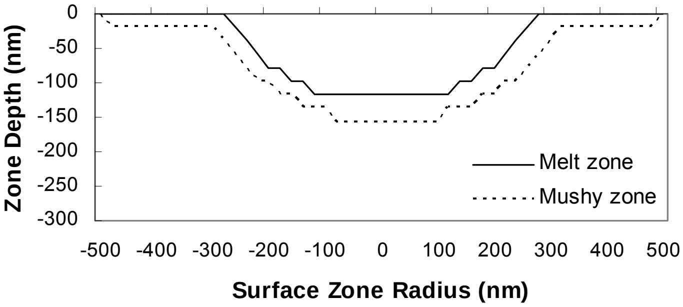

(c) 200 mJ/cm2

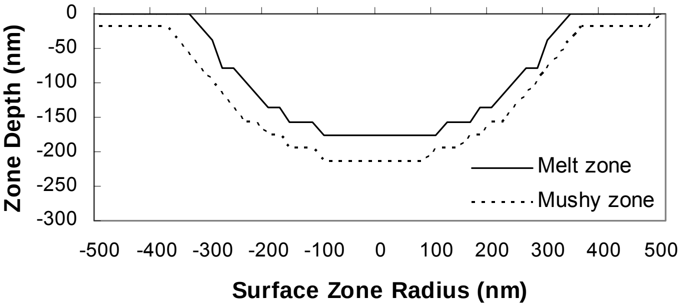

(d) 300 mJ/cm2

Figure 3.1: Predicted geometry of melt and mushy zones in silicon at laser fluence of (a) 50 mJ/cm^2, (b) 100 mJ/cm^2, (c) 200 mJ/cm^2, and (d) 300 mJ/cm^2.

Scanning electron microscope characterizations were obtained after the experimental procedure. There are essentially two points of comparison available between the SEM micrographs and the simulation results: the size of the surface damage, and the threshold energy below which no damage occurs. The micrographs presented in Figure 3.2 show very little damage to the substrate when the particles are irradiated at a fluence of 50 mJ/cm^2, and by comparison it is evident that this energy is very close to the threshold below which no damage to the silicon occurs. At 50 mJ/cm^2, the model predicts that the surface of the substrate barely reaches the melting temperature, with melt zone only a few nm wide and deep, and a mushy or heat-affected zone approximately 430 nm wide. The heat affected zone is very shallow, and in terms of transience the melting temperature is only attained for a few nanoseconds. At 100 mJ/cm^2, the model predicts a melted zone approximately 332 nm in diameter, which a total heat affected region of 548 nm diameter. At 200 mJ/cm^2, a zone of melted silicon 528 nm in diameter is predicted, with a heat affected region 939 nm in diameter. Here the predicted melt depth doubles to 156 nm. At energy of 300 mJ/cm^2, a zone of melted silicon approximately 645 nm with a total heat affected zone of 958 nm in diameter is predicted. A melt depth of 215 nm is also predicted.

Figure 3.2 is a SEM micrograph of the silicon substrate obtained by Theppakuttai (2006) after irradiation of the silica spheres at different laser fluences. At fluences of 200 and 300 mJ/cm^2 the diameter of the features obtained are ~1000 nm, matching the predictions well. However at 50 mJ/cm^2 and 100 mJ/cm^2 the size of the zone shrinks, but not quite to the degree predicted numerically. It can also be observed that some of the features obtained are not perfectly circular as predicted. This could be due partially to the slight variation in the laser incident angle due to the beam delivery optics used in the experiment, however the deformation due to the polarization and substrate effects are also likely and addressed in the following section. A direct comparison of the feature diameters between the predicted and experimental results is presented in Fig. 3.3.

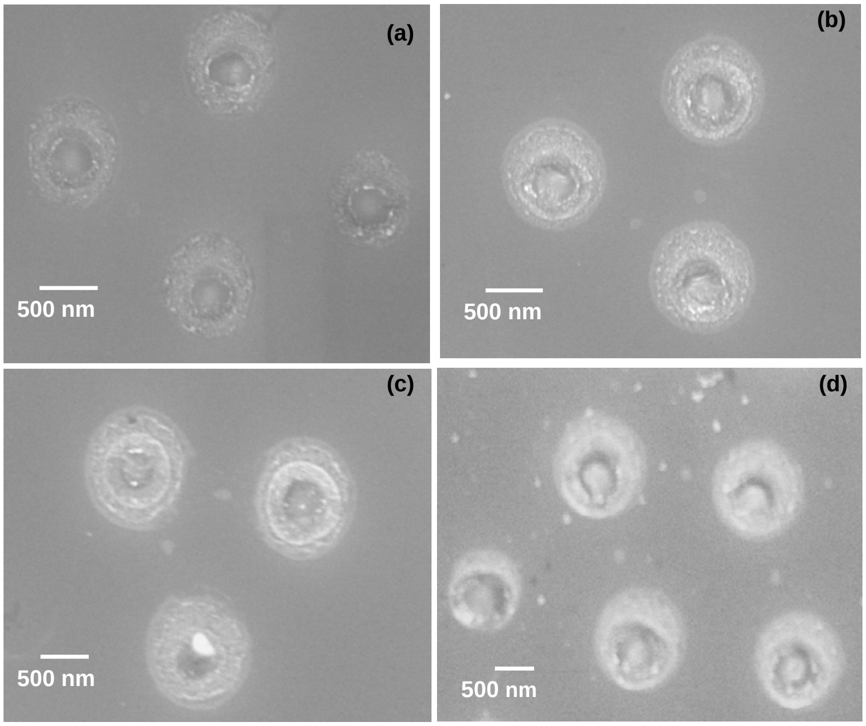

Figure 3.2: SEM micrograph of 1.76 µm SiO_2 spheres irradiated by 532 nm laser at a fluence of (a) 50 mJ/cm^2, (b) 100 mJ/cm^2, (c) 200 mJ/cm^2, and (d) 300 mJ/cm^2. (Theppakuttai, 2006)

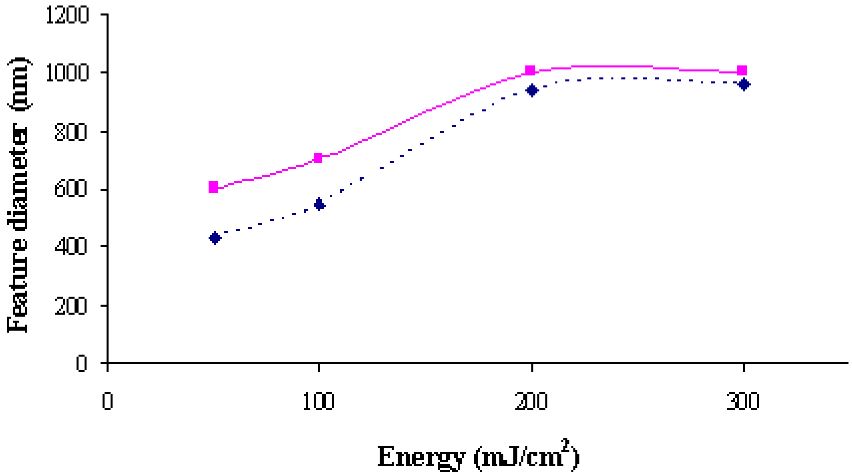

Figure 3.3: Comparison of the predicted and experimental feature diameters (Theppakuttai, 2006) for 1.76 µm SiO_2 spheres irradiated by 532 nm laser at different laser fluences.

Both the extent of the surface modification and the damage threshold predicted are close to what is observed experimentally. The experimental results show very little damage to the substrate when the particles are irradiated at a fluence of 50 mJ/cm^2, and by comparing with the modeling results it is evident that this energy is very close to the threshold below which no damage to silicon occurs. An additional simulation was conducted at a fluence of 40 mJ/cm^2, which returned a peak temperature below the melting point of silicon. This is a strong indication that the level of enhancement obtained from the near-field Mie calculations is accurate well within an order of magnitude.

Section 3.1.2 FDTD/conventional heat transfer results

In an effort to more accurately model the heat transfer through silicon due to a nanosecond laser pulse, the FDTD surface intensity profiles were employed. The two-dimensional heat transfer model given in the previous section would not sufficiently incorporate the three-dimensional input intensity supplied by the FDTD simulations. For this reason, a 3-D model was built, identical except for the inclusion of a second lateral direction in the heat equation, now given by Equation (3.13).

$$\rho \frac{\partial h}{\partial t} = \frac{\partial}{\partial x}\left(k \frac{\partial T}{\partial x}\right) + \frac{\partial}{\partial y}\left(k \frac{\partial T}{\partial y}\right) + \frac{\partial}{\partial z}\left(k \frac{\partial T}{\partial z}\right) + \dot{q} \tag{3.13}$$

The added dimension requires a more constrained stability condition, now given by Equation (3.14). The grid resolution was increased by a factor of ~2, to 10nm x 10nm x 10nm cubes.

$$\frac{\Delta t}{\Delta x^2} \leq \frac{\rho \cdot c}{6 \cdot k} \tag{3.14}$$

Runs of duration equal to the laser pulse duration (12 ns) and twice as long as the pulse duration were conducted to determine if diffusive effects could contribute to a local temperature maximum even with zero energy input. It was found that only a few nodes (out of 8 million nodes in each simulation) near the border of the melt zones actually increased in temperature beyond the melting point after the pulse was turned off. These nodes were located near the most extreme temperature gradients and are effectively negligible regarding to the overall crater formation. The maximum temperatures *above the melting point*, and hence the resulting crater shape, were achieved at or around 8 ns, after the Gaussian peak in time but before the energy input had extinguished.

Simulations were conducted using input fluences of 50, 100, 200, and 300 mJ/cm^2, identical to those presented above. The resulting crater shapes are given in Figure 3.4 (a-d). Maximum crater depths of 10, 40, 90, and 130 nm were predicted at the respective energies. Maximum crater widths of 520, 640, 820, and 840 nm were predicted at the respective energies.

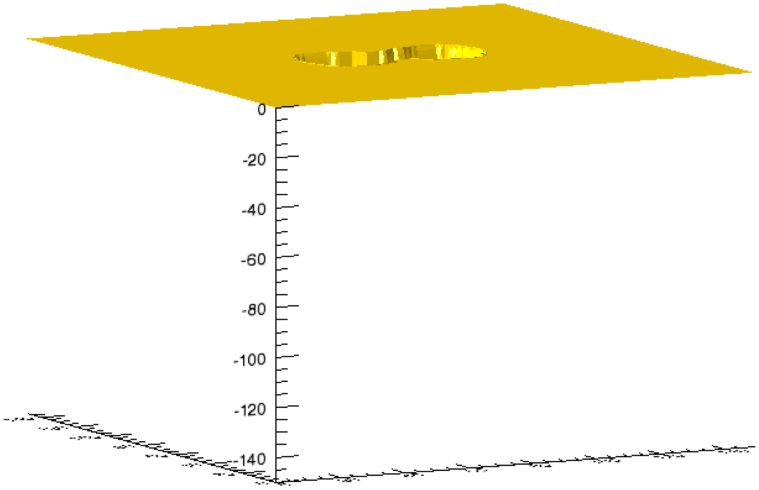

(a) F=50 mJ/cm^2, depth in nm, plot range 1.5 µm x 1.5 µm

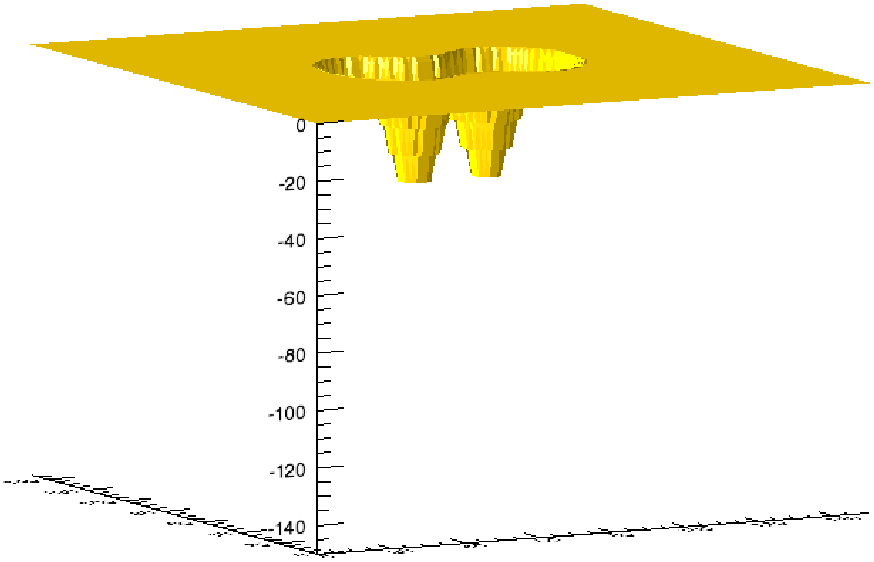

(b) F=100 mJ/cm^2, depth in nm, plot range 1.5 µm x 1.5 µm

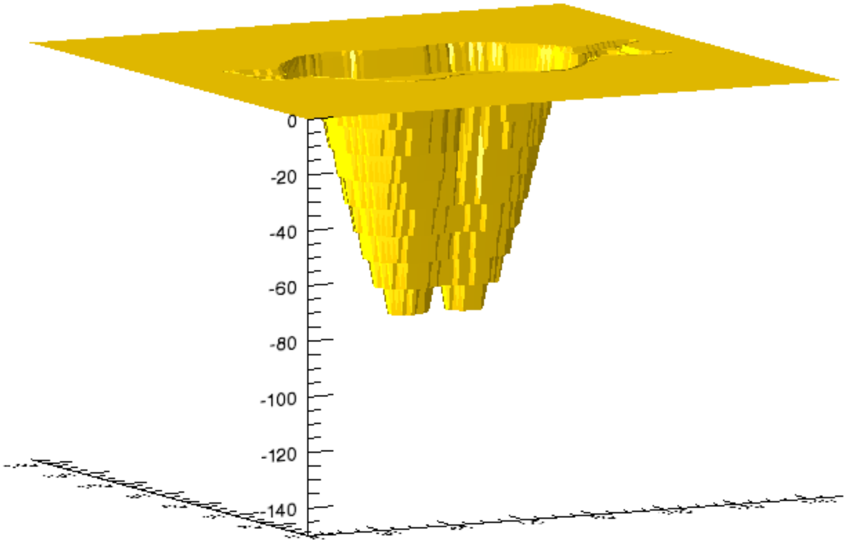

(c) F=200 mJ/cm^2, depth in nm, plot range 1.5 µm x 1.5 µm

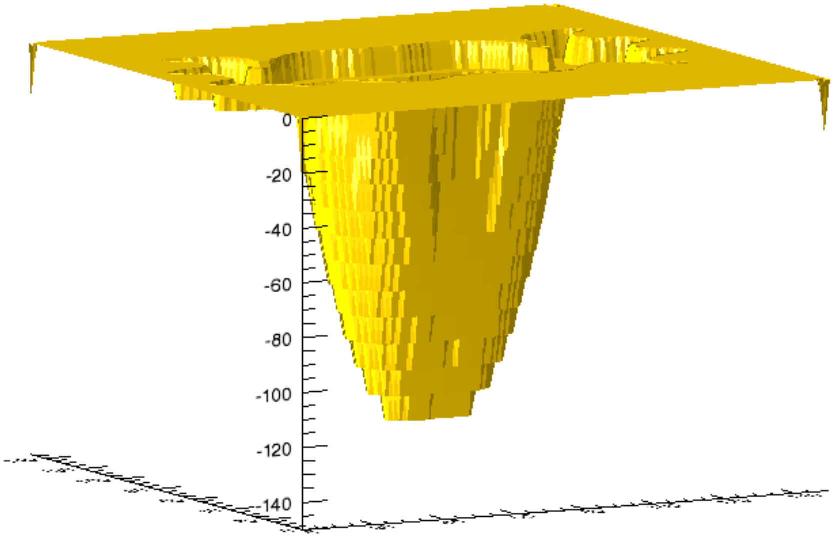

(d) F=300 mJ/cm^2, depth in nm, plot range 1.5 µm x 1.5 µm

Figure 3.4: Predicted crater shapes for 1.76 µm SiO_2 spheres irradiated by 532 nm laser at different laser fluences, due to FDTD-obtained input condition.

It is difficult to compare the exact morphologies to the SEM micrographs given in Figure 3.2, especially given the lack of cross-sectional characterizations, however size and shapes of both predicted and experimentally observed melt craters are in approximate agreement. An important consideration is the threshold fluence for material damage. Figure 3.4 (a) indicates 10 nm of melting at 50 mJ/cm^2, the minimum within grid resolution. This again matches the experimentally determined threshold fluence of between 40 and 50 mJ/cm^2.

The dimension added due to FDTD surface intensities is apparent through Figures 3.4 (a-d), as the craters are not conical, but slightly asymmetric in both vertical and horizontal directions. Diffusion of energy through the lattice mitigates this asymmetry however, “rounding off” the sharpest gradients in energy input. For instance, at the higher fluences, the crater bottom does not exhibit any of the dual-peak characteristic of the energy input. Diffusion between the peaks has melted the intervening silicon. This is in contrast to what will be shown in the following section, where the time scale of energy input is rapid enough to nearly eliminate thermal transport. It can be concluded that the diffusive effects serve to harmonize the results of the near-field Mie analysis and the FDTD simulations. This is applicable only when the laser pulse duration is sufficient that the Fourier approximation within the target material is valid.

3.2 Ultrafast Heat Transfer

In the field of optoelectronics and micro-electronics, fused quartz and related silicate glasses are very important materials due to their high transmission properties in the UV to

IR range, excellent thermal properties, good electrical insulation and high chemical stability (Zhang et al., 1999). Also, borosilicate glass has an excellent anodic bonding property and surface integrity which makes it the usual substrate for micro-electro mechanical systems (MEMS). Therefore in order to build a communication interface, micro/nano-holes free of micro-cracks, with good edge and surface quality as well as high aspect ratios need to be formed on the glass substrate. Using traditional micro-machining process for a micro-hole with a diameter below 200 μm is difficult because of the extreme hardness, brittleness, corrosion resistance and melting temperature of glass. Also the conventional thermal and/or chemical machining methods create an excessive heat-affected zone. Mechanical machining methods also have limitations in productivity and accuracy (Park et al., 2004). Hence, to solve this problem various machining methods have been proposed like the combination of microelectrical-discharge machining (MEDM) and microultrasonic vibration machining (MUSM), (Yan et al, 2002), micro-abrasive jet machining (AJM), (Park et al., 2004), laser-induced plasma-assisted ablation (LIPAA), (Zhang et al., 1998), direct laser write process using short pulses (Nikumb et al., 2005), combination of nanoindenter and HF wet etching (Youn et al., 2005), and hologram encoding system with femtosecond laser pulses (Hirano et al., 2002) etc. Due to the various working mechanisms of these methods, the results produced are distinct. However high-quality holes in nanoscale were not obtained using these techniques.

Laser induced ablation has several advantages over the conventional mechanical and/or chemical machining; it is a single-step process with very high flexibility, non-contact process, direct patterning without the resist process, good etch-rate and does not require any etchants. The femtosecond regime offers advantages over the nanosecond regime, by depositing energy into a material in a very short time period, before any thermal diffusion can occur. In this section, the theoretical analysis of energy transport through hard-to-machine borosilicate glass using a femtosecond laser pulse is presented. Computational results are then compared to experimental characterizations performed by Battula (Heltzel, et al., 2007).

3.2.1 Ultrafast model development

The essentially non-thermal process of femtosecond laser ablation makes it very attractive as a machining tool due to the clean features and negligible heat-affected zone. As a non-thermal process, standard heat transfer models must be discarded in favor of ideas that describe the complex photon energy absorption as well as the mechanisms that transport the energy between the electronic system and lattice system. Studies by Lenzner et al. (1998), Stuart et al. (1995), Perry et al. (1999) and others mentioned in Section 1.2 of this work have provided empirical data that make a theoretical investigation of ultrafast ablation of dielectrics possible.

Due to the wide energy gap between the valence and conduction bands of dielectrics, the conduction band is occupied by low electron densities within a large range of electron temperatures. Energy will not be transported by phonons through the dielectric material during a sub-picosecond laser pulse because the free electron thermal relaxation times are generally larger than the pulse duration, leaving lattice temperatures essentially unchanged. For these reasons, the popular two-temperature model used for femtosecond laser heating of metals (Anisimov and Rethfeld, 1997, Qiu and Tien, 1993) is invalid for dielectric materials or any material possessing a sufficiently wide bandgap. To model laser heating in fused silica and borosilicate glass, a relation derived by Stuart et al. (1995) is used, describing the evolution of free electron density in a dielectric medium exposed to intense laser radiation.

$$\frac{dn_e(r,z,t)}{dt} = a_i I(r,z,t) n_e(r,z,t) + \delta_N (I(r,z,t))^N \tag{3.15}$$

where I is the spatial and temporally dependent intensity of the laser pulse, n_e is the electron density, a_i is the avalanche ionization coefficient, and δ_N is the cross-section of N-photon absorption.

The first term on the RHS of Eqn. (3.15) denotes the contribution to free electron generation due to avalanche ionization, a nonlinear process where a single charged particle initiates the ionization of others around it. The "seed" ions needed for the avalanche process to progress are formed by multi-photon ionization (MPI) quantified along with impact ionization in the second term of Eqn. (3.15). MPI dominates the production of ions (and hence conduction band "free" electrons) in the first stages of a fs laser pulse (Lenzner et al., 1998). After several fs, the avalanche process dominates, which leads to a drastic change in the optical properties of the material and is instrumental in the final surface modification.

Lenzner et al. (1998) have experimentally determined the coefficients for fused silica: a_i=4±0.6 cm^2/J, δ_N=6x10$^{8\pm0.9}$ cm^{-3}ps^{-1}(cm^2/TW)^6 with N=6, and barium aluminum borosilicate (BBS): a_i=1.2±0.4 cm^2/J, δ_N=7x10$^{17\pm0.5}$ cm^{-3}ps^{-1}(cm^2/TW)^3 with N=3. A model has been proposed by Jiang and Tsai (2004, 2005) based on Eqn. (3.15) which has given ablation depths and crater shapes in good agreement with experiments. The model used for the present calculations draws heavily from that of Jiang and Tsai (2005) with exceptions to be noted during the discussion. The laser intensity within the material is described by

$$I(r,z,t)=\frac{2\cdot F_{peak}}{\sqrt{\pi/\ln 2}\cdot t_p}\left[1-\mathrm{R}(r,t)\right]\cdot\exp\left[-\frac{2\cdot r^2}{r_0^2}-(4\ln 2)\frac{t^2}{t_p^2}-\int_0^z \alpha(r,z,t)dz\right] \tag{3.16}$$

where t_p is the laser pulse duration, r_0 is the radius of the irradiated area, and α is the absorption coefficient of the material. Eqn. (3.16) provides for a Gaussian distribution of energy with space and time. The peak laser fluence, F_{peak}, is given by

$$F_{peak}=\frac{2\cdot E_{pulse}}{\pi\cdot r_0^2} \tag{3.17}$$

where E_{pulse} is the total pulse energy.

The reflectivity of the material to normal incidence, R, is calculated as the maximum of the inherent, or "steady-state" reflectivity of the glass and the reflectivity of the plasma: $\mathrm{R}(r,t)=\max(\mathrm{R}_{ss}, \mathrm{R}_p)$. Both values come from the complex refractive index of the material according to the Fresnel expression.

$$\mathrm{R}_p(r,t)=\frac{(n-1)^2+k^2}{(n+1)^2+k^2} \tag{3.18}$$

where n and k are the real and imaginary components of the refractive index, respectively. In the absence of plasma, the real refractive index for BBS of n=1.47 gives R_{ss}=.0362. As the electron density evolves, the indices are calculated from the complex dielectric function of the material, $\varepsilon = \varepsilon_r + i\varepsilon_i$ by the relations

$$n=\sqrt{\frac{\varepsilon_r+\sqrt{\varepsilon_r^2+\varepsilon_i^2}}{2}} \tag{3.19}$$

$$k = \sqrt{\frac{-\varepsilon_r + \sqrt{\varepsilon_r^2 + \varepsilon_i^2}}{2}} \tag{3.20}$$

The dielectric function of the plasma is calculated from Drude model (Kruer, 1987)

$$\varepsilon_r = \left(1 - \frac{\omega_p^2(n_e)\tau^2}{1+\omega^2\tau^2}\right) \tag{3.21}$$

$$\varepsilon_i = \left(\frac{\omega_p^2(n_e)\tau}{\omega(1+\omega^2\tau^2)}\right) \tag{3.22}$$

where the laser frequency, $\omega=2\pi c/\lambda$ with c as the speed of light in a vacuum and λ the laser wavelength. ω_p is the plasma frequency given by

$$\omega_p(n_e) = \sqrt{\frac{n_e(r,z,t)e^2}{m_e\varepsilon_0}} \tag{3.23}$$

and τ is the free electron relaxation time. The constant e is the electron charge, m_e is the electron mass, and ε_0 is the permittivity of free space.

The absorption coefficient in Eqn. (3.16) has components due to free electron heating as well as ionization, given by

$$\alpha(r,z,t) = \alpha_H(r,z,t) + a_i n_e(r,z,t)\mathrm{U} \tag{3.24}$$

Absorption due to free electron heating, α_H is

$$\alpha_H = \frac{4\pi k}{\lambda} \tag{3.25}$$

while U is the bandgap of the material. For fused silica, U≈9 eV. For BBS, U≈4 eV.

From Jiang and Tsai (2005), it is assumed that at the critical electron density, the plasma frequency is equal to the laser frequency. If a point in the material reaches the critical density, n_{cr}, a discrete amount of material is ablated.

$$n_{cr} = \frac{4\pi^2 c^2 m_e \varepsilon_0}{\lambda^2 e^2} \tag{3.26}$$

From Equations (3.18-3.23), it is evident that the reflectivity of the material is dependent on two variables, the electron relaxation time, τ, and the electron density. Jiang and Tsai (2005) proposed a variable calculation of the relaxation time based on quantum treatment of the electron specific heat and electron temperature. An investigation was conducted on the dependence of both relaxation time and electron density in R. It was found that the surface reflectivity varies greatly with electron density, a consequence of plasma generation, which has strong reflection and absorption properties. In contrast, reflectivity was essentially constant throughout a wide range of free electron relaxation time τ, varying significantly only when τ fell below 10 fs.

Metals with very large conduction band densities can exhibit relaxation times on the order of 1-10 fs (Kittel, 1996), however a dielectric with minimal conduction band density would be expected to show much larger periods between electron/ion collisions. A relaxation time of the semiconductor silicon has been measured at >200 fs for moderate carrier densities (Sjodin et al., 1998). Therefore, due to the order of magnitude increase in computational expense for a variable τ calculation, and the weak dependency on ablated volume, a constant relaxation time of 100 fs was used. The potential loss in accuracy due to the constant value of τ would not be removed even with a fully quantum calculation, which requires ionization state energies. These energies are unknown in a multi-element material with constantly changing internal energy, requiring an approximation regardless.

The numerical procedure involves calculating an electron density and intensity at each spatial point using the most recently updated reflectivity and absorption coefficient. Equations (3.18-3.25) are performed, and the density and intensity are updated. The cycle repeats until the densities and intensities have converged, completing the time step. Time step independence was achieved with values of Δt=0.01 fs for a 100 fs pulse.

3.2.2 Ultrafast laser/borosilicate glass energy transfer

An experimental investigation of femtosecond ablation of borosilicate glass was conducted by Ben-Yakar and Byer (2004) which offers excellent characterizations by which to verify the theoretical model. A quantitative evaluation of single shot ablated craters using several laser fluences with pulses of λ=780 nm and t_p=200 fs at normal incidence was carried out using an atomic force microscope. Figure (3.5) presents two of the AFM images obtained by Ben-Yakar of the circular craters resulting from ultrafast pulses at two fluences.

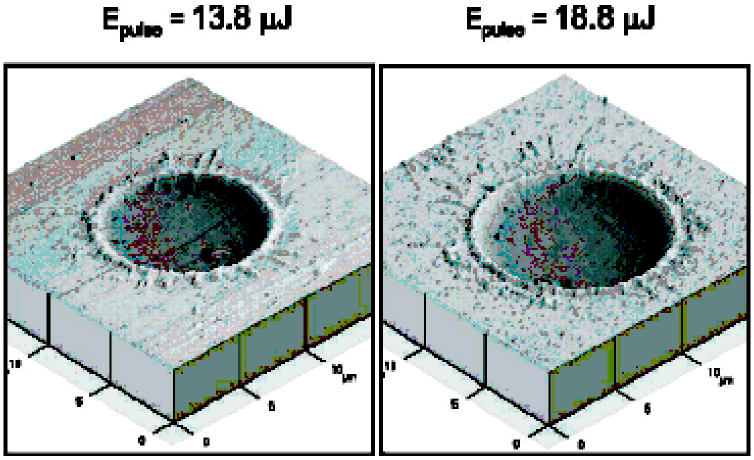

Figure 3.5: Ablation craters due to λ=780 nm, t_p=200 fs laser pulse at two fluences, characterized by Ben-Yakar and Byer (2004).

Figures 3.6 and 3.7 plot the experimental cross-sections of the circular craters shown above against the crater shapes predicted from the dielectric ablation model.

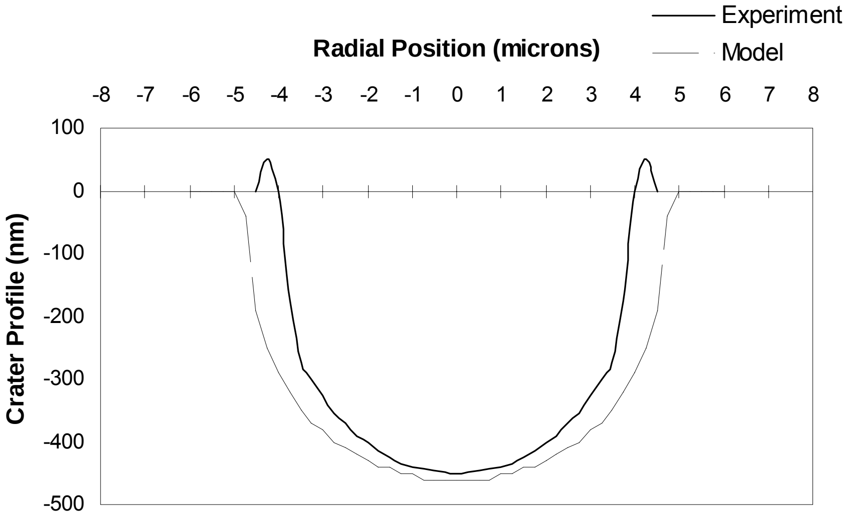

Figure 3.6: Single shot ablated crater, E_{pulse}=13.8 μJ. Predicted damage and observed damage (Ben-Yakar and Byer, 2004)

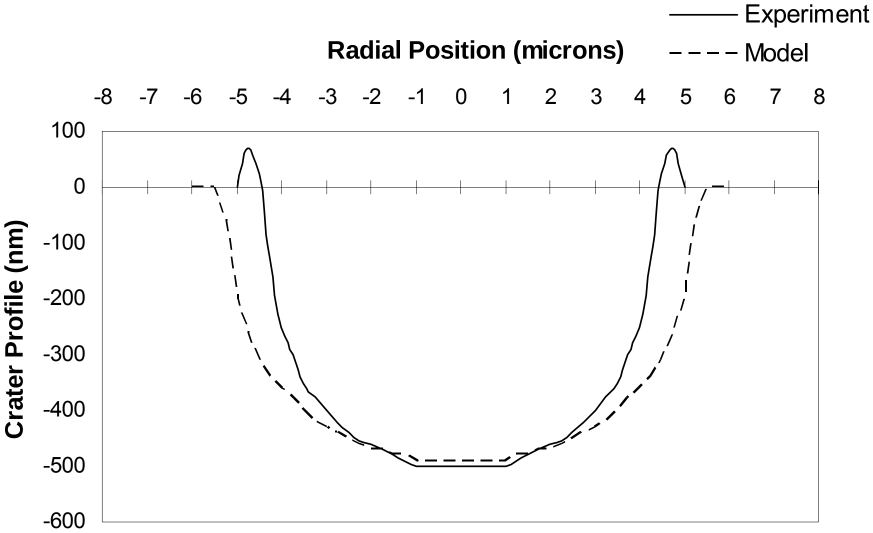

Figure 3.7: Single shot ablated crater, E_{pulse}=18.8 μJ. Predicted damage and observed damage (Ben-Yakar and Byer, 2004)

Figures 3.6 and 3.7 show a lip of material surrounding the experimental crater above the zero level of the substrate. This is assumed to be caused by a thermal after-effect of the excited electrons, which would heat the lattice and provoke both phonon and electron heat-transfer after the pulse. If the lattice temperature is raised above the melting temperature of the material, a flow of molten glass would be subject to the local forces. The ablation model does not take into account fluid dynamics that may be the cause of the lip structure.

A notable result of the model is the successful prediction of a flat-bottom crater. Conventional thermal energy transport predicts shapes conforming to the gaussian laser distribution, which result in round-bowl craters. Note the difference of scale in Figures 3.6 and 3.7; depth in nanometers, radial position in micrometers.

The single shot ablation threshold of the borosilicate glass, or the minimum fluence at which material is removed, was found to be 2.6 J/cm^2 in air and 4.1 J/cm^2 in vacuum (Ben-Yakar and Byer, 2004). The dielectric ablation model, which does not consider the effect of a surrounding medium, predicts an ablation threshold of 3.6 J/cm^2.

The overall material removal during the pulse is highly dependent upon the optical response of the system. During the first few femtoseconds, multi-photon ablation dominates within the glass. The avalanche ablation effect increases non-linearly as it becomes the dominant free-electron generation mechanism until the critical density is reached. At this point, plasma is formed at the surface as material is ejected. Figures 3.8 and 3.9 show how the surface reflectivity and absorption coefficient of the borosilicate glass transforms as the critical density is reached at approximately 50 fs. In the first stage of the pulse when the borosilicate is still transparent glass, the reflectivity retains its “standard” low value and the absorption coefficient is virtually zero. Near 50 fs, both values increase dramatically. The reflectivity levels to a nearly constant value where almost all energy is reflected, while the absorption of energy making it through the surface steadily increases as the plasma mass increases. Similar behavior was reported for fused silica (Jiang and Tsai, 2005).

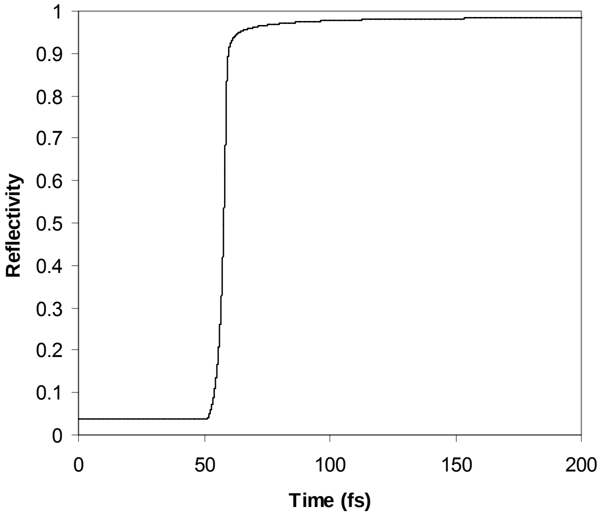

Figure 3.8: Surface reflectivity at r=0 during 200 fs pulse

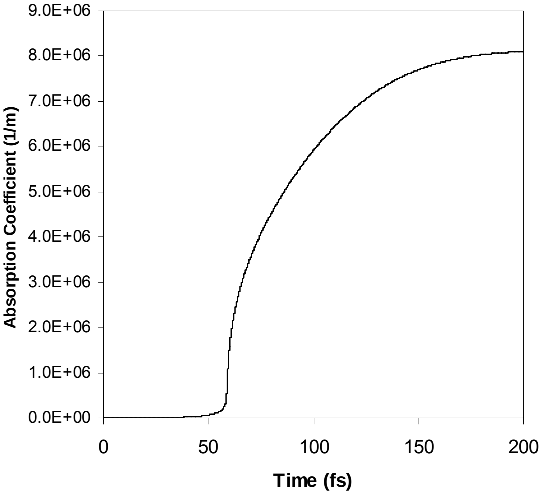

Figure 3.9: Absorption coefficient at r=0, z=0 during 200 fs pulse

Insight into the formation of the flat-bottom crater can be gained by a transient analysis of the intensity profile, as shown in Figure 3.10. The formation of plasma and dynamic change in optical properties essentially reshapes the beam during that portion of the pulse. The initial Gaussian shape becomes flattened due to the earlier formation of plasma at the higher intensities (peak of Guassian profile) than the lower intensities. The high reflectivity of the plasma offsets the larger energy input, smoothing out the profile of energy that is actually absorbed by the glass.

Finally, the evolution of conduction band electron density is plotted in Figure 3.11. The horizontal line at n_e=1.8313x10^{27} cm^{-3} represents the threshold for ablation. The plot was taken at the center of the laser spot. After an initial exponentially shaped increase in density, the profile assumes a linear shape. The effect of the competing reflectivity and absorption mechanisms can be seen as a sharp change in gradient when plasma forms, but retention of the linearity. Toward the end of the pulse, the density gain trails off as the energy input ceases.

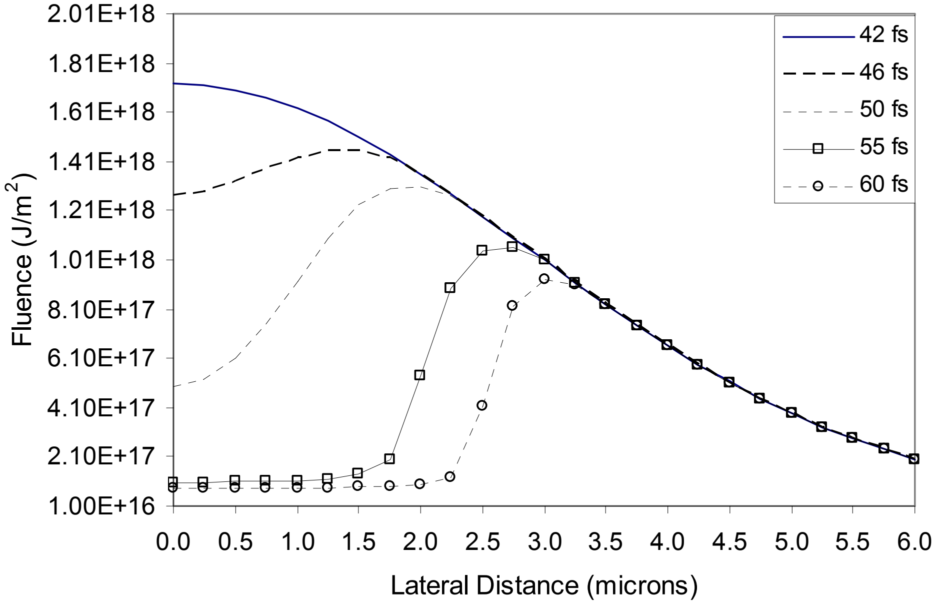

Figure 3.10: Absorbed intensity at several moments (normalized in time)

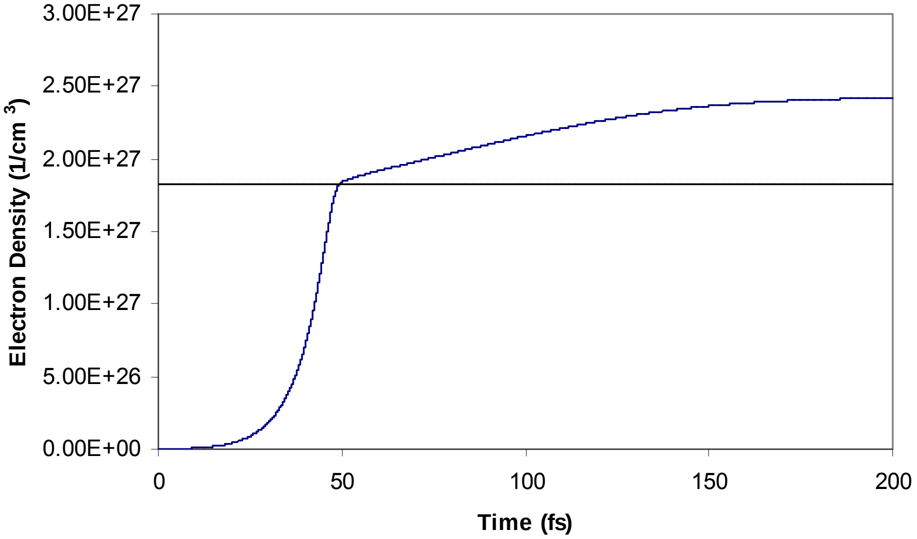

Figure 3.11: Absorption coefficient at r=0, z=0 during 200 fs pulse

3.2.3 Ultrafast near-field energy transfer, experimental study

UT-Austin's NOBEL lab has performed femtosecond ablation studies using the near-field energy of microspheres (Heltzel et al. 2007). In these experiments (performed by A.

Battula) a borosilicate glass wafer sample is used as the substrate and monodisperse silica (SiO_2) spherical particles with a diameter of 1.76 µm were used. These silica particles are transparent to the near infrared light (800 nm wavelength of the laser used). The particle suspension was diluted with de-ionized water (DI) water and deposited on the glass substrate using a dispenser. The sample was then stored at room temperature over a period of few hours for all the water solvent to evaporate. A titanium-doped sapphire (Ti:Sapphire), solid state laser with pulse at full width half maximum (FWHM) around 100 femtosecond (fs) and wavelength around 800 nm is used as the light source. The polarization of this fs laser pulse is linear and horizontal to the surface of the substrate. Similar to the setup shown in Figure 2.1, a fs laser irradiates the target at a zero angle of incidence (normal). Different laser fluences were used to study the laser energy dependence of the nanostructures formed on the glass substrate. The laser energies used in the experiments varied from approximately 200 mJ/cm^2 to 1 J/cm^2. Zhou et al. (2006) have recently used fs pulses to create sub-diffraction limit modifications, though at much higher laser energies. The energy of the incident laser is varied by changing the delay time between the two pockel cells during the amplification using a synchronization and delay generator (SDG). Due to different delay times, the laser beam has to be compressed accordingly to maintain a constant pulse width and this is done by moving the compressor optics while monitoring the output laser beam pulse width with a single shot auto-correlator (SSA) and an oscilloscope. The glass substrate after laser nanostructuring was characterized by using scanning electron microscope (SEM: Hitachi S4500) and the depths were measured by using an atomic force microscope (AFM: Nanoscope D3100). Figure 3.12 shows the SEM image of the monolayer of the silica spheres deposited on the borosilicate glass. To obtain good SEM images and in order to reduce the charging effects of the glass substrate a very thin layer of metal is deposited on the substrate.

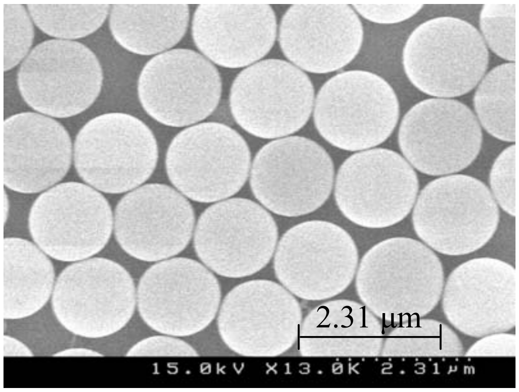

Figure 3.12**:** SEM image of the monolayer of silica spheres with a diameter of 1.76 μm.

Figure 3.13 (a-c) shows the SEM image of the nanostructures formed on the borosilicate glass by using the optical near-field enhancement for different laser fluences and one pulse irradiation. The nanostructures formed seem to be elliptical in shape, an effect likely due to the laser polarization, which plays an important role in optical enhancement and hole formation on a glass substrate. Also it was found that most of the silica particles are removed from the substrate surface. These particles are removed from the surface mainly due to the deformation force and/or the high ablative force exceeding the particle-surface adhesion force (Zheng et al., 2001). Figure 3.13 shows that as the laser fluence decreases the nanostructures formed did not change in shape, unlike in some studies where sombrero-shape nanodents are formed at high laser fluences and bowl-shape nanodents are formed at low laser fluences (Lu et al., 2003, Wang et al., 2004). Also, from Figure 3.13 it can be seen that for the incident laser fluences of 330 mJ/cm^2, 550 mJ/cm^2 and 765 mJ/cm^2 the diameter of the holes along the major axis are approximately 250 nm, 300 nm and 350 nm respectively. Hence, the diameter of the nanostructures formed on the borosilicate glass increases with the laser fluence. Figure 3.14 shows the 3D AFM scanning profile of the nanostructure formed on the borosilicate glass and it can be seen that the structures formed have depths that are elliptical in shape which is in agreement with the SEM images (Figure 3.13). Also the shapes of the nanostructures formed on the glass substrate remains the same for different laser fluences as seen earlier in Figure 3.13.

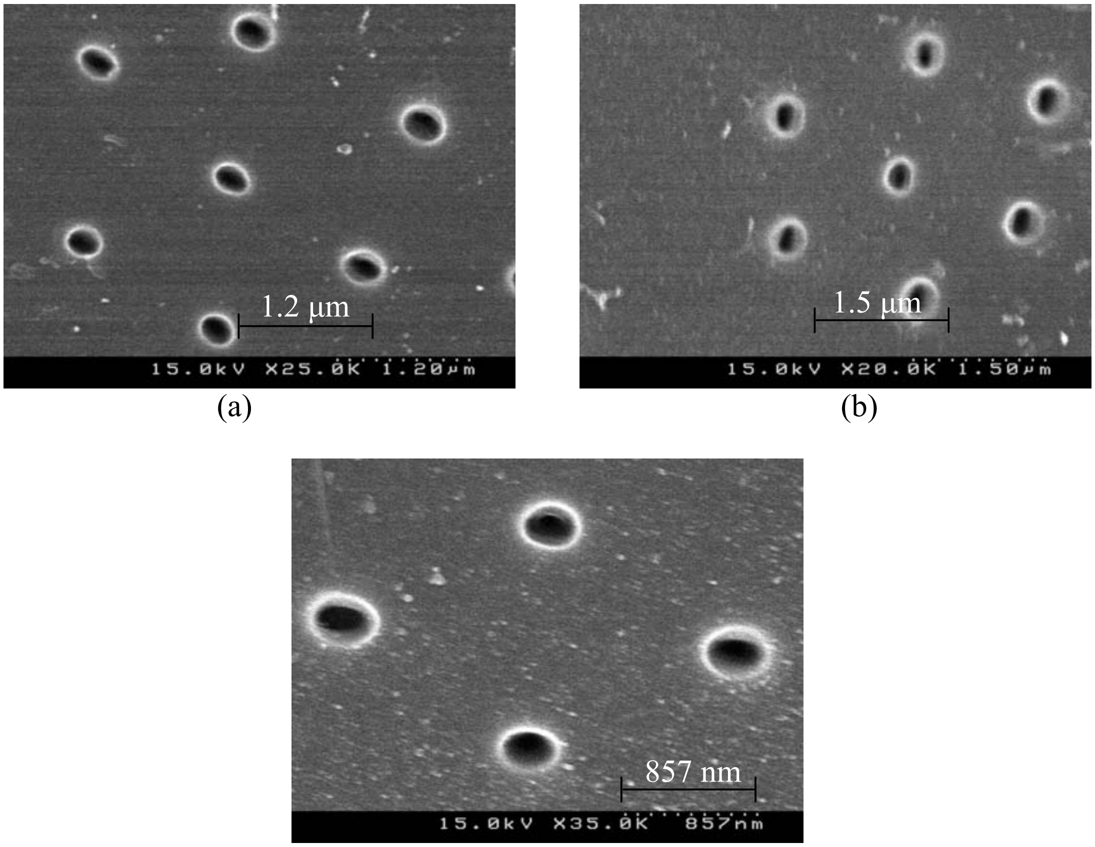

(a) (b)

(c)

Figure 3.13**:** SEM micrograph of the features formed on the glass substrate using microspheres with a single laser pulse irradiation (λ = 800 nm and FWHM = 100 fs) having laser fluence of (a) 330 mJ/cm^2, (b) 550 mJ/cm^2 and (c) 765 mJ/cm^2.

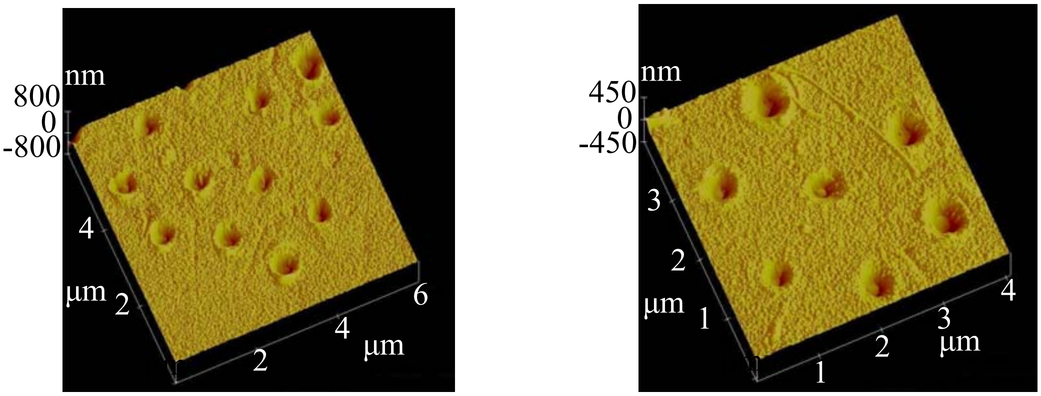

(a) (b)

Figure 3.14: AFM profiles of the features formed on the glass substrate using microspheres with a single laser pulse irradiation (λ=800 nm and FWHM= 100 fs) having laser fluence of (a) 230 mJ/cm^2 and (b) 405 mJ/cm^2

Figure 3.15 (a-c) shows the cross-sectional (or 2D) AFM profile of the nanostructures along their major axis and it can be seen clearly that for laser fluences of 230 mJ/cm^2, 550 mJ/cm^2 and 950 mJ/cm^2 the depth of the structures formed are approximately 180 nm, 250 nm and 290 nm respectively.

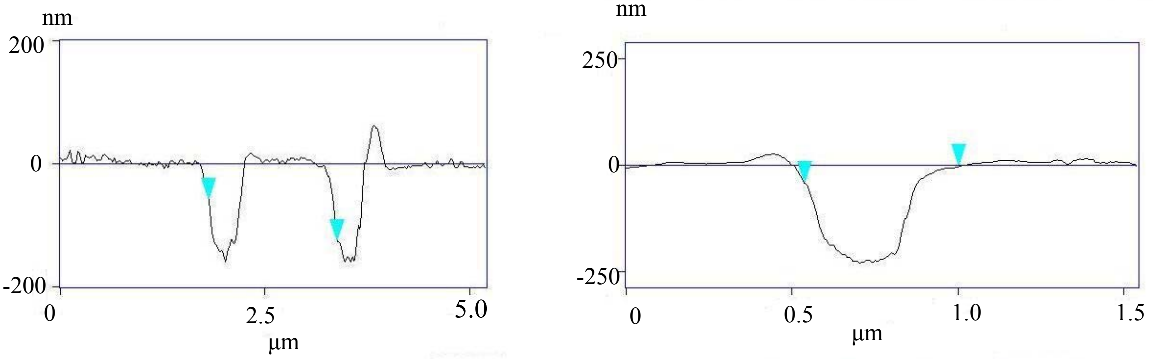

(a) (b)

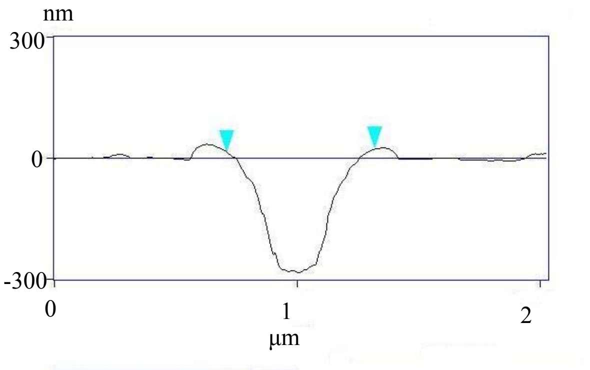

(c)

Figure 3.15: AFM cross-section profiles of the features formed on the glass substrate using microspheres with a single laser pulse irradiation (λ = 800 nm and FWHM = 100 fs) having laser fluence of (a) 230 mJ/cm^2, (b) 550 mJ/cm^2, and (c) 950 mJ/cm^2.

3.2.4 Ultrafast near-field energy transfer, theoretical study

In order to model the material removal and energy transport taking place in the experiments described above, the enhanced surface intensities are employed in the ultrafast ablation model presented in this chapter. Specifically, the profile presented in Figure 2.30 corresponds to the experimental parameters used. Figure 2.30 also predicts an asymmetrical angular energy distribution, a consequence of polarization. An ideal ablation simulation would then be three-dimensional to account for the ovular enhanced energy profile, however the non-diffusive ablation mechanisms contained in the model dictate lateral independence of energy transport. Therefore, several 2-D calculations can take the place of a single 3-D calculation to determine the damage profile.

With the enhanced energy input, Eqn. (3.16) becomes modified as follows:

$$I(r,z,t)=\frac{2\cdot F_{peak}}{\sqrt{\pi/\ln 2}\cdot t_p}I_{FDTD}(r)\left[1-\mathrm{R}(r,t)\right]\cdot\exp\left[-(4\ln 2)\frac{t^2}{t_p^2}-\int_0^z\alpha(r,z,t)dz\right] \qquad (3.27)$$

where the additional $I_{FDTD}(r)$ term refers to the normalized level of enhancement relative to the incident plane wave prior to interaction with the sphere. The radial decay in the exponential argument is removed, as the spatial profile is accounted for in the FDTD results. Several pulses at a range of fluences were modeled with the enhanced laser input employed in Eqn. (3.27). Figure 3.16 presents the damage profile predicted for a fluence of 950 mJ/cm^2. The oval-shaped crater has axes of length ~350nm and ~700nm, with a maximum depth of ~400 nm. The profile is in decent quantitative agreement with the experimental results presented, and qualitatively captures the ovular effect of polarization. Figure 3.17 presents the damage profile predicted for the fluence of 550 mJ/cm^2 used in the experiments performed by Battula (2006). At this energy, the ablated crater has maximum dimensions of 300 x 580 nm x 330 nm depth, again showing fair agreement with the AFM cross-sections. A third series of simulations conducted for the case of 330 mJ/cm^2 predicts crater dimensions of 160 x 380 nm x 200 nm depth. A predicted threshold fluence of 240 mJ/cm^2 was calculated, which matches neatly with both the theoretical adjustment discussed above as well as experimental results to be presented.

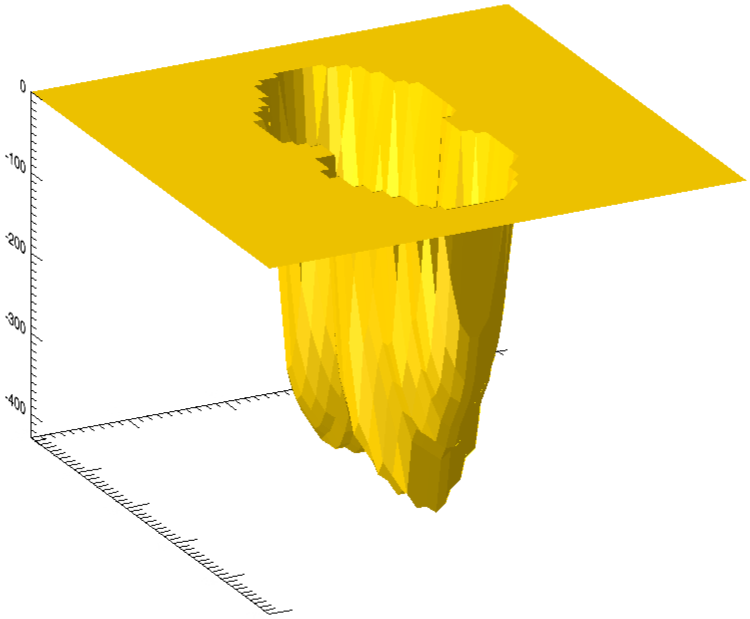

Figure 3.16**:** Predicted ablation crater from near-field enhanced energy at 950mJ/cm^2. Plot range 1.0 µm x 1.0 µm, ablation depth in nm.

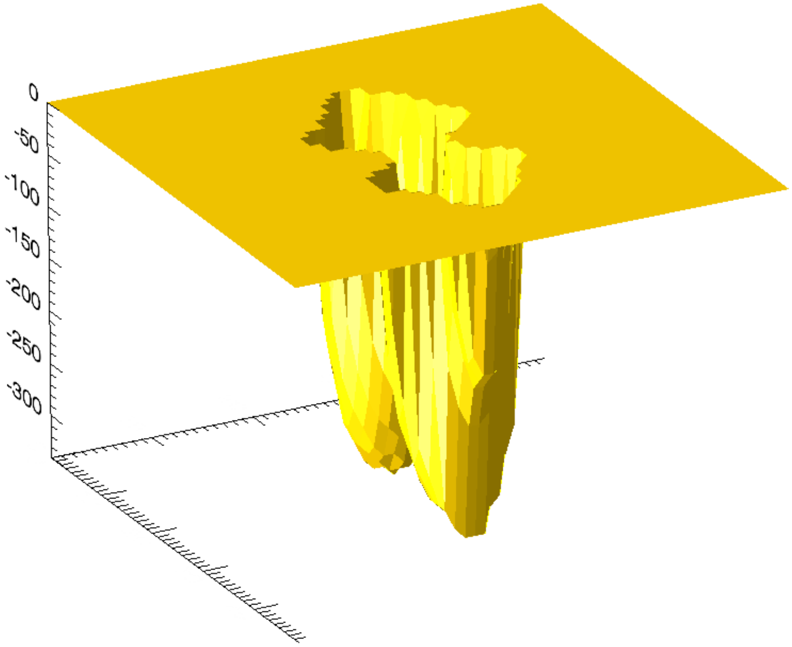

Figure 3.17**:** Predicted ablation crater from near-field enhanced energy at 550mJ/cm^2. Plot range 1.0 µm x 1.0 µm, ablation depth in nm.

It is clear from Figure 3.14 that the energy required to damage the glass substrate has been significantly reduced due to the presence of the sphere. A notable distinction between the damage profiles occurs with the enhanced energy, enabling depth to width ratios greater than unity to be achieved. The minimum obtainable dimensions predicted are also much smaller than those obtained with identical spheres using nanosecond laser pulses. Laser enhancement due to the presence of the spheres breaks the optical diffraction limit, allowing optical machining at the sub-micrometer level. In this computational work, the diffraction limit has been undercut by an entire order of magnitude. The crater morphology due to femtosecond machining coincides to a greater degree with the FDTD enhancement profiles than the craters due to nanosecond machining. This is due to the lack of diffusive thermal transport during such an ultrafast pulse.

3.3 Summary

Both two-dimensional and three-dimensional two-phase Fourier heat transfer models were built to describe the energy transport within a silicon substrate due to laser/microsphere interaction. Nanosecond pulses provide enough time for diffusion effects to be important. From a computational standpoint, this effect mitigates the asymmetry of the surface intensity profile predicted from FDTD solutions. In this case, the surface modifications predicted due to both near-field Mie theory enhancement profiles as well as FDTD profiles agree well with the experimental observations. Both experiment and modeling show that the minimum energy required for surface damage is lowered by an order of magnitude or more due to the presence of microspheres. The localization of this energy is such that sub-wavelength optical lithography is achievable. Both near-field Mie analysis and FDTD in combination with Fourier-based heat transfer can provide a predictive tool for this phenomenon. The model shows that thermal radiation heat transfer from the substrate is substantial at the high temperatures within liquid silicon.

An ultrafast energy transport model has been built to describe the effect of femtosecond laser interaction with a borosilicate glass substrate with and without the presence of microspheres. The model is based on the evolution of electron density derived from the Fokker-Planck equation and employs empirical coefficients obtained from experimental studies. The mechanisms of energy transport include multi-photon ionization (MPI), which initiates the dissociation of electron and nuclei, forming seed ions in the glass. Following MPI, ablation becomes dominated by impact and avalanche ionization processes, which transports the high energy of conduction band electrons in a kinetic manner. The flat-bottomed craters predicted from the computations are consistent with experimental characterizations over a range of laser energies.

Analysis of the material property changes during the femtosecond pulse reveals a dynamic dependence on the optical response of the glass. When the conduction band electron density is high enough to assume ablation, a plasma is generated which is both highly reflecting, yet highly absorbing (as opposed to transmitting). The plasma properties serve to flatten the incident laser pulse within the glass from a Gaussian shape to a top-hat profile, explaining the flat bottom craters resulting from an ultrafast pulse. The non-thermal nature of this energy transport contains the substrate modification to within the actual zone of energy deposition, creating clean features free of heat-affected warping and deformation. The predicted threshold fluence for ablation is consistent with experimental observations.

FDTD enhanced profiles due to the presence of microspheres are applied within the framework of the ultrafast ablation model. Predicted surface modifications are well under the diffraction limit and smaller than those predicted due to Fourier-based heat transfer. The energy enhancement due to the laser/microsphere interaction predicts substrate damage below 1 J/cm^2. Both of these predictions correlate well with experiments performed at UT's NOBEL laboratory. Unlike the heat transfer due to nanosecond laser pulses, the asymmetry in the craters predicted using FDTD-obtained profiles is evident in both model and experiment. Without thermal diffusion, the deformation of enhancement due to the reflection from the substrate will indeed be a factor in the final lithographic effect. It is concluded that both Mie theory and FDTD near-field analyses can be used with nanosecond heat transfer modeling, however only FDTD modeling accurately predicts the ovular shape of damage in conjunction with ultrafast modeling. The overall agreement between modeling and experiment over a range of energies allows the use of the combined electrodynamics/heat transfer approach to predict near-field optical surface modification with confidence.

Chapter 4:
Plasmonics

4.1 Introduction

The miniaturization of conventional photonic devices is limited by diffraction effects due to the wave nature of light. In order to push the miniaturization of optical elements and devices, new concepts are needed. In this context, research has recently intensified on noble metal nanoparticles (Klar et al., 1998). The high electron mobility in noble metals make them useful electrical conductors and also attractive candidates for surface plasmonic applications. Within such particles visible light can resonantly excite collective electron oscillations, known as surface plasmons (Raether, 1988). Surface plasmon resonances in metallic nanoparticles are of interest for a variety of applications due to the large electromagnetic field enhancement that occurs at the interface between the metal and dielectric materials as well as the sub-wavelength localization of these fields. Recent advances in fabrication techniques that allow metals to be structured and characterized on the nanometer scale have facilitated the interest and research.

Surface plasmons can be categorized into two types: localized plasmon resonances (Hutter and Fendler, 2004), in which incident light is absorbed or scattered by the oscillating electric dipoles within a metal nanoparticle; and surface plasmon polaritons (SPP's) (Sambles et al., 1991), which propagate along metal surfaces in a waveguide-like fashion until released at some distance from their point of origin. The former are important for generating local field factors, which enhance linear and nonlinear optical effects near the metal surface. However, metal nanostructures often support both types of plasmons simultaneously. It is the particle plasmon effect that is studied here for the purpose of nanoscale modification of solids. Nevertheless, the plasmonic coupling of metal nanoparticles with light opens a broad range of useful optical phenomena, such as resonant light scattering, surface plasmon resonance (Murray et al., 2004), and surface-enhanced Raman scattering (Grand et al., 2005), all of which have tremendous potential for ultra-sensitive chemical and biomolecular detection and analysis.

Recently, a new field named ‘Plasmonic nanolithography’ has emerged (Shao and Chen, 2005). Here the electric field enhancement by the plasmon has been utilized for nanostructuring. Sub-100 nm lines were patterned photolithographically using SPP interference in the optical near field excited by a wavelength of 436 nm (Luoa and Ishihara, 2004). Using 2-D hole arrays on an aluminum substrate, features as small as 90 nm have been realized (Srituravanich et al., 2004). Instead of using metallic masks to generate the plasmon resonance, silver nanospheres have been used, and features as small as 50 nm were obtained (Kik et al., 2002). However, since all the above mentioned works were developed as a parallel route to optical lithography, they focused only on patterning photoresists.

This chapter presents a numerical investigation into the interaction between laser light and metallic nanostructures capable of supporting localized plasmon resonances and surface plasmon polaritons (SPP’s). The FDTD method introduced in Chapter 2 is adapted to accommodate the negative refractive indices and frequency-dependent optical response of noble metals. Computations geared toward nanolithography applications will be compared to experimental characterizations obtained by UT’s NOBEL lab. The calculations are then extended to optical signal propagation for photonic circuit applications. Finally, the use of SPP’s for ignition purposes is proposed in a potential design incorporating the observed plasmonic activity of multi-walled carbon nanotubes.

4.2 Numerical method

Within the context of the finite-difference time-domain algorithm, both the Drude and modified Debye models for optical properties of gold and silver are used. The Drude expression for complex permittivity is given by

$$\varepsilon(\omega) = \varepsilon_\infty - \frac{\omega_P^2}{\omega^2 - j\omega\gamma_P} \tag{4.1}$$

where the constants ε_∞, γ_P, and the Drude pole frequency, ω_P are obtained from empirical fits based on experimental data. The modified Debye fit is given by

$$\varepsilon(\omega) = \varepsilon_\infty + \frac{\varepsilon_{s,P} - \varepsilon_{\infty,P}}{1 + j\omega\tau_P} + \frac{\sigma}{j\omega\varepsilon_0} \tag{4.2}$$

where $\varepsilon_{s,P}$ is the static or zero frequency relative permittivity, ε_∞ is the relative permittivity at infinite frequency, τ_P is the pole relaxation time, and γ_P is the inverse of the pole relaxation time.

There are few comprehensive optical diagnostic studies for gold and silver, however the experiments performed by Johnson and Christy (1972) and Lynch and Hunter (1985) provide curves by which to fit the Drude and Debye models accurately within the range of plasmonic resonance for both gold and silver. The Debye model is preferable at higher frequencies where the Drude model does not describe both the real and imaginary refractive indices with high accuracy. The appropriate model is chosen based on the incident wavelength and availability of data. Tables 4.1 and 4.2 provides the values for these constants for the Drude and Debye models respectively.

Table 4.1: Drude constants used in plasmonic FDTD modeling

	Au (J & C, 1972)	**Ag** (J & C, 1972)	**Ag** (L&H, 1985), λ~300nm	**Ag** (L&H, 1985), λ~500nm
ε_∞	9.5	5	8.926	5.976
γ_P	.06909 eV	.0987 eV	.203 eV	.259 eV
ω_P	8.9488 eV	9.5 eV	11.585 eV	9.812 eV
σ	4.521e7 S/m	6.31e7 S/m	6.31e7 S/m	6.31e7 S/m

Table 4.2: Debye constants used in plasmonic FDTD modeling

	Au (L&H, 1985), λ~700-1000nm	**Ag** (L&H, 1985), λ~488nm
ε_S	-12987	-1313.5469
ε_∞	9.012	1.022
τ_P	8.017e-15 s	3.1326e-15 s
σ	1.464e7 S/m	3.7155e6 S/m

The coefficients used in the FDTD algorithm outlined in Chapter 2 are now modified to accommodate the permittivities calculated from Eqs. (4.1) and (4.2). For a Drude formulation, they are given by

$$k_d = \left(1 - \frac{\gamma_P \Delta t}{2}\right) / \left(1 + \frac{\gamma_P \Delta t}{2}\right) \tag{4.3}$$

$$\beta = \left(\frac{\omega_P^2 \varepsilon_0 \Delta t}{2}\right) / \left(1 + \frac{\gamma_P \Delta t}{2}\right) \tag{4.4}$$

$$C_a = \left(\frac{2\varepsilon_0 \varepsilon_\infty - \sigma \Delta t - \beta \Delta t}{2\varepsilon_0 \varepsilon_\infty + \sigma \Delta t + \beta \Delta t}\right) \tag{4.5}$$

$$C_b = \left(\frac{2\Delta t}{2\varepsilon_0 \varepsilon_\infty + \sigma \Delta t + \beta \Delta t}\right) \tag{4.6}$$

For a modified Debye formulation, they are given by

$$k_d = \frac{2\tau_P - \Delta t}{2\tau_P + \Delta t} \tag{4.7}$$

$$\beta = \frac{2\varepsilon_0(\varepsilon_s - \varepsilon_\infty)\Delta t}{2\tau_P + \Delta t} \tag{4.8}$$

$$C_a = \left(\frac{2\varepsilon_0\varepsilon_\infty - \sigma\Delta t + \beta}{2\varepsilon_0\varepsilon_\infty + \sigma\Delta t + \beta}\right) \tag{4.9}$$

$$C_b = \left(\frac{2\Delta t}{2\varepsilon_0\varepsilon_\infty + \sigma\Delta t + \beta}\right) \tag{4.10}$$

The coefficients k_d, β, C_a, and C_b are then used in the FDTD algorithm of Chapter 2 without further change. The need for current density updates to maintain numerical stability when refractive indices are negative requires nine stored components in each Yee cell (Ex, Ey, Ez, Jx, Jy, Jz, Hx, Hy, Hz) rather than six. The number of Yee cells available for a given amount of RAM therefore decreases proportionally. Another numerical concern involves a longer convergence time when dealing with light/metal interaction. Compounded with the extremely small mesh size necessary to resolve nanoscale objects, the number of time steps for nano-plasmonic FDTD simulations can reach into the many tens of thousands. The clock time is naturally longer for the researcher, but this also precludes any possibility of utilizing easier-to-implement absorbing boundary conditions such as the Mur and Liao ABC's due to the eventual accumulating reflection error.

4.3 Plasmonics for lithography

In NOBEL lab experiments, Theppakuttai (2006) used plasmons to directly pattern various substrates. This was achieved by illuminating gold nanospheres at their resonant frequency by using a 532 nm laser beam. The field enhancement as a result of this excitation is directly absorbed by the substrate and nanofeatures are realized. The features thus obtained are characterized using a scanning electron microscope and are available for comparison with FDTD simulation results.

4.3.1 Plasmonic generation and behavior

First, an irradiated gold nanowire is modeled suspended in a vacuum. The resulting electromagnetic field can offer insight into surface plasmon generation and behavior and will highlight the differences between scattering and enhancement due to dielectric structures. A 2-D transverse magnetic (TM) formulation of FDTD is used to model the 50 nm diameter gold wire with a mesh size of 2.5 Angstroms per side of each Yee cell. The TM formulation solves for Ex, Ey, and Hz field components.

Figure 4.1 presents the converged intensity field for this 2-D simulation. The laser is incident from the top of the wire and polarized perpendicularly (in horizontal direction). The energy deformation due to the presence of the wire is drastically different than the fields surrounding dielectric objects given in Chapter 2. The field enhancement is not along the axis of incident light, but the axis of polarization. In contrast to dielectric scattering of light, the interior of the wire is nearly devoid of any electromagnetic field. This agrees with SPP theory, which dictates that the incident field provokes a congregation of interior electrons at the surface, generating the plasmonic enhancement. This bulk relocation of charge due to an external field is suspiciously similar to the application of Gauss' law in which an enclosure, or Faraday cage, will exclude all external EM fields due to reallocation of charge in the metallic "cage". In the case of the nanowire, the analogous cage is the dielectric/metal boundary and the interior of the gold wire is field-free.

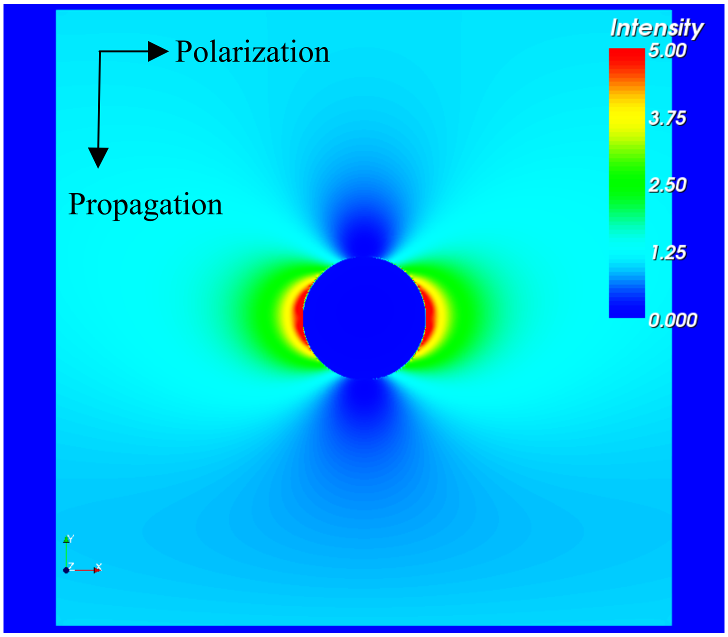

Figure 4.1: Suspended 50 nm gold nanowire irradiated by λ=532 nm laser light

Decay of the plasmonic field perpendicular to the interface is presented in Figure 4.2. This property of the enhanced field again differs from decay investigated surrounding dielectric microstructures. Whereas those fields exhibited oscillatory behavior likely due to interference effects, the enhanced field due to plasmons exhibits smooth and rapid degradation. This would make sense if the enhancement is due solely to charge concentration at the boundary. The electric field at any point due to a given population of electrons at another point would then be described merely by Coulomb's law, an inverse function of distance squared. If this electrostatic situation is indeed the physical explanation for the plasmonic enhancement around the nanowire, a curve such as that given in Figure 4.2 would be expected.

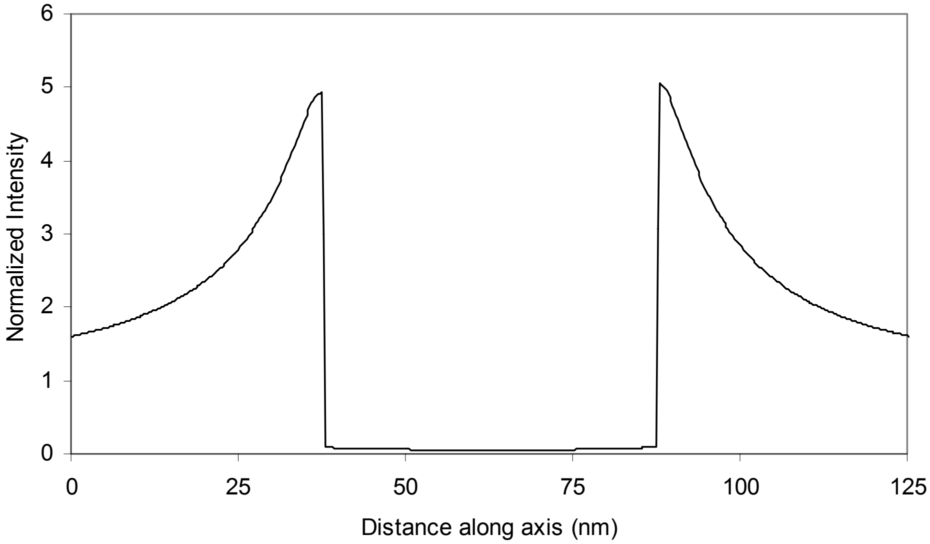

Figure 4.2: Intensity slice through center of 50 nm diameter gold nanowire

A dimer of 50 nm diameter silver wires at 4 nm separation distance was simulated to demonstrate the coupling effect of plasmonic fields. The dielectric simulations of microsphere arrays show that there was little effect on the peak enhancement due to the presence of adjacent spheres. Figures 4.3 and 4.4 show the opposite is true during irradiation of noble metals. The enhanced field between the spheres (along the polarization axis) is dramatically more intense.

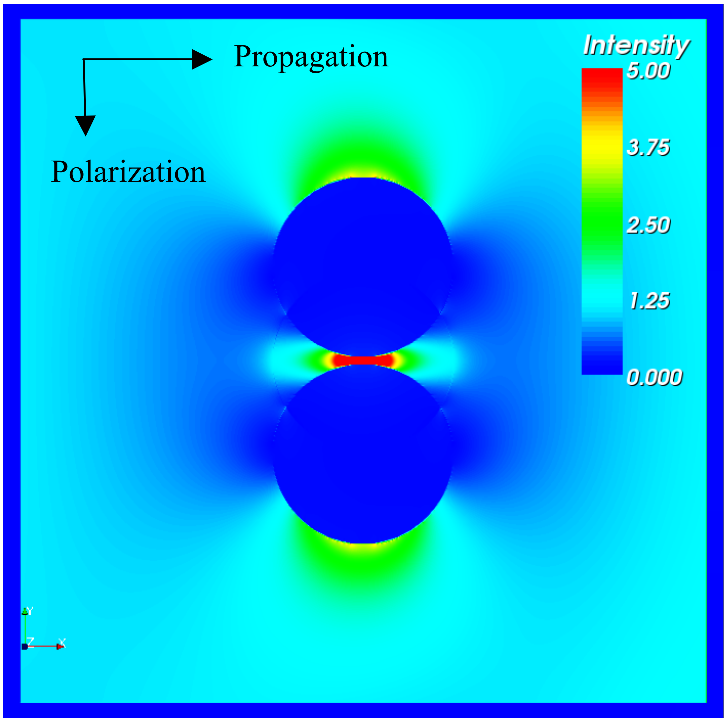

Figure 4.3: Suspended 50 nm silver wire dimer irradiated by λ=532 nm laser light

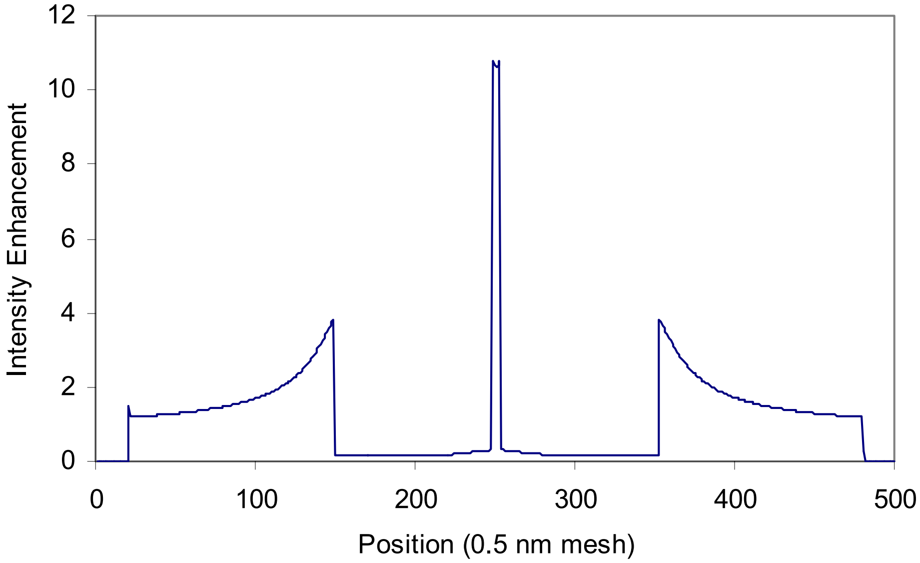

Figure 4.4: Intensity slice through center of 50 nm silver dimer

An initial supposition might be that the overlapping enhancements of each particle linearly sum to the total enhancement value. But Figure 4.4 indicates the peak enhancement is more than twice as strong as the effect on the opposite sides of the wires, evidence that the coupling is nonlinear. In fact, Hao and Schatz (2004) predicted enhancement levels of up to 4000 times incident within a dimer of silver spheres using the discrete dipole approximation. Sweatlock et al. (2005) used a finite-element integration technique with the Drude model to predict enhancement levels up to 5000-fold between silver nanoparticles at separation distances of only 1nm. Stockman (2004) predicted SPP normalized enhancements greater than 1000 at the tip of a silver cone.

4.3.2 Gold nanosphere lithography

In a study presented recently (Heltzel et al., 2006), plasmons are used to directly pattern various substrates. This is achieved by illuminating gold nanospheres at their resonant frequency by using a 532 nm laser beam. The field enhancement as a result of this excitation is directly absorbed by the substrate and nanofeatures are realized. The features thus obtained are characterized using a scanning electron microscope. The effect of the substrate, sphere size, laser energy, polarization, and incidence angle was studied both theoretically and experimentally.

Four scenarios were modeled (3-D) and are presented here. Solitary 250 nm gold spheres resting on a silicon substrate were irradiated with a λ=532nm Nd:YAG laser at incident angles $\theta=0^{o}$ (parallel to substrate), 45^{o}, and 90^{o} (normal to substrate). A single 40 nm gold sphere is also modeled with laser incidence parallel to the substrate. The laser is polarized perpendicular to the propagation direction in both simulation and experiment. Plasmon generation is expected in the polarization direction.

Figures 4.5(a) and 4.5(b) show the electromagnetic intensity cross-sections due to a 0° incident laser angle (parallel to substrate). The plasmonic enhancement is evident at the bottom of the nanosphere, corresponding to the polarization axis. Figure 4.5(b) shows the energy profile the silicon would "see". It is clear that a very localized area of significantly enhanced energy is present, which can be utilized for nanopatterning purposes. A moderate enhancement is present within a 100nm spot size, and an increased intensity spike is present at a scale of 10-20 nm. The scale of Figures 4.5(b), 4.6(b), and 4.7(b) are 625nm x 625nm.

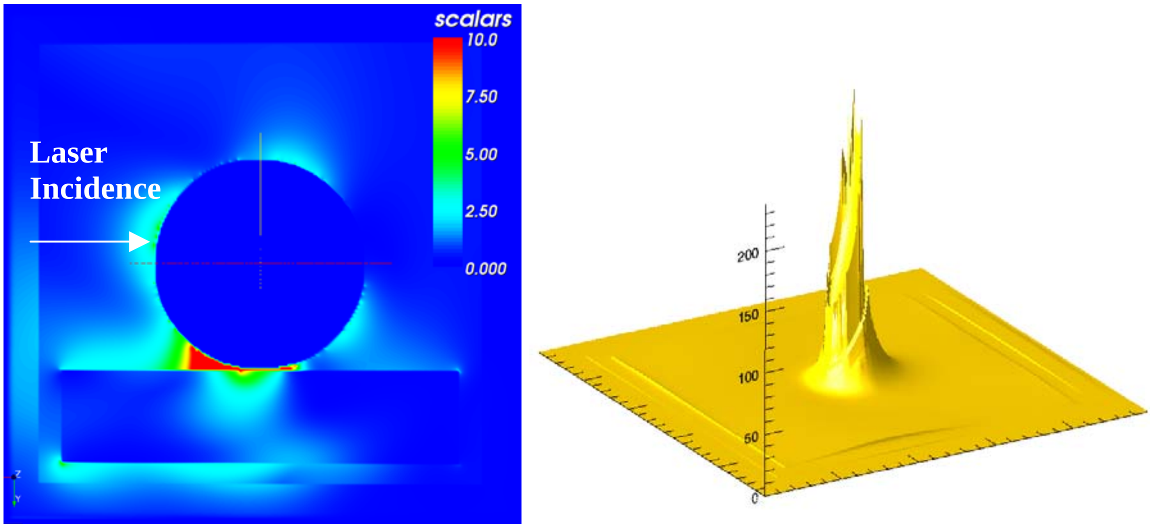

(a) (b)

Figure 4.5: FDTD plasmon simulation around 250nm Au sphere, 0° incident angle; (a) vertical slice of 3-D intensity distribution, (b) distribution on surface of silicon substrate, 625nm x 625 nm

Figures 4.6(a) and 4.6(b) give the laser/sphere interaction for a more practical case of 45° incident angle. This angle could be expected to irradiate large arrays of spheres while maintaining a significant component of polarization directed toward the substrate. The figures indicate a strong plasmonic enhancement and a coupling of the energy between the silicon and gold interfaces. Again, the enhanced intensity is confined within a 100 nm spot size.

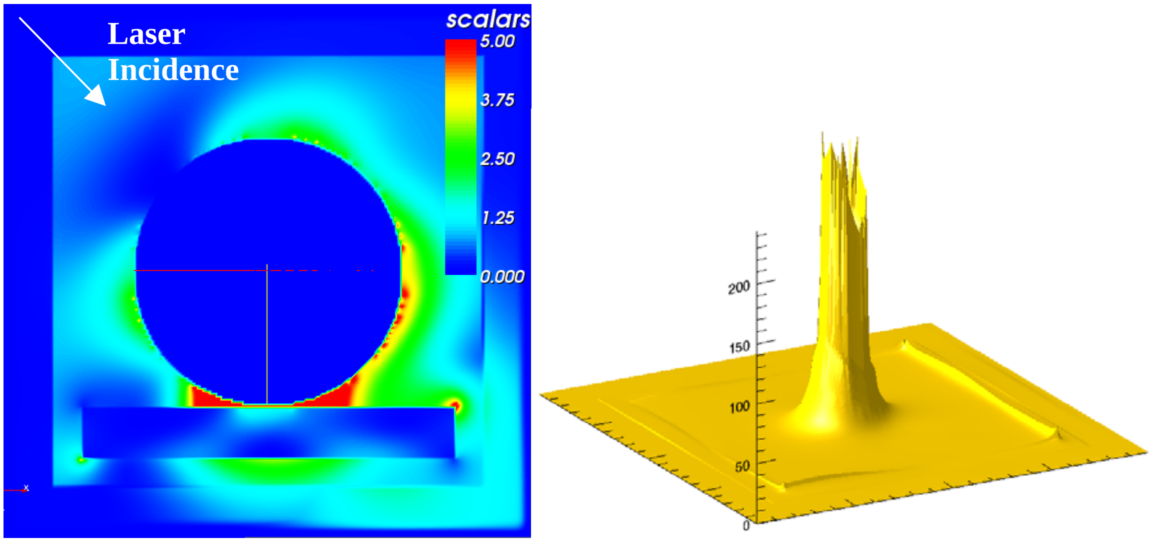

(a) (b)

Figure 4.6: FDTD plasmon simulation around 250nm Au sphere, 45° incident angle; (a) vertical slice of 3-D intensity distribution, (b) distribution on surface of silicon substrate, 625nm x 625 nm

Figures 4.7(a) and 4.7(b) show the profiles from the 90° normal incident angle. Whereas the plasmons surrounding a sphere in vacuum would be solely along the polarization direction, the silicon serves to draw them toward the contact area. The overall enhancement is severely diminished, however, compared to the 0° and 45° cases, which would limit the lithographic capability. This behavior is in contrast with illumination of dielectric microspheres, where the primary effect of the substrate is reflection and interference.

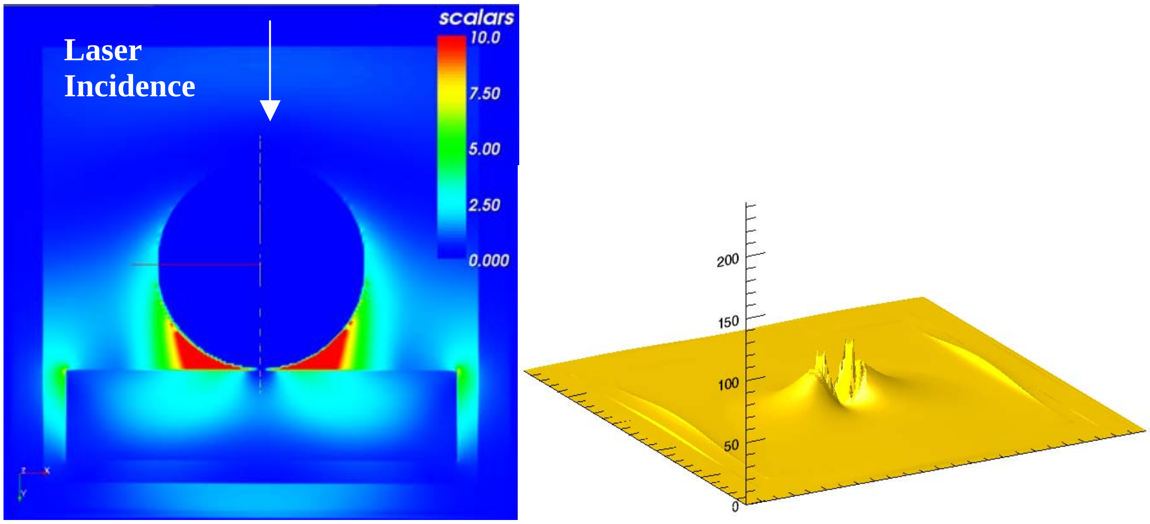

(a) (b)

Figure 4.7: FDTD plasmon simulation around 250nm Au sphere, 90^o incident angle; (a) vertical slice of 3-D intensity distribution, (b) distribution on surface of silicon substrate, 625nm x 625nm

Finally, Figures 4.8(a) and 4.8(b) show the predicted enhancement surrounding a 40 nm gold sphere irradiated at an angle 0^o, parallel to the substrate. The overall enhancement is weaker than surrounding the larger spheres, but can still be utilized for lithographic purposes as will be shown. The scale of Figure 4.8(b) is now 100nm x 100nm. The dimensional lower limit of the FDTD capability is approached when modeling such small structures. In order to resolve the shape of the sphere, node spacing must be on the order of angstroms. The time steps used must be smaller than the time for light to propagate across nodes. Three dimensional environments containing several hundred million nodes such as these presented can therefore require the speed and memory only available in massively parallel systems. On an individual workstation with dual 3.0 Ghz processors and 3 GB RAM, a single simulation requires up to 72 hours.

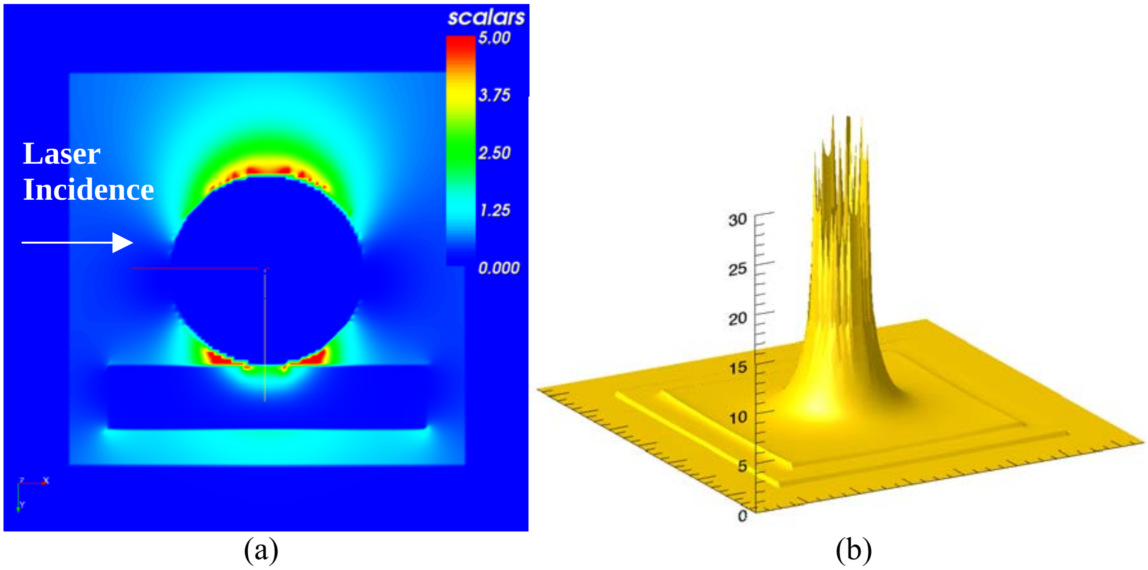

(a) (b)

Figure 4.8: FDTD plasmon simulation around 40nm Au sphere, 0° incident angle; (a) vertical slice of 3-D intensity distribution, (b) distribution on surface of silicon substrate, 100nm x 100nm

Plasmonic lithography experiments performed by S. Theppakuttai are presented in Heltzel et al., (2006). The experiment is performed on three different materials (Silicon, polyimide, and PMMA) using gold spheres of different diameters (250 nm and 40 nm). The effect of laser polarization (s and p-polarization) at various incident angles (0° and 90°) is studied in detail in order to understand the role of each of these parameters. Then an optical microscope and a scanning electron microscope were used to characterize the features obtained and the resulting images are presented and explained below. In the case of 250 nm gold spheres, approximately 100 nm features are created. A scanning electron microscope image of the features formed at a laser fluence of 50 mJ/cm^2 is shown in Figure 4.9. For the case of 40 nm gold spheres irradiated at a fluence of 50 mJ/cm^2, the features obtained are roughly the diameter of the sphere or slightly smaller. Figure 4.10 demonstrates optical lithograpy a full order of magnitude below the diffraction limit. The feature sizes correlates well with the FDTD intensity distributions given in Figures 4.5 and 4.8.

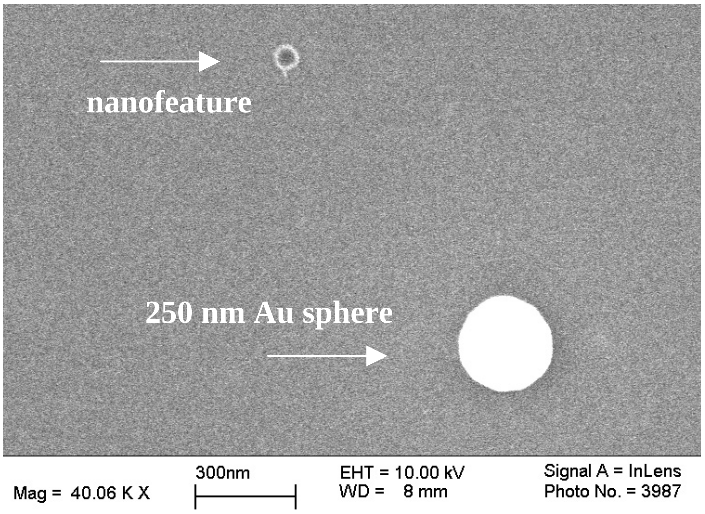

Figure 4.9: SEM micrograph of the features on silicon obtained by irradiating 250 nm gold spheres with a 532 nm laser at 50 mJ/cm^2 fluence (Theppakuttai, 2006)

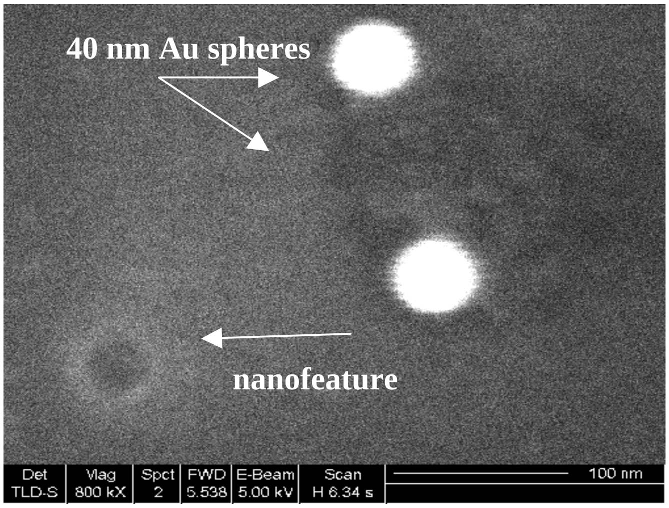

Figure 4.10: SEM micrograph of the features on silicon obtained by irradiating 40 nm gold spheres with a 532 nm laser at 50 mJ/cm^2 fluence (Theppakuttai, 2006)

The effect of two angles of incidence – normal incidence (90°) and glancing incidence (0°), were studied. Nanofeatures were observed only for the p – polarized glancing incidence and not for the normal incidence (irrespective of the polarization).

This is because only under glancing incidence and p – polarization is the plasmon oscillation directed at the substrate. This is shown quantitatively by the FDTD surface enhancement result presented in Figure 4.7(b).

Based on the theoretical predictions and experimental characterizations, it is possible to use the well-established property of localized enhancement at a conductor/dielectric interface known as a surface plasmon polariton to create nanoscale surface modifications. The technique can be used in local or parallel fashion, with laser incident angles between 45^o and glancing for optimum results.

4.3.3 AFM/STM tip lithography

Sub-wavelength surface modification of gold, germanium, and various polymers has been demonstrated through the interaction of lasers with atomic force microscopy (AFM) tips and scanning tunneling microscopy (STM) tips. Gorbunov and Pompe (1994) first proposed and experimentally verified this technique using a silver STM tip to create 10-40 nm modifications on thin gold films. Jersch and Dickmann (1996) also used a silver STM tip on a gold substrate to create craters and hillocks down to a resolution of 10 nm. A Nd:YAG short-pulse laser was used by Lu et al. (1999) with a tungsten tip to create nano-dot arrays of 20-30 nm resolution on germanium. More recently, Chimmalgi et al. (2005) used femtosecond laser pulses with gold-coated silicon nitride AFM tips to create linear modifications on thin gold films, semiconductor films, and bulk silicon with linewidths between 15 and 50 nm. These techniques all demonstrate resolution well below the present ultraviolet lithography currently used in industry. With this in mind, computational studies have been performed with the goal to design optical probes for optimal field enhancement and lithographic results (Krug et al., 2002).

Rather than proposing a new probe design, the work presented in this section will model an existing AFM tip design with a variety of lasers at different incident angles to determine the optimum experimental setup for localization and magnitude of near-field enhancement. The FDTD method is used with the current density formulation for treatment of metallic tip coatings. A two dimensional transverse magnetic formulation (solving for Ex, Ey, and Hz field components) is used for all simulations consisting of one million Yee cells (1000 x 1000). Grid resolution is five Angstroms (0.5 nm). The Courant stability condition requires time steps of less than one attosecond (10^{-18}) to be used. Convergence was obtained after 12,000 time steps.

The generic AFM tip design used in this study consists of a silicon cone (18^{o} half cone angle) coated with a 20 nm thick gold layer, with a 6 nm tip radius. Tip length is cut off at 375 nm, though this is shown to be sufficient length to accommodate the enhancement effects. Substrates of both gold and silicon are simulated over a wide range of incident laser angles, incident laser wavelengths and tip/substrate separation distances.

Figure 4.11-4.14 present the converged intensity fields above a silicon substrate for four incident angles using λ=532 nm irradiation and a tip separation distance of 2.5 nm. In figures 4.11-4.14, the environment is rotated 90^{o} with the substrate oriented vertically on the right and the AFM tip horizontal on the left. The value in the inserted plots is the substrate surface intensity along the line demarcated by the silver circles. The insert plot range is 125 nm along the substrate for all figures.

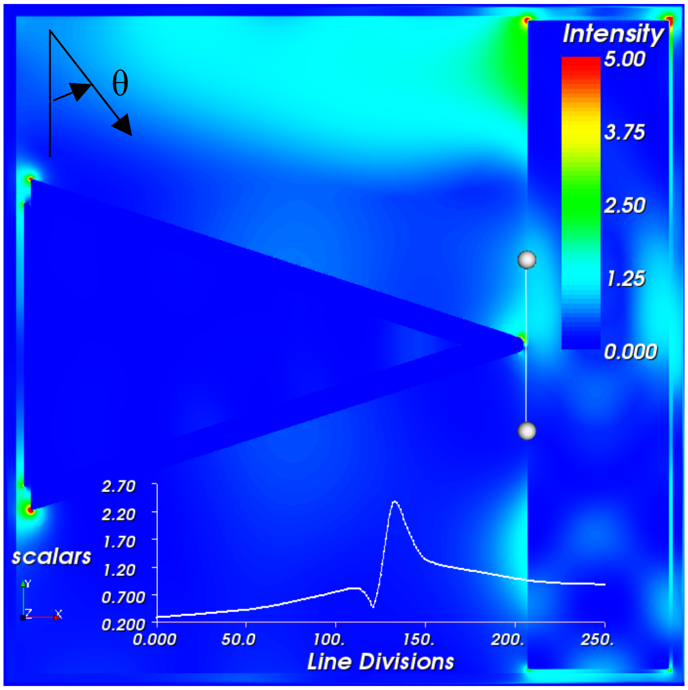

Figure 4.11: Gold/silicon AFM tip irradiated by λ=532 nm laser over silicon substrate at 2° incident angle (glancing angle)

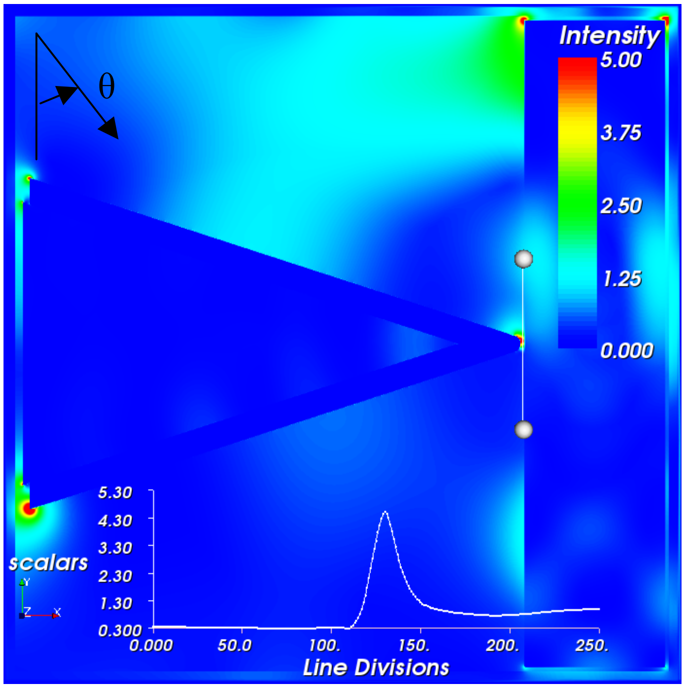

Figure 4.12: Gold/silicon AFM tip irradiated by λ=532 nm laser over silicon substrate at 10° incident angle

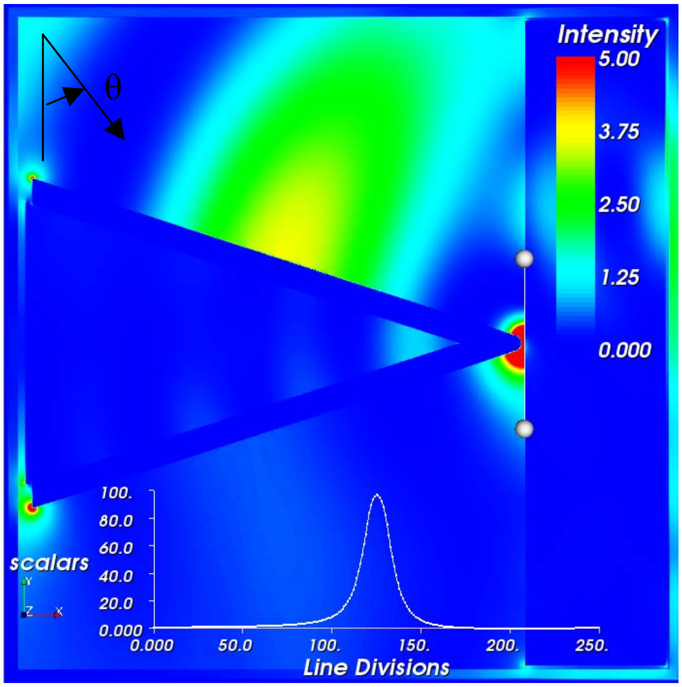

Figure 4.13: Gold/silicon AFM tip irradiated by λ=532 nm laser over silicon substrate at 45° incident angle

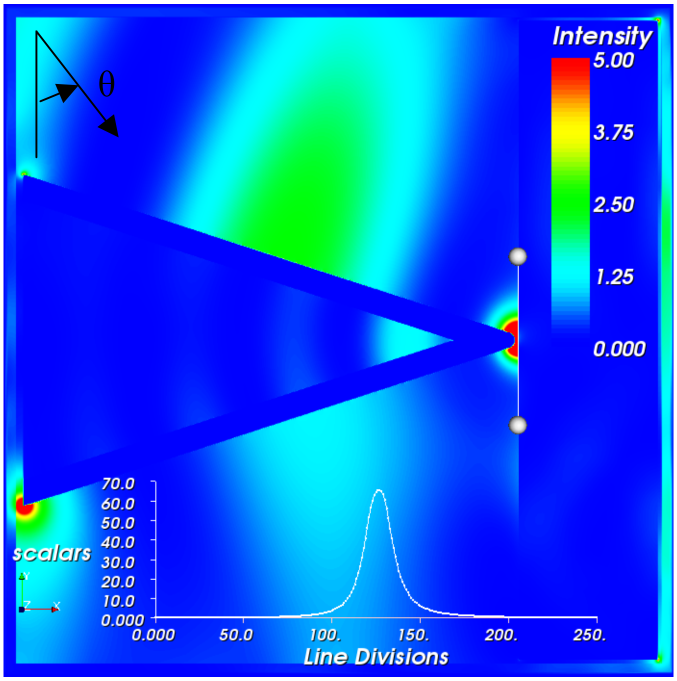

Figure 4.14: Gold/silicon AFM tip irradiated by λ=532 nm laser over silicon substrate at 70° incident angle (parallel to tip angle)

Both the color schemes and inset plots on Figures 4.11-4.14 indicate a dependence on the plasmonic enhancement effect at the tip/substrate junction on incident laser angle. The scale of the insets shows that the smaller angles (0^o = parallel to substrate) exhibit much smaller levels of energy enhancement, and asymmetric profiles. These glancing angles have been used in the majority of the experimental demonstrations referenced above. Therefore, consideration of this and other dependencies to be presented may offer room for improvement of lithographic results and a template for tuning the technique.

Figures 4.15 and 4.16 present data obtained from the angular dependence investigation. The value plotted in 4.15 is the peak enhancement as a function of incident laser angle, and is given for simulations of both gold and silicon substrates (gold coated AFM tip remains unchanged). Figure 4.16 plots the full-width-half-maximum of the enhanced profile at the substrate surface, in nanometers, as an indication of the potential size of surface modifications. As in Figures 4.11-4.14, the tip distance from substrate and incident wavelength remain constant at 2.5 nm and 532 nm, respectively.

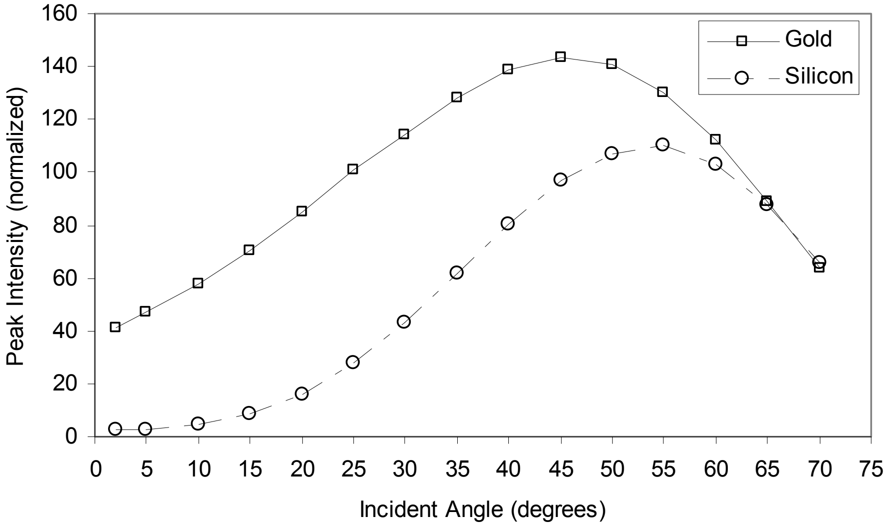

Figure 4.15: Angular dependence of peak enhancement at AFM tip/substrate junction with λ=532 nm irradiation

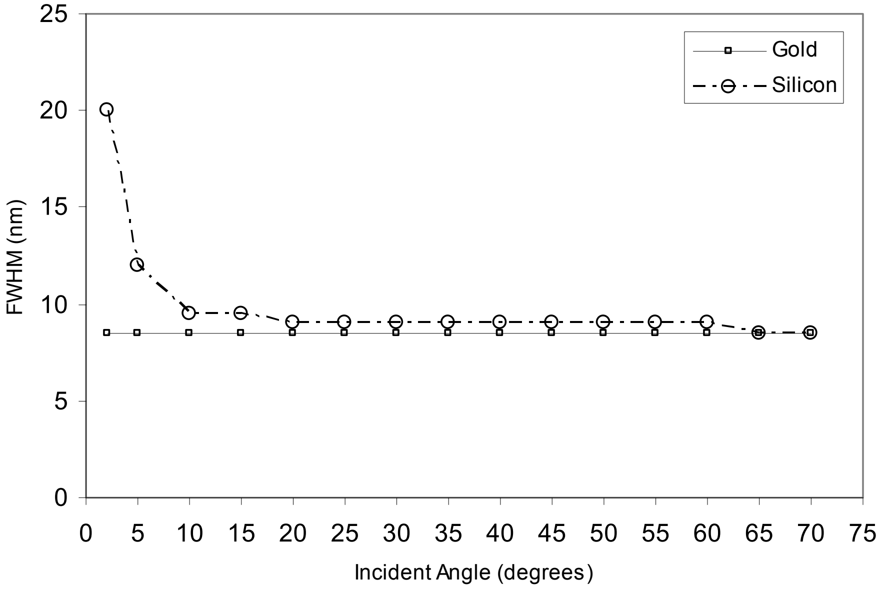

Figure 4.16: Angular dependence of enhanced FWHM at AFM tip/substrate junction with λ=532 nm irradiation

The data in Figure 4.15 indicates the strong angular dependency as well as a substrate material effect. Importantly, there is clearly an angle at which a maximum enhancement is generated for both silicon and gold substrates. For AFM tip on gold substrate, this angle is close to 45 degrees above parallel, while on silicon it appears to be ~ 55 degrees above parallel. Within the range of modeled angles, the enhancement profile can exhibit extremely large changes in peak enhancement, more than one order of magnitude for the case of silicon substrate. From Figure 4.16, however, the width of the enhanced profile remains essentially constant. The relatively large FWHM value for silicon at a glancing angle is understood by examining the inset plot on figure 4.11. Whereas at larger angles which exhibit guassian shapes, the profile shown in figure 4.11 is asymmetrical, driving up the FWHM value. For this specific data point, the concept of full-width-half-maximum is corrupted, so it can be concluded that the FWHM is independent of incident laser angle. From an experimental viewpoint, adjusting the incident laser angle can then be substituted for adjusting the input energy, without a corresponding change in energy profile. This may prove advantageous when using inconsistent energy diagnostic instruments with short-pulse and ultrafast lasers.

The second investigation studied dependency on tip distance from the substrate. From the results of the previous investigation, the angle was chosen which provided for peak enhancement for each substrate, so 45^o was used for gold and 55^o for silicon. Again, an incident beam with 532 nm wavelength was used for all simulations. Figures 4.17-4.20 present converged intensity profiles for several separation distances above a silicon substrate. The inset plots are of the substrate surface intensity along the line between the silver circles, which is 125 nm in length for all cases.

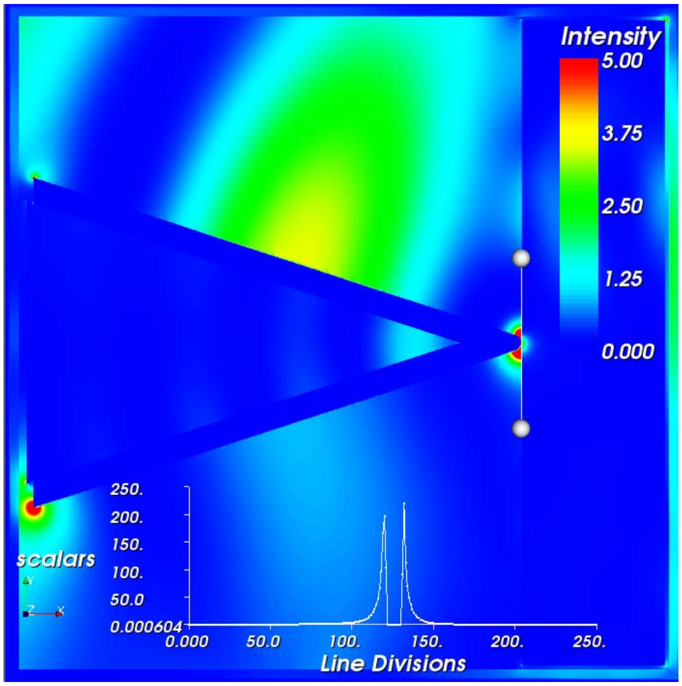

Figure 4.17: Gold/silicon AFM tip irradiated by λ=532 nm laser over silicon substrate at a separation distance of 0 nm (contact)

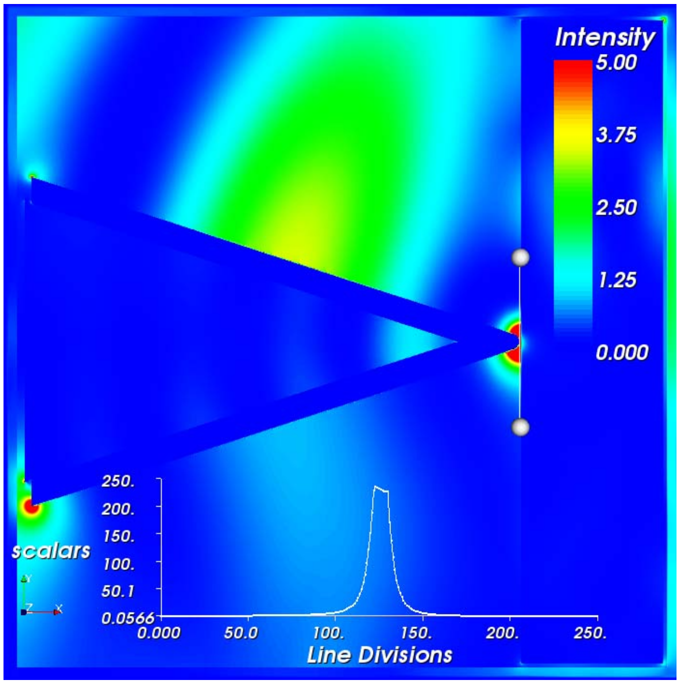

Figure 4.18: Gold/silicon AFM tip irradiated by λ=532 nm laser over silicon substrate at a separation distance of 1.0 nm

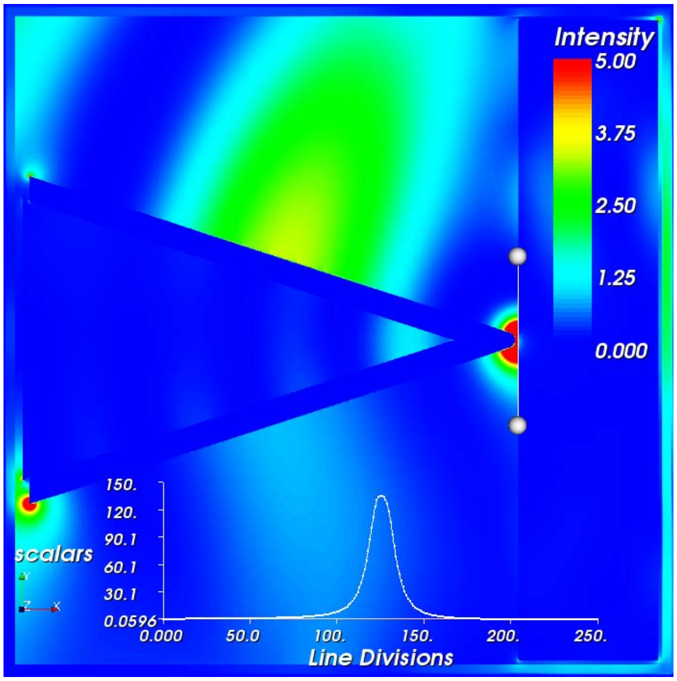

Figure 4.19: Gold/silicon AFM tip irradiated by λ=532 nm laser over silicon substrate at a separation distance of 2.0 nm

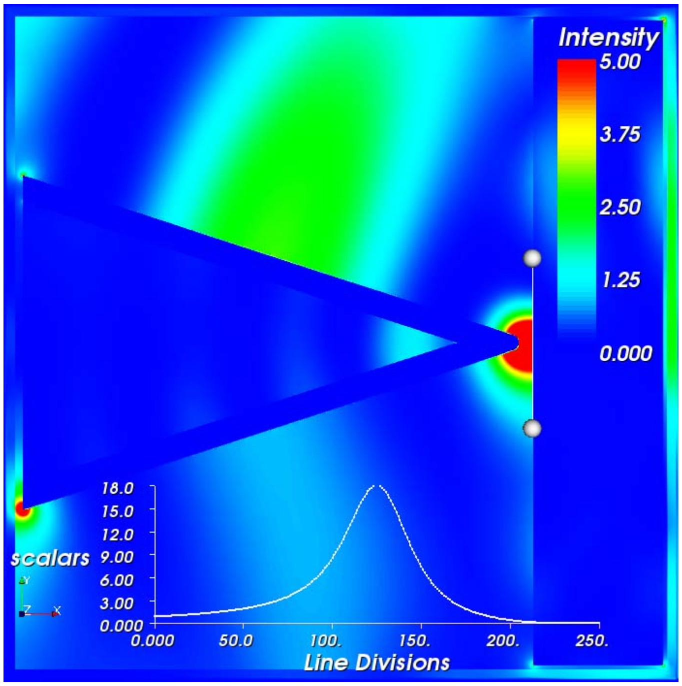

Figure 4.20: Gold/silicon AFM tip irradiated by λ=532 nm laser over silicon substrate at a separation distance of 10.0 nm

The figures above indicate that the surface intensity profile is a strong function of tip distance from the substrate. The inset plot of figure 4.17 exhibits the dual intensity peaks similar to the cases presented in Chapter 2 with a microsphere in contact with a substrate. As the distance is increased, even very slightly, the central dip vanishes and the Gaussian profile takes shape. Scrolling through all four figures, it is clear that now the profile expands with distance as well. Figures 4.21 and 4.22 present all the data points from the separation distance investigation for the peak enhancement and FWHM properties. Again, both gold and silicon substrates are modeled for all tip distances.

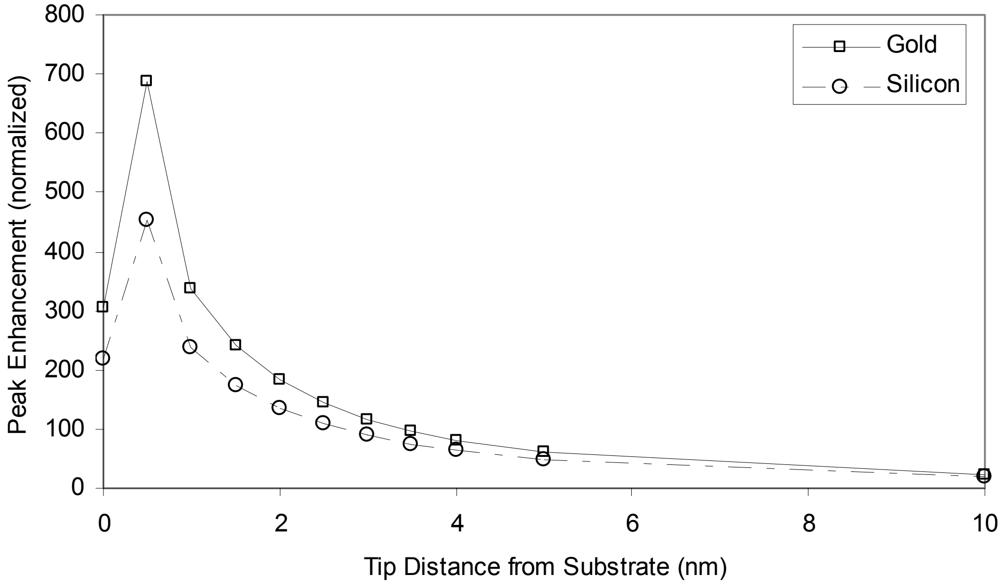

Figure 4.21: Tip-separation dependence of peak enhancement at AFM tip/substrate junction with λ=532 nm irradiation

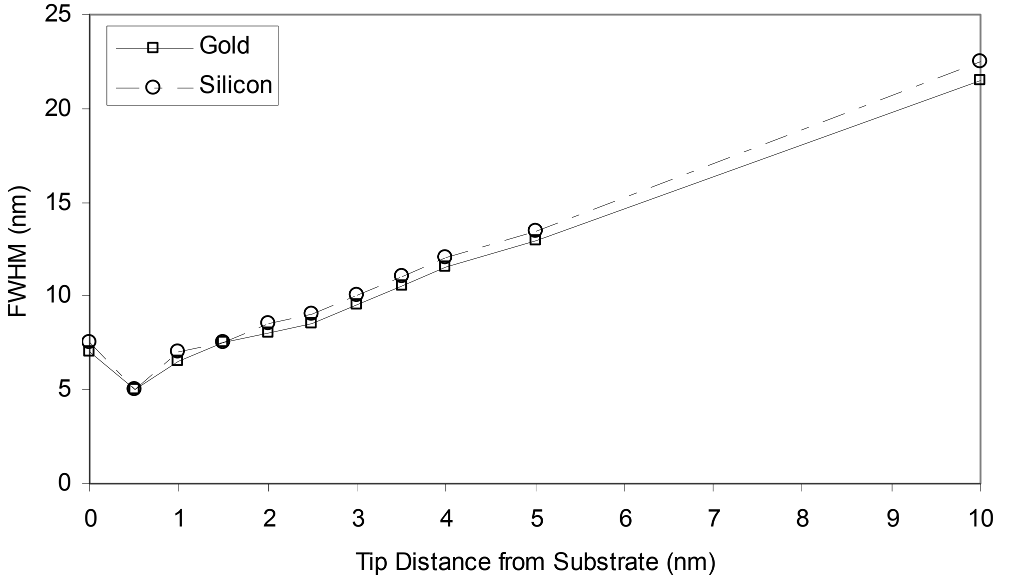

Figure 4.22: Tip-separation dependence of enhanced FWHM at AFM tip/substrate junction with λ=532 nm irradiation

Interestingly, there is a distance (other than contact) at which the peak enhancement is maximized. This distance is exceedingly small, however and lies between 0 and 1 nm for both silicon and gold substrates. Even with more controllable distances of 2-5 nm, the peak enhancement is still up to 100 times the incident wavelength. The energy required to damage the substrate and create surface modifications can therefore be orders of magnitude lower than without the presence of the AFM tip. The more distance separating tip and substrate, the larger the lithographic result will be, judging from the values in figure 4.21. Between 0 and 1 nm, likely at or very near the point of maximum enhancement, lies the distance at which the FWHM of the enhanced profile will be the smallest. After 1 nm, the FWHM's seem to increase linearly with separation distance. This is an important consideration if the goal is to produce the smallest features possible. The FWHM's in figure 4.22 are of the same order in size as the experimentally obtained modifications presented in the works referenced at the beginning of this section. However, at ~ 5 nm, the minimum FWHM predicted through this modeling could create features smaller than any presented in the literature and possibly the smallest obtained through optical lithography of any kind.

The third and final dependency investigation focuses on the incident laser wavelength. Five values were used which correspond to commonly used operating modes in many laboratories: λ= 266, 355, 532, 800, and 1064 nm. The angles of 45^{o} and 55^{o} were used again for gold and silicon respectively, and a tip separation distance of 2.5 nm was modeled. The peak enhancement values obtained from these simulations are given in Figure 4.23.

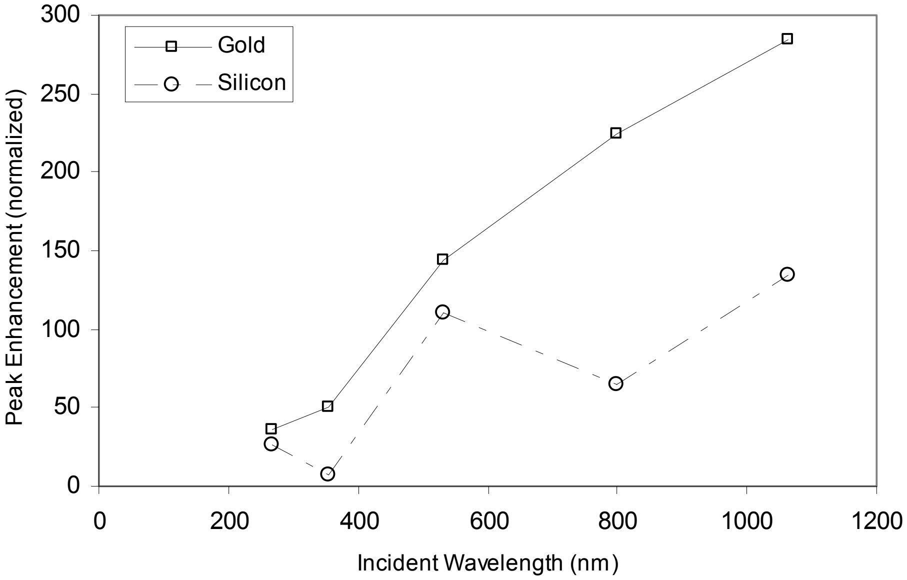

Figure 4.23: Wavelength dependence of peak enhancement at AFM tip/substrate junction

A general trend of higher enhancement at longer wavelength is seen from Figure 4.23, however it must be noted that angular dependence at the other wavelengths has not been quantified. The 45^o optimum angle at λ=532 nm irradiation may not be optimal at the other wavelengths. Performing these simulations is precluded by the geometric increase required to investigate the dependence at every angle at every wavelength at every separation distance, etc. The enhanced profile FWHM's remained essentially constant at between 8.5 and 9.5 nm for both substrates at every angle modeled. The feature size obtained using this method may be dependent solely on tip separation distance (for a given tip geometry), in the case of ultrafast machining where thermal diffusion effects are minimal. For longer pulses and continuous-wave lasers, a combination of the conditions modeled above may contribute to the final lithographic effect.

4.4 Plasmonics for photonic circuits

The first chapter of this work outlined several proposed and existing applications for the surface plasmon. As yet, microscopy and sensing have led the way from research to development of useful tools and even commercially viable products. Sub-diffraction limit plasmonic lithography has been demonstrated, but not yet implemented in higher-order devices. The other branch of interest, coupling of photonic and electronic circuits by way of SPP's, generates perhaps the most interest as well as the heaviest intellectual and experimental challenges.

4.4.1 Introduction

In recent years, the primary bottleneck for increasing single microprocessor performance has been interconnect scaling. Transistors can be fabricated routinely at dimensions near 50 nm, and in fact their performance exhibits improvement with decreased size. The copper interconnects, however, support smaller information carriage capacity with decreasing size, becoming a major limiting factor in speed of digital signal processing. In addition, the increased density of such small electronic circuits generates a great deal of waste energy, resulting in complicated thermal management issues and increased possibility for short-circuiting and interconnect failure.

Photonic circuits, employed widely as fiber optic cables, have ~ three orders of magnitude greater data carriage capacity than electronic circuits. Diffraction limits their lower dimension to the order of a micrometer, making a coupling of optical fiber and electronic circuits in a microprocessor unfeasible. Surface plasmons provide the mechanism (in theory) by which to bridge that dimensional gap and couple photonic and electrical signal processing. As conductors, surface plasmon waveguides could accomplish both, and do so at the nanoscale, breaking the bottleneck of interconnect capacity and allowing increase in microprocessor speed.

The recent progress in pursuit of this goal has been exciting as the fundamental behaviors and SPP propagation and decay are being uncovered. Weeber et al. (1996) observed light propagating tens of microns on a 2.5 μm wide gold waveguide before decay due to absorption and re-coupling to freely propagating radiation. It has been shown that both silver and gold nanowires (20-100 nm diameter) can function as surface plasmon resonantors, guiding an optical signal at least 10 μm in length (Ditlbacher et al., 2005), (Dickson and Lyon, 2000). Stockman (2004) published computational results that predict a guiding and focusing of plasmon energy along a tapered silver cone 2.5 μm in length. It was realized that nanoparticle arrays could guide light similarly to nanowires, but the reduced volume of metal would reduce absorption (ohmic loss), thereby increasing plasmon propagation length. Maier et al. (2005b) demonstrated such a plasmonic waveguide strip consisting of gold nanodots, and found propagation distances of greater than 50 μm. Nanodots have also been used as focusing arrays to direct plasmon energy into silver strip guides (Yin et al., 2005). This technique of amplifying the initial optical signal before guiding will be utilized in the work presented in this section.

Semiconductor nanowires have also been used to guide sub-wavelength light. Barrelet et al. (2004) found that light can travel through sharp bends in cadmium sulfide nanowires with only moderate losses. Greytak et al. (2005) of the same research group used exiting cadmium sulfide and gallium nitride nanowires as nanoscale lasers. Sirbuly et al. (2005) demonstrated coupling of GaN and ZnO nanowires with ribbon waveguides, and subsequent pulse lengths on the order of millimeters. Energy coupling between linkages was found to be a function of both volume and angle of interaction

In this section, multi-wall carbon nanotubes (MWCNT's) are proposed and modeled as photonic circuit interconnects. Surface plasmons have been observed in MWCNT's by Bursill et al. (1994), Bommeli et al. (1996), and Lu et al. (2005) using both electron energy loss spectroscopy and fluorescent microbead detection. A theoretical investigation of plasmons in isolated single-wall carbon nanotubes (SWCNT's) reported a strong dependence of plasmon dispersion on the chirality of the tubes, or the angle the tubes are rolled up with respect to the lattice bonding (Perez and Que, 2006).

There are two primary reasons for proposing MWCNT's as a potential plasmonic media. Theoretically, carbon nanotubes can be either semiconducting, semi-metallic, or metallic, depending on their chirality and thickness. Metallic CNT's have been shown to exhibit very small electrical resistance (Ebbesen et al., 1996, Gao et al., 2005). This high conductivity should mitigate one of the largest factors in plasmonic decay: ohmic loss. More practically, mass fabrication (growth) of high-quality carbon nanotubes has become possible and firmly established since the work of Ebbesen (1992). A computational investigation of plasmon generation and propagation in MWCNT's can therefore be a useful first step to introducing them as potential photonic interconnects.

4.4.2 Modeling MWCNT's

Given the many variations in carbon nanotube chirality, inside diameter, outside diameter and number of wall layers, all of which affect the optical and electronic properties, certain generic assumptions must be made in order to model the interaction between laser light and a nanotube. First, the walls of a single-wall nanotube consist of only one atomic layer. This structure can only be modeled with precision using molecular dynamics simulations, preferably quantum-based, and using ab-initio derived data. Therefore, the decision was made to model multi-wall tubes, where the optical response of ten to twenty atomic layers can be considered more homogenous and fit within the context of the FDTD method and a dielectric function. Second, the nanotube's chirality is addressed only through the assumption of a metallic nanotube. This should be noted in the event an experimental comparison is made using the results of this section.

The optical response of nanotube arrays embedded in dielectric material has been fit successfully from the far infrared to the ultraviolet using a combined Drude-Lorentz model (Bommeli et al., 1996), (Jeon et al., 2004).

$$\varepsilon(\omega) = \varepsilon_\infty - \frac{\omega_P^2}{\omega^2 - j\omega\gamma_P} + \sum_j \frac{\omega_{P,j}^2}{\left(\omega_j^2 - \omega^2\right) - j\Gamma_j \omega} \tag{4.11}$$

The first two Drude terms describe the metallic contribution of the tubes, and the third Lorentz term quantifies the response of the dielectric material. The dynamic response of the combined medium was then described in these works by the Maxwell-Garnett model, which uses filling and geometric factors to determine the effective complex permittivity. Not being concerned with the dielectric medium, MWCNT's are modeled here by merely extracting the Drude values which fit the experimental data obtained from the research referenced above. In particular, ω_P=2.0 eV and γ_P=0.2 eV from Bommeli et al. (1996), and the infinite frequency response value of ε_∞=3.49 was used based on the work of Jeon et al. (2004). The value for electrical conductivity used is calculated from the average of resistance values reported by Gao et al. (2005), σ=8.48*10^7 (Ω-m)$^{-1}$. The complex permittivity defined by these values are intended to represent an approximate cross-section of metallic nanotubes, which are famously unique even within a common batch. While this function has fit the experimental data well, it will be shown that the strongest dependency in the plasmon propagation effect lies within the value of electrical conductivity, a measurement undertaken by others with a level of certainty that provides confidence in the results presented here.

FDTD simulations are undertaken in both 2-D and 3-D, however the extremely large length to diameter ratio of a typical CNT precludes a superior mesh resolution in three dimensions when more than a single nanotube is modeled. With more complex combinations of tubes and dielectric amplifiers, the results are naturally contrained under the two-dimensional approximation, however fundamental behaviors and dependencies can still be elucidated.

4.4.3 MWCNT modeling results

As mentioned, preliminary simulations indicated weak energy propagation on individual carbon nanotubes, but strong energy coupling with two or more irradiated tubes in range of each other's near-field. The initial simulation presented is a simple setup of two 20 nm diameter nanotubes aligned in parallel and irradiated axially (separation distance of 20 nm). A 3-D computation is performed using a mesh resolution of 1 nm. The 150 x 150 x 500 cell domain cannot simulate close to the full length of a typical nanotube, but can offer insight into the morphology of the EM field and allow a comparison to an identical simulation in two dimensions, giving an idea of the accuracy of more complex 2-D simulations to be presented.

Figure 4.24 (a) gives a cross-sectional view of the intensity field cut through the nanotubes perpendicular to the polarization direction. As can be seen by the color scheme, a wave of energy confined to the 20 nm separation distance propagates between the nanotubes. Figure 4.24 (b) shows the cross-section normal to the axial direction. The butterfly shape of the energy corresponds to a weakening coupling between nanotube walls. Even though the individual nanotubes are hollow, the deep blue throughout the length of the tubes indicates a lack of any electromagnetic energy in the interior. The tubes are close-ended at the incident side (left) and open-ended on the right.

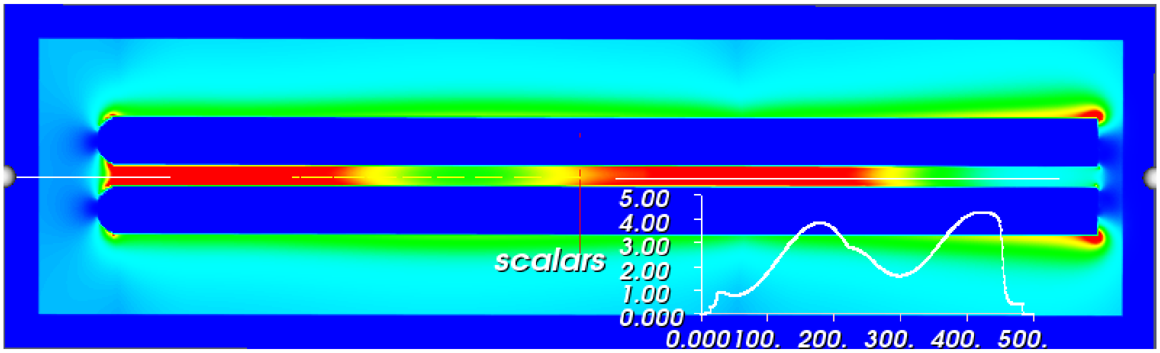

(a)

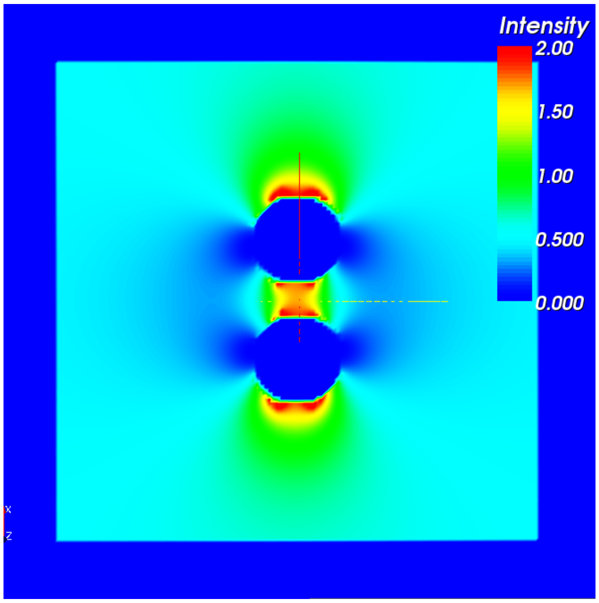

(b)

Figure 4.24: Cross-sectional intensity field through two multi-wall carbon nanotubes irradiated by λ=532 nm laser pulse (a) axial, and (b) radial

Figure 4.25 is the corresponding two-dimensional image of intensity field for identical simulation parameters. Here, the two nanotubes are not hollow, to eliminate the two-dimensional neglect of Faraday shielding. Otherwise, a system of four smaller tubes would actually be simulated.

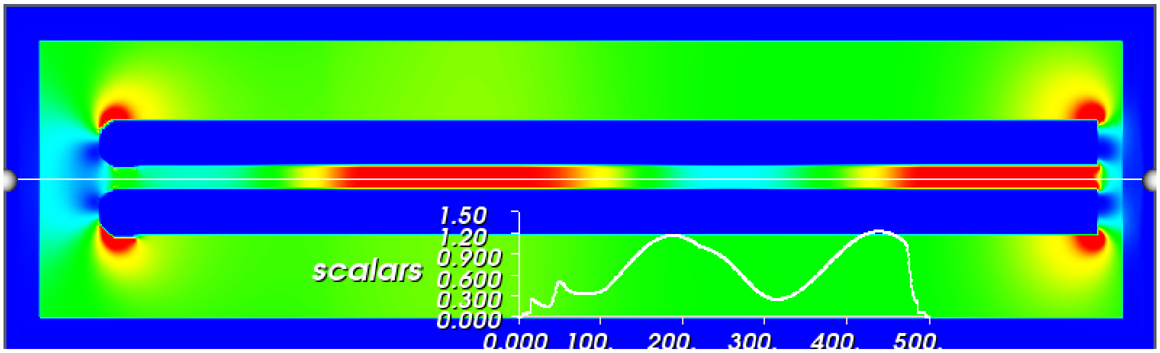

Figure 4.25: 2-D intensity field surrounding two multi-wall carbon nanotubes irradiated by λ=532 nm laser pulse.

Comparison of Figures 4.24 (a) and 4.25 allows a level of qualitative comfort for analysis of purely two-dimensional MWCNT simulations. As with dielectric spheres vs. cylinders, the ultimate level of near-field enhancement is higher with the added micro-dimension, however the behavior of the enhanced energy is mathematically similar in shape (spatially). This allows the use of two dimensional FDTD to investigate more complex plasmonic propagation on a qualitative basis.

A natural method to pre-localize the energy before introduction into a plasmonic circuit is the use of dielectric microspheres/microtubes, given the effects presented in Chapter 2 of this work. The utility of this would be to amplify the signal in anticipation of absorption and radiation loss, in order to increase the distance of propagation while maintaining a usable signal strength. Predictions based on this technique are presented in Figures 4.26-4.29. It was determined that the nanotube separation distance in the direction of polarization (and plasmonic coupling) greatly affected the signal decay length. Separation distances of 10, 20, 30, and 40 nm are simulated here. The silica amplifier is 1.0 µm in diameter and an incident wavelength of λ=532 nm is modeled.

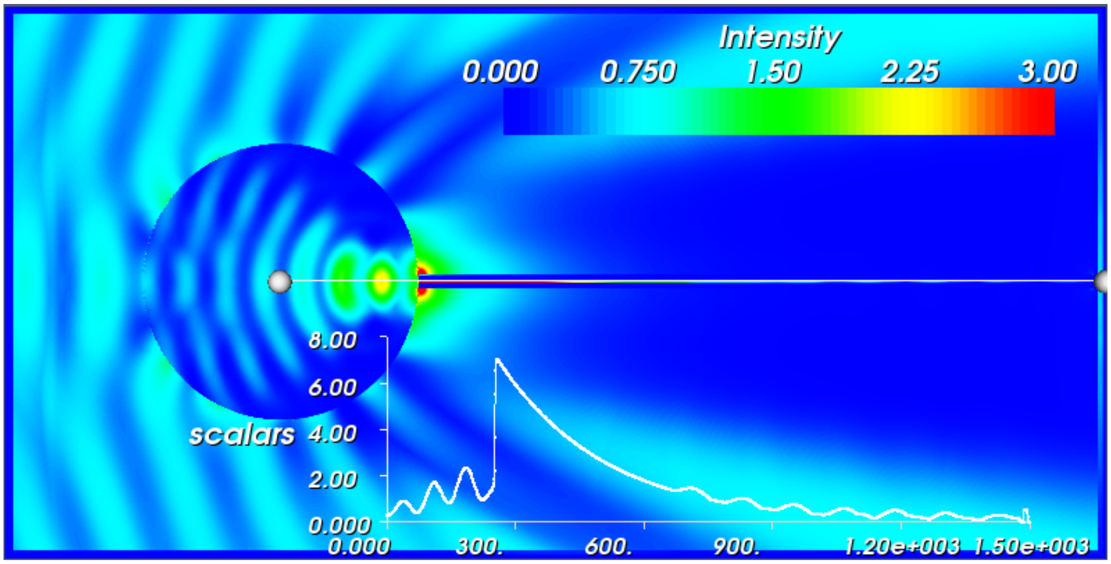

Figure 4.26: Coupling of silica microtube and carbon nanotube for photonic signal propagation, tube separation of 10 nm. (Plot range 2.0 µm x 4.0 µm)

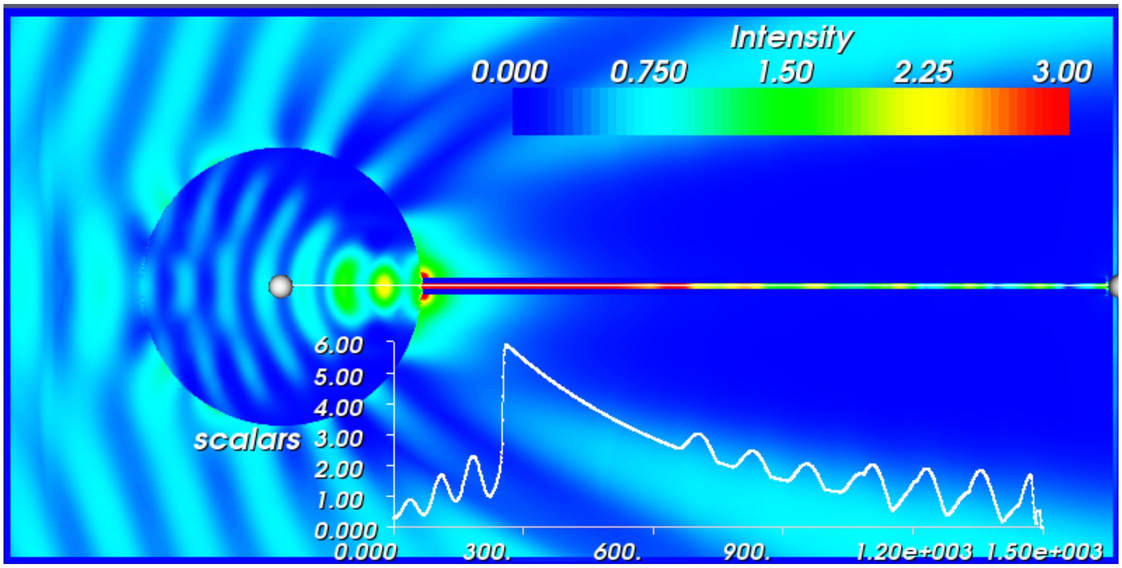

Figure 4.27: Coupling of silica microtube and carbon nanotube for photonic signal propagation, tube separation of 20 nm. (Plot range 2.0 µm x 4.0 µm)

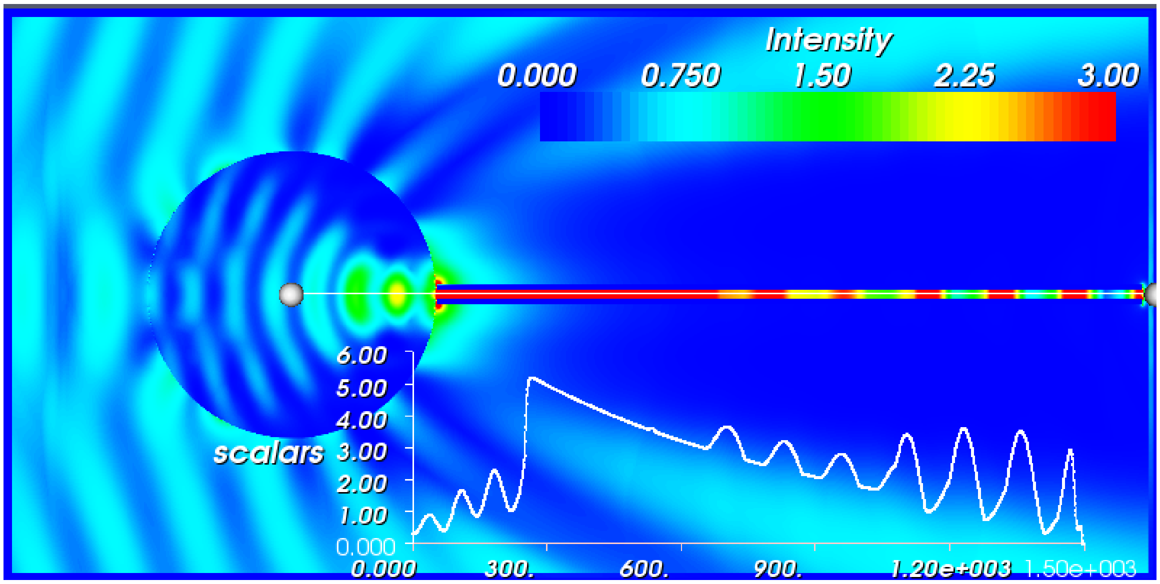

Figure 4.28: Coupling of silica microtube and carbon nanotube for photonic signal propagation, tube separation of 30 nm. (Plot range 2.0 µm x 4.0 µm)

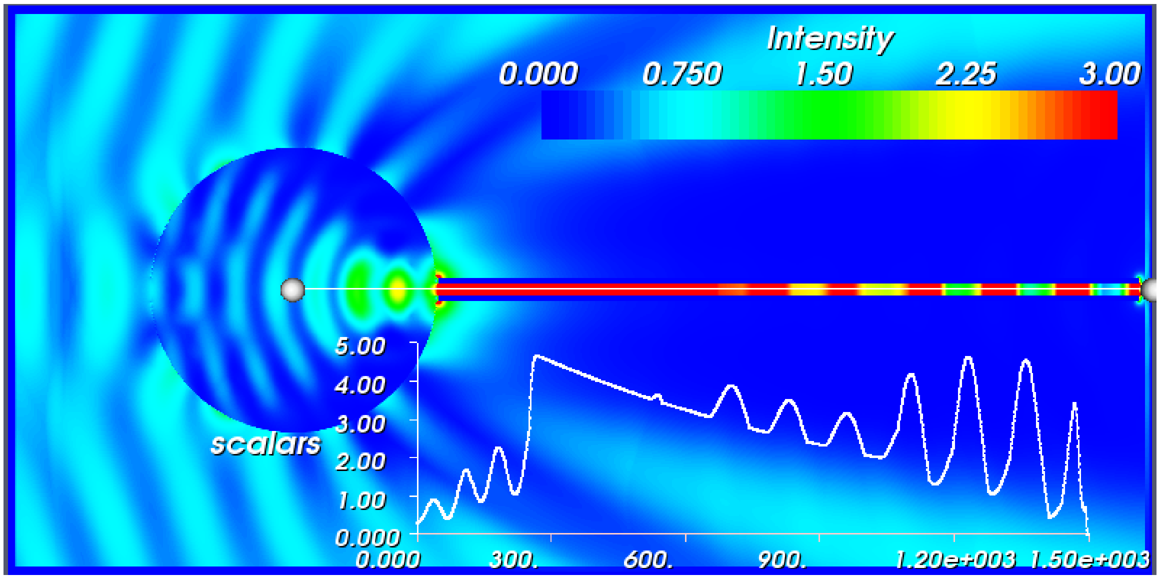

Figure 4.29: Coupling of silica microtube and carbon nanotube for photonic signal propagation, tube separation of 40 nm. (Plot range 2.0 µm x 4.0 µm)

It is clear that the confinement and propagation of the energy is suppressed when nanotubes are spaced too closely. With a distance of 20 nm or more, the signal can maintain a strength of the initial incident pulse over a distance of a few microns. It should be noted that the initial values of enhancement are a very modest five to six times as given by the inset plots. The information provided earlier in this work can offer combinations of amplifier and wavelength that could increase this by an order of magnitude.

A curious resonance occurs as the signal decays and the plasmonic coupling becomes weaker. It actually has the effect of localizing the energy even further in the radial direction, and creates a standing wave-like energy profile which essentially increases the distance before which the strength drops below incident level in select locations. The utility of separation distances of over 40 nm starts to drop, as the combined circuit and dual tube system approaches dimensions that are attainable routinely using ultraviolet lithography techniques.

The effect of bends and acute angles in the nanotube circuit is now investigated. Figures 4.30 and 4.31 present a similar amplifier/dual tube system in which two 45^{o} sharp bends exist. An incident wavelength of 532 nm is modeled in Figure 4.30. Based on the electron energy loss spectroscopy work of Bursill et al. (1994), in which a weak plasmon resonance was found at an energy of 15 eV (corresponding to 83 nm wavelength), far-ultraviolet radiation is modeled in Figure 4.31 using an identical setup. Bursill found a much stronger resonance at 24 eV, however the corresponding wavelength of 50 nm is not modeled here.

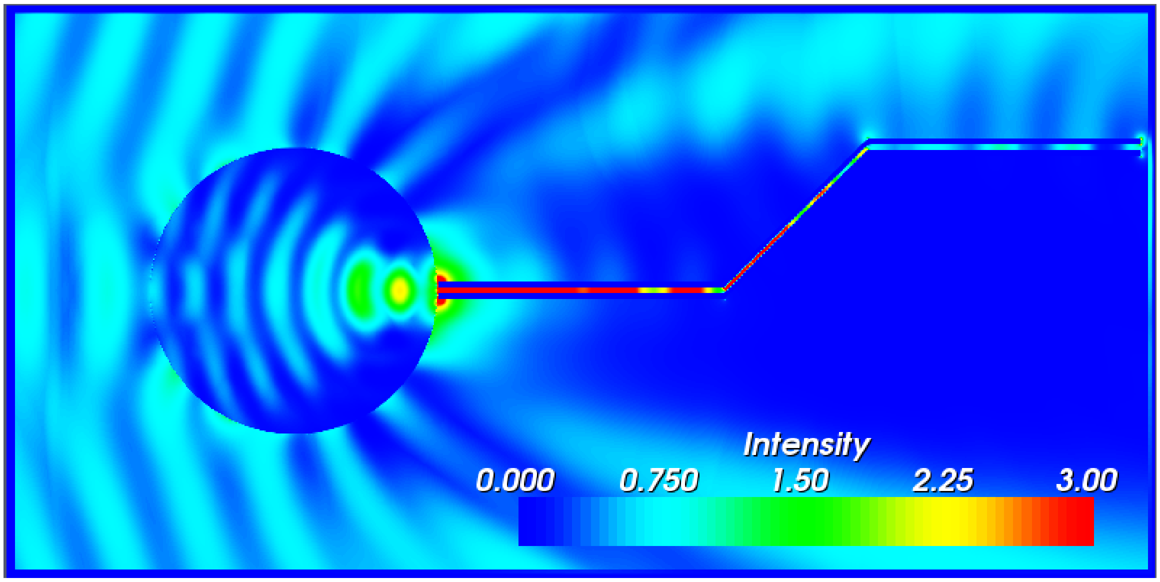

Figure 4.30: Silica amplifier/dual nanotube photonic circuit with two 45o angles, incident wavelength λ=532 nm.

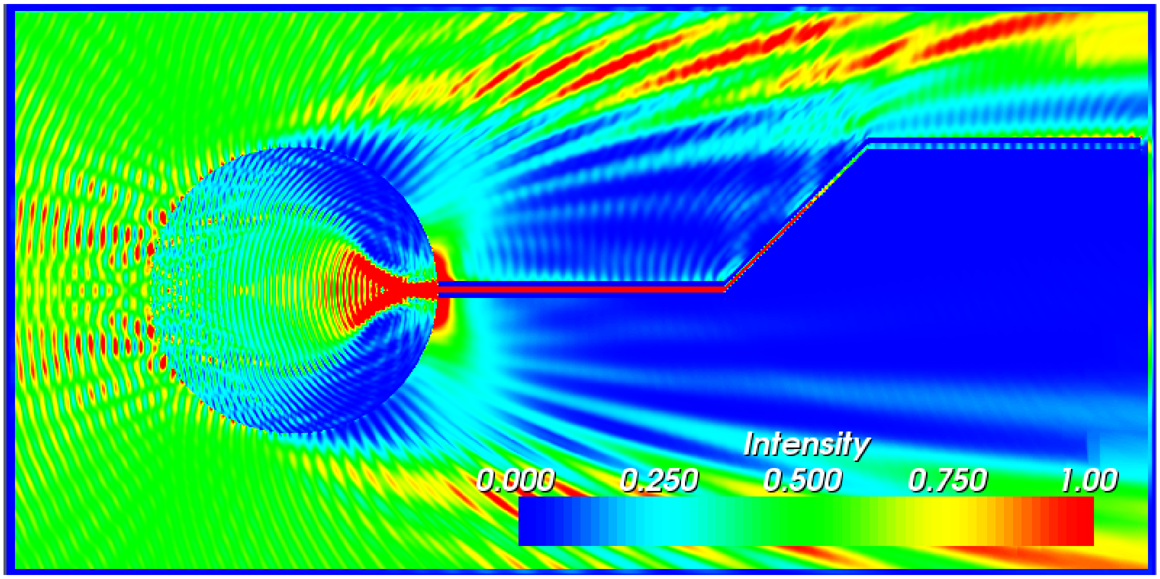

Figure 4.31: Silica amplifier/dual nanotube photonic circuit with two 45o angles, incident wavelength λ=83 nm

Though difficult to see, the signal maintains a strength greater than one times incident at the end of the circuit modeled in Figure 4.30. The most noticeable decay occurs not at the bends themselves, but in the more constricted slanted section, which has tube separation of 0.707*20nm=14.1 nm. Figure 4.31 predicts a similar plasmonic confinement and propagation using ultraviolet energy, however not an obvious improvement. The difficulty of such irradiation would seem to preclude a UV signal, given a lack of visible improvement. Performance of both circuits would likely be increased by increasing the space between the slanted tube segments.

The final photonic circuit simulations presented here incorporate a splitting of the signal and an acute 90° angle. Again, both visible and far-ultraviolet wavelengths are simulated. Figures 4.32 and 4.33 present the converged intensity distributions.

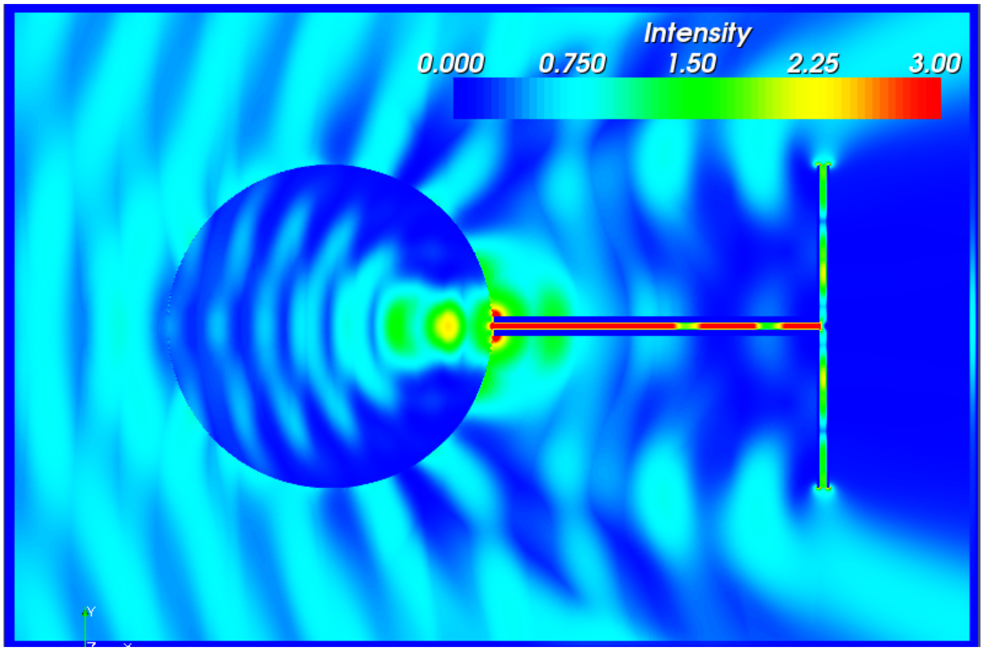

Figure 4.32: Silica amplifier/dual nanotube photonic circuit with T-split, incident wavelength λ=532 nm

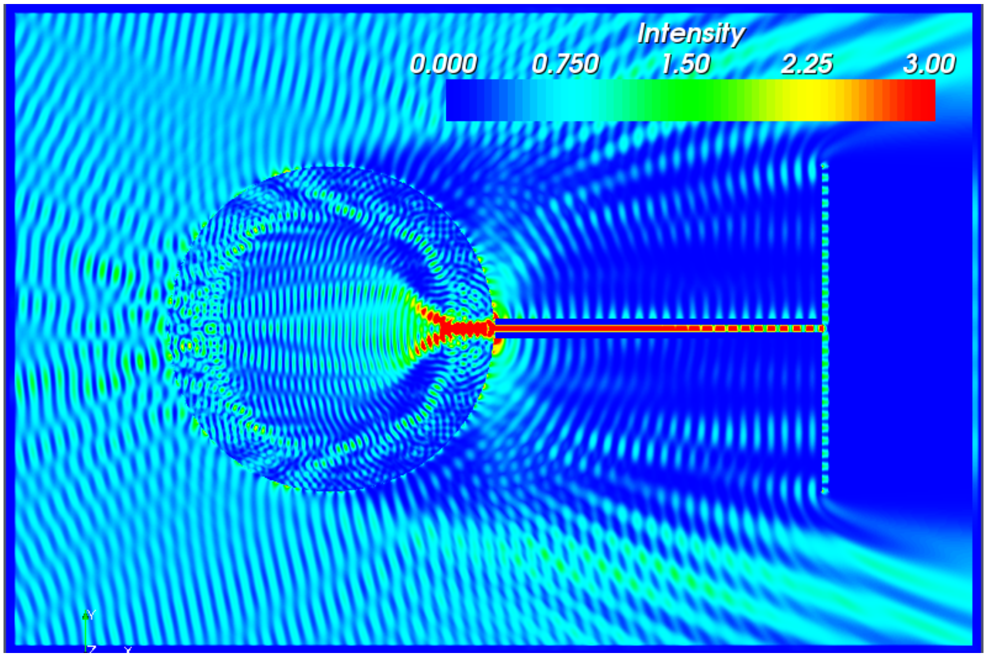

Figure 4.33: Silica amplifier/dual nanotube photonic circuit with T-split, incident wavelength λ=83 nm

While the color scheme seems to show a dramatic decrease in signal strength after the split, the intensity levels in both branches are nearly exactly half the strength of the signal before the split. This indicates extremely efficient maintenance even with sharp 90^o angles, as well as a clean split for routing the signal to multiple destinations. The channel width is maintained at 20 nm after the split, evidence that this parameter is a critical consideration. As with the 45^o bend simulations, the propagation effect does not seem to be wavelength-dependent, at least between the visible and ultraviolet range.

4.5 Summary

The current density formulation of the FDTD algorithm is introduced with coefficients structured to describe the optical response of metals using the Drude and modified Debye models. Values for infinite frequency response, zero frequency response, pole relaxation time, and electric conductivity are provided for the calculation of the complex permittivity within these models at relevant frequency ranges. The FDTD algorithm is used to model suspended gold and silver nanostructures to uncover fundamentals in plasmonic generation and coupling behavior. It is determined that surface plasmon enhancement is highly dependent on the existence of metallic structures in the near-vicinity. The plasmonic enhancement is generated along the axis of polarization, an important consideration when applying the phenomenon for surface modification.

This numerical method is then used to simulate the response of laser/gold nanosphere interaction for the purpose of plasmon-based nanolithography. Two gold sphere sizes are modeled in three dimensions at three incident laser angles. A silicon substrate is modeled as the target material. The results confirm an intense localization of energy beneath the spheres at sub-wavelength dimensions. Experiments performed under identical conditions by Theppakuttai (2006) exhibit lithographic results consistent with the modeling, and well beneath the diffraction limit. The incident laser angle should have a substantial component of polarization directed normal to the substrate for improved lithographic results.

The FDTD method, Drude and modified Debye models are then used to theoretically optimize the AFM/STM nanolithography technique on both silicon and gold substrates. Directed energy profiles are analyzed for both enhancement level and full-width half-maximum (FWHM). A strong peak enhancement dependency is found with variation in both incident angle and tip distance from the substrate. Maxima and minima are pinpointed for both effects on both substrates. The FWHM is found to be dependent tip distance from substrate, but constant with changes in both incident angle and incident laser wavelength. A minimum FWHM is predicted with tip distance between 0.5 and 1.0 nm above the substrate. A theoretically minimal FWHM of 5 nm is found, while peak enhancement can reach several hundred times the incident laser energy.

The possibility of using multi-wall carbon nanotubes as photonic circuit interconnects is discussed. Surface plasmons have been observed in MWCNT's, and the high electrical conductivity of MWCNT's is well documented, allowing the possibility for sub-wavelength optical signal propagation with large data capacity as well as conventional electric signal capacity. The Drude model is employed to model the optical response of MWCNT's in the FDTD algorithm using experimental data from multiple sources. It is predicted that MWCNT's can sustain plasmon propagation at lengths of several micrometers. The enclosed nature of the hollow tubes prevents electromagnetic fields from propagating in the tube interiors, however the combination of two or more MWCNT's can result in a strong plasmonic coupling and propagation of surface plasmons even through acute angles with high efficiency. It is shown that the nanotube separation distance heavily affects the plasmonic coupling and propagation length of the sub-wavelength signal. The use of dielectric microspheres is proposed as a signal amplifier. Upon interaction with MWCNT arrays, the enhanced signal output provides pre-localization and can provoke propagation distances potentially long enough for use in microprocessing devices.

Appendix A:
MaxTex.cpp User’s Guide

A.1 Introduction

As discussed in Chapter 2, MaxTex is a three dimensional Maxwell equation solver that employs the finite-difference time-domain method to “leapfrog” through time providing solutions to both magnetic and electric field distributions. The algorithm is covered in Chapter 2, so the focus of this guide will be to provide working knowledge for the user.

MaxTex must be re-compiled following a change in parameters to conduct a new electrodynamic simulation. This is mainly due to a lack of time and/or knowledge on the author’s part regarding the construction of a graphical user interface. The ambitious user has permission to modify and improve the program in any way, including the addition of a GUI and any FDTD constructs that may be conceived in the future. The code has been compiled and verified on Borland and Intel C++ compilers. It is important for any user to realize that the MaxTex code is currently set up to model a specific optical situation, but that the algorithm is very general and can be adapted to model a wide range of situations with knowledge of the variables, parameter, and the method. I highly recommend reading some of the literature referenced in this dissertation and/or the text by A. Taflove and S. Hagness, *Computational Electrodynamics*, 2005, Artech House, Boston-London.

A.2 Simulation parameters

Nx	Number of Yee cells in the x-direction
Ny	Number of Yee cells in the y-direction
Nz	Number of Yee cells in the z-direction
TFSF	On/Off switch for the total-field/scattered-field construct. 1=On, which will generate the user-defined plane wave. 0=Off

Nsf	Thickness of scattered field buffer (refer to Figure 2.16). Default=20, however literature indicates fewer may be required, reducing required memory and time
ABC	On/Off switch for Absorbing Boundary Condition (which is CPML in the latest version). 1=On, 0=Off. Off setting will provide a perfect electric conductor boundary condition.
CPML	Thickness of ABC layer. Default=10. Literature indicates at least six is needed. Changing CPML value will require changing calculation of CPML variable grids.
theta	Incident angle of plane wave in degrees (refer to Figure 2.16)
phi	Incident angle of plane wave in degrees (refer to Figure 2.16)
psi	Incident angle of plane wave in degrees(refer to Figure 2.16)
T	Number of time steps to run simulation. The time step duration, dt, is automatically defined from stability criterion. A small dd value will dictate a small dt value, increasing the number of steps needed (T) for convergence. Convergence checks should be performed. i.e. simulation can be considered converged when the waveform at an arbitrary point is constant for at least 7 periods.
dd	Size of Yee cell (cubic cells) in meters.
lambda	Wavelength of incident plane wave
Oradius	Outer radius of sphere to be modeled (if not modeling sphere, will not affect solution)
Iradius	Inner radius of sphere to be modeled if a shell or two-material sphere is desired.

Other definitions are variables, physical constants and material parameters that should not be changed unless the user is fundamentally modifying the program and understands their use.

A.3 Modeling Geometry

Material properties are accessed in the electric field updates segment of the code. The TFSF boundary and CPML layers are in vacuum, so the interior of the modeling environment (loops Ex, Ey, and Ez) contain the “target” geometry and material information.

Optical properties of a given material are defined before time-stepping through the four parameters, kd, Betad, Ca, and Cb, by equating them to pre-defined material parameters:

```
kd_material
Beta_material
Ca_material
Cb_material
```

where ‘material’ is currently one of the following: vacuum, silica, silicon, SU8 (polymer), Pyrex, silver, and gold, and CNT (carbon nanotube). A non-absorbing dielectric can be defined solely through its relative permittivity (F/m) as indicated in the code.

To assign a material property at a given point, the four properties above must be specified before the electric field update. For example, the following code snip defines a silica sphere, followed by the electric field and current density update:

```
if ((sqrt((Ox-i)*(Ox-i)+(Oy-j)*(Oy-j)+(Oz-k)*(Oz-k)))<(OR)){
	Ca_x=Ca_silica;
	Cb_x=Cb_silica;
	kd=kd_silica;
	Betad=Beta_silica;
}
Eold=Ex[i][j][k];
Ex[i][j][k]=Ca_x*Ex[i][j][k]+…;
Jx[i][j][k]=…;
```

where Ox, Oy, and Oz, define the center of the modeling grid (Ox=Nx/2).

Therefore, objects that can be defined by a mathematical curve are the easiest to model. Anything that can be modeled as an amalgamation of straight lines is possible, however, simply requiring more “if” loops. Individual cells can be specified, though that would be an extremely lengthy process for a complex geometry. A motivated individual could significantly increase the flexibility of MaxTex by building a mesh-importation scheme from a CAD drawing.

The material properties must be defined identically before all three electric field updates, Ex, Ey, and Ez, or the simulation will not reflect a realistic situation. I have found it suitable to initially define the modeling environment as vacuum and then overlay material objects in following loops.

A.4 Data output

The user can choose to record any combination of EM field data that can be recovered from all electric and magnetic field components through time. Currently, MaxTex writes files of 2-D cross-sections of time-averaged intensity (square of the electric field) for planes midway through the environment on all three axes. The file Avex is binary ASCII data of intensity through the plane where x is held constant at Nx/2. Likewise, Avey and Avez are intensity distributions halfway through the y and z axes, respectively. The files T0x, T0y, and T0z, are instantaneous “snapshots” of intensity taken at the final timestep, at the same midpoint planes.

Transient data is accomplished by writing values at each timestep. The output file Zcenterx writes a 1-D line of intensity data at each step. Plotting select columns of this file is helpful when checking convergence. Improper use (or mistakes made in the algorithm) of the ABC CPML would be evident by plotting columns of this file, which would likely diverge. The user would then find erratic increasing intensity values which never level off to the converged solution. The error would likely be due to un-absorbed reflection of EM waves from the boundary, which would compound over time.

Some versions of MaxTex save up to 200 files of the same data at equally spaced timesteps in order to compile movie files. The program Paraview has a movie creation wizard, as well as Windows movie maker and the visualization program IDL.

Visualization of results must be performed in a separate program. Microsoft Excel is useful for plotting single column results such as the convergence checks. The freeware program Paraview is useful for plotting the 2-D time-averaged cross-section data, however data must be first transformed into vtk format using another freeware program 'Databridge'. The commercial program IDL, which can be purchased on a student basis, can directly import the ASCII data. Several paraview and IDL visualizations are presented in this dissertation.

Appendix B:
FDTD Predictions of Light Pipe Inaccuracy Due to Micro-Abrasion

B.1 Introduction

Measurement of extreme high temperatures such as those encountered in the semiconductor industry is often accomplished using light pipe radiation thermometers (LPRT's). LPRT's are usually made of quartz or sapphire and use total internal reflection to funnel radiation detected at the tip placed near the target material. The semiconductor industry requires accuracy of within 2^o C at temperatures of 1000^o C, which in turn requires precise knowledge of any LPRT uncertainty (Adams, 1999).

Error can be introduced through radiation leakage, both internal and external. It has been shown by Lovas et al. (1998) that the environmental temperature can affect the LPRT reading enough to violate the above industry requirement. Experimental studies by Tsai et al. (2000) and Meyer (2001) have been performed with a range of operating temperatures in an effort to establish error ranges and provide correction factors. They have shown that the error increases dramatically when the environmental temperature is much higher than the target temperature, and that discrepancies vary widely between different types of light pipes.

In this strictly theoretical work, the assumption is made that both external and internal leakage is due to inevitable flaws in the light pipe surface, causing diffuse scattering where only specular reflection of internal radiation or transmission of external radiation is desired. Computational electrodynamics is used to model the scattering of a narrow band of radiation centered around 1 μm. The product of the modeling is a 360 degree scattering spectrum for the full range of possible angular incidence. This data can in turn be used as input for a Monte Carlo-based model which should describe the total gain/loss of unwanted radiation through the light pipe.

B.2 Model Development

Rather than speculating the geometry and prevalence of the unknown flaws, a specific damage pattern is transferred to the surface of the light pipe with fine-grit sandpaper. The surface modification is then distinguishable using a Mitutuyo surface roughness tester. Table 1 gives the results of the roughness testing conducted by Puttitwong (2005).

This modeling effort concentrates on the average depth of the finer grit paper of 11 micro-inches, or ~ 260 nm. The geometry is assumed to be regularly spaced triangular shaped grooves.

Table B.1: Surface roughness measurement of abraded light pipes (Puttitwong, 2005)

Surface Roughness Measurement (microinches) using Portable Surface Roughness Tester Model: Surftest SJ-201P, Brand: Mitutoyo

No.	Fused Quartz		Sapphire		Fused Silica		Fused Silica rubbed by 120	Fused Silica rubbed by 800
	Case A	Case B	Case A	Case B	Case A	Case B		
1	4.1	11.4	18.7	6.1	2.2	2.1	34.0	10.8
2	3.1	3.5	9.8	8.7	2.4	3.1	26.8	9.8
3	1.3	7.6	10.8	6.8	1.7	4.3	31.7	12.2
4	2.0	5.3	14.8	6.7	1.2	2.4	30.2	12.6
5	4.3	6.7	10.9	8.0	1.4	4.0	29.8	9.7
6	3.9	4.3	21.1	6.9	1.9	3.2	33.3	10.9
7	2.3	5.1	8.4	11.7	1.4	3.8	27.6	12.2
8	1.7	6.0	22.9	5.9	2.1	4.5	27.5	10.0
9	4.0	5.8	11.5	11.6	1.5	3.7	30.9	11.0
10	2.4	7.4	20.7	7.0	1.9	4.1	31.7	10.9
Avg.	2.91	6.31	14.96	7.94	1.77	3.52	30.35	11.01

The finite-difference time-domain (FDTD) method discussed in Chapter 2 of this work is employed due to the impossibility of resolving a scattering pattern analytically. Whereas the laser/microsphere modeling was necessarily three dimensional, it was considered suitable in this case to obtain two dimensional scattering spectra for use in a second stage radiation transport code. Equations B.1 give the form of Maxwell's equations used in the transverse magnetic (TMz) modeling environment.

$$\frac{\partial E_z}{\partial t} = \frac{1}{\varepsilon}\left(\frac{\partial H_y}{\partial x} - \frac{\partial H_x}{\partial y} - \sigma E_z\right) \tag{B.1a}$$

$$\frac{\partial H_x}{\partial t} = \frac{-1}{\mu}\left(\frac{\partial E_z}{\partial y}\right) \tag{B.1b}$$

$$\frac{\partial H_y}{\partial t} = \frac{1}{\mu}\left(\frac{\partial E_z}{\partial x}\right) \tag{B.1c}$$

where E_z is the electric field component normal to the grid, H_x and H_y are the magnetic field components paralled to the grid, σ is the magnetic conductivity of the material, and ε and μ are the electrical permittivity and magnetic permeability of the material, respectively. The Yee cell modeling geometry defines the mesh. The incident radiation signal is generated using the total field/scattered field formulation, and the Liao extrapolation absorbing boundary condition is employed at the boundary (Liao et al., 1984).

After initializing the property grids consistent with a vacuum, the abraded quartz light pipe is placed in the environment by modifying the permittivity and permeability appropriately. The values used in this effort are μ=.0005 S/m and $\varepsilon=3.9*\varepsilon_0$, where the permittivity of free space, ε_0=8.8541878e-12 F/m. The resulting property grid is shown in Figure B.1.

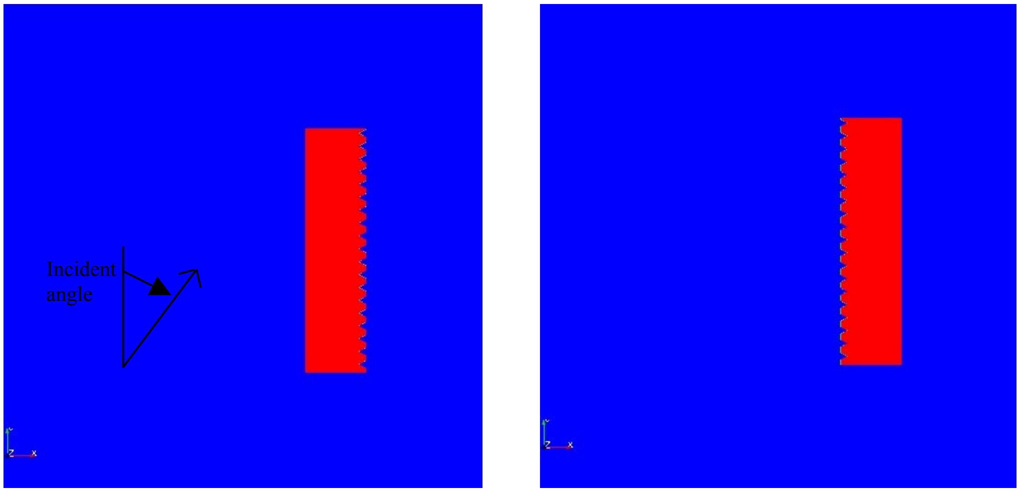

(a) (b)

Figure B.1: Abraded quartz segment in modeling environment, simulating internal radiation (a) and environment external radiation (b)

Electromagnetic plane waves of wavelength 1 μm and unit intensity were directed toward the quartz segment at incident angles of 10, 20, 30, 40, 50, 60, 70, 80, and 90 degrees (normal). As shown in Figure B.2a, the recording surface is located very close to the boundary, and the origin is taken in the center of the roughened side of the quartz. The wave is allowed to propagate until a stable scattering pattern is recorded throughout the 360 degree angle of rotation. The orientation shown corresponds to the analysis of the scattering of internal radiation, where the wave would travel through the solid quartz before interacting with the roughened outer surface. Figures B.2-B.10 give the simulation results corresponding to the setup in Figure 1a.

External scattering from micro-abrasions, i.e. the error that would be introduced due to a changing environmental temperature, is modeled by reversing the orientation of the quartz segment. The wave will then interact with the roughened surface first, as it would if entering the pipe from the outside. Figures B.11-B.19 display the results of these simulations, corresponding to the property grid in Figure B.1b.

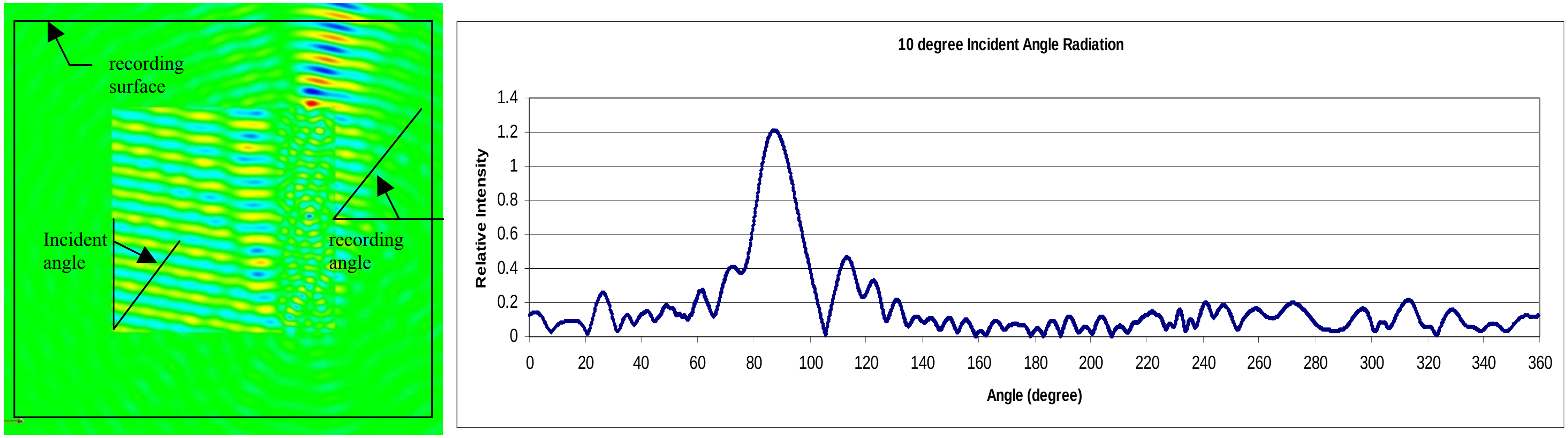

Figure B.2: Scattering pattern generated by 10 degree incident angle wave

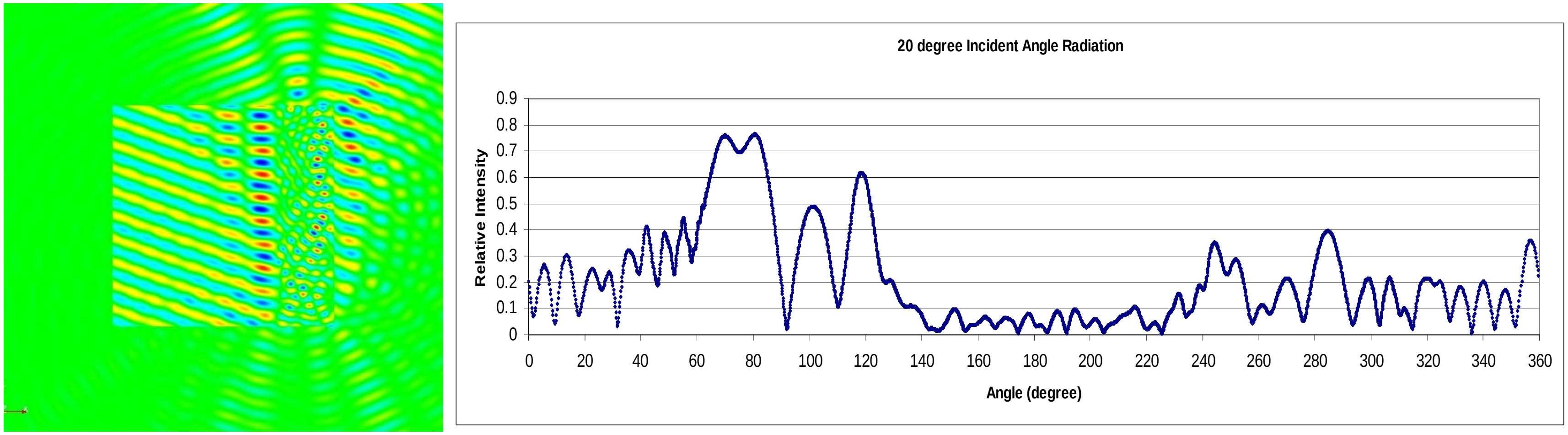

Figure B.3: Scattering pattern generated by 20 degree incident angle wave

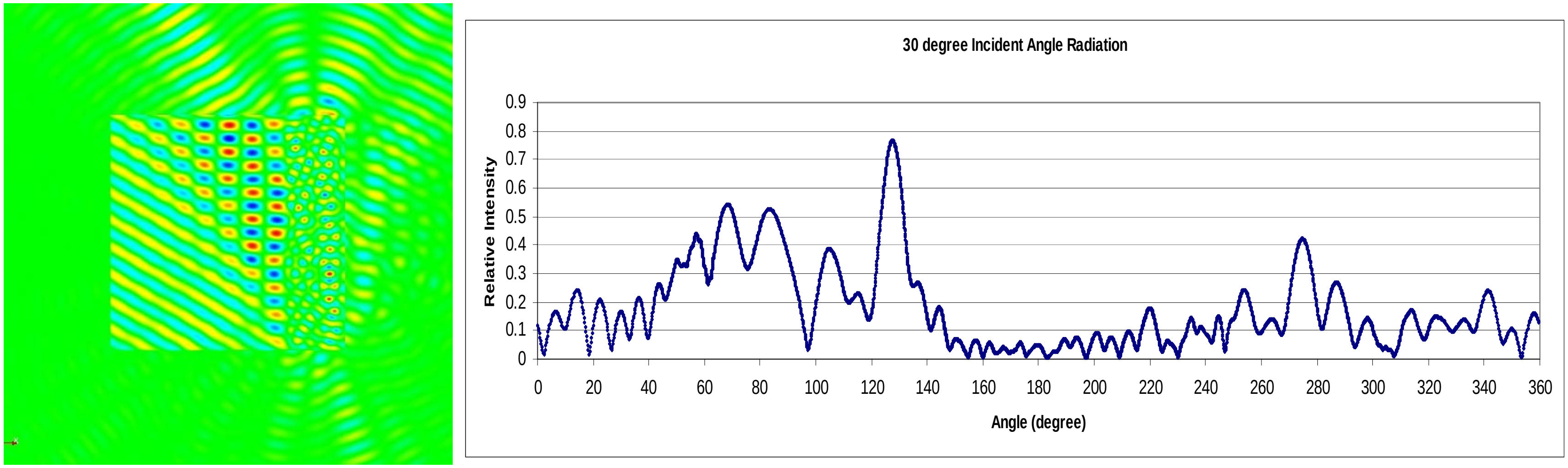

Figure B.4: Scattering pattern generated by 30 degree incident angle wave

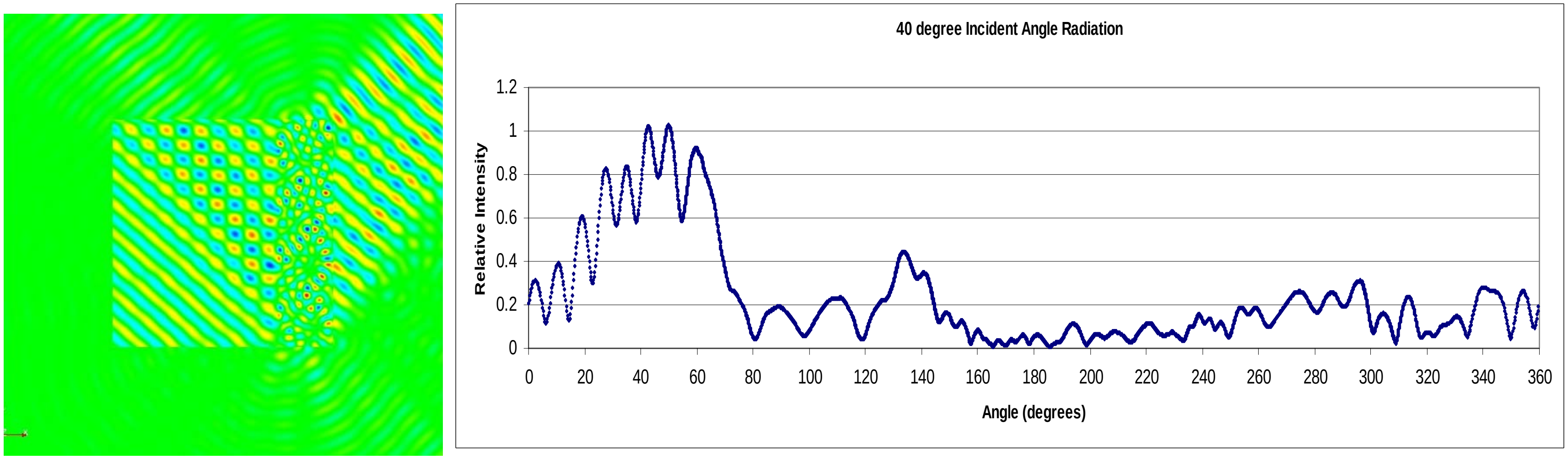

Figure B.5: Scattering pattern generated by 40 degree incident angle wave

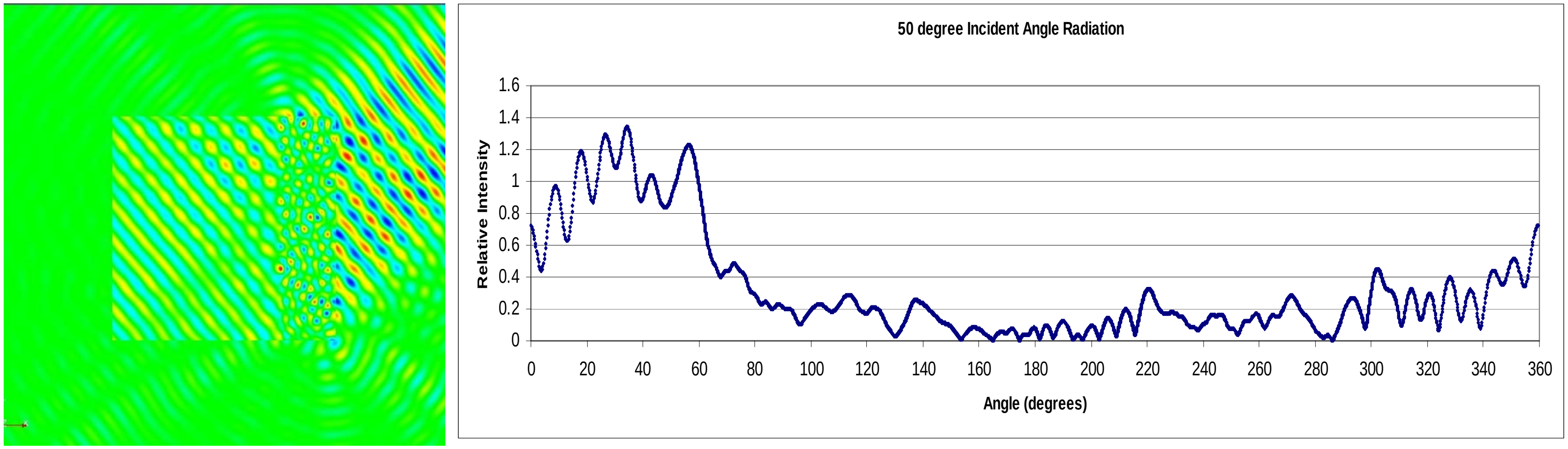

Figure 6: Scattering pattern generated by 50 degree incident angle wave

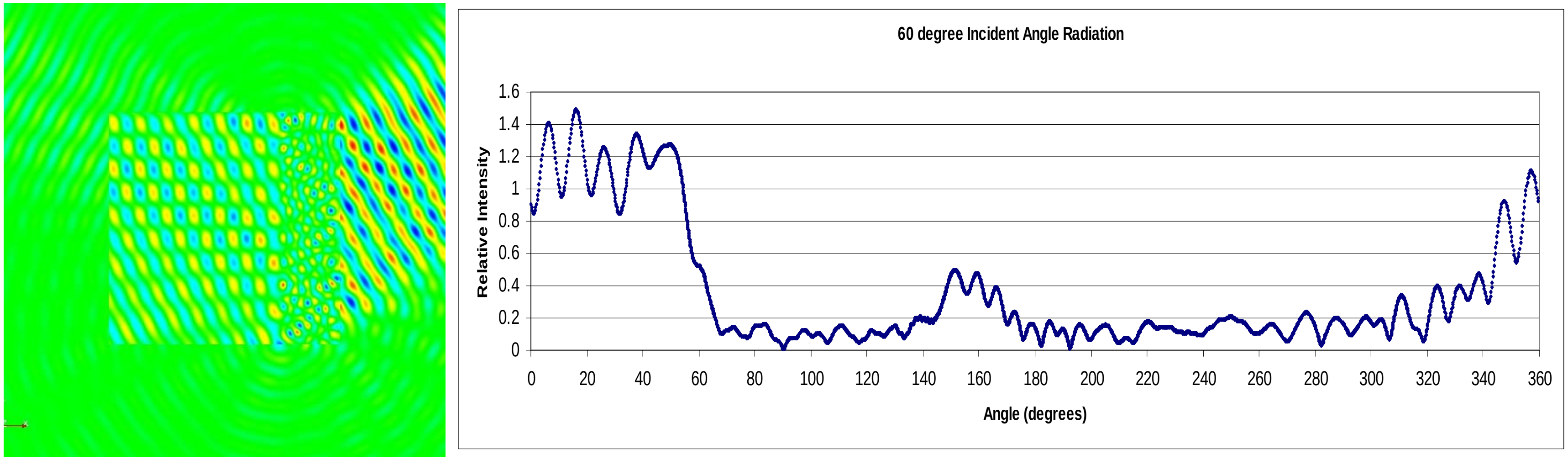

Figure 7: Scattering pattern generated by 60 degree incident angle wave

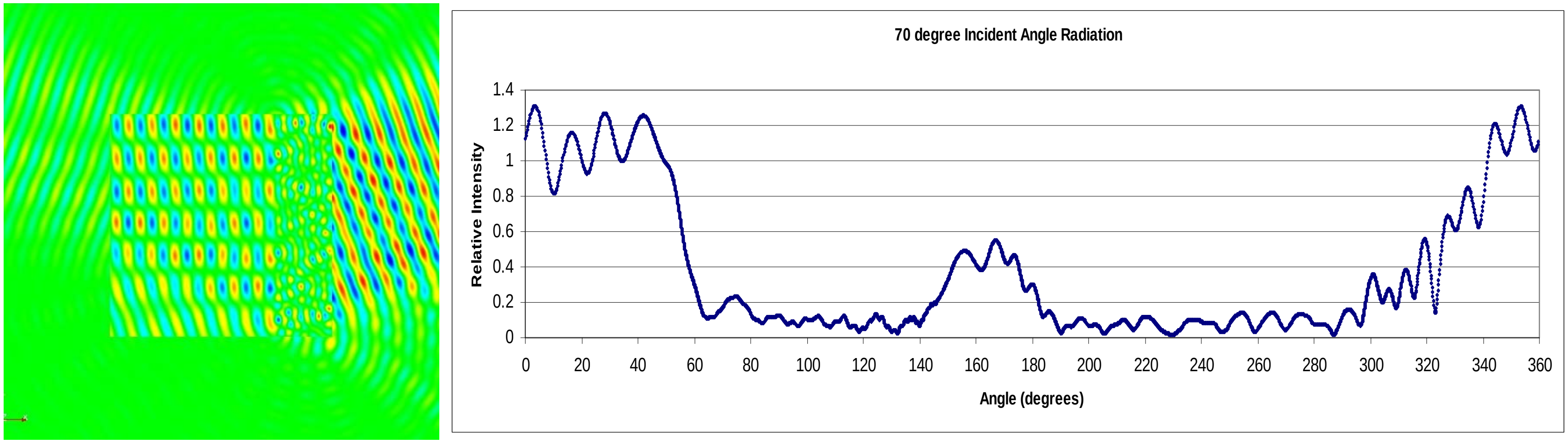

Figure 8: Scattering pattern generated by 70 degree incident angle wave

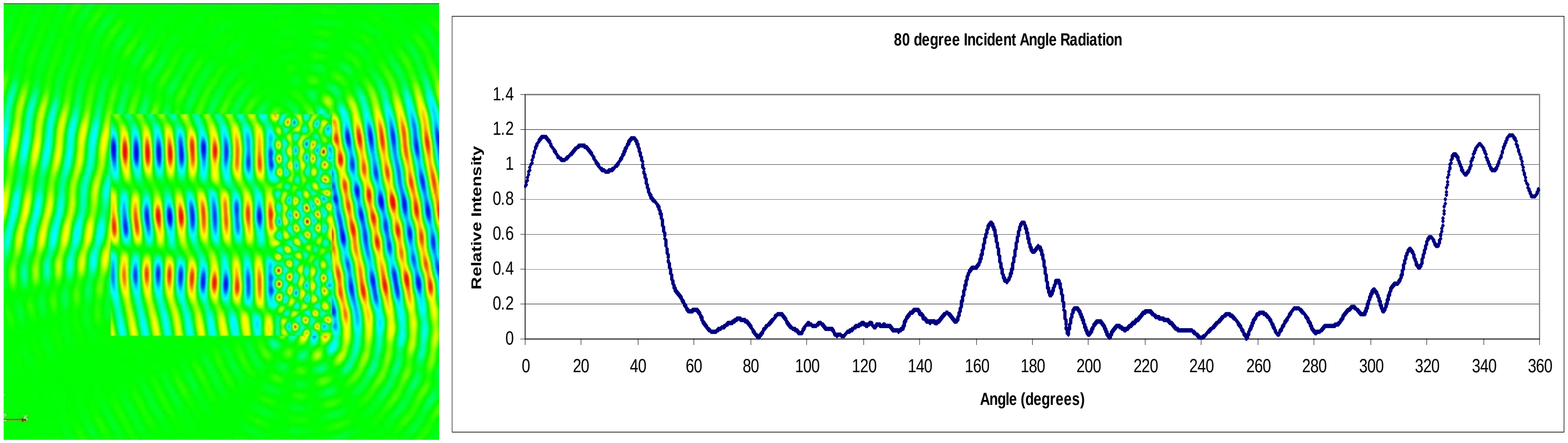

Figure 9: Scattering pattern generated by 80 degree incident angle wave

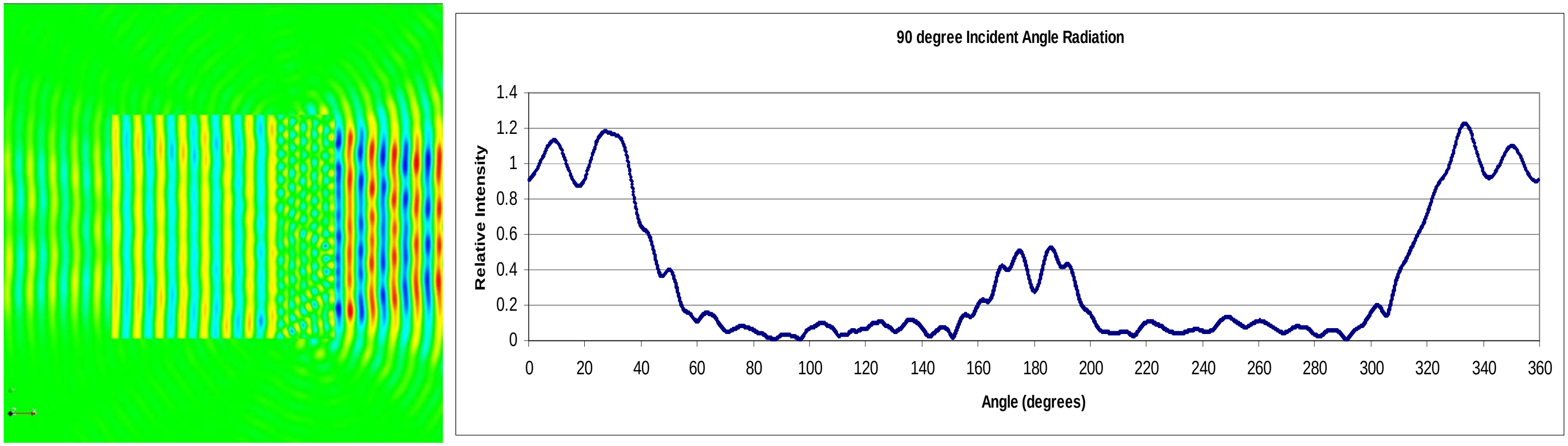

Figure 10: Scattering pattern generated by 90 degree incident angle wave

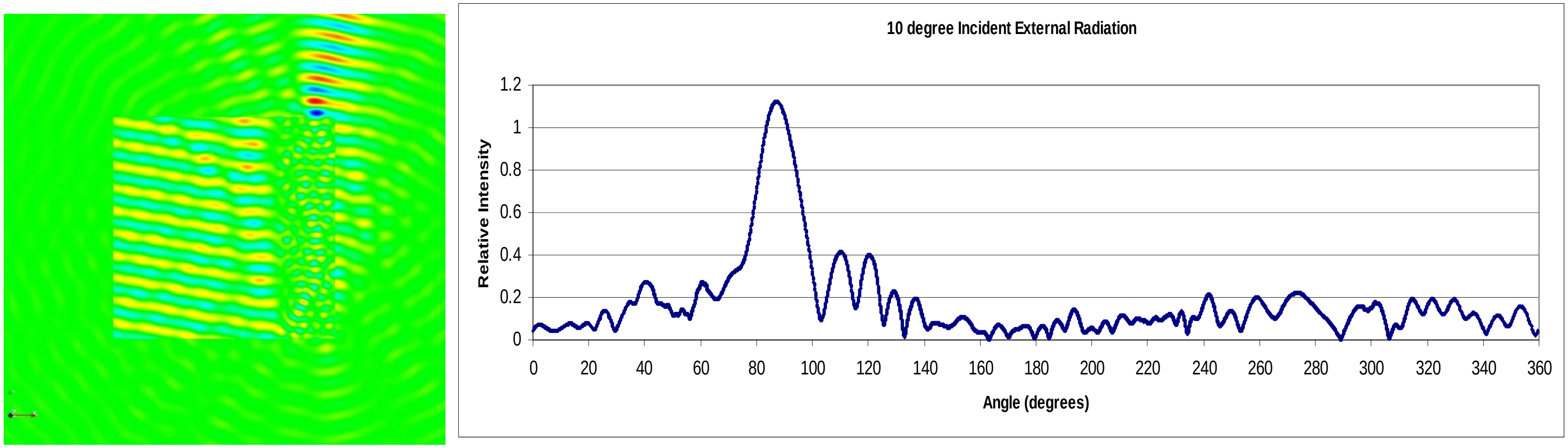

Figure 11: Scattering pattern generated by 10 degree external incident angle wave

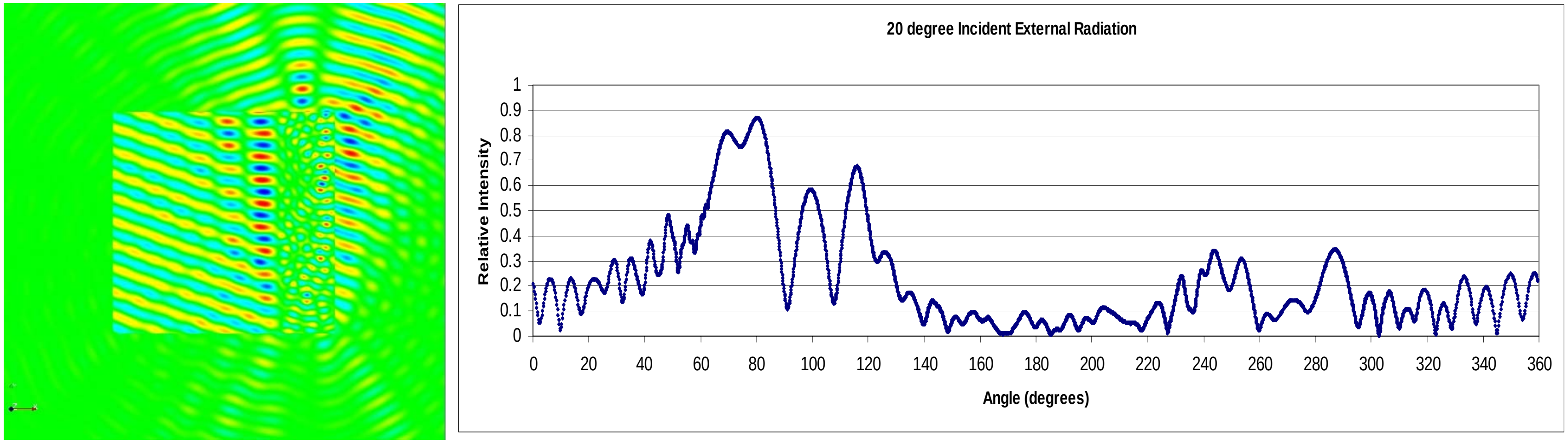

Figure 12: Scattering pattern generated by 20 degree external incident angle wave

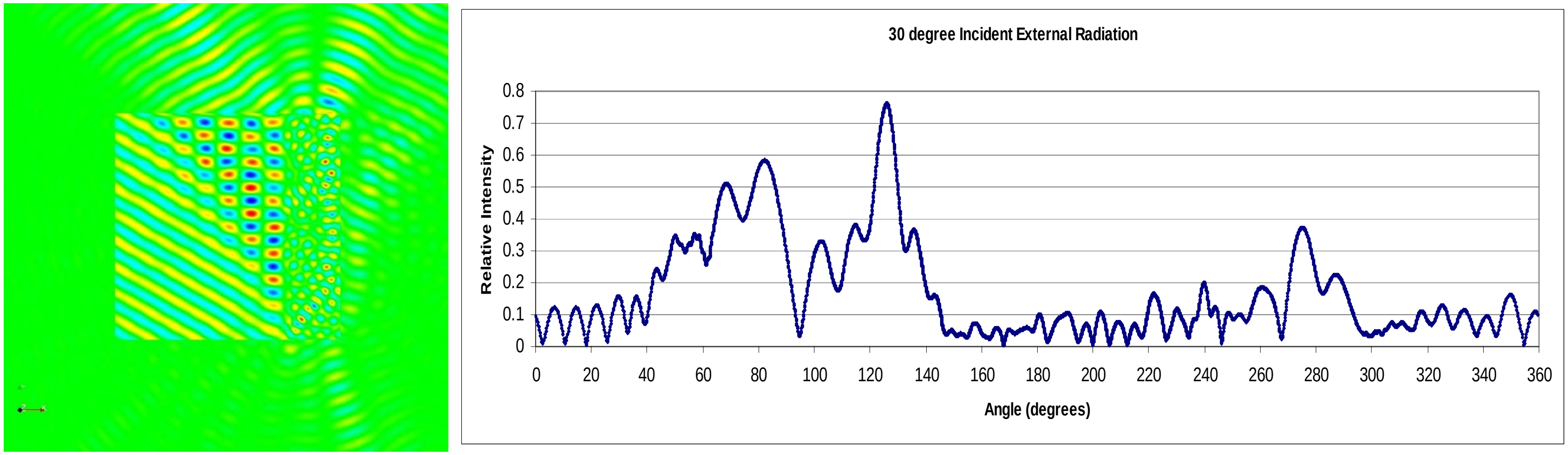

Figure 13: Scattering pattern generated by 30 degree external incident angle wave

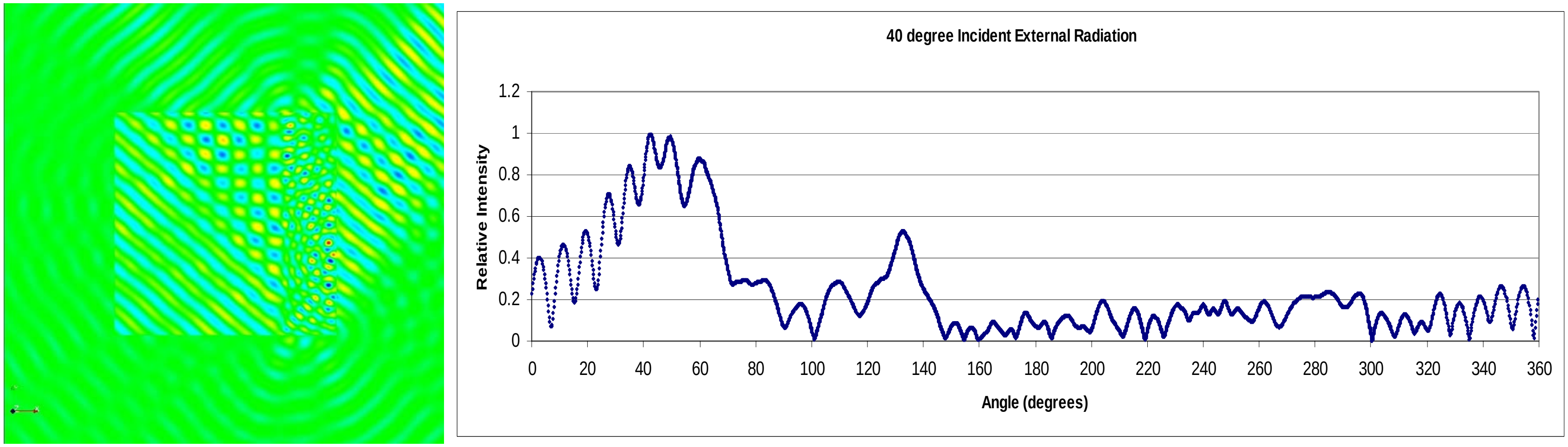

Figure 14: Scattering pattern generated by 40 degree external incident angle wave

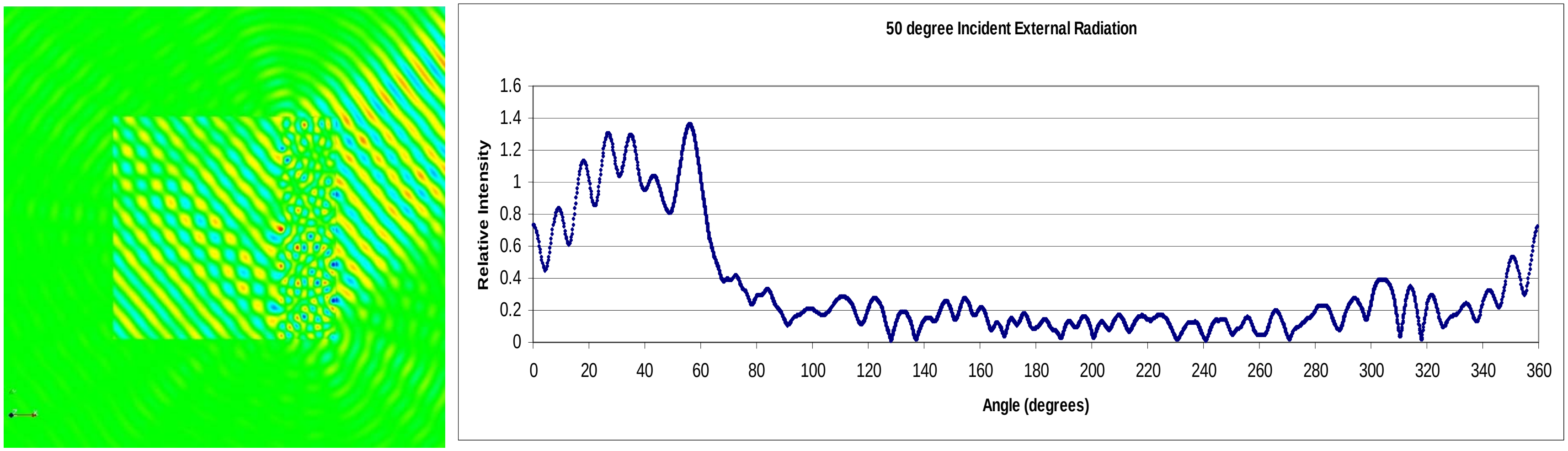

Figure 15: Scattering pattern generated by 50 degree external incident angle wave

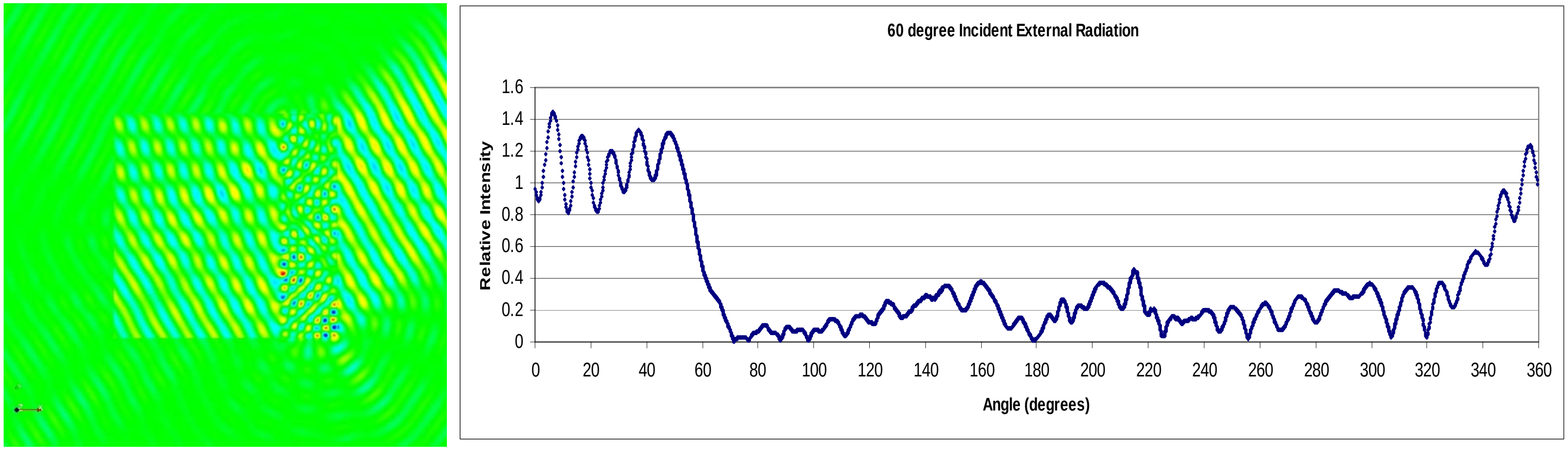

Figure 16: Scattering pattern generated by 60 degree external incident angle wave

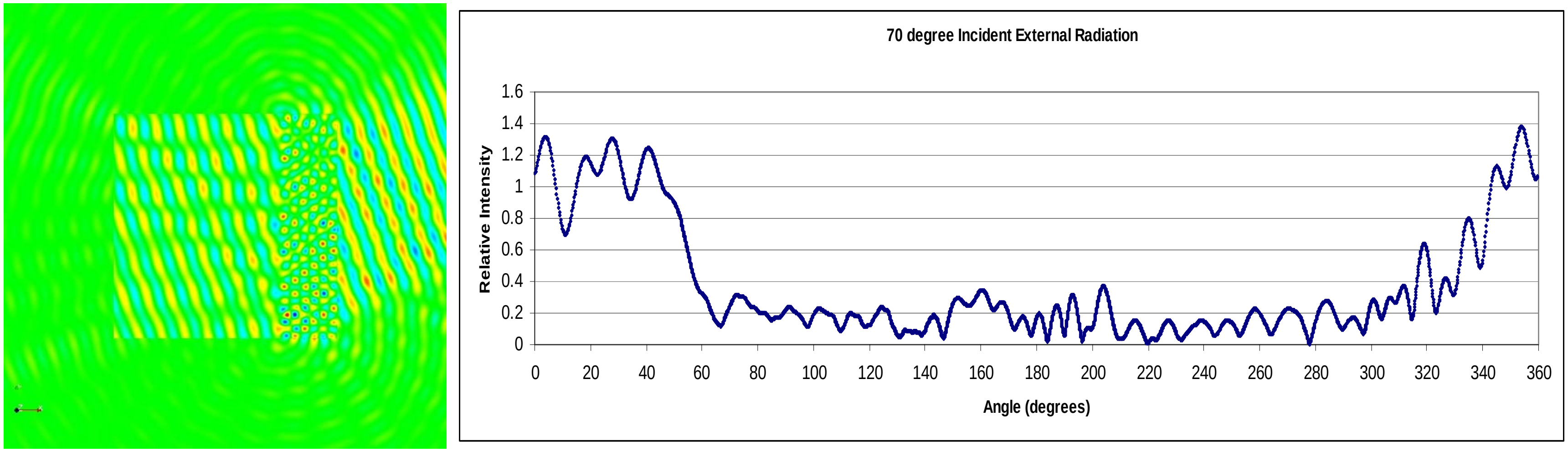

Figure 17: Scattering pattern generated by 70 degree external incident angle wave

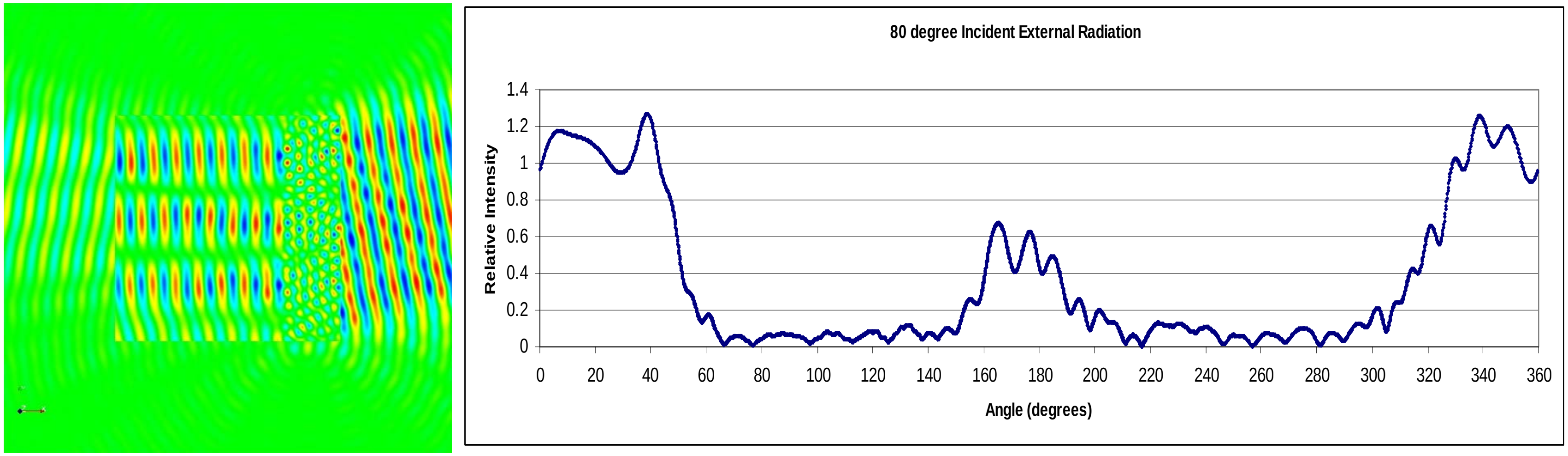

Figure 18: Scattering pattern generated by 80 degree external incident angle wave

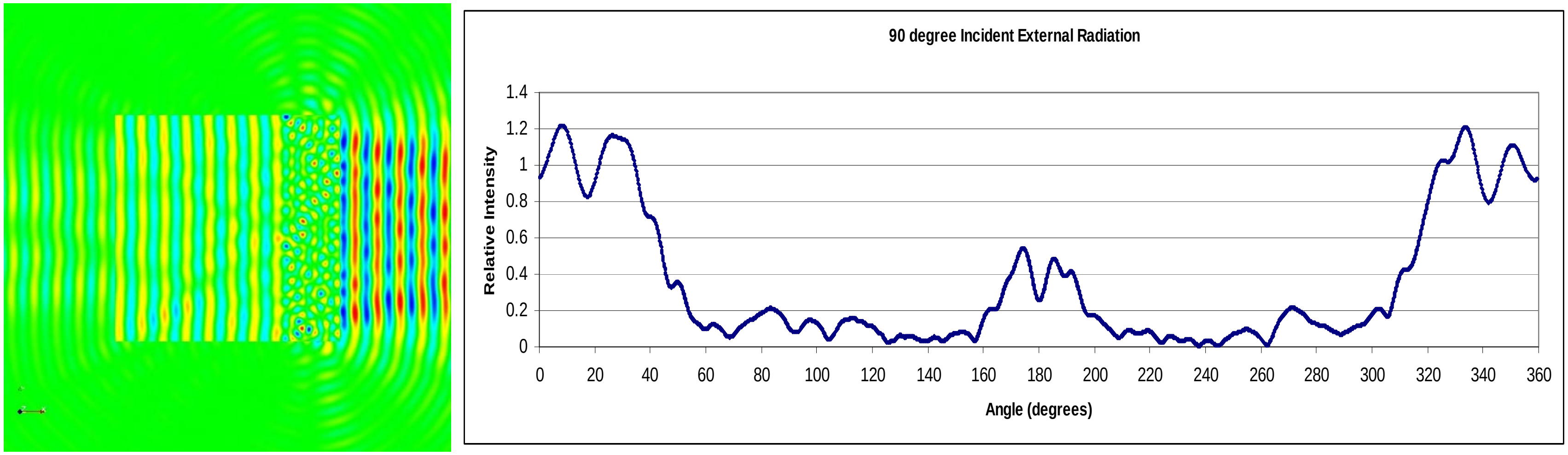

Figure 19: Scattering pattern generated by 90 degree external incident angle wave (normal to face)

B.3 Discussion

The incident plane wave is primarily transmitted at all angles, as expected through the low-loss dielectric material. An examination of Figures 2-19 reveal that the abraded surface has the largest disrupting effect at the smaller angles of incidence, primarily 20, 30 and 40 degrees. The combination of specular and diffuse scattering is apparent both visually in the electric field representations as well as quantitatively in the intensity plots. One effect of the heavy scattering at these angles is a decrease in peak transmitted intensity. Conversely, at large angles of 70, 80, and 90 degrees, the presence of grooves does little to affect the overall transmission through the quartz. The grooves do act like a diffraction grating, causing recognizable interference patterns on the recording surface. These patterns are most pronounced at angles close to normal, but are present through the whole range of incidence. At large incident angles, constructive interference and efficient transmission generate peak intensities up to 20% higher than the unit intensity of the incident wave.

The overall effect of the orientation of the quartz segment with respect to the incident wave is very small, with perhaps a slight angular shift on the dependence of the effects mentioned above. This is assumed due to the change of the incident angle as it enters the quartz, based on the refractive index of the material. The “external” simulations help describe the already known effect of environmental temperature dependence on LPRT measurement.

An increased level of accuracy would likely be obtained with a fully three-dimensional FDTD simulation, which would account for the changing groove geometry as seen by the different incident angle waves as well as the curvature of the LPRT. Other potentially useful work could include a complementary set of simulations corresponding to Figures 2-19, with undamaged, smooth quartz as the scatterer. That would allow other extraneous effects, such as near-field enhancement or geometric error due to a finite quartz segment, to be subtracted out, giving a clearer description of how the grooves alone change the scattering patterns.

Bibliography

Abramowitz, M. and Stegun, I., 1965, *Handbook of Mathematical Functions*, Dover, New York.

Adams B.E., 1999, In proceedings of *TEMPMEKO '99* (Edited by J.F. Dubbeldam, M.J. de Groot), Delft, NMi, pp. 3-10

Albrecht, M. G. and Creighton, J. A., 1977, "Anomalously Intense Raman Spectra of Pyridine at a Silver Electrode," *Journal of the American Chemical Society*, **99**, pp. 5215-5217.

Anisimov, S. I., Kapeliovich, B. L. and Perel'man, T. L., 1974, "Electron Emission from Metal Surfaces Exposed to Ultrashort Laser Pulses," *Journal of Experimental and Theoretical Physics (Russia)*, **39**, pp. 375-377.

Anisimov, S. I. and Rethfeld, B., 1997, "On the Theory of Ultrashort Laser Pulse Interaction with a Metal," *Proceedings of SPIE*, **3093**, pp. 192-203.

Balistreri, M. L. M., Gersen, H., Korterik, J. P., Kuipers, L. and Van Hulst, N. F., 2001, "Tracking Femtosecond Laser Pulses in Space and Time," *Science*, **294**, pp. 1080-1082.

Barnes, W. L., Kitson, S. C., Priest, T. W. and Sambles, J. R., 1997, "Photonic Surfaces for Surface Plasmon Polaritons," *J. of the Optical Society of America*, **14**, pp. 1654-1661.

Barnes, W. L., Dereux, A. and Ebbesen, T. W., 2003, "Surface Plasmon Subwavelength Optics," *Nature*, **424**, pp. 824-830.

Barrelet, C. J., Greytak, A. B., and Lieber, C. M., 2004, "Nanowire Photonic Circuit Elements," *Nano Letters*, **4**, pp.1981-1985.

Battula, A., Theppakuttai, S., and Chen, S., 2006, "Direct Parallel Nano-patterning of SiC by Laser Nanosphere Lithography", *Journal of Microlithography, Microfabrication, and Microsystems*, **5**, 011009.

Ben-Yakar, A., Byer, R.L., Harkin, A., Ashmore, J., Stone, H. A., Shen, M. and Mazur, E., 2003, "Morphology of Femtosecond-Laser-Ablated Borosilicate Glass Surfaces," *Applied Physics Letters*, **83**, pp. 3030-3032.

Ben-Yakar, A., Byer, R. L., 2004, "Femtosecond Laser Ablation Properties of Borosilicate Glass," *Journal of Applied Physics*, **96**, pp. 5316-5323.

Berenger, J. P., 1994, "A Perfectly Matched Layer for the Absorption of Electromagnetic Waves," *J. Computational Physics*, **114**, pp. 185-200.

Betzig, E, Harootunian, A., Lewis, A. and Isaacson, M., 1986, "Near-Field Diffraction by a Slit: Implications for Superresolution Microscopy," *Applied Optics*, **25**, pp. 1890-1900.

Bobbert, P. A., and Vlieger, J., 1987, "Light Scattering by a Sphere on a Substrate," *Physica*, **137A**, pp.209-242.

Bohren, C. and Huffman, D., 1983, *Absorption and Scattering of Light by Small Particles*, Wiley, New York, NY.

Bommeli, F., Degiorgi, L., Wachter, P., Bacsa, W. S., de Heer, W.A., and Forro, L., 1996, "Evidence of Anisotropic Metallic Behaviour in the Optical Properties of Carbon Nanotubes," *Solid State Communications*, **99**, pp. 513-517.

Born, M. and Wolf, E., 1999, *Principles of Optics*, 7th ed., Cambridge University, Cambridge, England.

Bursill, L. A., Stadelmann, P. A., Peng, J. L., and Prawer, S., 1994, "Surface Plasmon Observed for Carbon Nanotubes," *Physical Review B*, **49**, pp. 2882-2887.

Campbell, S., Dear, F. C., Hand, D. P. and Reid, D. T., 2005, "Single-Pulse Femtosecond Laser Machining of Glass," *Journal of Optics A*, **7**, pp. 162-168.

Carminati, R. and Greffet, J., 1999, "Near-Field Effects in Spatial Coherence of Thermal Sources," *Physical Review Letters*, **82**, pp. 1660-1663.

Chan, C. L. and Mazumder, J., 1987, "One-Dimensional Steady-State Model for Damage by Vaporization and Liquid Expulsion Due to Laser-Material Interaction," *Journal of Applied Physics*, **62**, pp. 4579-4586.

Chevalier, N., Nasse, M. J., Woehl, J. C., Reiss, P., Bleuse, J., Chandezon, F. and Huant, S., 2005, "CdSe Single-Nanoparticle Based Active Tips for Near-Field Optical Microscopy," *Nanotechnology*, **16**, pp. 613-618.

Chimmalgi, A., Grigoropoulos, C. P. and Komvopoulos, K., 2005, "Surface Nanostructuring by Nano-/Femtosecond Laser-Assisted Scanning Force Microscopy," *Journal of Applied Physics*, **97**, 104319.

Cohen, G., and Monk, P., 1998, "Gauss Point Mass Lumping Schemes for Maxwell's Equations," *Numerical Methods for Partial Differential Equations*, **14**, pp. 63-88.

Cotton, T. M., Kim, Jae-Ho and Chumanov, G. D., 1991, "Application of Surface-Enhanced Raman Spectroscopy to Biological Systems," *Journal of Raman Spectroscopy*, **22**, pp. 729-742.

Dickson, R. M. and Lyon, L. A., 2000, “Unidirectional Plasmon Propagation in Metallic Nanowires,” *Journal of Physical Chemistry B,* **104**, pp. 6095-6098.

Ditlbacher, H., Krenn, J. R., Felidj, N., Lamprecht, B., Schider, G., Salerno, M., Leitner, A. and Aussenegg, F. R., 2002, “Fluorescence Imaging of Surface Plasmon Fields,” *Applied Physics Letters*, **80**, pp. 404-406.

Ditlbacher, H., Hohenau, A., Wagner, D., Kreibig, U., Rogers, M., Hofer, F., Aussenegg, F. R., and Krenn, J. R., 2005, “Silver Nanowires as Surface Plasmon Resonators,” *Physical Review Letters*, **95**, 257403.

Draine, B. and Flatau, P. J., 1994, "Discrete-dipole approximation for scattering calculations," *Journal of Optical Society of America A*, **11**, pp. 1491-1499.

Ebbesen, T. W., and Ajayan, P. M., 1992, “Large Scale Synthesis of Carbon Nanotubes,” *Nature*, **358**, pp. 220-222.

Ebbesen, T. W., Lezec, H. J., hiura, H., Bennett, J. W., Ghaemi, H. F., and Thio, T., 1996, “Electrical Conductivity of Individual Carbon Nanotubes,” *Nature*, **382**, pp. 54-56.

Fang, N., Lee, h., Sun, C. and Zhang, X., 2005, “Sub-Diffraction-Limited Optical Imaging with a Silver Superlens,” *Science*, **308**, pp. 534-537.

Fischer, U., Duerig, U. and Pohl, D., 1988, “Near-Field Optical Scanning Microscopy in Reflection,” *Applied Physics Letters*, **52**, pp. 249-251.

Fleischman, M., Hendra, P. J. and McQuillan, A. J., 1974, “Raman Spectra of Pyridine Absorbed at a Silver Electrode,” *Chemical Physics Letters*, **26**, pp. 163-166.

Gao, B., Chen, Y. F., Fuhrer, M. S., Glattli, D. C., and Bachtold, A., 2005, “Four-Point Resistance of Individual Single-Wall Carbon Nanotubes,” *Physical Review Letters*, **95**, 196802.

Gedney, S. D., 1996, “An Anisotropic PML Absorbing Media for FDTD Simulation of Fields in Lossy Dispersive Media,” *Electromagnetics*, **16**, pp. 399-415.

Gedney, S. D., Liu, G., Roden, J. A. and Zhu, A., 2001, “Perfectly Matched Layer Media with CFS for an Unconditionally Stable ADI-FDTD Method,*” IEEE Trans. Antennas Propagat*., **49**, pp. 1554-1559.

Girard, C., 2005, “Near Fields in Nanostructures,” *Reports on Progress in Physics*, **68**, pp. 1883-1933.

Girard, C. and Dereux, A., 1996, “Near-Field Optics Theories,” *Reports on Progress in Physics*, **59**, pp. 657-699.

Goodson, K. E., Asheghi, M., 1997, “Near-Field Optical Thermometry,” *Microscale Thermophysical Engineering*, **1**, pp. 225-235.

Gorbunov, A.A., and Pompe, W., 1994, ”Thin Film Nanoprocessing by Laser/STM Combination,” *Phys. Stat. Sol. (A)*, **145**, pp. 333–338.

Grand, J., de la Chapelle, M.L., Bijeon, J.-L., Adam, P.-M., Vial, A., Royer, P., 2005, "Role of localized surface plasmons in surface-enhanced Raman scattering of shape-controlled metallic particles in regular arrays", *Physical Review B*, **72,** 33407/1-4.

Gray, S. K. and Kupka, T., 2003, “Propagation of Light in Metallic Nanowire Arrays: Finite-Difference Time-Domain Studies of Silver Cylinders,” *Physical Review B*, **68**, 045415.

Greytak, A. B., Barrelet, C. J., Li, Y., and Lieber, C. M., 2005, "Semiconductor Nanowire Laser and Nanowire Waveguide Electro-optic Modulators," *Applied Physics Letters*, **87**, 151103.

Guest, J. R., Stievater, T. H., Chen, G., Tabak, E. A., Orr, B. G., Steel, D. G., Gammon, D. and Katzer, D. S., 2001, “Near-Field Coherent Spectroscopy and Microscopy of a Quantum Dot System,” *Science*, **293**, pp. 2224-2227.

Hao, E., and Schatz, G., 2004, “Electromagnetic Fields Around Silver Nanoparticles and Dimers,” *Journal of Chemical Physics*, **120**, pp. 357-366.

Heltzel, A., Theppakuttai, S., Howell, J. R., and Chen, S. C., 2005. “Analytical and Experimental Investigation of Laser-Microsphere Interaction for Nanoscale Surface Modification,” *Journal of Heat Transfer*, **127**, pp. 1231-1235.

Heltzel, A., Theppakuttai, S., Chen, S. C., and Howell, J. R., 2006, “Excitation of Surface Plasmons with Gold Microspheres,” Proceedings of AIAA/ASME Joint Heat Transfer Conference, San Francisco.

Heltzel, A., Battula, A., Chen, S. C. and Howell, J. R., 2007, “Nanostructuring Borosilicate Glass with Near-Field Enhanced Energy Using a Femtosecond Laser Pulse,” *Journal of Heat Transfer*, accepted for publication.

Henry, C. H. and Hopfield, J. J., 1965, “Raman Scattering by Polaritons,” *Physical Review Letters*, **15**, pp. 964-966.

Hirano, M., Kawamura, K. I., Hosono, H., 2002, "Encoding of holographic grating and periodic nanostructure by femtosecond laser pulse," *Applied Surface Science,* **197**, pp. 688-698.

Ho, J. R., Grigoropoulos, C. P. and Humphrey, J. A. C., 1995, "Computational Study of Heat Transfer and Gas Dynamics in the Pulsed Laser Evaporation of Metals," *Journal of Applied Physics*, **78**, pp. 4696-4709.

Holway, L. H. and Fradin, D. W., 1974, "Electron Avalanche Breakdown by Laser Radiation in Insulating Crystals," *Journal of Applied Physics*, **46**, pp. 279-291.

Homola, J., Yee, S. S. and Gauglitz, G., 1999, "Surface Plasmon Resonance Sensors: Review," *Sensors and Actuators B*, **54**, pp. 3-15.

Huang, S. M., Hong, M. H., Luk'yanchuk, B. S., Zheng, Y. W., Song, W. D., Lu, Y. F., and Chong, T. C., 2002, "Pulsed Laser-Assisted Surface Structuring with Optical Near-Field Enhanced Effects," *Journal of Applied Physics*, **92**, pp. 2495-2500.

Hull, R., 1999, "Properties of Crystalline Silicon," INSPEC publication, London.

Hutter, E., and Fendler, H., 2004, "Exploitation of localized surface plasmon resonance", *Advanced Materials*, **16,** pp.1685-1706.

Jeanmaire, D. L. and Duyne, R. P. V., 1977, "Surface Raman Spectroelectrochemistry Part I. Heterocyclic, Aromatic, and Aliphatic Amines Adsorbed on the Anodized Silver Electrode," *Journal of Electroanalytical Chemistry*, **84**, pp. 1-20.

Jellison, G.E. and Lowndes, D.H., 1982, "Optical Absorption Coefficient of Silicon at 1.152 µm at Elevated Temperatures." *Applied Physics Letters*, **41**, pp. 594-596.

Jeon, T-I., Kim, K-J., Kang, C., Mang, I. H., Son, J-H., An, K. Y., Lee, J. Y., and Lee, Y. H., 2004, "Optical and Electrical Properties of Preferentially Anisotropic Single-Walled Carbon-Nanotube Films in Terahertz Region," *Journal of Applied Physics*, **95**, pp. 5736-5740.

Jersch, J., and Dickmann, K., 1996, "Nanostructure Fabrication Using Laser Field Enhancement in the Near Field of a Scanning Tunneling Microscope Tip," *Applied Physics Letters*, **68**, pp. 868-870.

Jiang, L. and Tsai, H. L., 2005, "Energy Transport and Material Removal in Wide Bandgap Materials by a Femtosecond Laser Pulse," *International Journal of Heat and Mass Transfer*, **48**, pp. 487-499.

Johnson, P. B., and Christy, R. W., 1972, "Optical Constants of Noble Metals," Physical Review B, 6, pp. 4370-4379.

Kaganov, M. I., Lifshitz, I. M. and Tantarov, L. V., 1957, "Relaxation Between Electrons and Crystalline Lattices," *Journal of Experimental and Theoretical Physics (Russia)*, **4**, pp. 173-178.

Kautek, W., Kruger, J., Lenzner, M., Sartania, S., Spielmann, Ch. And Krausz, F., 1996, "Laser Ablation of Dielectrics with Pulse Durations Between 20 fs and 3 ps," *Applied Physics Letters*, **69**, pp. 3146-3148.

Ki, H. and Mazumder, J., 2005, "Numerical Simulation of Femtosecond Laser Interaction with Silicon," *Journal of Laser Applications*, **17**, pp. 110-117.

Kik, P. G., Martin, A. L., Maier, S. A. and Atwater, H. A., 2002, "Metal Nanoparticle Arrays for Near-Field Optical Lithography," *Proceedings of SPIE*, 4810.

Kitson, S. C., Barnes, W. L., Sambles, J. R., 1996, "Full Photonic Band Gap for Surface Modes in the Visible," *Physical Review Letters*, **77**, 2670-2673.

Klar, T.A., Perner, M., Grosse, S., Plessen, G., Spirkl, W., and Feldmann, J., 1998, "Surface-plasmon resonances in single metallic particles", *Physical Review Letters*, **80,** pp.4249-4252.

Kneipp, K., Kneipp, H., Kartha, V. B., Manoharan, R., Deinum, G., Itzkan, I., Dasari, R. R. and Feld, M. S., 1998, "Detection and Identification of a Single DNA Base Molecule Using Surface-Enhanced Raman Scattering (SERS)," *Physical Review E*, **57**, pp. R6281-R6284.

Kneipp, K., Kneipp, H., Itzkan, I. Dasari, R. R. and Feld, M. S., 1999, "Surface-Enhanced Raman Scattering and Biophysics," *Journal of Physics: Condensed Matter*, **14**, pp. 597-624.

Kneipp, K., Kneipp, H., Corio, P., Brown, S. D. M., Shafer, K., Motz, J., Perleman, L. T., Hanlon, E. B., Marucci, A., Dresslehaus, G. and Dresselhaus, M. S., 2000, "Surface-Enhanced and Normal Stokes and Anti-Stokes Raman Spectroscopy of Single-Walled Carbon Nanotubes," *Physical Review Letters*, **84**, pp. 3470-3473.

Krenn, J. R., Dereux, A. Weeber, J. C., Bourillot, Lacroute, Y., Goudonnet, J. P., Schider, G., Gotschy, W., Leitner, A., Aussenegg, F. R. and Girard, C., 1999, "Squeezing the Optical Near-Field Zone by Plasmon coupling of Metallic Nanoparticles," *Physical Review Letters*, **82**, pp. 2590-2593.

Krenn, J. R., Lamprecht, B., Ditlbacher, H., Schider G., Salerno, M., Leitner, A. and Aussenegg, F. R., 2002, “Non-Diffraction Limited Light Transport by Gold Nanowires,” *Europhysics Letters*, **60**, pp. 663-669.

Krug, J. T., Sanchez, E. J. and Xie, X., S., 2002, “Design of Near-Field Optical Probes with Optimal Field Enhancement by Finite Difference Time Domain Electromagnetic Simulation,” *Journal of Chemical Physics*, **116**, pp. 10895-10901.

Kuwata, H., Tamaru, H., Esumi, K. and Miyano, K., 2003, “Resonant Light Scattering from Metal Nanoparticles: Practical Analysis Beyond Rayleigh Approximation,” *Applied Physics Letters*, **83**, pp. 4625-4627.

Lenzner, M., Kruger, J., Sartania, S., Cheng, Z., Spielmann, Ch., Mourou, G., Kautek, W. and Krausz, F., 1998, “Femtosecond Optical Breakdown in Dielectrics,” *Physical Review Letters*, **80**, pp. 4076-4079.

Levine, H. and Schwinger, J., 1950, “On the Theory of Electromagnetic Wave Diffraction by an Aperture in an Infinite Plane Conducting Screen,”*Communications on Pure and Applied Mathematics*, **3**, pp. 335-391.

Liao, Z. P., Wong, B. P., Yang, B. P. and Yuan, Y. F., 1984, “A Transmitting Boundary for Transient Wave Analyses,” *Scientia Sinica A*, **27**, pp. 1063-1076.

Loomis, J. J. and Maris, H. J., 1994, “Theory of Heat Transfer by Evanescent Electromagnetic Waves,” *Physical Review B*, **50**, pp. 517-524.

Lovas F.J., Tsai B.K., Gibson C.E., 1998, *Mat. Res. Soc. Symp. Proc*., Vol. 525 (Edited by Ozturk, Roozeboom, Timans, Pas), San Francisco, MRS, pp. 127-133.

Lowan, A., et al. 1945, *Tables of Associated Legendre Functions*, Columbia University Press, New York.

Lu, Q., Rao, R., Sadanadan, B., Que, W., Rao, A. M., and Ke, P. C., 2005, “Coupling of Photon Energy Via a Multiwalled Carbon Nanotube Array,” *Applied Physics Letters*, **87**, 173102.

Lu, Y. and Chen, S. C., 2003, “Nanopatterning of a Silicon Surface by Near-Field Enhanced Laser Irradiation,” *Nanotechnology*, **14**, pp. 505-508.

Lu, Y., Theppakuttai, S., Chen, S.C., 2003, “Marangoni effect in nanosphere-enhanced laser nanopatterning of silicon,” *App. Phys. Lett.*, **82**, 4143.

Lu, Y. F., Mai, Z. H., Qiu, G., and Chim, W. K., 1999, “Laser-Induced Nano-Oxidation on Hydrogen-Passivated Ge (100) Surfaces Under a Scanning Tunneling Microscope Tip,” *Applied Physics Letters*, **75**, pp. 2350-2361,

Luoa, X., and Ishihara, T., 2004, "Surface plasmon resonant interference nanolithography technique", *Applied Physics Letters*, **84**, pp. 4780-4782.

Lynch, D. W., and Hunter, W. R., 1985, in: E.D. Palik (Ed.), *Handbook of Optical Constants of Solids*, Academic Press, New York, p. 350.

Maier, S. A., Brongersma, M. L., Kik, P. G. and Atwater, H. A., 2002, “Observation of Near-Field Coupling in Metal Nanoparticle Chains Using Far-Field Polarization Spectroscopy,” *Physical Review B*, **65**, 193408.

Maier, S. A., Kik, P. G. and Atwater, H. A., 2003a, “Optical Pulse Propagation in Metal Nanoparticle Chain Waveguides,” *Physical Review B*, **67**, 205402.

Maier, S. A., Kik, P. G., Atwater, H. A., Meltzer, S., Harel, E., Koel, B. E., Requicha, A. A. G., 2003b, “Local Detection of Electromagnetic Energy Transport Below the Diffraction Limit in Metal Nanoparticle Plasmon Waveguides,” *Nature Materials*, **2**, pp. 229-232.

Maier, S. A. and Atwater, H. A., 2005a, “Plasmonics: Localization and Guiding of Electromagnetic Energy in Metal/Dielectric Structures,” *Journal of Applied Physics*, **98**, 011101.

Maier, S. A., Friedman, M. D., Barclay, P. E., Painter, O., 2005b, “Experimental Demonstration of Fiber-Accessible Metal Nanoparticle Plasmon Waveguides for Planar Energy Guiding and Sensing,” *Applied Physics Letters*, **86**, 071103.

Martin, O. J. F. and Paulus, M., 2002, “Influence of Metal Roughness on the Near-Field Generated by an Aperture/Apertureless Probe,” *Journal of Microscopy*, **205**, pp. 147-152.

Maurer, M. J., 1969, “Relaxation Model for Heat Conduction in Metals,” *Journal of Applied Physics*, **40**, pp. 5123-5130.

Meyer, C., 2001, “Effects of Extraneous Radiation on the Performance of Lightpipe Radiation Thermometers,” National Institute of Standards and Technology (NIST), www.cstl.nist.gov/div836/836.05/papers/Meyer01TEMPMEKO_LRPTs.pdf

Mie, G., 1908, “Bietrage zur Optik Truber Medien Speziell Kolloidaler Metallosungen,” *Annals of Physics*, **25**, pp. 377-445.

Milster, T., 2001, “Near-Field Optical Data Storage: Avenues for Improved Performance,” *Optics Engineering*, **40**, pp. 2255-2260.

Mullin, D., Spajer, M., Courjon, D., Carcenac, F. and Chen, Y., 2000, “Near-Field Probing Control of Optical Propagation in Bidimensional Guiding Mesostructures,” *Journal of Applied Physics*, **87**, pp. 534-537.

Mur, G., 1981, “Absorbing Boundary Conditions for the Finite-Difference Approximation of the Time-Domain Electromagnetic Field Equations,” *IEEE Trans. Electromagn. Compat*., **23**, pp. 377-382.

Murray, W. A., Astilean, S. and Barnes, W. L., 2004, “Transition from Localized Surface Plasmon Resonance to Extended Surface Plasmon-Polariton as Metallic Nanoparticles Merge to Form a Periodic Hole Array,” *Physical Review B*, **69**, 165407.

Nahm, K. B., and Wolfe, W. L., 1986, “Light-Scattering Models for Spheres on a Conducting Plane: Comparison with Experiment,” *Applied Optics*, **26**, pp. 2995-2999.

Nikumb, S., Chen, Q., Li, C., Reshef, H., Aheng, H. F., Qiu, H., Low, D., 2005, “Precision glass machining, drilling and profile cutting by short pulse Lasers,” *Thin Solid Films*, **477(1-2)**, pp. 216-221.

Olstad, R. A. and Olander, D. R., 1975, “Evaporation of Solids by Laser Pulses. I. Iron,” *Journal of Applied Physics*, **46**, pp. 1499-1508.

Olstad, R. A. and Olander, D. R., 1975, “Evaporation of Solids by Laser Pulses. II. Zirconium Hydride,” *Journal of Applied Physics*, **46**, pp. 1509-1518.

Otto, A., 1968, “Exitation of Nonradiative Surface Plasma Waves in Silver by the Method of Frustrated Total Reflection,” *Zeitschrift fur Physik*, **216**, p. 398.

Oubre, C. and Norlander, P., 2004, “Optical Properties of Metallodielectric Nanostructures Calculated Using the Finite Difference Time Domain Method,” *Journal of Physical Chemistry B*, **108**, pp. 17740-17747.

Ozbay, E., 2006, “Plasmonics: Merging Photonics and Electronics at Nanoscale Dimensions.” *Science*, **311**, pp. 189-193.

Park, D. S., Cho, M. W., Lee, H., Cho, W. S., 2004, “Micro-grooving of glass using micro-abrasive jet machining,” *Journal of Materials Processing Technology*, **146**, pp. 234-240.

Pendry, J. B., 1999, “Radiative Exchange of Heat Between Nanostructures,” *Journal of Physics: Condensed Matter*, **11**, pp. 6621-6633.

Pendry, J. B., 2000, "Negative Refraction Makes a Perfect Lens," *Physical Review Letters*, **85,** pp. 3966-3969.

Perez, R., and Que, W., 2006, "Plasmons in Isolated Single-Walled Carbon Nanotubes," *Journal of Physics: Condensed Matter*, **18**, pp. 3197-3216.

Perry, M. D., Stuart, B. C., Banks, P. S., Feit, M. D., Yanovsky, V. and Rubenchik, A. M., 1999, "Ultrashort-Pulse Laser Machining of Dielectric Materials," *Journal of Applied Physics*, **85**, pp. 6803-6810.

Pronko, P. P., VanRompay, P. A., Singh, R. K., Qian, F., Du, D. and Liu, X., 1996, "Laser Induced Avalanche Ionization and Electron-Lattice Heating of Silicon with Intense Near IR Femtosecond Pulses," *Materials Research Society Symposium Proceedings*, **397**, pp. 45-51.

Puttitwong, E., 2005, personal conversation, The University of Texas at Austin.

Qiu, T. Q. and Tien, C. L., 1993, "Heat Transfer Mechanisms During Short-Pulse Laser Heating of Metals," *Journal of Heat Transfer*, **115**, pp. 835-841.

Raether, H., *Surface plasmons*, Springer, Berlin, 1988.

Reddick, R. C., Warmack, R. J. and Ferrell, T. L., 1989, "New Form of Scanning Optical Microscopy," *Physical Review B*, **39**, pp. 767-770.

Ritchie, R. H., 1957, "Plasma Losses by Fast Electrons in Thin Films," *Physical Review*, **106**, pp. 874-881.

Roden, J. A. and Gedney, S. D., 2000, "Convolutional PML (CPML): An Efficient FDTD Implementation of the CFS-PML for Arbitrary Media," *Microwave Optical Tech. Letters*, **27**, pp. 334-339.

Rylander, T., and Bondeson, A., 2000, "Stable FDTD-FEM Hybrid Method for Maxwell's Equations," *Computational Physics Communications*, **125**, pp. 75-82.

Safanov, V. P., Shalaev, v. M., Markel, V. A., Danilova, Y. E., Lepeshkin, N. N., Kim, W., Rautian, S. G. and Armstrong, R. L., 1998, "Spectral Dependence of Selective Photomodification in Fractal Aggregates of Colloidal Particles," *Physical Review Letters*, **80**, pp. 1102-1105.

Sambles, J. R., Bradbery, G. W. and Fang, F. Z., 1991, "Optical Excitation of Surface Plasmons-an Introduction," *Contemporary Physics*, **32**, pp. 173-183.

Shao, D.B. and Chen, S.C., 2005, “Surface Plasmon Assisted Nanoscale Photolithography,” *Applied Physics Letters*, **86**, pp 2531071-2531073.

Sirbuly, D. J., Law, M., Pauzauskie, P., Yan, H., Maslov, A. V., Knutsen, K., Ning, C-Z., Saykally, R. J., and Yang, P., 2005, “Optical Routing and Sensing with Nanowire Assemblies,” *Proceedings of the National Academy of Science*, **102**, pp. 7800-7805.

Sokolov, K., Khodorchenko, P., Petukhov, A., Nabiev, I., Chumanov, G. and Cotton, T. M., 1993, “Contributions of Short-Range and Classical Electromagnetic Mechanisms to SERS from Several Types of Biomolecules Adsorbed on Cold-Deposited Island Films,” *Applied Spectroscopy*, **41**, pp. 515-522.

Sommerfeld, A. M., 1909, “Propagation of Waves in Wireless Telegraphy,” *Annals of Physics* (Paris), **28**, pp. 665-736.

Sparks, M., Mills, D. L., Warren, R., Holstein, T., Maradudin, A. A., Sham, L. J., Loh, E. and King, D. F., 1981, “Theory of Electron-Avalanche Breakdown in Solids,” *Physical Review B*, **24**, pp. 3519-3536.

Srituravanich, W., Fang, N., Sun, C., Luo, Q., and Zhang, X., 2004, "Plasmonic Nanolithography", *Nano Letters*, **4**, pp. 1085-1088.

Stockman, M., 2004, “Nanofocusing of Optical Energy in Tapered Plasmonic Waveguides,” Physical Review Letters, **93**, 137404.

Stuart, B. C., Feit, M. D., Rubenchik, A. M., Shore, B. W. and Perry, M. D., 1995, “Laser-Induced Damage in Dielectrics with Nanosecond to Subpicosecond Pulses,” *Physical Review Letters*, **74**, pp. 2248-2251.

Stuart, B. C., Feit, M. D., Herman, S., Rubenchik, A. M., Shore, B. W. and Perry, M. D., 1996, “Nanosecond-to-Femtosecond Laser Induced Breakdown in Dielectrics,” *Physical Review B*, **53**, pp. 1749-1761.

Sun, Z. and Kim, H. K., 2004, “Refractive Transmission of Light and Beam Shaping with Metallic Nano-optic Lenses,” *Applied Physics Letters*, **85**, pp. 642-644.

Sweatlock, L. A., Maier, S. A., Atwater, H. A., Penninkhof, J. J. and Polman, A., 2005, “Highly Confined Electromagnetic Fields in Arrays of Strongly Coupled Ag Nanoparticles,” *Physical Review B*, **71**, 235408.

Taflove, A. and Hagness, S., 2005, *Computational Electrodynamics, Third Edition*, Artech House, Boston-London.

Teperik, T. V., Popov, V. V. and Garcia de Abajo, F. J., 2004, “Radiative Decay of Plasmons in a Metallic Nanoshell,” *Physical Review B*, **69**, 155402.

Theppakuttai, S., Shao, D., and Chen, S.C., 2004, "Localized Laser Transmission Bonding for Microsystem Fabrication and Packaging", *Journal of Manufacturing Processes*, **6**, pp. 24-31.

Theppakuttai, S., 2006, “Laser Micro/Nano Scale Processing of Glass and Silicon,” Ph.D Dissertation, The University of Texas at Austin.

Town, R. P. J., Bell, A. R. and Rose, S. J., 1995, “Fokker-Planck Calculations with Ionization Dynamics of Short-Pulse Laser-Solid Interactions,” *Physical Review Letters*, **74**, pp. 924-927.

Tsai B.K., Meyer C.W., Lovas, F.J., 2000, In proceedings of *8th Int. Conf. On Adv. Therm. Process of Semicond—RTP ’2000* (Edited by D.P. DeWitt, J. Kowalski, B. Lojek, A. Tillmann), Gaithersburg, RTP‘2000, pp. 83-93

Van de Hulst, H., 1957, *Light Scattering by Small Particles*, Wiley, New York, NY.

Van Marum, M., 1799, “Beschreibung einer grossen electrischen Batterie von 550 Quadratfuss Belegung und einiger damit angestellter Versuche,” *Annalen der Physik*, **1**, pp.68-87.

Volokitin, A. I. and Persson, B. N. J., 2001, “Radiative Heat Transfer Between Nanostructures,” *Physical Review B*, **63**, 205404.

Wang, Z.B., Hong, M.H., Luk’yanchuk, B.S., Huang, S.M., Wang, Q.F., Shi, L.P., Chong, T.C., 2004, “Parallel nanostructuring of GeSbTe film with particle mask,” *Appl. Phys. A:Mater. Sci. Process*, **79**, 1603.

Weeber, J. C., Bourillot, E., Dereux, A., Goudonnet, J-P, Chen, Y., and Girard, C., 1996, **“**Observation of Light Confinement Effects with a Near-Field Optical Microscope,” *Physical Review Letters*, **77**, pp. 5332-5335.

Worthing, P. T. and Barnes, W. L., 2001, “Efficient Coupling of Surface Plasmon Polaritons to Radiation Using a Bi-Grating,” *Applied Physics Letters*, **79**, pp. 3035-3037.

Wurtz, G. A., Im, J. S., Gray, S. K. and Wiederrecht, G. P., 2003, “Optical Scattering from Isolated Metal Nanoparticles and Arrays,” *Journal of Physical Chemistry B*, **107**, pp. 14191-14198.

Yan, B. H., Wang, A. C., Huang, C. Y., Hunag, F. Y., 2002, “Study of precision micro-holes in borosilicate glass using micro EDM combined with micro ultrasonic vibration machining,” *International Journal of Machine Tools & Manufacture*, **42**, pp. 1105-1112.

Yang, W.-H., Schatz, G. C. and Van Duyne, R. P., 1995, “Discrete Dipole approximation for Calculating Extinction and Raman Intensities for Small Particles with Arbitrary Shapes,” *Journal of Chemical Physics*, **103**, pp. 869-875.

Ye, M. and Grigoropoulos, C. P., 2001, “Time-of-Flight and Emission Spectroscopy Study of Femtosecond Laser Ablation of Titanium,” *Journal of Applied Physics*, **89**, pp. 5183-5190.

Yee, K. S., 1966, “Numerical Solution of Initial Boundary Value Problems Involving Maxwell’s Equations in Isotropic Media,” *IEEE Trans. Antennas Propagat*., **14**, pp. 302-307.

Yin, L., Vlasko-Vlasov, V. K., Pearson, J., Hiller, J. M., Hua, J., Welp, U., Brown, D., and Kimball, C. W., 2005, “Subwavelength Focusing and Guiding of Surface Plasmons,” *Nano Letters*, **5**, pp. 1399-1402.

Youn, S. W., Kang, C. G., 2005, “Maskless Patterning of Borosilicate Glass Nanoindentation-Induced Etch-Hillock Surface Using Phenomena,” *Journal of Non-Crystalline Solids*, **351(37-39)**, pp. 3065-3074.

Zenneck, J., 1907, (*Tr*. "Over the reproduction of even electromagnetic waves of an even leader-flat and their relationship with the wireless telegraphy"), *Annalen der Physik*, **23**, pp. 846-866.

Zhao, J., Huettener, B. and Menschig, A., 2001, “Microablation with Ultrashort Laser Pulses,” *Optics and Laser Technology*, **33**, pp. 487-491.

Zhang, J., Sugioka, K., Midorikawa, K., 1998, “High-speed machining of glass materials by laser induced plasma assisted ablation using a 532-nm laser,” *Applied Physics A-Materials Science & Processing*, **67**, pp. 499-501.

Zhang, J., Sugioka, K., Midorikawa, K., 1999, “High-Quality and High-Efficiency Machining of Glass Materials by Laser-Induced Plasma-Assisted Ablation Using Conventional Nanosecond UV, Visible, and Infrared Lasers,” *Applied Physics A*, **69**, 879.

Zheng, Y.W., Luk’yanchuk, B.S., Lu, Y.F., Song, W.D. Mai, Z.H., 2001, “Dry Laser Cleaning of Particles from Solid Substrates: Experiments and Theory,” *J. Appl. Phys*., **90**, 2135.

Zhou, Y., Hong, M. H., Fuh, JYH, Lu, L., Luk'yanchuk, B. S., Wang, Z. B., Shi, L. P. and Chong, T. C., 2006, "Direct Femtosecond Laser Nanopatterning of Glass Substrate by Particle-Assisted Near-Field Enhancement," *Applied Physics Letters*, **88**, 023110.

Vita

Alexander John Heltzel was born in Columbia, South Carolina on October 31, 1979, the son of Terence and Cathy. Ten days later, he moved to Warren, Ohio where he was raised for 17 years. After graduating from John F. Kennedy High School in 1997, he attended The University of Dayton in Dayton, Ohio, obtaining a bachelor's degree in 2002 and a master's degree in 2003, both in mechanical engineering. After his marriage to wife, Leigh, in August 2003, he moved to Austin, Texas to pursue doctoral studies under Professor John R. Howell. As a graduate student in the thermal/fluids systems section of the department, his research focused on computational electrodynamics and heat transfer. During their time in Texas, he and his wife welcomed two daughters, Margot and Samantha into their family.

Permanent address: 4600 Seton Center Parkway
Apt. 408
Austin, TX, 78759

This dissertation was typed by the author.